



**Mondragon  
Unibertsitatea**

**Faculty of  
Engineering**

**PhD Course in Applied Engineering**

**Design and characterization of lightweight non-equiatomic  
Al-Zn-Mg-Si Medium Entropy Alloys**

**Juan José Trujillo Tadeo**

Supervised by:

Dr. Iñaki Hurtado

Dr. Gurutze Arruebarrena Lizarralde

Mechanical and industrial production department

Mondragon Unibertsitatea

February 2024



## Declaration of originality

---

I hereby declare that this dissertation and the work described in it are the product of my own work and that, to the best of my knowledge, it contains no previously published material except where due acknowledgement has been made in the text as noted by citations. This PhD thesis has not been submitted for any other degree or diploma of Mondragon Unibertsitatea or other institute of higher education. The copyright of this document including data, figures, tables, and text rests with the author and all the assistance received in preparing it have been acknowledged.

Signed: Juan José Trujillo Tadeo

Mondragon, February 2024

## Copyright and reproduction rights

The copyright of this thesis belongs to Juan José Trujillo Tadeo, 2024.

I authorize the University of Mondragon to reproduce this document, in full or in part, for other institutions or individuals with exclusively academic objectives.







## Agradecimientos

---

Recuerdo que, en noviembre de 2019, tuve una entrevista para aplicar a una posición de doctorado en el País Vasco. La entrevista fue a las 4 am, hora de México, y a las 12 pm en el País Vasco. La realicé con mis asesores de tesis, Gurutze e Iñaki, quienes ahora son más que eso, son parte de mi familia. A pesar de tener pocos conocimientos de metalurgia, la entrevista me dio muchos ánimos para aplicar, ya que la confianza y el apoyo que me ofrecieron desde el primer momento me animó a venir. Así fue como, a finales de febrero de 2020, llegué a la Universidad de Mondragon. He pasado de estar solo y encerrado en un piso a solo dos semanas de haber llegado, a después de mejorar en cierta medida la situación de la pandemia, tener bonitas experiencias en las cuales he aprendido mucho. He hecho buenas amistades, he conocido un poco de la cultura del País Vasco y disfrutado de sus hermosos paisajes, y de eso siempre lo llevaré conmigo. Por eso, quiero dedicar esta tesis y, sobre todo, agradecer a las personas que siempre estuvieron apoyándome en cualquier momento.

En primer lugar, agradezco a mis directores de tesis, la Dra. Gurutze Arruebarruena Lizarralde y al Dr. Iñaki Hurtado Hurtado, por su valiosa contribución a esta tesis. Su guía no se limitó solo al aspecto técnico, sino que también abarcó una dimensión humana, y por eso les estoy profundamente agradecido. Su constante apoyo, tanto en lo técnico como en lo personal, ha sido fundamental, y considero a ambos como parte de mi familia. También quiero agradecer por los recursos materiales y económicos proporcionados por el Departamento de Mecánica de Producción Industrial de MGEP. Especialmente, quiero agradecer a todo el equipo de Fundación-NSF por tratarme como uno más del equipo.

De igual manera, expreso mi reconocimiento, agradecimiento y confianza que me han brindado y lo siguen haciendo, además de compartir su conocimiento y amistad, a la Dra. Teresa Guraya, Dr. Jose Victoria Hernández, Dr. Xabier Chamorro, Dr. Jokin Lozare, Dr. Gorka Plata, Dr. Iban Vicario, Yoana Bilbao y al Dr. Dorantes por su contribución a este trabajo.

A mis compis, Pablo, Dani, Olaia, Sajjad y Andrea, les agradezco todas las horas y toda la cafeína que hemos compartido en el laboratorio de conformado de Garaia. De igual manera, a todos mis compañeros de la sala de doctorandos, tanto aquellos que han llegado antes a la meta como aquellos que siguen en el camino de terminar su tesis doctoral. A todos los amigos que he hecho a lo largo de esta etapa, y que no terminaría de escribir sus nombres aquí, entre ellos (Faruk, Adrian, Gio, Manex, Enrique, Harby, Chloe, Kerlys, Harry, Rodolfo, Miriam, Joana, Hiram, Markel, Junghoon, ...).

No puedo olvidarme de mis compadres Pablo Michelena y Pablo Sanchez que me han aceptado como parte de su familia y me han apoyado en cualquier situación y me han dado ánimos para seguir adelante con la tesis. Agradezco de corazón su amistad y saben que donde yo esté siempre contarán conmigo y tienen lugar siempre donde llegar, ya sea en México, Alemania, Hong Kong o donde esté.

Y por último y más importante, agradezco a mi familia, mi padre Juan, mi madre Cristina, mi hermana Ruby y mi hermano Moisés, por siempre estar al pendiente de mí y por su apoyo y amor incondicional. Sé que estamos lejos, pero siempre los llevo en mi corazón a donde vaya y quiero que sepan lo orgulloso que estoy de tenerlos y lo mucho que los amo.

Juan José Trujillo Tadeo: *Design and characterization of lightweight non-equiatomic Al-Zn-Mg-Si Medium Entropy Alloys*, PhD course in applied engineering, February 2024

## Abstract

---

The development of lightweight materials for the transportation and aerospace industry is a crucial challenge today. Reducing weight without compromising structural properties and without significantly increasing costs is essential to mitigate fuel consumption and greenhouse gas emissions. While alloys of aluminum, magnesium, titanium, and beryllium, with densities ranging from 1.74 to 4.43 g/cm<sup>3</sup>, are commonly used, their limited properties and costs have driven the search for new alloys.

High entropy alloys (HEAs), complex composition alloys (CCAs), and multiple element alloys (MPEAs) have gained attention due to their unique combination of properties. By exploring the central region of phase diagrams with multiple components, these alloys offer high strength, ductility, superconductivity, catalytic activity, corrosion resistance, and radiation tolerance.

A novel subcategory, lightweight high-entropy alloys, incorporates light metallic elements to reduce weight while maintaining exceptional mechanical properties. Leveraging the high-entropy effect, these alloys promote the formation of solid solution phases instead of complex intermetallic phases. This innovative approach opens up new possibilities for developing advanced materials that outperform some established ones, showing great potential.

However, these new lightweight high-entropy alloys exhibit high compression strength and hardness but often have little to no ductility. Therefore, this thesis focuses on designing lightweight alloys applying the high-entropy concept to select elements that can form an alloy with a high FCC solid solution, a crystal structure known for its high ductility, to address this issue.

Furthermore, a thorough understanding of the physical and mechanical properties of these alloys is sought to evaluate their potential in future applications. To achieve this, chemical compositions have been defined to ensure good compatibility, high solubility, and melting at intermediate temperatures to form a high FCC solid solution. In-depth research into phase transformations in the designed alloy provides profound insights.

From this perspective, compression properties were evaluated, and two techniques were applied to optimize and enhance mechanical properties, with a particular focus on achieving ductility. For the first technique, chemical composition was adjusted, and modifying elements like Sr and Sb were used, followed by heat treatments for phase modification, aiming to improve mechanical properties with special attention to ductility.

For the second technique, two manufacturing methods, Near Solidus Forming and Directional Solidification, followed by heat treatments, were explored to change the microstructure and improve strength properties and achieve ductility through another approach. The results obtained from these two approaches, both chemical and process-related, have shown good compression strength properties. However, ductility has not been achieved through either of these methods. It is confirmed that the designed alloy is not suitable for applications requiring ductility. Nevertheless, it might find other applications where high hardness, compression strength, or wear resistance are needed.

Juan José Trujillo Tadeo: *Design and characterization of lightweight non-equiatomic Al-Zn-Mg-Si Medium Entropy Alloys*, PhD course in applied engineering, February 2024

## Resumen

---

El desarrollo de materiales ligeros para la industria del transporte y aeroespacial representa un desafío crucial en la actualidad. Reducir el peso sin comprometer las propiedades estructurales y sin aumentar significativamente los costos es esencial para mitigar el consumo de combustible y las emisiones de gases de efecto invernadero. Aunque las aleaciones de aluminio, magnesio, titanio y berilio, con densidades entre 1.74 y 4.43 g/cm<sup>3</sup>, son comúnmente utilizadas, sus propiedades limitadas y costos han impulsado la búsqueda de nuevas aleaciones.

Las aleaciones de alta entropía (HEAs), composición compleja (CCAs) y elementos múltiples (MPEAs) han ganado atención gracias a su combinación única de propiedades. Al explorar la región central de diagramas de fases de varios componentes, estas aleaciones ofrecen alta resistencia, ductilidad, superconductividad, actividad catalítica, resistencia a la corrosión y tolerancia a la radiación. Una subcategoría novedosa, las aleaciones ligeras de alta entropía, incorpora elementos metálicos ligeros para reducir el peso manteniendo propiedades mecánicas excepcionales. Aprovechando el efecto de alta entropía, estas aleaciones fomentan la formación de fases de solución sólida en lugar de fases intermetálicas complejas. Este enfoque innovador abre nuevas posibilidades para desarrollar materiales avanzados que superan a algunos establecidos, mostrando un gran potencial. Sin embargo, estas nuevas aleaciones ligeras de alta entropía poseen alta resistencia a la compresión y dureza, pero suelen tener poca o nula ductilidad. Por lo tanto, la presente tesis se centra en diseñar aleaciones ligeras aplicando el concepto de alta entropía con el objetivo de seleccionar los elementos que logren formar una aleación con una alta solución sólida FCC, una estructura cristalina conocida por su alta ductilidad, para abordar este problema.

Además, se busca comprender a fondo las propiedades físicas y mecánicas de estas aleaciones para evaluar su potencial en futuras aplicaciones. Para lograr esto, se han definido composiciones químicas que aseguran buena compatibilidad, alta solubilidad y fusión a temperaturas intermedias para formar una alta solución sólida FCC. La investigación de las transformaciones de fase en la aleación diseñada proporciona un conocimiento profundo. Desde este enfoque, se evaluaron las propiedades a compresión y se aplicaron dos técnicas para optimizar y mejorar las propiedades mecánicas, centrándose especialmente en lograr ductilidad.

Para la primera técnica, se ajustó la composición química y se utilizaron elementos modificadores como Sr y Sb, seguido de tratamientos térmicos para la modificación de fases, buscando mejorar las propiedades mecánicas con especial atención a la ductilidad.

Para la segunda técnica, se exploraron dos métodos de fabricación, Near Solidus Forming (NSF) y Solidificación Direccional seguidos de tratamientos térmicos, con el objetivo de cambiar la microestructura y así mejorar las propiedades de resistencia y obtener ductilidad por otro camino. Los resultados obtenidos de estos dos enfoques, tanto químico como de proceso, han mostrado buenas propiedades de resistencia a la compresión. Sin embargo, no se ha logrado obtener ductilidad por ninguna de estas vías. Se confirma que la aleación diseñada no es apta para aplicaciones donde se requiera ductilidad; no obstante, podría tener otras aplicaciones donde se necesite alta dureza, resistencia a la compresión o resistencia al desgaste.

Juan José Trujillo Tadeo: *Design and characterization of lightweight non-equiatomic Al-Zn-Mg-Si Medium Entropy Alloys*, PhD course in applied engineering, February 2024

## Laburpena

---

Nabarmendu beharrezkoa da, garraketa eta hegazkina industriari zuzendutako materialen garapena erronka garrantzitsua dela egun. Pisua murriztea, egitura propietateak kentzea eta kostuak nabarmen handitzea garrantzitsua da, kutsaduren kontsumoa eta kasu efektu berdearen gasak murrizteko. Aluminio, magnesio, titanio eta berilio aleazioak, 1.74 eta 4.43 g/cm<sup>3</sup> arteko densitateekin, ohiko erabiltzen diren, baina propietate mugatuak eta kostuak beren bilaketa bultzatu dute.

Entropia handiko aleazioak (HEAs), konposizio konplexuak (CCAs) eta elementu anitzak (MPEAs) atentzioa jaso dute propietate bereziak uztartzen dituztenak. Hainbat konponenteen diagramen eremu erdiko esploratzean, aleazio horiek indar handiko, haustekortasun handiko, superkonduktibitatea, katalizatzaile jarduera, korrosioa eta erradiadura tolerantzia eskaintzen dituzte. Kategoría berri bat, entropia handiko aleazio arinak, metal larrizko elementuak hartzen ditu pisua murrizteko eta propietate mekaniko apartak mantentzeko. Entropia handiko efektua aprobeztatuz, aleazio hauen soluzio solidoen faseak sortzeko xedea dute fase intermetaliko konplexuak baino. Ikuspegi berritzaile honek aukera berriak irekitzen ditu material aurreratuak garatzeko, batera ezarritako batzuei gainera potentzial handia erakusten duena. Hala ere, entropia handiko aleazio arin berri hauek indar handiko konpresioa eta gogortasuna izaten dute, baina ohiz gutxi edo ez dute haustekortasuna. Horregatik, tesi honen ardatza entropia handiko kontzeptua aplikatzen aleazio arinak diseinatzen duten aldean kokatzen da, aluminiozko soluzio solido FCC handia sortzeko elementuak hautatzeko helburuarekin, hauxe izanik arazo hau arakatzeko.

Gainera, aleazio horien propietate fisiko eta mekanikoak ondo ulertzeko asmoa dugu, etorkizuneko aplikazioetan duten potentziala aztertzeko. Horretarako, bateragarritasun ona, solubilitate handia eta tenperatura ertainean funtzionatzeko konposizio kimikoak definitu dira, aluminiozko soluzio solido FCC handia sortzeko. Diseinatutako aleazioan fase aldaketak aztertzeko ikerketa sakona egin da. Ikuspegi honetatik, konpresio propietateak aztertu dira eta propietate mekanikoak optimizatzeko eta hobetzeko bi teknika aplikatu dira, hauek bereziki haustekortasuna lortzeko arreta jarraituz.

Lehenengo teknika gisa, konposizio kimikoak moldatu dira eta Sr eta Sb bezalako elementu moldatzaileak erabiliz, fase aldaketarako tenperatura tratamenduak erabiliz, mekaniko propietateak hobetzeko, haustekortasunari bereziki arreta jarraituz.

Bigarren teknika gisa, fabrikazio metodo bi esploratu dira, Solidifikazio Zuzena (NSF) eta Solidifikazio Zuzena, eta ondoren tenperatura tratamenduak, mikro-egitura aldatzeko helburuarekin, indarraren propietateak hobetzeko eta haustekortasuna beste bide batean eskuratzea. Bi hurbilketa hauetatik lortutako emaitzak, kimiko eta prozesuari begirakoak, konpresio propietate onak erakutsi dituzte. Hala ere, haustekortasuna lortu ez da inongo bidez. Dena den, diseinatutako aleazioa ez da haustekortasun bat eskatzen duten aplikazioetarako egokia dela baieztatu da; hala ere, luzeran, gogortasun handia, konpresioaren erresistentzia edo gastuaren erresistentzia behar duten aplikazioetarako erabilgarria izan daiteke.



Juan José Trujillo Tadeo: *Design and characterization of lightweight non-equiatomic Al-Zn-Mg-Si Medium Entropy Alloys*, PhD course in applied engineering, February 2024

# Contents

---

1. Introduction.....	1
1.1. Context.....	1
1.2. Motivation.....	3
1.3. Objectives .....	4
1.4. Dissertation outline .....	4
2. Literature Review .....	7
2.1. Definitions .....	7
2.2. Thermodynamic aspects .....	9
2.2.1. Entropy.....	10
2.3. Four core effects of HEAs .....	13
2.4. Light weight HEAs .....	14
2.5. Alloy design and phase selection rules in LW-HEAs.....	15
2.5.1. Predicting solid solubility from Hume-Rothery rules.....	15
2.5.2. Parameters to predict the formation of solid solution in LW-HEAs.....	16
2.6. LW-HEAs design using integrated computational materials engineering (ICME)...	20
2.6.1. CALPHAD method.....	20
2.7. Processing of LW-HEAs .....	21
2.7.1. Casting method .....	21
2.8. Microstructural and mechanical properties of LW-HEAs .....	22
2.9. Critical review.....	25
3. Numerical and experimental procedures .....	26
3.1. Design strategy .....	27
3.1.1. Alloy design using empirical parameters and CALPHAD .....	27
3.2. Alloy Casting Processes.....	27
3.2.1. First alloy casting .....	27
3.2.2. Alloy casting with optimized composition .....	28
3.3. Additional processing routes .....	29
3.3.1. Sand casting process .....	30
3.3.2. Near Solidus Forming process .....	32
3.3.3. Directional Forming process.....	33
3.4. Design of heat treatments using CALPHAD & DSC .....	34
3.5. Material characterization .....	34
3.5.1. Preparation for microstructural analysis. ....	34
3.5.2. SEM and EDX analysis.....	34
3.5.3. TEM analysis .....	35
3.5.4. XRD phase analysis .....	35
3.5.5. EBSD analysis.....	36
3.5.6. Compression test.....	36
3.5.7. Hardness measurements.....	37
3.5.8. DSC.....	38
3.5.9. Density measurements .....	38

4.	Alloy design and heat treatments of LW-MEA .....	39
4.1.	Introduction.....	39
4.1.1.	CALPHAD approach to design LW-MEA .....	40
4.2.	Results.....	45
4.2.1.	Prediction of solid solution formation using empirical parameters .....	45
4.2.2.	Phase stability simulations by CALPHAD .....	47
4.2.3.	Analysis of microstructure prior to heat treatments.....	49
4.2.4.	Design of heat treatments.....	50
4.2.5.	Effect of the heat treatment on the microstructure.....	52
4.2.6.	Hardness of samples.....	53
4.3.	Discussion.....	54
4.3.1.	Solid solution prediction by empirical parameters .....	54
4.3.2.	Phase evolution analysis .....	54
4.3.3.	Miscibility gap validation and HCP evolution.....	57
4.4.	Conclusions.....	59
5.	Optimizing and Customizing Chemical Composition of LW-MEA .....	61
5.1.	Introduction.....	61
5.2.	Results.....	66
5.2.1.	Composition optimization by CALPHAD .....	66
5.2.2.	Microstructural analysis of the alloy and Mg <sub>2</sub> Si phase modification .....	72
5.2.3.	Impact of heat treatment on microstructure and Mg <sub>2</sub> Si phase modification.....	78
5.2.4.	Mechanical properties in compression of optimized alloys.....	84
5.3.	Discussion.....	85
5.3.1.	Composition optimization analysis .....	85
5.3.2.	Modification of Mg <sub>2</sub> Si phase .....	86
5.3.3.	Mechanisms for modification and refinement of Mg <sub>2</sub> Si phase.....	86
5.3.4.	Compression behaviours of modified alloys.....	89
5.4.	Conclusions.....	90
6.	Enhancing Microstructure via Manufacturing Methods of LW-MEA .....	91
6.1.	Introduction.....	91
6.2.	Results.....	93
6.2.1.	Solidification rate in sand casting .....	93
6.2.2.	Component manufacturing by NSF .....	95
6.2.3.	Solidification rate in directional solidification process.....	97
6.2.4.	Microstructural examination .....	100
6.2.5.	XRD analysis of the optimized LW-MEA.....	101
6.2.6.	Compression properties.....	102
6.2.7.	Fractographic observations .....	104
6.3.	Discussion.....	108
6.3.1.	Effect of different manufacturing processes on LW-MEA.....	108
6.3.2.	Effect of the heat treatment on LW-MEA. ....	108
6.4.	Conclusions.....	109
7.	Conclusions and Future Work .....	110
7.1.	General Conclusions .....	110
7.2.	Future work.....	112

7.3. Publications and conferences.....	113
Bibliographic References.....	114

## List of figures

Fig. 1-1. Historical evolution of engineering materials - marked by the emergence of high entropy alloys, adapted from [13].	2
Fig. 1-2. a) Statistics on the number of publications on high entropy alloys per year until September 2023 b) Statistics on the main countries conducting research on high entropy alloys up to September 2023.	3
Fig. 1-3. Document structure and research workflow.	6
Fig. 2-1. Evolution of alloys, adapted from [33].	8
Fig. 2-2. The configurational entropy reaches its maximum when in a binary system the composition is equimolar [2].	11
Fig. 2-3. Entropy of mixing as a function of the number of elements for equimolar alloys in completely disordered states [37].	11
Fig. 2-4. Classification of alloys based on entropy quantification [39].	12
Fig. 2-5. Schematic diagram showing large lattice distortion exists in five component BCC lattice [3].	14
Fig. 2-6. The effect of $\Delta S_{mix}$ , $\Delta H_{mix}$ and $\delta$ on the phase formation in HEAs and typical multicomponent Bulk Metallic Glasses (BMGs) [52].	17
Fig. 2-7. Plots for annealed HEAs with different phase contents after annealing [62].	19
Fig. 3-1 Research workflow.	26
Fig. 3-2 Stepped mold made of AISI H13 steel (Total volume: 29,177 mm <sup>3</sup> ).	28
Fig. 3-3 Inductotherm induction furnace.	29
Fig. 3-4 Stepped mold made of AISI H13 steel (Total volume: 141,547 mm <sup>3</sup> ).	29
Fig. 3-5 Schematic diagram of the Sand Casting, Near Solidus Forming, Directional Solidification processes, and the associated heat treatments employed in this study.	30
Fig. 3-6 (a) CAD model of the gate and feed system designed using FLOW 3D software; (b) 3D printed mold, filter and insulating sleeve; (c) one half of the mold (cope); (d) the other half the mold(drag).	31
Fig. 3-7 (a) NSF cell (b) The dies used for the NSF process are made of AISI H13 steel, while the forming specimens are fabricated from the LW-MEA.	32
Fig. 3-8 Directional Solidification system. (1) motorized arm; (2) steel crucible coated with boron nitride; (3) induction furnace; (4) bucket filled with water; (5) cylindrical casting ingots.	33
Fig. 3-9 Scanning Electron Microscope model FEI Nova Nano SEM 450.	34
Fig. 3-10 Fischione Model 110 Automatic Twin-Jet Electropolisher.	35
Fig. 3-11 Transmission electron microscope model JEM 2000FXII, JEOL.	35
Fig. 3-12 BRUKER-binary V3 X-ray diffractometer.	36
Fig. 3-13 Interface of the AZtecHKL acquisition and analysis software; The (SrZn <sub>13</sub> ) phase is identified from the candidate list using electron backscatter diffraction pattern (EBSP). This sample corresponds to the Sr and Sb modified alloy detailed in Chapter 6.	36
Fig. 3-14 Zwick 050TM universal testing machine (depicting a test specimen during testing).	37
Fig. 3-15 Zwick Micro Vickers hardness tester.	37
Fig. 3-16 DSC equipment model NETZSCH STA 449 F3 Jupiter.	38
Fig. 4-1 Simplified outline of the contents of Chapter 4: "Alloy design and heat treatments of LW-MEA".	40
Fig. 4-2 Phase diagrams: a) Al-Zn, b) Al-Mg and c) Al-Si (temperature where maximum FCC solid solution is obtained is shown).	42

Fig. 4-3 Isothermal sections at 370°C: a) Al-Zn-Mg system, b) Al-Zn-Mg system with 4 at.% Si, and c) Al-Zn-Mg system with 8 at.% Si. (The shaded region corresponds to the studied zone where the target composition is determined). .....	44
Fig. 4-4 Equilibrium solidification diagram for $Al_{58}Zn_{28}Mg_6Si_8$ LW-MEA calculated by FactSage (The shaded region corresponds to the temperature interval where there is a high percentage of solid solution with an FCC crystal structure). .....	45
Fig. 4-5 The relationship between the parameters $\delta$ and $\Omega$ for multi-component alloys. (“Solid Solutions” indicates the alloy contains only solid solution; “Intermetallics” indicates the alloy mainly contains intermetallic compound and other ordered phases; “S + I” indicates that not only the solid solution could form, but also the ordered compounds could precipitate in multi-component alloys; and “BMGs” indicates the alloy can form amorphous phase) [54]. .....	47
Fig. 4-6 Solidification simulations for $Al_{58}Zn_{28}Mg_6Si_8$ LW-MEA calculated by FactSage (CALPHAD): a) Equilibrium solidification, and b) non-equilibrium solidification (Gulliver - Scheil). .....	48
Fig. 4-7 XRD diffraction patterns for the $Al_{58}Zn_{28}Mg_6Si_8$ LW-MEA “as-cast”, “DHHT” (Double Homogenization Heat Treatment) and “AA” (Artificial Aging) specimens. ....	49
Fig. 4-8 SEM/EDS of the $Al_{58}Zn_{28}Mg_6Si_8$ LW-MEA in condition: a) “As-Cast”, b) “DHHT” (Double Homogenization Heat Treatment) and c) “AA” (Artificial Aging). ....	50
Fig. 4-9 DSC curve of the $Al_{58}Zn_{28}Mg_6Si_8$ LW-MEA heating process. ....	51
Fig. 4-10 Projection of the liquid on the Al-Si-Zn ternary diagram calculated by FactSage (The intersection of the dotted lines determines the composition of the alloy). .....	51
Fig. 4-11 DSC heating curves for the three conditions, “As-Cast”, “DHHT” (Double Homogenization Heat Treatment) and “AA” (Artificial Aging). .....	53
Fig. 4-12 The Zn-Mg binary phase diagram calculated by FactSage. ....	56
Fig. 4-13 Binary Al-Zn diagram showing the miscibility gap of the (Al) phase calculated by FactSage. ....	56
Fig. 4-14 (a-b) Bright-field TEM micrographs and (c-d) selected area electron diffraction patterns (SADP) confirming the phases in the $Al_{58}Zn_{28}Mg_6Si_8$ LW-MEA after double homogenization heat treatment and quenching, (c) SADP of the (Al) FCC phase and (d) SADP of the (Si) phase. ....	58
Fig. 4-15 Micrograph of the specimen in the “AA” (Artificial Aging) condition. In detail, aluminum matrix with precipitated zinc phase. ....	59
Fig. 5-1 Simplified outline of the contents of Chapter 5: “Optimizing and Customizing the Chemical Composition of LW-MEA”. .....	65
Fig. 5-2 Solidification simulations for the optimized $Al_{60}Zn_{27}Mg_{11}Si_2$ (Alloy 1), lightweight multicomponent alloy calculated by FactSage (CALPHAD): a) Equilibrium solidification, and b) non-equilibrium solidification (Gulliver -Scheil). .....	67
Fig. 5-3 Solidification simulations for the optimized $Al_{60}Zn_{27}Mg_{11}Si_2 + Sr_{0.021}Sb_{0.001}$ (Alloy 2), lightweight multicomponent alloy calculated by FactSage (CALPHAD): a) Equilibrium solidification, and b) non-equilibrium solidification (Gulliver -Scheil). .....	69
Fig. 5-4 Solidification simulations for the optimized $Al_{60}Zn_{27}Mg_{11}Si_2 + Sr_{0.136}Sb_{0.031}$ (Alloy 3), lightweight multicomponent alloy calculated by FactSage (CALPHAD): a) Equilibrium solidification, and b) non-equilibrium solidification (Gulliver -Scheil). ....	71
Fig. 5-5 a) SEM-BSE of cast $Al_{60}Zn_{27}Mg_{11}Si_2$ (Alloy 1); b) EDS elemental mapping of the cast $Al_{60}Zn_{27}Mg_{11}Si_2$ (Alloy 1) and, c) high magnification of the $Mg_2Si$ phase. ....	73
Fig. 5-6 a) SEM-BSE of cast $Al_{60}Zn_{27}Mg_{11}Si_2 + Sr_{0.021}Sb_{0.001}$ (Alloy 2); b) EDS elemental mapping of the cast $Al_{60}Zn_{27}Mg_{11}Si_2 + Sr_{0.021}Sb_{0.001}$ (Alloy 2) and, c) high magnification of the $Mg_2Si$ phase. ....	75

Fig. 5-7 a) SEM-BSE of cast $\text{Al}_{60}\text{Zn}_{27}\text{Mg}_{11}\text{Si}_2 + \text{Sr}_{0.136}\text{Sb}_{0.031}$ (Alloy 3); b) EDS elemental mapping of the cast $\text{Al}_{60}\text{Zn}_{27}\text{Mg}_{11}\text{Si}_2 + \text{Sr}_{0.136}\text{Sb}_{0.031}$ (Alloy 3) and, c) high magnification of the $\text{Mg}_2\text{Si}$ phase. ....	77
Fig. 5-8 a) SEM-BSE of the heat-treated $\text{Al}_{60}\text{Zn}_{27}\text{Mg}_{11}\text{Si}_2$ (Alloy 1); b) EDS elemental mapping of the heat-treated $\text{Al}_{60}\text{Zn}_{27}\text{Mg}_{11}\text{Si}_2$ (Alloy 1) and, c) high magnification of the $\text{Mg}_2\text{Si}$ phase.....	79
Fig. 5-9 a) SEM-BSE of the heat-treated $\text{Al}_{60}\text{Zn}_{27}\text{Mg}_{11}\text{Si}_2 + \text{Sr}_{0.021}\text{Sb}_{0.001}$ (Alloy 2); b) EDS elemental mapping of the heat-treated $\text{Al}_{60}\text{Zn}_{27}\text{Mg}_{11}\text{Si}_2 + \text{Sr}_{0.021}\text{Sb}_{0.001}$ (Alloy 2) and, c) high magnification of the $\text{Mg}_2\text{Si}$ phase. ....	81
Fig. 5-10 a) SEM-BSE of the heat-treated $\text{Al}_{60}\text{Zn}_{27}\text{Mg}_{11}\text{Si}_2 + \text{Sr}_{0.136}\text{Sb}_{0.031}$ (Alloy 3); b) EDS elemental mapping of the heat-treated $\text{Al}_{60}\text{Zn}_{27}\text{Mg}_{11}\text{Si}_2 + \text{Sr}_{0.136}\text{Sb}_{0.031}$ (Alloy 3)and, c) high magnification of the $\text{Mg}_2\text{Si}$ phase. ....	83
Fig. 5-11 Compressive curves of Sr-Sb modified and unmodified $\text{Al}_{60}\text{Zn}_{27}\text{Mg}_{11}\text{Si}_2$ alloy at room temperature.....	84
Fig. 5-12 Phase diagram prediction. a) Isopleth of $\text{Al}_{60}\text{Zn}_{27}\text{Mg}_{11}\text{Si}_2\text{Sb}_{0.13}\text{Sr}_x$ highlighting the composition ranges for each alloy, from the unmodified alloy (Alloy 1) to those modified with Sr and Sb (Alloy 2 and Alloy 3) b) Zoom of isopleth diagram. ....	87
Fig. 5-13 Phase mapping of the $\text{Al}_{60}\text{Zn}_{27}\text{Mg}_{11}\text{Si}_2 + \text{Sr}_{0.136}\text{Sb}_{0.031}$ (Alloy 3): a) SEM Secondary electron (SE) image, b) Backscattered electron (BSE) image, and c) Hough transform EBSD map with user-selected libraries for (Al), ( $\text{MgZn}_2$ ), ( $\text{Mg}_2\text{Si}$ ), (Zn) and ( $\text{SrZn}_{13}$ ). ....	89
Fig. 6-1 Simplified outline of the contents of Chapter 6: “Microstructure improvement by LW-MEA fabrication methods”. ....	93
Fig. 6-2 Thermophysical properties of the optimized LW-MEA alloy. ....	94
Fig. 6-3 Cooling curves obtained during the sand-casting process.....	94
Fig. 6-4 Equivalent strain distribution along the specimens with different angles $20^\circ/45^\circ/70^\circ$ . ....	96
Fig. 6-5 The equivalent strain distribution along the specimen with a $45^\circ$ angle during the NSF process at different times. ....	97
Fig. 6-6 Cooling curves obtained during the directional solidification process. ....	98
Fig. 6-7 Cooling curves obtained during the directional solidification process. ....	99
Fig. 6-8 SEM of the $\text{Al}_{60}\text{Zn}_{27}\text{Mg}_{11}\text{Si}_2 + \text{Sr}_{0.021}\text{Sb}_{0.001}$ LW-MEA in condition: a) “Sand Casting As-Cast”, b) “Sand Casting DHHT”, c) “Directional Solidification As-Cast”, d) “Directional Solidification DHHT”, e) “Near Solidus Forming As-Cast”, f) “Near Solidus Forming DHHT”. .	101
Fig. 6-9 XRD diffraction patterns for the $\text{Al}_{60}\text{Zn}_{27}\text{Mg}_{11}\text{Si}_2 + \text{Sr}_{0.021}\text{Sb}_{0.001}$ LW-MEA: a) before and after heat treatment “as-cast” and “DHHT” (Double Homogenization Heat Treatment); comparison of the FCC peak of as-cast and solutionized sample. ....	102
Fig. 6-10 Stress-strain curves in uniaxial compression: a) Non-heat treated alloys processed by Sand Casting, Directional Solidification, and Near Solidus Forming; b) Heat treated alloys processed by Sand Casting, Directional Solidification, and Near Solidus Forming. ....	103
Fig. 6-11 Fracture surfaces of the $\text{Al}_{60}\text{Zn}_{27}\text{Mg}_{11}\text{Si}_2 + \text{Sr}_{0.021}\text{Sb}_{0.001}$ LW-MEA under the following conditions: a) Sand casting “As-cast”, and b) Sand casting “Heat-treated” (Cleavage crack initiated in Laves phase $\text{MgZn}_2$ ). ....	105
Fig. 6-12 Fracture surfaces of the $\text{Al}_{60}\text{Zn}_{27}\text{Mg}_{11}\text{Si}_2 + \text{Sr}_{0.021}\text{Sb}_{0.001}$ LW-MEA under the following conditions: a) NSF “As-cast”, and b) NSF “Heat-treated”. ....	106
Fig. 6-13 Fracture surfaces of the $\text{Al}_{60}\text{Zn}_{27}\text{Mg}_{11}\text{Si}_2 + \text{Sr}_{0.021}\text{Sb}_{0.001}$ LW-MEA under the following conditions: a) DS “As-cast”, and b) DS “Heat-treated”.....	107
Fig. 7-1 Compressive yield strength vs Density of light alloys designed using the high entropy concept. ....	112

## List of tables

---

Table 2-1. The main High Entropy Alloys (HEAs) related definitions. ....	8
Table 2-2. Characteristics for the traditional alloys and the two generations of HEAs, adapted from [33]. ....	9
Table 2-3. Configurational entropies calculated for commercial alloys at their liquid state or random state [2]. ....	13
Table 2-4. Thermodynamic and topological parameters to predict the formation of phases. ....	16
Table 2-5. List of lightweight HEAs, along with their phase involved, density, mechanical properties, and processing route. ....	23
Table 4-1 Characteristics and properties of the selected elements for the design of the LW-MEA. ....	43
Table 4-2. Thermodynamic, topological, and electronic parameters calculated for the Al <sub>58</sub> Zn <sub>28</sub> Mg <sub>6</sub> Si <sub>8</sub> (at. %) alloy to predict the formation of solid solutions and the type of crystalline structure. ....	45
Table 4-3 Chemical composition of LW-MEA obtained with ICP. ....	47
Table 4-4 Heat treatment schedules for the Al <sub>58</sub> Zn <sub>28</sub> Mg <sub>6</sub> Si <sub>8</sub> LW-MEA. ....	52
Table 4-5 Microhardness of the Al <sub>58</sub> Zn <sub>28</sub> Mg <sub>6</sub> Si <sub>8</sub> LW-MEA. ....	54
Table 4-6 The proposed invariant points of the system Al <sub>58</sub> Zn <sub>28</sub> Mg <sub>6</sub> Si <sub>8</sub> LW-MEA. ....	55
Table 5-1 Impact of the modifying elements Sr and Sb on the modification of the intermetallic Mg <sub>2</sub> Si. ....	62
Table 5-2 Chemical compositions of Al <sub>60</sub> Zn <sub>27</sub> Mg <sub>11</sub> Si <sub>2</sub> LW-MEA and Sb-Sr modified Al <sub>60</sub> Zn <sub>27</sub> Mg <sub>11</sub> Si <sub>2</sub> LW-MEA (in atomic percentage at. % and weight percentage wt.%). ....	66
Table 5-3 Heat treatment for the Al <sub>60</sub> Zn <sub>27</sub> Mg <sub>11</sub> Si <sub>2</sub> lightweight multicomponent alloy. ....	78
Table 5-4 Compressive mechanical properties of Sr-Sb modified and unmodified Al <sub>60</sub> Zn <sub>27</sub> Mg <sub>11</sub> Si <sub>2</sub> alloy at room temperature. ....	85
Table 5-5 Electronegativity of Al, Zn, Mg, Si, Sr and Sb elements. ....	86
Table 6-1 Average cooling rate during solidification ....	95
Table 6-2 The average equivalent strain of the NSF (Non-Steady State Flow) process for four different materials extruded in dies with different entry angles (20°/45°/70°). ....	96
Table 6-3 Average cooling rate during the directional solidification. ....	98
Table 6-4 Average cooling rate during the directional solidification. ....	100
Table 6-5 Compression mechanical properties of the Al <sub>60</sub> Zn <sub>27</sub> Mg <sub>11</sub> Si <sub>2</sub> + Sr <sub>0.021</sub> Sb <sub>0.001</sub> LW-MEA at ambient temperature. ....	104



## Acronyms

---

AA	Artificial Aging
AM	Amorphous Phases
ANN	Artificial Neural Networks
BCC	Body Center Cubic
BF	Bright Field
BKD	Backscatter Kikuchi Diffraction
BSE	Backscattered Electron
CALPHAD	Computer Coupling of Phase Diagrams and Thermochemistry
CCA	Complex Concentrated Alloy
CRSS	Critical Resolved Shear Stress
DFT	Density Functional Theory
DHHT	Double Homogenization Heat Treatment
DS	Directional Solidification
DSC	Differential Scanning Calorimetry
EBSD	Electron Backscatter Diffraction
EBSP	Backscatter Diffraction Pattern
EDS	Energy Dispersive X-ray Spectroscopy
FCC	Face Center Cubic
FEM	Finite Element Methods
GPZ	Guinier Preston Zone
HCP	Hexagonal Close Packed
HEA	High Entropy Alloy
HTC	Heat Transfer Coefficient
IC	Intermetallic Compounds
ICDD	International Center for Diffraction Data
ICME	Integrated Computational Materials Engineering
ICP-OES	Inductively Coupled Plasma Optical Emission Spectroscopy
LFA	Laser Flash Analysis
LPE	Lattice Potential Energy
LW-HEA	Lightweight High Entropy Alloy
LW-MEA	Lightweight Medium Entropy Alloy
MA	Mechanical Alloying
MC	Monte Carlo
MD	Molecular Dynamics
MPEA	Multi Principal Elements Alloy
NSF	Near Solidus Forming

PF	Phase Field
RT	Room Temperature
SADP	Selected Area Electron Diffraction
SEM	Scanning Electron Microscope
SPS	Spark Plasma Sintering
SS	Solid Solution
SSM	Semi Solid Metal
TEM	Transmission Electron Microscopy
UTS	Ultimate Tensile Strength
VEB	Valence Electron Bonds
VEC	Valence Electron Concentration
XRD	X-ray Diffraction
YS	Yield Strength

## Symbols

Notation	Unit	Description
$\Delta G_{mix}$	kJ/mol	Gibbs free energy of mixing change
$\Delta H_{mix}$	kJ/mol	Change in enthalpy of mixing
$\Delta S_{mix}$	J/(mol K)	Change in entropy of mixing
$T$	K	Absolute temperature
$\Delta S$	J/K	Entropy changes
$\Delta Q$	J/s	Heat flow changes
$S$	J/K	Entropy
$k_B$	J/K	Boltzmann's constant
$\Delta S_\sigma$	J/(mol K)	Mismatch entropy normalized
$VEC$	-	Valence electron concentration
$W$	-	Frecuency of ocurrence of a microstate
$\Delta S_{magn}$	J/K	Change in magnetic entropy of mixing
$\Delta S_{elec}$	J/K	Change in electronic entropy of mixing
$\Delta S_{vibr}$	J/K	Change in vibrational entropy of mixing
$\Delta S_{conf}$	J/K	Change in configurational entropy of mixing
$R$	J/(mol K)	Gas constant
$X_i$	-	Atomic percentage of component
$\Omega$	-	Omega parameter to predict solid solution formation
$\gamma$	-	Critical value of packing misfitting
$\delta$	-	Atomic size differences between the constituent elements
$\mu$	-	The ratio of the ideal melting temperature of the alloy
$\Delta\chi$	-	Electronegativity difference between the constituent elements
$\Phi$	-	The relationship between the Gibbs free energies of a solid solution and intermetallics
$S_m$	-	Interatomic spacing mismatch
$K_m$	-	Bulk modulus mismatch
$r_i$	nm	Atomic raddi of ith element
$c_i$	-	Composition of ith element
$\bar{r}$	nm	Average atomic radius
$T_m$	K	Hypothetical melting temperature
$\Delta H_{IM}$	kJ/mol	Enthalpy of formation for intermetallic phases
$\Delta S_{IM}$	kJ/(mol K)	Entropy of formation for intermetallic phases

$\kappa_1^{cr}(T)$

$\frac{e}{a}$

- Parameter for predict phase formation in high entropy alloys
- Electron concentration based on the average number of valence electrons per atom."



# Chapter 1

## 1. Introduction

*This chapter explores the historical evolution of materials, underscoring the significance of research in high entropy alloys. It emphasizes that this field is crucial for advancing materials science and unlocking the full potential of these innovative alloys. The increasing popularity of high entropy alloys and the leadership of advanced nations in this research underscore their importance and the need to continue exploring this exciting field.*

### 1.1. Context

Throughout history, the discovery of new materials has been crucial for the advancement of civilization. Epochs such as the Stone Age, Copper Age, Bronze Age, and Iron Age mark the milestones of these discoveries that shaped technology [1]. Fig. 1-1 illustrates this historical journey of engineering materials.

During the First Industrial Revolution in the 18th century, particularly in England, there was a significant breakthrough in alloy development. About 30 alloy systems based on a principal metal element, such as high-speed steels, stainless steels, and aluminum and titanium alloys, were created [2,3].

However, the traditional approach to designing alloys, based on established phase diagrams and the addition of secondary elements, has limitations. This method often explores the boundaries of phase diagrams, making it challenging to discover alloys with multiple components in significant quantities. This led to the need for innovative methods [2].

In 2004, two independent research studies broke away from the traditional approach to alloy design with the publication of two scientific papers titled "*Nanostructured high-entropy alloys with multiple principal elements*" by the Yeh team in Taiwan [4], and "*Microstructural development in equiatomic multicomponent alloys*" by the Cantor team in the United Kingdom [5].

Despite differences in the definitions used by Yeh and Cantor to describe these new alloys, both research studies have focused on investigating alloys composed of five or more metallic elements in equimolar or non-equimolar quantities. Surprisingly, the results have shown the formation of stable single-phase solid solutions (SS) either FCC or BCC rather than complex intermetallic compounds (IC), which contradicts the traditional alloy design concept.

Therefore, these novel alloys have gained significant attention due to their remarkable properties, including high hardness, high strength at both room and elevated temperatures, ductility, superconductivity, high catalytic activity, radiation tolerance, high toughness, oxidation resistance, good wear resistance, corrosion resistance, and diffusion barrier capabilities, among others [1–3,6–12]. This new alloy design concept offers a new path for developing advanced materials with unique

properties and promising opportunities that cannot be achieved by the classical microalloying technique, which is based on a single dominant element.

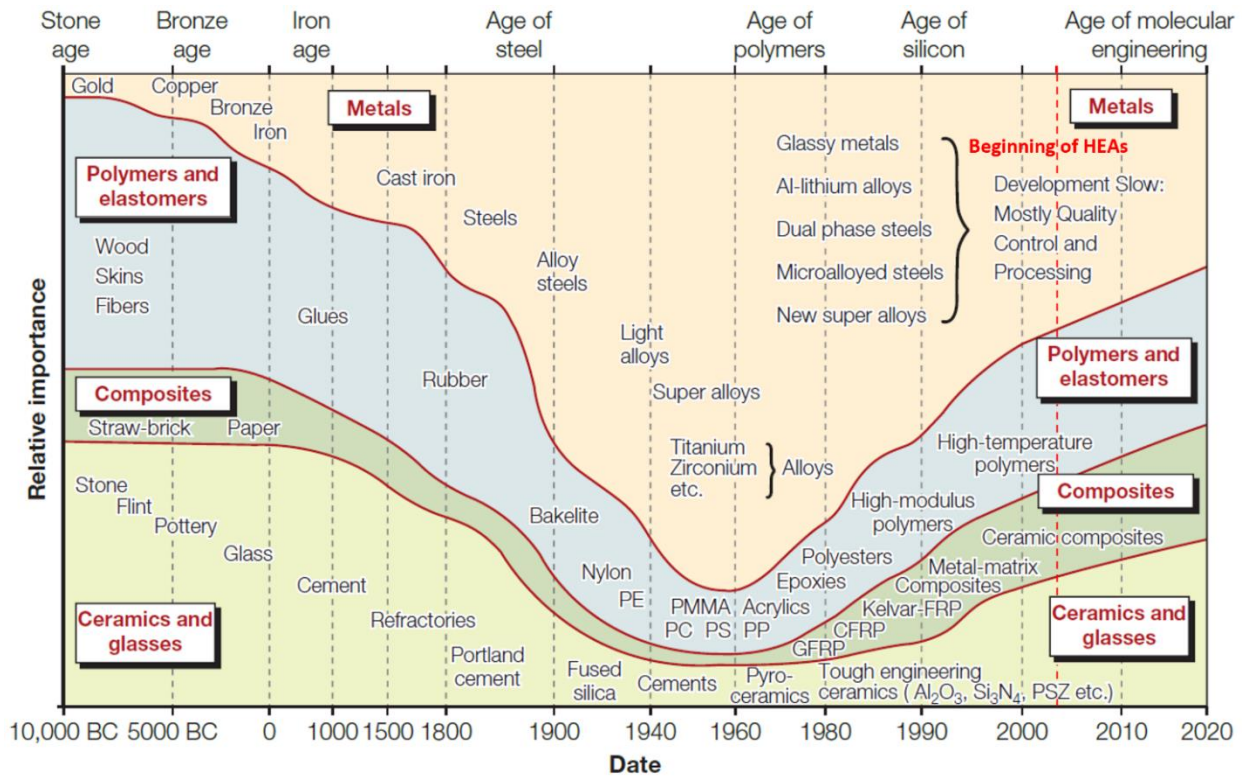


Fig. 1-1. Historical evolution of engineering materials - marked by the emergence of high entropy alloys, adapted from [13].

For the design and prediction of solid solution phase formation in these novel alloys, criteria based on thermodynamic parameters and rules are used, employing methodologies such as Calculation of Phase Diagrams (CALPHAD), ab initio models, molecular dynamics (MD), density functional theory (DFT), and artificial neural networks (ANN) [14–19]. To date, the CALPHAD method could be considered the most direct approach for the design of lightweight multicomponent alloys [20]. The most significant advantage of the CALPHAD method is that it predicts higher-order phase diagrams by extrapolating from its lower-order constituent systems, such as binary and ternary systems [21].

As we approach 2024, there is an increase in publications on high-entropy alloys, indicating a growing interest, as depicted in Fig. 1-2a. Leading countries such as China, the United States, Korea, and Japan are at the forefront of research, recognizing the revolutionary potential and allocating substantial resources, as illustrated in Fig. 1-2b.

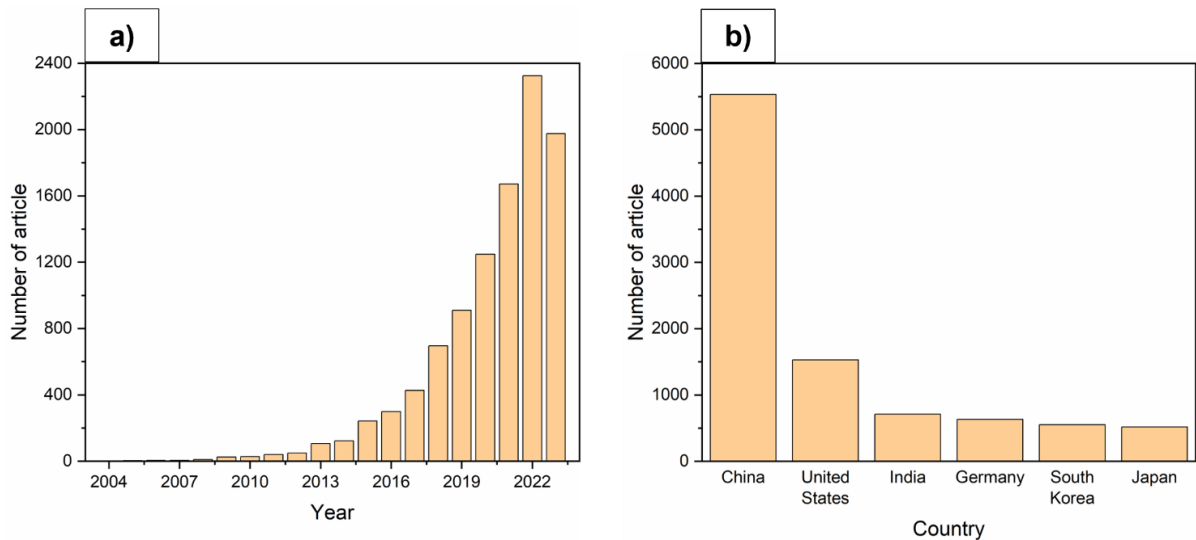


Fig. 1-2. a) Statistics on the number of publications on high entropy alloys per year until September 2023 b) Statistics on the main countries conducting research on high entropy alloys up to September 2023.

This interest is justified, as these alloys offer properties surpassing conventional alloys, promising significant advancements in various applications. Investigating and understanding these alloys is essential to leverage their benefits and foster innovation in aerospace, electronics, and medicine, among other areas. In summary, research on high-entropy alloys is crucial for advancing materials science and capitalizing on the opportunities presented by these innovative materials.

## 1.2. Motivation

A new subcategory of high-entropy alloys has been developed, known as lightweight high-entropy alloys (LW-HEA). These alloys incorporate lightweight metallic elements to reduce weight without compromising the exceptional mechanical properties mentioned earlier. Globally, various research groups have contributed to the design of LW-HEAs with a density below  $4 \text{ g/cm}^3$ , notable for their high compressive strength and hardness. However, in many cases, these alloys tend to be excessively brittle and exhibit little to no ductility.

In response to these challenges, the central motivation of this thesis is to specifically address the limitation of ductility in LW-HEAs. The proposal is to design a new generation of low-density alloys by applying the high-entropy concept. The key strategy will be to select an alloy with a high proportion of solid solution and a face-centered cubic (FCC) crystal structure, which is expected to resolve the ductility issue, as alloys with FCC crystal structures tend to exhibit favorable properties in this aspect.

In summary, the research will focus on overcoming the current limitations of LW-HEAs, prioritizing not only hardness and compressive strength but also a substantial improvement in ductility. The combination of low density and high entropy will be crucial for developing advanced alloys with exceptional mechanical properties.



### 1.3. Objectives

The main objective of this thesis is to design, manufacture, and analyze lightweight alloys composed of multiple components. These alloys are developed following the principles of high-entropy alloys, and their physical and mechanical properties are thoroughly examined to assess their potential suitability for future applications. Special attention is given to designing an alloy with ductility, considering its potential use in structural applications.

With this purpose in mind, we have established the following specific goals:

- I. Define and select chemical compositions in which alloying elements exhibit optimal compatibility, have a wide solubility range to form a solid solution with a face-centered cubic (FCC) crystal structure, and could melt at intermediate temperatures. This process is carried out with the aim of designing lightweight high entropy alloys.
- II. Identify and understand the phase transformations in the designed alloy to gain a profound knowledge of its nature and thereby have the capability to customize the alloy according to our specific needs.
- III. Enhancing alloy performance through the modification of chemical compositions, the use of heat treatments, and the exploration of different manufacturing processes to achieve improved microstructures with better physical and mechanical properties.

### 1.4. Dissertation outline

To achieve the objectives outlined in the previous section consistently, this dissertation project has been organized into seven chapters, including the introduction. To provide a clearer overview of the manuscript, Fig. 1-3 illustrates the overall structure, highlighting the different chapters, their respective objectives, and the connections between them. The following paragraphs offer a brief overview of each chapter.

#### CHAPTER 1: Introduction

This chapter looks at how materials have changed over time, highlighting the importance of studying high entropy alloys. It stresses that this area is essential for advancing materials science and realizing the full potential of these innovative alloys. The growing interest in high entropy alloys and the leading role of advanced nations in this research highlight their importance and the necessity to keep exploring this exciting field.

#### CHAPTER 2: Literature Review

This chapter introduces high entropy alloys (HEAs) as a foundational concept for studying a specific alloy. It discusses various definitions of HEAs, their evolving concept, and key aspects including

thermodynamics and the four main effects. The focus then turns to low-density high entropy alloys, relevant to the studied alloy, presenting design methods using phase selection rules and exploring physical and thermodynamic parameters predicting solid solution phase formation. The chapter also examines computational techniques for designing and predicting phases in HEAs. Processing techniques for low-density HEAs, such as casting and mechanical alloying, are explored with examples detailing microstructures, densities, mechanical properties, and fabrication methods. The discussion concludes with considerations of potential future developments and promising research areas in HEAs.

### CHAPTER 3: Experimental procedures

In this chapter, we delve into the primary methods and equipment employed for the design, fabrication, and optimization of low-density medium entropy alloys, including their characterization.

### CHAPTER 4: Alloy design and heat treatments

This chapter provides a comprehensive analysis of the  $\text{Al}_{58}\text{Zn}_{28}\text{Mg}_6\text{Si}_8$  alloy, emphasizing the intricate interplay between empirical predictions, thermodynamics, phase evolution and heat treatments. The objective is to obtain a comprehensive understanding of the microstructure and properties of the alloy.

### CHAPTER 5: Optimizing and Customizing Chemical Composition

This chapter focuses on improving the mechanical properties of the  $\text{Al}_{58}\text{Zn}_{28}\text{Mg}_6\text{Si}_8$  alloy. The improvement consists of adjusting the alloy composition and applying a heat treatment to increase its resistance to compressive forces, resulting in the modified composition  $\text{Al}_{60}\text{Zn}_{27}\text{Mg}_{11}\text{Si}_2$ . In addition, the chapter explores the influence of modifying elements, such as strontium (Sr) and antimony (Sb), on the  $\text{Mg}_2\text{Si}$  phase, leading to its modification and refinement.

### CHAPTER 6: Enhancing Microstructure via Manufacturing Methods

This chapter investigates the enhancement of the previously optimized  $\text{Al}_{60}\text{Zn}_{27}\text{Mg}_{11}\text{Si}_2$  alloy using various methods, including traditional sand casting, near solid forming (NSF) for deformation, and directional solidification (DS). The objective is to boost material density, eliminate porosities and defects, and enhance the internal structure. Subsequently, the chapter compares microstructures and mechanical properties through compression tests. The primary goal is to assess the impact of each method on the alloy's mechanical performance and identify the most effective technique for improving its properties.

### CHAPTER 7: Conclusions and future work

In this final chapter we discuss in depth the main conclusions drawn from the present research project, in line with the objectives set out in Chapter 1. Based on these conclusions, we outline possible directions for moving forward with the work presented here.

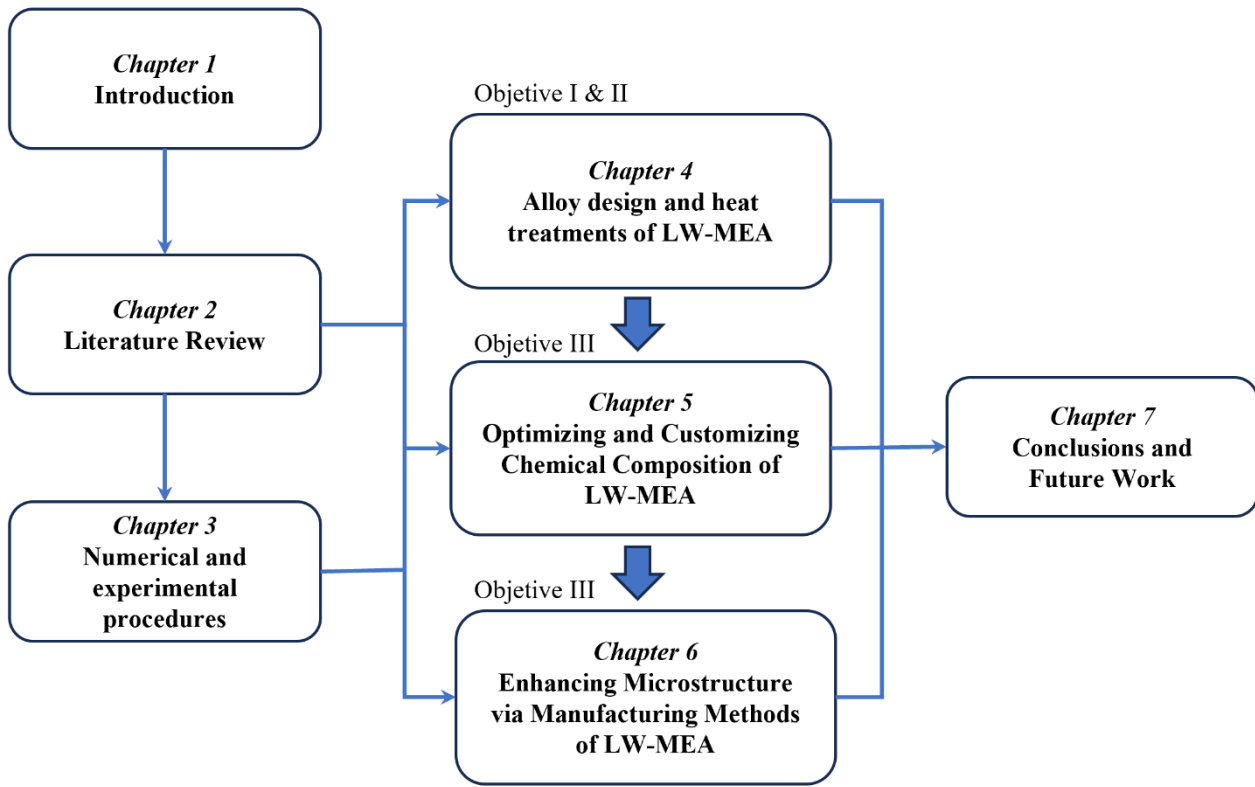


Fig. 1-3. Document structure and research workflow.

# Chapter 2

## 2. Literature Review

*In this chapter, the concept of high entropy alloys is introduced, which serves as a basis for the development of the alloy under study. Various definitions of this type of alloys and how their concept has evolved over time are discussed. Key points are addressed, including thermodynamic aspects and the four main effects of these alloys. Then, attention is focused on low density high entropy alloys, which is relevant since the alloy under investigation belongs to this category. Design methods for low density high entropy alloys using phase selection rules are presented. Some of these rules are examined, as well as physical and thermodynamic parameters that allow predicting the formation of solid solution phases. In addition, computational techniques that facilitate the design and prediction of phases in these high entropy alloys are explored. In the next segment of the chapter, processing techniques used in low density high entropy alloys, such as casting and mechanical alloying, among others, are explored. A list of examples of low-density high-entropy alloys is provided, detailing their microstructures, densities, mechanical properties, and fabrication methods. Finally, the possible future development of these alloys and areas of research that offer promising opportunities are discussed.*

### 2.1. Definitions

As mentioned in Chapter 1, the first results on multicomponent and high-entropy crystalline alloys were published in 2004, approximately 19 years ago. This innovative approach opened up a vast and unexplored range of alloy compositions, capturing the attention of the materials science community and generating numerous findings, unexplained results, controversies, and new questions. An extensive body of work has been published, including compilations and two books. While there is data available to evaluate initial concepts and establish trends, a concrete definition for these rapidly evolving alloys is still not available [22].

These new materials have been given different names, such as high-entropy alloys (HEAs), multi-principal element alloys (MPEAs), and complex concentrated alloys (CCAs). Table 2-1 outlines the primary definitions associated with these new alloys. Additionally, Zhang *et al.* [23] have proposed dividing HEAs into two generations and have emphasized the need for further research to explore various aspects related to their development, definition, characteristics of each generation, and their physical and mechanical properties.

Table 2-1. The main High Entropy Alloys (HEAs) related definitions.

Term	Abbreviation	Definition	Ref.
High Entropy Alloys	HEAs	Multi-component alloys with concentration of each element being between 35 and 5 at.%, based on the high entropy effect to produce single solid solution structures	[2,3,22,24,25]
Multi Principal Element Alloys	MPEAs	A composition-based definition for alloys with a large number of elements in high concentrations.	[26–28]
Complex Concentrated Alloys	CCAs	Alloys with a complex composition, containing a large number of elements, but not necessarily in a large proportion for each element	[29–32]

While the search for HEAs with a single-phase solid-solution structure and more than five principal elements was a primary research focus for decades, the restrictions on these alloys have been overcome with a deeper understanding of their properties. Non-equimolar complex-phase HEAs, where the matrix is a solid solution, have now become an integral part of HEAs. As a result, HEAs can be categorized into the first and second generations, as illustrated in Fig. 2-1 and Table 2-2.

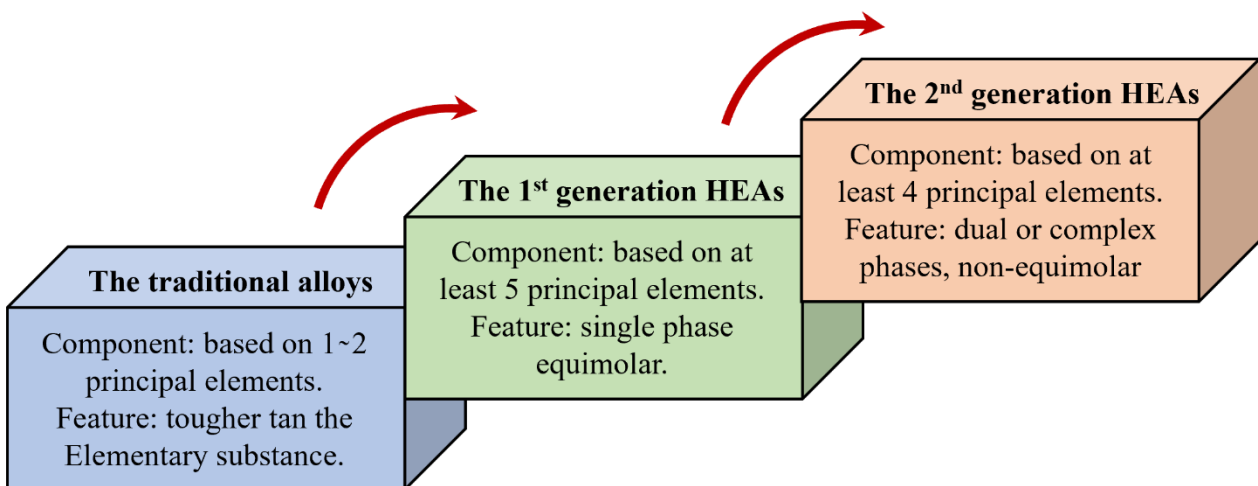
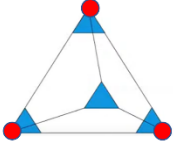
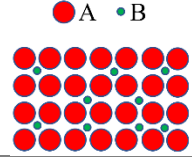
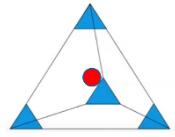
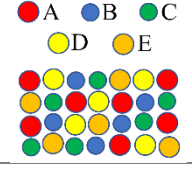
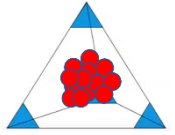
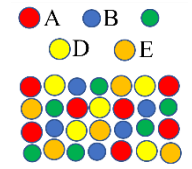


Fig. 2-1. Evolution of alloys, adapted from [33].

Table 2-2. Characteristics for the traditional alloys and the two generations of HEAs, adapted from [33].

Classification	Component	Feature	Composition	Atoms arrangement	Typical alloys
The traditional alloys	1~2 principal elements	Tougher than the Elementary substance			Al-Zn, Al-Mg, Cu-Al, Fe-Ni Fe-C
The 1 <sup>st</sup> generation HEAs	At least 5 principal elements	Single phase, equimolar			CoCrFeNiMn AlCoCrFeNi
The 2 <sup>nd</sup> generation HEAs	At least 4 principal elements	Dual or complex phases, non-equimolar			NbMoTaW Al <sub>0.3</sub> CoCrFeNi Fe <sub>50</sub> Mn <sub>30</sub> Cr <sub>10</sub> Co <sub>10</sub>

The research scope of HEAs has also expanded from the central region to the surroundings, encompassing the development of non-equimolar multi-phase solid-solution alloys from equimolar single-phase solid-solution alloys. This expansion has impacted the definition of HEAs and the research scope, making the evolution of the HEAs conception crucial to facilitate material design and development. Instead of rigidly adhering to the classical high-entropy definition, this concept can now be extended to meet specific needs.

Despite the different definitions and divisions, these alloys share a common characteristic: being composed of multiple principal components located in the central region of a multicomponent phase diagram, away from the vertices, edges, and faces. However, "high entropy alloys" is the term most commonly used to describe these materials. As a result, we have considered adopting this entropy-based terminology for the purposes of this work.

The underlying principle of HEAs suggests that the high configurational entropy in these alloys enhances mutual solubility to form solid solution phases (disordered or partially ordered) and, therefore, restricts the formation of intermetallic compounds, especially at high temperatures [2–4]. Therefore, the thermodynamic aspects of these alloys will be defined next.

## 2.2. Thermodynamic aspects

In single-component systems, all phases have the same composition, and equilibrium is determined simply by pressure and temperature. However, in alloys, the composition is variable, and understanding phase changes in alloys requires an appreciation of how the Gibbs free energy of a given phase depends not only on temperature and pressure but also on composition [34]. To describe the formation of alloys from a mixture of elemental components, the Gibbs free energy of mixing is expressed as:

$$\Delta G_{mix} = \Delta H_{mix} - T\Delta S_{mix} \quad (2-1)$$

where  $\Delta G_{mix}$  is the Gibbs free energy change arising from the mixing of the individual constituents.  $\Delta H_{mix}$  and  $\Delta S_{mix}$  are the changes in enthalpy and entropy.

Solid solutions have relatively higher configurational entropy compared to intermetallic compounds. That is, the solid solution phase is expected to have a low  $\Delta G_{mix}$  at high temperatures due to the temperature-dependent expression of  $\Delta S_{mix}$

### 2.2.1. Entropy

Entropy is a thermodynamic property that measures the thermal energy of a system per unit temperature that is not available to do mechanical work. It can be thought of as a measure of molecular disorder. The equation of entropy is as follow:

$$\Delta S = \frac{\Delta Q}{T} \quad (2-2)$$

where  $S$  is the entropy,  $T$  is the absolute temperature and  $Q$  is the heat flow.

The statistical mechanical definition of entropy was developed by Ludwig Boltzmann through an analysis of the statistical behavior of the microscopic components of a system. Boltzmann established that the entropy of a system is linearly related to logarithm of the frequency of occurrence of a microstate or the number  $W$  which provides the possible possible microstates that correspond to the macroscopic state of the system [35].

$$S = k \ln W \quad (2-3)$$

where  $k$  is Boltzmann's constant =  $1.38 * 10^{23}$  J/K, and the logarithm is taken as to be natural base "e".

The mixing entropy from the equation (2-1) has a total of four main parts contributing to the entropy including such as configurational entropy, vibrational entropy, magnetic dipole and electronic randomness and their relation is per given as:

$$\Delta S_{mix} = \Delta S_{conf} + \Delta S_{vibr} + \Delta S_{elec} + \Delta S_{magn} \quad (2-4)$$

Fultz [36], states that configurational entropy is the most significant among the three types of mixing entropy. Therefore, it is commonly used to represent mixing entropy in complex calculations and to account for the remaining contributions. Based on Boltzmann's theory, the configurational entropy of an equimolar alloy going from an ordered elementary state to a disordered solution state is expressed as [37]:

$$\Delta S_{conf} = -R \sum_{i=1}^n X_i \ln X_i \quad (2-5)$$

where  $R$  is the gas constant (8.314 J/K mol),  $X_i$  is the atomic percentage of component  $i$ , and  $n$  is the number of components in the alloy. The configurational entropy of a mixture increases when the mole fraction of all components is equal [35,38], as illustrated in Fig. 2-2. Moreover, as the number of elements ( $N$ ) in a system increases, the maximum configurational entropy in the system also increases [37], as shown in Fig. 2-3.

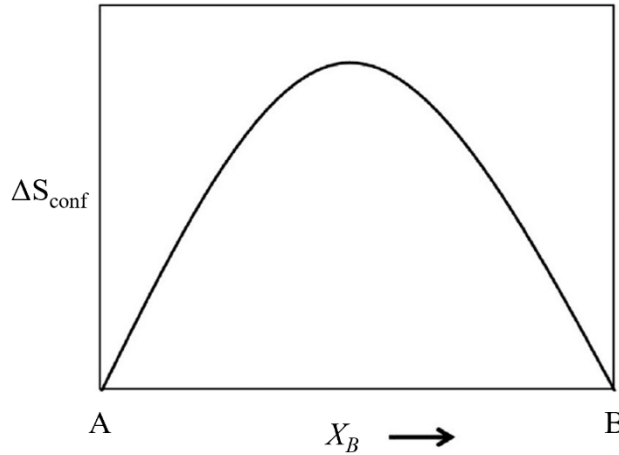


Fig. 2-2. The configurational entropy reaches its maximum when in a binary system the composition is equimolar [2].

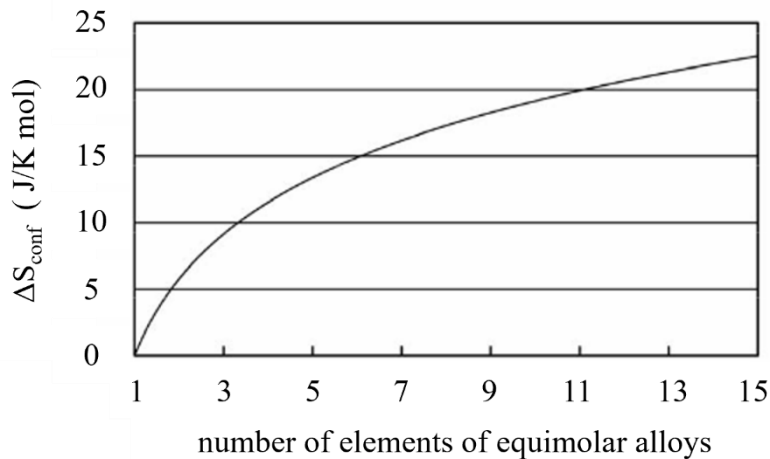


Fig. 2-3. Entropy of mixing as a function of the number of elements for equimolar alloys in completely disordered states [37].

Although the total mixing entropy of a system can be attributed to four contributions such as configurational, vibrational, magnetic dipole, and electronic randomness, the configurational entropy is the dominant contribution among the four [2]. Several authors, [2,3] have proposed a classification system for alloys based on the quantification of configurational entropy, typically expressed as a function of the gas constant  $R$ . According to this classification, alloys with a configurational entropy equal to or less than  $1R$  are considered low entropy alloys. Those with an entropy greater than  $1R$  but



less than  $1.5R$  are classified as medium entropy alloys, while high entropy alloys are those with an entropy equal to or greater than  $1.5R$  (See Fig. 2-4).

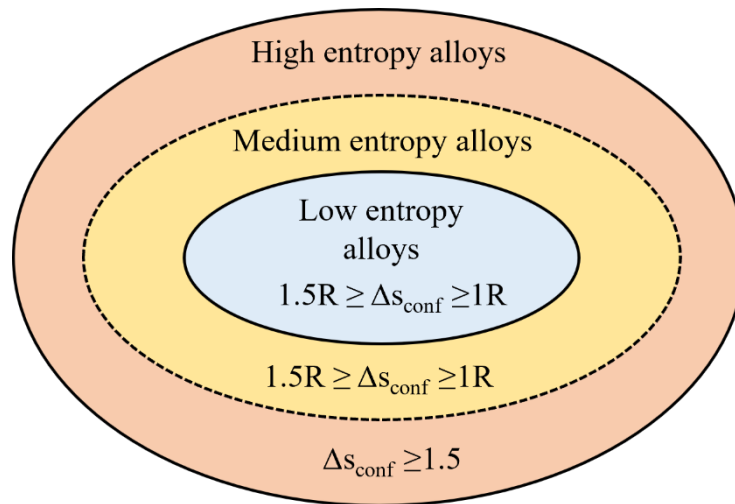


Fig. 2-4. Classification of alloys based on entropy quantification [39].

Table 2-3 shows different families of alloys according to entropy quantification. Commercial alloys made of aluminum, magnesium, copper, and steel are typically categorized as low entropy alloys, while more intricate alloys like superalloys or metallic glasses are referred to as medium entropy alloys. Although, there is some confusion regarding high entropy alloys because an alloy with a composition of  $A_{35}B_{35}C_{20}D_5E_5$  is considered a high entropy alloy based on its elemental composition, according to the definition provided in Table 2-1. However, when considering configurational entropy quantification, this alloy would be classified as a medium entropy alloy.

The term high entropy alloy (HEA) has faced criticism and controversy over the extent to which various multicomponent materials exhibit high entropy [39–42]. Nonetheless, it remains the most used term for these alloys, even in cases where they do not display high entropy. Multiple definitions for HEAs exist, including those based on composition, phases, configurational entropy, and more [43,44]. There is no definitive right or wrong approach, as the appropriate definition to use will depend on the specific research goals and objectives.

Table 2-3. Configurational entropies calculated for commercial alloys at their liquid state or random state [2].

System	Alloys	$\Delta S_{conf}$ at liquid state	Classification
<b>Al alloy</b>	2024	0.22 R	Low entropy
	7075	0.43 R	Low entropy
	AlSi10Mg	0.38 R	Low entropy
	AlSi9Cu3	0.37 R	Low entropy
<b>Mg alloy</b>	AZ91D	0.35 R	Low entropy
<b>Cu alloy</b>	7-3 brass	0.61 R	Low entropy
<b>Stainless steel</b>	304	0.96 R	Low entropy
	316	1.15 R	Medium entropy
<b>Ni-base superalloy</b>	Inconel 718	1.31 R	Medium entropy
	Hastelloy X	1.37 R	Medium entropy
<b>Co-base superalloy</b>	Stellite 6	1.13 R	Medium entropy
<b>Bulk metallic glasses</b>	Cu47Zr11Ti34Ni8	1.17 R	Medium entropy
	Zr53Ti5Cu16Ni10Al16	1.30 R	Medium entropy
<b>HEAs</b>	FeCrMnNiCo	1.60 R	High entropy
	AlCoCrCuNi	1.61 R	High entropy
	Al35Co35Cr20Cu5Ni5	1.36 R	Medium entropy
	Al35Cu5Fe5Mn5Si30V10Zr10	1.64 R	High entropy

### 2.3. Four core effects of HEAs

There are several factors that can affect the microstructure and properties of high-entropy alloys. The four main factors are high-entropy, severe lattice distortion, sluggish diffusion, and cocktail effects.

The high-entropy effect can interfere with complex phase formation in terms of thermodynamics. In the context of the thermodynamics of solid solution formation the high-entropy effect is a critical factor. This effect can simplify the microstructure of HEAs beyond what is expected. The Gibbs free energy of mixing  $\Delta G_{mix}$  depends on both the enthalpy of mixing  $\Delta H_{mix}$  and the entropy of mixing  $\Delta S_{mix}$ . In HEAs with a higher number of elements, the  $\Delta G_{mix}$  will be lower, as the  $\Delta S_{mix}$  contribution will be large, particularly at high temperatures. This means that the higher the entropy of configuration, the lower the energy of the random solid solution phase, leading to a simpler microstructure formed at equilibrium.

For the stability of phase and kinetics of phase transformation, sluggish diffusion effect is responsible in HEAs. Diffusion is the process by which atoms in a material move to their equilibrium position, typically driven by thermal vibrations or the presence of crystalline defects like vacancies. In high-entropy alloys (HEAs), slow diffusion and higher activation energy can be attributed to the large fluctuation of the lattice potential energy (LPE) between lattice sites. The abundant low LPE sites can act as traps and hinder the diffusion of atoms, resulting in the slow diffusion effect [45]. Slow diffusion can have various effects on the microstructure and properties of HEAs, such as affecting nucleation, growth, distribution, morphology, and phase transformation. However, it also provides several advantages for controlling microstructure and properties, including the ease of obtaining a

supersaturated state and fine precipitates, increased recrystallization temperature, slower grain growth, lower particle coarsening rate, and creep resistance [3].

For better structural properties, severe lattice distortion effect is responsible to an extent. HEA alloys consist of solute atoms from various elements, each surrounded by different types and sizes of atoms, resulting in concentrated and complex phases as can be seen in Fig. 2-5. This causes lattice deformations and stresses [46]. Moreover, due to the differences in atomic size, binding energies, and crystal structures among the constituent elements, even greater lattice distortion is expected [47].

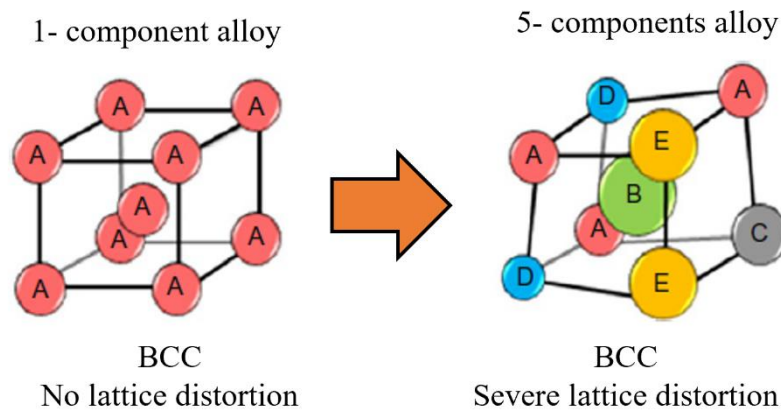


Fig. 2-5. Schematic diagram showing large lattice distortion exists in five component BCC lattice [3].

Lastly, the cocktail effect was first described by Ranganathan [48] for conventional alloys, being reinforced for HEA. Considering that an HEA alloy can be formed by a single phase, two phases or several phases depending on the composition and the manufacturing process. The set of properties will be the result of the global contribution of the existing phases. Therefore, the final properties are not only the result of the basic properties of the elements, but also of the interactions between all the elements in the crystal lattice and their corresponding distortion. In summary, these factors play a critical role in determining the properties of high-entropy alloys.

## 2.4. Light weight HEAs

Over the past two decades, significant progress has been made in the development of High Entropy Alloys. These alloys can be broadly classified based on their crystal structure, including face-centered cubic (FCC), body-centered cubic (BCC), close-packed hexagonal (HCP), amorphous, and multi-phase composite HEAs. The physical properties and functions of HEAs have led to their categorization into lightweight HEAs (LW-HEAs), high-temperature resistant HEAs, radiation-resistant HEAs, and soft magnetic HEAs [2,49].

In the 21st century, the development of lightweight materials has become a significant research focus, particularly in energy-efficient industries such as transport and aerospace. LW-HEAs, primarily composed of elements such as Al, Mg, Ti, Li, Be, Cu, Sc, Sn, Fe, Mn, Co, Ni, and Zn, have gained attention due to their capacity for use in lightweight equipment and circular economies [2,49].

Recently, researchers have coined the term Lightweight HEAs, also known as low-density HEAs, as they seek to expand the world of HEAs to lightweight applications. However, there is no consensus on the definition of LW-HEAs. Some have classified them as having a density of less than 3 g/cm<sup>3</sup> [50], while others suggest that a density below 7 g/cm<sup>3</sup> is considered lightweight [51]. To provide a point of comparison, current alloys such as Al and Ti-based alloys have densities of approximately 2.8 and 4.5 g/cm<sup>3</sup>, respectively. Therefore, it is recommended that new lightweight alloys should be comparable to these values.

Thus far, there are only a few investigations made on the fabrication of LW-HEAs with a density of less than 6 g/cm<sup>3</sup>. Overall, the development of LW-HEAs is a promising field of research with potential applications in various industries such as aerospace, automotive, and biomedical [50].

## 2.5. Alloy design and phase selection rules in LW-HEAs

Predicting phase formation in HEAs has been a significant challenge since identifying beneficial phases and avoiding undesirable phases is crucial for designing materials with customized properties for each application [46].

HEAs primarily form solid solutions, including random and partially ordered ones, with some cases forming amorphous alloys. The selection of elements used for alloying plays a crucial role in determining the formation of a single-phase solid solution in HEAs.

In general, the basic principles of designing LW-HEAs are the same as that for HEAs, except that the selection of the principal alloying elements determines the density of the alloy [50].

### 2.5.1. Predicting solid solubility from Hume-Rothery rules

The Hume-Rothery (H-R) rules were created to identify the conditions for one element to dissolve in another. In the 1920s, H-R studied solubility data and found that atomic size, crystal structure, valence, and electronegativity are essential factors that affect compound formation and alloying behavior. Despite other attempts to address this issue, the simplicity and general applicability of H-R rules have made them a cornerstone in materials science.

The general statement of the Hume-Rothery rules for binary substitutional solid solutions is as follows:

1. The difference in radii between the solute and solvent atoms should be less than about 15%, and for complete solubility, the atomic size difference should be less than 8%.
2. The crystal structures of the two elements should be the same for extended solid solubility.
3. The solvent and solute should have the same valency for extended solubility.
4. The two elements should have similar electronegativity to prevent the formation of intermetallic compounds.

However, these rules require reconsideration when applied to multicomponent solid solutions, as the interactions between the various components need to be considered.

### 2.5.2. Parameters to predict the formation of solid solution in LW-HEAs

A compilation of the physical and thermodynamic parameters proposed in various investigations for predicting phase formation has been compiled in Table 2-4. The phases that can be predicted with these parameters are solid solutions (SS), amorphous phases (AM), and intermetallic compounds (IC).

Table 2-4. Thermodynamic and topological parameters to predict the formation of phases.

<b>Physical or thermodynamic parameter</b>	<b>Predicting Phase Transformation</b>	<b>Ref.</b>
$\Delta H_{mix}$	SS	[52]
$\Delta S_{mix}$	SS	[52]
$\delta$	SS	[52]
$\Omega$	SS	[53,54]
$VEC$	SS, AM	[55]
$\Delta\chi$	SS	[56]
$\Delta S_{\sigma}, k_B$	SS, AM	[57]
$\gamma$	SS, IC	[58]
$\mu$	SS	[59]
$\Phi$	SS, IC	[60]
$k_1^{cr}$	SS, IC	[61,62]
$S_m, K_m$	SS, IC	[63]

From the proposed parameters in the previous table, only the most commonly used for predicting phase formation will be mentioned and defined below. Among them, thermodynamic parameters such as the configurational entropy of mixing ( $\Delta H_{mix}$ ), and the omega parameter ( $\Omega$ ). Topological parameters, such as the atomic size difference ( $\delta$ ) between the constituent elements, are also important. Additionally, other important parameters include the valence electron concentration ( $VEC$ ) and the chemical parameter that measures the electronegativity difference ( $\Delta\chi$ ).

As mentioned above, the formation of phases is thermodynamically controlled by the Gibbs energy, which is related to enthalpy and entropy by equation 2-1. Equation 2-2 is the Boltzmann equation used to determine the configurational entropy of mixing. The enthalpy of mixing is the heat absorbed or released when a substance is mixed. Although this thermodynamic parameter can be obtained experimentally by calorimetric methods [64], it is difficult to determine its value for an ideal solid solution, and therefore data for this parameter in the literature are limited. One approach to obtain this value is through the Miedema method [65], which evaluates the enthalpy using three critical parameters: the chemical contribution due to the mixing of the atoms of the two metals, the elastic contribution due to the atomic size difference, and, in the case that the alloy is composed of two transition metals, the variation of the atomic stability as a function of the average number of valence electrons per atom. Another way to estimate this property is through the following formula:

$$\Delta H_{mix} = \sum_{i=1, j \neq i}^n 4\Delta H_{AB}^{mix} X_i X_j \quad (2-6)$$

where  $\Delta H_{AB}^{mix}$  is the enthalpy of mixing of the binary AB equiatomic alloys. The topological parameter  $\delta$  it is defined as:

$$\delta = 100 \sqrt{\sum_{i=1}^n c_i (1 - r_i/\bar{r})^2} \quad (2-7)$$

$$\bar{r} = \sum_{i=1}^n c_i r_i \quad (2-8)$$

wherein  $c_i$  and  $r_i$  are the composition and atomic radii of  $i$ th element and  $\bar{r}$  is the average atomic radius.

Zhang *et al.* [52] found that simple solid solutions are formed when the following criteria are satisfied:  $-20 \leq \Delta H_{mix} \leq 5$  kJ/mol,  $12 \leq \Delta S_{mix} \leq 17.5$  J/Kmol, and  $\delta \leq 6.4\%$ . However, for predicting solid solutions in disordered phases, the parameters are more restrictive, with  $\Delta H_{mix} \leq 5$  kJ/mol and  $\delta \leq 4.6\%$  (see Fig. 2-6).

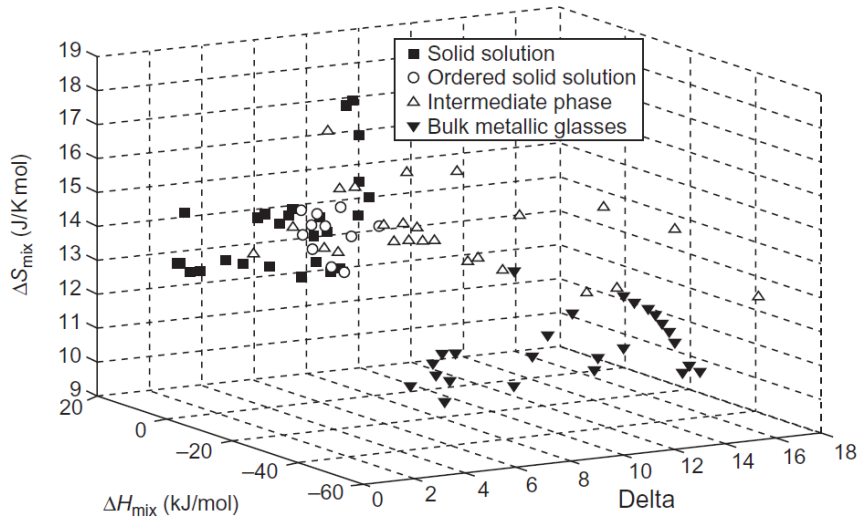


Fig. 2-6. The effect of  $\Delta S_{mix}$ ,  $\Delta H_{mix}$  and  $\delta$  on the phase formation in HEAs and typical multicomponent Bulk Metallic Glasses (BMGs) [52].

Guo *et al.* [66] proposed that the formation of a simple solid solution microstructure is influenced by  $\Delta H_{mix}$ ,  $\Delta S_{mix}$ , and  $\delta$ , with criteria of  $11 \leq \Delta S_{mix} \leq 19.5$  J/Kmol,  $-11.6 \leq \Delta H_{mix} \leq 3.2$  J/Kmol and  $\delta < 5\%$ .

In addition, other parameters such as  $\Omega$  have also been proposed for predicting solid solution formation, as shown in equation 2-5 [53,54].

$$\Omega = \frac{T_m \Delta S_{mix}}{|\Delta H_{mix}|} \quad (2-9)$$

where  $T_m$  is the hypothetical melting temperature calculated according to the rule of mixtures, as shown below.

$$T_m = \sum_{i=1}^n c_i (T_m)_i \quad (2-10)$$

and  $(T_m)_i$  is the melting point of each element. They placed a new criterion that simple solid solutions form when  $\Omega \geq 1.1$  and  $\delta \leq 6.6\%$ .

It has been proposed that if  $\Omega \geq 1$ , then the contribution of  $T\Delta S_{mix}$  will exceed that of  $\Delta H_{mix}$ , leading to the formation of solid solutions in HEAs. Conversely, if  $\Omega < 1$ ,  $\Delta H_{mix}$  will be the predominant factor, resulting in the formation of intermetallic compounds in HEAs.

Electronegativity also plays an important role in stabilization of solid solution in HEAs. Electronegativity is a chemical property that describes an atom's tendency to attract electrons to itself [56]. According to the Hume-Rothery electronegativity rule, the formation of solid solutions requires similar electronegativity between the solvent and solute in a binary system. Otherwise, intermetallic compounds would form [67]. The electronegativity difference between the elements of a HEAs is defined by the following equation:

$$\Delta\chi = \sqrt{\sum_{i=1}^n c_i (\chi_i - \chi_{av})^2} \quad (2-11)$$

where  $n$  is the number of elements,  $c_i$  and  $\chi_i$  are the composition and electronegativity of the elements and  $\chi_{av}$  is the average electronegativity.

Senkov *et al.* [62] recently proposed a new parameter for phase formation in HEAs. They assumed linear relationships between the enthalpy of formation for intermetallic phases  $\Delta H_{IM}$  and  $\Delta H_{mix}$ , as well as between the entropy of formation of IM phases  $\Delta S_{IM}$  and  $\Delta S_{mix}$  for HEAs. They concluded that Equation 9 provides the critical value  $\Delta S_{mix}$  that must be satisfied for the formation of a solid solution.

$$\kappa_1^{cr}(T) = -\frac{T\Delta S_{mix}}{\Delta H_{mix}}(1 - \kappa_2) + 1 \quad (2-12)$$

where  $0 \leq VEC < 1$ .

The value of  $\kappa_1^{cr}(T)$  should be greater than  $\Delta H_{IM}/\Delta H_{mix}$  ie.

$$\kappa_1^{cr} > \Delta H_{IM}/\Delta H_{mix} \quad (2-13)$$

Fig. 2-7 shows the plot between  $\kappa_1^{cr}$  and  $\Delta H_{IM}/\Delta H_{mix}$ , which clearly separates solid solution (SS) alloys from those containing intermetallic (IM) phases. With the exception of two SS alloys with a body-centered cubic (BCC) structure, all other SS alloys fall above the dashed line, while almost all IM-containing HEAs fall below it. Therefore, it has been predicted that the  $\kappa_1^{cr}(T)$  parameter has an improved ability to predict SS and SS+IM phase formation in HEAs.

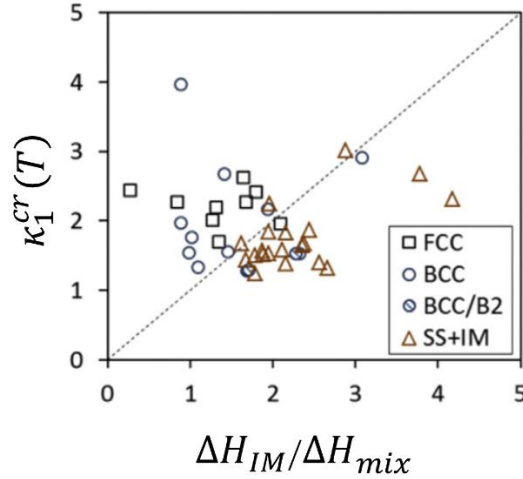


Fig. 2-7. Plots for annealed HEAs with different phase contents after annealing [62].

While the parameters discussed above are effective in predicting the formation of a solid solution, they generally do not provide information about the type of crystal structure obtained. To predict the crystal structure of HEAs Guo [68] proposed the valence electron concentration (VEC) to determine the formation of FCC or BCC phases, which also influences the phase stability with solid solution. There are two other ways to calculate the electron concentration, which are from the average number of valence electrons per atom ( $e/a$ ) and by the valence electron bonds [60]. These parameters are shown below:

$$\frac{e}{a} = \sum_{i=1}^n c_i (e/a)_i \quad (2-14)$$

$$VEC = \sum c_i (VEC_i) \quad (2-15)$$

where  $c_i$  is the atomic percentage,  $(e/a)_i$  and  $VEC_i$  are the concentration of valence electrons. These parameters are effective for separating phases with BCC crystal structure from FCCs in the following ranges [68]:  $VEC \leq 6.87 \rightarrow$  BCC,  $6.87 \leq VEC \leq 8 \rightarrow$  BCC + FCC y  $VEC \geq 8 \rightarrow$  FCC.

The empirical phase formation parameters presented above are guidelines for predicting solid solutions, intermetallic compounds, amorphous phases, and disordered solid solutions. While most alloys that form solid solutions fall within these guidelines, these parameters do not guarantee that these phases will form. Moreover, some parameters have certain limitations and are not fully established, and therefore, further work is needed to refine and improve them [67].



## 2.6. LW-HEAs design using integrated computational materials engineering (ICME)

HEAs offer unique compositions and properties that make them suitable for various applications. Thus, effective alloy design, including composition and process selection, is crucial. Predictions based on mixing entropy, mixing enthalpy, atomic size difference, and valence electron concentration are helpful, but experimentation is required for more quantitative predictions. Integrated Computational Materials Engineering (ICME) is a multidisciplinary field that integrates materials science, engineering, and computational methods to design optimized materials and products by linking material models at multiple length scales. ICME is crucial in identifying and realizing new HEA materials efficiently [2,3,14,15].

One important aspect of ICME is the Computer Coupling of Phase Diagrams and Thermochemistry method (CALPHAD), which involves collecting thermodynamic databases and using computational techniques to determine phase stabilities, component solubilities, transition temperatures, rate constants, and phase fractions. Other simulation techniques, such as ab initio methods such as density functional theory (DFT), atomistic methods such as Monte Carlo (MC) and molecular dynamics (MD), and continuum techniques such as phase field (PF) and finite element methods (FEM). Simulation techniques such as DFT are typically used to expand the information already existing in databases or create new databases for calculated phases.

MD and MC simulations are typically used to answer questions about the structures of nucleating phases, phase clusters, and initial growth, using information obtained through fitting to experimental data or ab initio DFT computations. On the other hand, phase-field and finite element methods are commonly utilized to investigate questions related to microstructure evolution and pattern formation that occur during material processing. These methods also rely on thermodynamic information obtained from databases.

The combination and application of these computational methods provide a powerful methodology for establishing correlations between process, structure, and properties of materials, thereby accelerating the pace of discovery and development of new materials. The combination and application of these computational methods provide a powerful methodology for establishing correlations between process, structure, and properties of materials, thereby accelerating the pace of discovery and development of new materials.

### 2.6.1. CALPHAD method

The CALPHAD method uses the Gibbs free energy to determine the thermodynamic properties of each phase of the system. The description is semi-empirical and is based on thermodynamic models developed for the Gibbs energy and on selected and critically evaluated experimental data. The models describe the Gibbs energy of each phase in a system within a chosen temperature and composition range. The total Gibbs energy of a system is minimized by adjusting the model parameters so that the best possible agreement between measured and calculated data is obtained. The optimized parameters are stored in a thermodynamic database. The data can be estimated from simple to complex systems [69].

CALPHAD has been successfully used to predict the formation of HEA phases. For example, Zhang *et al.* [69,70] calculated binary and multi-component phase diagrams to explain phenomena observed

during the preparation of HEAs and to describe the prospects for developing alloys using phase diagram calculations. They used possible phase diagram calculations to explain the influence of various elements on phase stability and the FCC/BCC phase transition, providing useful guidance for the development of novel HEAs. Raghavan [71] used the CALPHAD method to predict the phase formation of many mixtures containing FCC, BCC, or FCC + BCC phases. The results demonstrated the usefulness of the CALPHAD approach for predicting BCC phase formation compared to FCC phase.

Nowadays, many software have been developed to accelerate the development of alloys based on the CALPHAD method. Examples include FactSage, MTDATA, PANDAT, MatCalc, JMatPro, and Thermo-Calc. With these tools, it is possible to calculate properties and simulate transformations of multicomponent systems by modeling Gibbs energy and its derivatives, such as entropy, enthalpy, volume, chemical potential, heat capacity, thermal expansion, isothermal compressibility, solidification, and more [2,3,69].

These resources are helpful tools in research and industrial development, saving time and reducing the need for experimental work. This approach has a profound influence in the case of multicomponent systems because thermodynamic descriptions of the constituents (binaries and ternaries) can be combined and extrapolated using geometric models to develop a thermodynamic description of a multicomponent system that would otherwise be experimentally challenging or require a significant number of experiments. However, it is essential to note that the created databases must be experimentally validated to establish confidence in the derived information [2,3].

## 2.7. Processing of LW-HEAs

Several processing methods have been employed in the synthesis of High Entropy Alloys, such as the casting method, powder metallurgy, and additive manufacturing technology. Currently, the casting method stands out as the predominant technique for producing the majority of HEAs. Specifically, for Low-Weight High Entropy Alloys, the casting method continues to be a suitable and effective approach. This is why we will focus on the casting method [72,73].

### 2.7.1. Casting method

The casting method can be categorized into vacuum-arc melting and vacuum-induction melting. Currently, vacuum arc smelting is the most widely employed technique for preparing Low-Weight High Entropy Alloys. In vacuum-arc melting, various high-purity metal element blocks or particles are placed in a crucible within a vacuum-arc furnace, melted at high temperatures, and then directly cast into products based on a specific composition ratio. The melt casting method offers advantages such as a short production cycle, low cost, energy efficiency, and ease of operation [73].

Additionally, the melt casting method allows for high temperatures (around 3000 °C), enabling the melting of most elements in the periodic table. Due to these advantages, the melt casting method can be more extensively utilized for manufacturing LW-HEAs. However, a drawback is the prevalence of large internal stress and component segregation, necessitating multiple melting processes to ensure

uniformity. To achieve fine grains and reduce element segregation, a water-cooled copper crucible is often employed to enhance the solidification rate.

In contrast, the vacuum-arc melting method may lead to the premature evaporation of low melting point metals. When low melting point active metal elements like Mg and Li are present in the alloy, the induction melting method is generally used for alloy preparation. Induction melting utilizes the electromagnetic induction process to generate eddy currents, resulting in metal melting. This method experiences fewer evaporation and burning losses of elements and provides precise control over the proportion of active elements in the alloy [74,75].

For instance, alloys such as  $\text{Al}_{20}\text{Be}_{20}\text{Fe}_{10}\text{Si}_{15}\text{Ti}_{35}$  and  $\text{Mg}_x(\text{AlCuMnZn})_{100-x}$  have been synthesized using the induction melting and casting route [50,76]. The lowest density lightweight HEAs, such as  $\text{MgCaAlLiCu}$  and  $\text{Mg}_{50}(\text{MnAlZnCu})_{50}$ , have been synthesized using the induction melting route, with a density of approximately  $2.2 \text{ g/cm}^3$  [72]. The challenge in the production of LW-HEA parts through melting and casting lies in finding solutions to reduce elemental segregation and internal stresses in the final product.

## 2.8. Microstructural and mechanical properties of LW-HEAs

An exhaustive search has been conducted on LW-HEAs developed to date, considering alloys with a density equal to or less than  $6 \text{ g/cm}^3$ . These have been categorized based on the type of structure they form, their density, compressive yield strength, ultimate compressive strength, microhardness, and processing route. The results are presented in the following Table 2-5, which will be useful for comparisons with the designed alloys.

It is important to note that LW-HEA alloys are typically too hard and lack elongation, making them unsuitable for tensile testing. As a result, they are primarily characterized by their compressive properties. To date, the highest compressive yield strength observed in LW-HEA has been reported in the study by Stepanov *et al.* [77]. The researchers fabricated an  $\text{AlCr}_{1.5}\text{NbTiV}$  alloy with a density of  $5.90 \text{ g/cm}^3$  using vacuum arc melting. The alloy's microstructure consisted of both BCC and Laves (C14) phases. The alloy exhibited a compressive yield strength of 1.70 GPa at room temperature.

In the same year Stepanov *et al.* [78] developed the LW-HEA  $\text{Al}_{1.5}\text{NbVZrTi}$ , which has shown remarkable compressive strength despite its low density. The alloy was fabricated using arc melting and has a density of  $5.50 \text{ g/cm}^3$ . The microstructure of the alloy consists of a BCC matrix with hexagonal particles of the Laves C14 phase. In its as-cast state, the alloy demonstrated a compressive strength of 1.31 GPa and a microhardness of 620 HV. Tseng *et al.* [79] produced a LW-HEA with remarkable microhardness and high-temperature oxidation resistance. The alloy, designated as  $\text{Al}_{20}\text{Be}_{20}\text{Fe}_{10}\text{Si}_{15}\text{Ti}_{35}$ , was fabricated using vacuum arc melting, and has a low density of  $3.91 \text{ g/cm}^3$ . The microstructure of the alloy consists of two phases with HCP crystalline structures, namely  $\text{Fe}_2\text{Ti}$  and  $\text{Si}_3\text{Ti}_5$  phase. Notably, the alloy exhibited a microhardness of 911 HV, surpassing even that of quartz. The LW-HEA that has recorded the lowest density and shown high ductility to date is the  $\text{Al}_{15}\text{Li}_{39}\text{Mg}_{45}\text{Ca}_{0.5}\text{Si}_{0.5}$  alloy developed by Jia *et al.* [80]. The alloy was fabricated by induction melting and has a density of  $1.46 \text{ g/cm}^3$ . Its microstructure consists of a BCC solid solution together with  $\text{AlLi}$  and  $\text{Li}_2\text{MgAl}$  intermetallics. The alloy has demonstrated a high yield strength of 3.42 GPa and good compressive ductility more than 60%. On the other hand, LW-HEA that has demonstrated

the highest hardness to density ratio reported to date is the  $\text{Al}_{65}\text{Cu}_5\text{Cr}_5\text{Si}_{15}\text{Mn}_5\text{Ti}_5$  alloy developed by Sanchez *et al.* [81]. The alloy was fabricated using large scale vacuum die casting and consists of a BCC phase as well as different intermetallic phases. The alloy has a density of  $3.70 \text{ g/cm}^3$  and exhibits a microhardness of 889 HV.

Table 2-5. List of lightweight HEAs, along with their phase involved, density, mechanical properties, and processing route.

Alloys	Structure	Density $\text{g/cm}^3$	Yield strength GPa	Ultimate compressive strength GPa	Micro-hardness HV	Processing route	Ref
$\text{Al}_{0.5}\text{NbTiVZr}$	BCC + Laves + $\text{Zr}_2\text{Al}$	6.04	0.96	1.10	470±10	Arc melting	[82]
$\text{Al}_{15}\text{Zr}_{40}\text{Ti}_{28}\text{Nb}_{12}\text{Mo}_5$	BCC + B2	6.00	1.27	-	-	Arc melting	[83]
$\text{AlCr}_{1.5}\text{NbTiV}$	BCC + Laves	5.90	1.70	-	-	Arc melting	[77]
$\text{AlCrFeMnTi}_{0.25}$	BCC + L21	5.87	-	-	-	Arc melting	[51]
$\text{AlCrNbTiV}$	BCC + Laves	5.82	1.55	-	-	Arc melting	[77]
$\text{Al}_{15}\text{Zr}_{40}\text{Ti}_{28}\text{Nb}_{12}\text{Cr}_5$	BCC + B2	5.82	1.36	-	-	Arc melting	[83]
$\text{Al}_{15}\text{Zr}_{40}\text{Ti}_{28}\text{Nb}_{12}\text{Si}_5$	BCC	5.79	1.35	-	-	Arc melting	[83]
$\text{AlNbTiVZr}$	BCC + Laves (C14)	5.76	1.08	1.21	540±10	Arc melting	[78]
$\text{AlCr}_{0.5}\text{NbTiV}$	BCC	5.71	1.30	-	-	Arc melting	[77]
$\text{AlNbTiV}$	BCC	5.59	1.02	1.31	-	Arc melting	[77,84]
$\text{Al}_{26.6}\text{Nb}_{23.8}\text{Ti}_{25.1}\text{V}_{24.5}$	BCC	5.59	-	-	448±12	Casting	[84]
$\text{Al}_{1.5}\text{NbVZrTi}$	BCC, Laves (C14), $\text{AlZr}_2$	5.50	-	1.31	620±20	Arc melting	[78]
$\text{Al}_{1.5}\text{CrFeMnTi}$	BCC + L21 + Laves	5.31	-	-	-	Arc melting	[51]
$\text{Al}_2\text{CrFeMnTi}_{0.25}$	BCC + L21	5.16	-	-	-	Arc melting	[51]
$\text{Al}_2\text{CrFeMnTi}$	BCC + L21 + Laves	5.06	-	-	-	Arc melting	[51]
$\text{AlFeCuCrMg}_{1.7}$	B <sub>2</sub> , BCC, $\text{Cu}_2\text{Mg}$ , $\text{Mg}_2\text{Cu}$ , $\sigma$ phase	4.90	-	-	533	MA + SPS	[85]
$\text{Al}_3\text{CrFeMnTi}_{0.25}$	BCC + L21 + Laves	4.71	-	-	-	Arc melting	[51]
$\text{Al}_4\text{CrFeMnTi}_{0.25}$	BCC + L21 + Laves	4.40	-	-	-	Arc melting	[51]
$\text{AlFeMgTiZn}$	BCC + IM	4.34	-	-	-	MA	[86]
$\text{Mg}_{20}(\text{AlCuMnZn})_{80}$	HCP + Al-Mn icosahedral Quasi-crystal	4.29	0.42	0.42	431	MA + SPS	[76]
$\text{AlLiMgZnSn}$	FCC + IM	4.23	0.60	-	-	Arc melting	[87]

$\text{Al}_{35}\text{Cr}_{14}\text{Mg}_6\text{Ti}_{35}\text{V}_{10}$	HCP + FCC + BCC	4.05	-	-	460	MA + SPS	[88]
$\text{Al}_{20}\text{Be}_{20}\text{Fe}_{10}\text{Si}_{15}\text{Ti}_{35}$	Ti (Be, Al, Si, Fe) <sub>2</sub> , Al <sub>2</sub> (Ti, Fe), Ti <sub>5</sub> Si <sub>3</sub>	3.91	-	-	911	Arc melting	[79]
$\text{AlLi}_{0.5}\text{MgZn}_{0.5}\text{Cu}_{0.2}$	FCC + IM	3.73	0.48	-	-	Arc melting	[87]
$\text{Al}_{65}\text{Cu}_5\text{Cr}_5\text{Si}_{15}\text{Mn}_5\text{Ti}_5$	FCC + IM	3.70	-	-	889	Vacuum Induction Melting	[81]
$\text{AlLi}_{0.5}\text{MgCu}_{0.5}\text{Sn}_{0.2}$	FCC + IM	3.69	-	-	-	Arc melting	[87]
$\text{Mg}_{33}(\text{AlCuMnZn})_{67}$	HCP + Al- Mn icosahedral Quasi- crystal	3.26	0.43	0.43	430	MA + SPS	[76]
$\text{AlLi}_{0.5}\text{MgZn}_{0.5}\text{Sn}_{0.2}$	FCC + IM	3.22	-	-	-	Arc melting	[87]
$\text{Al}_{80}\text{Li}_5\text{Mg}_5\text{Zn}_5\text{Cu}_5$	FCC + IM	3.08	0.48	-	-	Arc melting	[87]
$\text{Al}_{80}\text{Li}_5\text{Mg}_5\text{Zn}_5\text{Sn}_5$	FCC + IM	3.05	0.41	-	-	Arc melting	[87]
$\text{Al}_{20}\text{Li}_{20}\text{Mg}_{10}\text{Sc}_{20}\text{Ti}_{30}$ (N, O)	FCC	2.67	-	-	599	MA + Sintering	[89]
$\text{Al}_{20}\text{Li}_{20}\text{Mg}_{10}\text{Sc}_{20}\text{Ti}_{30}$	HCP	2.67	-	-	499	MA + Sintering	[89]
$\text{Mg}_{43}(\text{AlCuMnZn})_{57}$	HCP + Al- Mn icosahedral Quasi- crystal	2.51	0.50	0.50	255	MA + SPS	[76]
$\text{Mg}_{45.6}(\text{AlCuMnZn})_{54.4}$	HCP + Al- Mn icosahedral Quasi- crystal	2.30	0.48	0.48	225	MA + SPS	[76]
$\text{Mg}_{50}(\text{AlCuMnZn})_{50}$	HCP + Al- Mn icosahedral Quasi- crystal	2.20	0.34	0.40	178	MA + SPS	[76]
$\text{MgCaAlLiCu}$	Tetragonal	2.20	0.91	2.2	-	Casting	[90]
$\text{Al}_{19.9}\text{Li}_{30}\text{Mg}_{35}\text{Si}_{10}\text{Ca}_5$ Y <sub>0.1</sub>	HCP + IM	1.70	0.55	0.72	-	Induction melting	[80]
$\text{Al}_{15}\text{Li}_{35}\text{Mg}_{35}\text{Ca}_{10}\text{Si}_5$	BCC + HCP + IM	1.57	0.42	0.53	-	Induction melting	[80]
$\text{Al}_{15}\text{Li}_{35}\text{Mg}_{48}\text{Ca}_1\text{Si}_1$	BCC + HCP + IM	1.52	0.36	0.61	-	Induction melting	[80]
$\text{Al}_{15}\text{Li}_{38}\text{Mg}_{45}\text{Ca}_{0.5}\text{Si}_{1.5}$	BCC + HCP + IM	1.50	0.35	0.41	-	Induction melting	[80]
$\text{Al}_{15}\text{Li}_{39}\text{Mg}_{45}\text{Ca}_{0.5}\text{Si}_{0.5}$	BCC + IM	1.46	0.30	0.33	-	Induction melting	[80]

## 2.9. Critical review

To date, high-entropy alloys lack a precise definition due to their complexity and the rapid evolution of these materials. Despite various denominations and criticisms surrounding the term "high-entropy alloy," they share the fundamental characteristic of being composed of multiple principal components located in the central region of a multicomponent phase diagram. Despite lacking a universally agreed-upon definition, "high-entropy alloys" is the preferred term, given its widespread usage in scientific discourse.

From this concept, as mentioned earlier, emerges the category of lightweight or low-density high-entropy alloys, composed mostly of light elements, and they have garnered significant attention. Lightweight high entropy alloys stand out for their exceptional mechanical and physical properties, such as compressive strength and microhardness, despite their lightweight composition. This attractiveness has translated into various applications, from the aerospace industry to biomedical applications. Interest intensifies due to the pursuit of more efficient technologies, especially in transportation, where reducing the weight of structural components without compromising strength and durability is crucial. Additionally, in line with the growing importance of sustainability and emissions reduction, lightweight alloys offer an alternative that supports environmental objectives.

Technological advancements, both in manufacturing techniques and design methodologies, whether through empirical parameters or computational techniques like CALPHAD, have facilitated research and application of these alloys, driving development and innovation. In this context, the exploration of new materials with improved properties has placed LW-HEA in the spotlight, propelling research to find innovative applications and solutions to current challenges in materials engineering.

Although advancements in lightweight high-entropy alloys are expected to benefit the efficiency of vehicles and aircraft, manufacturing these materials requires specialized techniques or the careful selection of master alloys to address variations in melting and boiling points. However, the adoption of specialized casting methods could significantly increase the design costs of the alloy, potentially making it economically unviable.

Additionally, despite the outstanding compressive strength and microhardness of LW-HEAs, it is crucial to consider limitations in terms of ductility, as this could affect their applicability in structural situations. However, many applications of LW-HEA remain unexplored. While many LW-HEAs have been designed and studied recently, their performance in tensile tests has rarely been explored. Instead, mechanical properties are often characterized in terms of compression tests or hardness. Most LW-HEAs designed to date have very limited tensile ductility, often not exceeding a few percentage points of strain prior to fracture.

As a result, the creation of a lightweight and ductile alloy is proposed, focusing on designing an alloy with an FCC crystal structure using the principles of high entropy. For its design, empirical parameters and CALPHAD methodology will be used, which have proven effective in designing numerous LW-HEA alloys. Additionally, experimental techniques will be combined to achieve an optimal design. Furthermore, the selection of a casting technique and methodology that addresses challenges associated with different melting points is proposed, ensuring it is both cost-effective and viable for implementation in the industry. In summary, the pursuit of a balance between distinctive properties and challenges in the manufacturing process underscores the ongoing need for innovation in the field of LW-HEAs.

# Chapter 3

## 3. Numerical and experimental procedures

*In this chapter, we delve into the fundamental methods and equipment utilized for the design, fabrication, and optimization of low-density medium entropy alloys, specifically addressing Chapters 4, 5, and 6 and placing a particular emphasis on their characterization.*

*The methodology employed in this doctoral thesis is illustrated in Fig. 3-1 below. It is noteworthy that certain equipment and techniques are recurrently utilized throughout the thesis, with occasional adjustments to measurement parameters. Detailed information will be provided only when necessary to emphasize specific changes.*

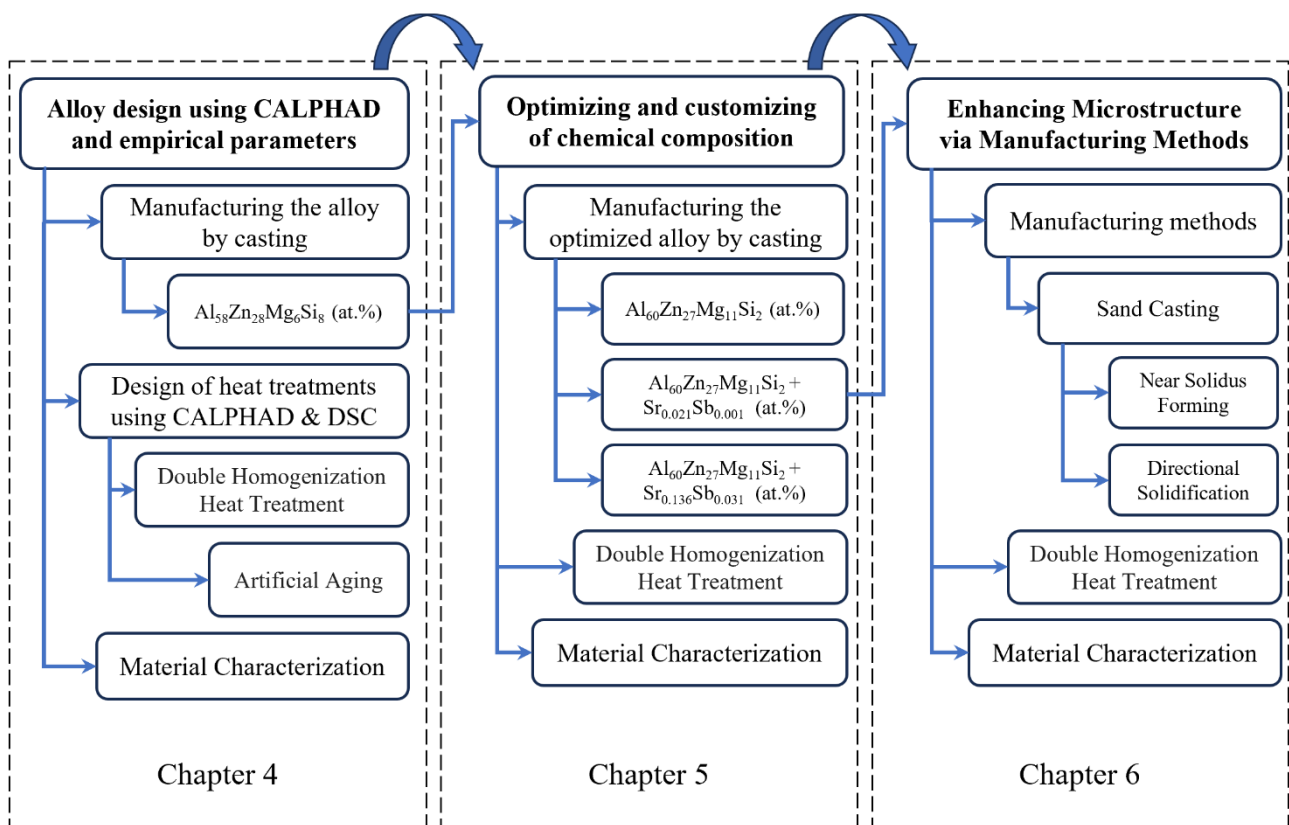


Fig. 3-1 Research workflow.



### 3.1. Design strategy

#### 3.1.1. Alloy design using empirical parameters and CALPHAD

For the design and development of the alloy, thermodynamic, topological, and electronic parameters such as the entropy of mixing ( $\Delta S_{mix}$ ), configurational enthalpy of mixing ( $\Delta H_{mix}$ ), omega parameter ( $\Omega$ ), atomic size difference ( $\delta$ ) between the constituent elements, valence electron concentration (VEC), and electronegativity difference ( $\Delta\chi$ ) were utilized to predict solid solution formation in the LW-HEA. However, the CALPHAD method was the primary design strategy to determine the concentration of each element, phase stabilities, and heat treatment schedules.

Solidification calculations and phase diagrams were conducted for the designed alloys in Chapter 4, Chapter 5, and Chapter 6. These calculations were carried out using FactSage™ 8.2 software and utilized the FTlite database [91]. In these solidification calculations, equilibrium and Scheil cooling conditions were assumed to predict the microstructural characteristics of the alloys. It was also assumed that there was complete diffusion in the liquid phase and no diffusion in the solid phases. This assumption is considered reasonable for determining microstructural features such as chemistry and the number of phases that form during the solidification process in the present study. Additionally, FactSage™ 8.2 was utilized to determine the appropriate heat treatment temperature range.

### 3.2. Alloy Casting Processes

#### 3.2.1. First alloy casting

For the first target alloy, the raw materials utilized were high-purity Al, Si, and Mg, while Zamak5, a Zn4Al1Cu mass % master alloy, was employed for Zn. The charge balance for each alloy was calculated based on the desired nominal composition. Each alloying element was prepared by sectioning into pieces larger than required for melting, followed by mechanical abrasion and ultrasonic cleaning in ethanol. The weight was confirmed with an accuracy of 0.10 g using a precision balance.

These elements were melted in an alumina crucible inside a Nabertherm K4/13 resistance furnace with forced convection. During the melting process, a continuous Ar gas flow was used, and the temperature of the melting was monitored with a type K thermocouple. This prevented the LW-HEA from undergoing oxidation and mold-metal interaction. To reduce the burning loss of Mg, the fusion order of the elements was the following: 1) Al was melted first at a temperature of 750°C, 2) Si and Zamak5 alloy were added, and the melt was left to homogenize for fifteen minutes, and 3) Mg was added. Then the melt was cast into a steel mold. This mold featured a stepped structure and was constructed using AISI H13 steel, as shown in Fig. 3-2.





Fig. 3-2 Stepped mold made of AISI H13 steel (Total volume: 29,177 mm<sup>3</sup>).

The steel mold was preheated to a temperature of 250 °C, and the mold was coated with boron nitride to prevent sticking, thermal shock, and prolong their lifetime.

For composition analysis, chips from the as-cast samples were machined and digested with pure nitric acid (HNO<sub>3</sub>), followed by Inductively Coupled Plasma-Optical Emission Spectroscopy measurements (ICP-OES, Thermo Fisher Scientific iCAP duo 6500, USA). All measurements were repeated 3 times to ensure the repeatability.

### 3.2.2. Alloy casting with optimized composition

For this second casting, we relied on the knowledge gained from the first alloy to adjust it for subsequent compositions. Our focus is on retaining the key elements for alloy manufacturing while adjusting the chemical composition to avoid the formation of undesirable phases, especially primary silicon, while maintaining the high solid solution of aluminum (FCC).

Additionally, we plan to enhance the mechanical properties of the alloys by modifying the morphology and size of the Mg<sub>2</sub>Si intermetallic phase through the introduction of additional elements such as strontium (Sr) and antimony (Sb). This strategy will be detailed in Chapter 4.

The initial alloy Al<sub>58</sub>Zn<sub>28</sub>Mg<sub>6</sub>Si<sub>8</sub> alloy [92] serves as a starting point for optimizing its composition by reducing the silicon content and adding modifying elements, strontium, and antimony.

The optimized alloys were prepared by gravity die casting, using commercially pure Al, Zn, Mg, and Si as alloying elements. Al-10%Sr and Al-10%Sb master alloys were utilized as modifiers. These elements were melted in an alumina crucible inside an induction furnace under an argon atmosphere. This prevented the multicomponent alloy from undergoing oxidation and mold-metal interaction. To reduce the burning loss of Mg, the fusion order of the elements was the following: 1) Al was melted first at a temperature of 750°C, 2) Si and Zn were added, and the broth was left to homogenize for a few minutes, 3) Then Mg was added and 5) Finally, once all the elements were melted, Al-10%Sr &

Al-10%Sb master alloys were added to the modified alloys and the broth was allowed to homogenize for 20 minutes.



Fig. 3-3 Inductotherm induction furnace.

Therefore, the molten alloy was poured into a mold preheated to 300°C. This mold featured a stepped structure and was constructed using AISI H13 steel, as shown in Fig. 3-4. The mold was coated with boron nitride to prevent adhesion, offer protection against thermal shock, and improve overall durability. The analysis primarily concentrated on the initial step of the mold, which represents the largest dimensions. This step was selected for study due to its practicality in fabricating compression specimens. For composition analysis, the same methodology has been used as shown in the previous section.



Fig. 3-4 Stepped mold made of AISI H13 steel (Total volume: 141,547 mm<sup>3</sup>).

### 3.3. Additional processing routes

The purpose of this section is to utilize the knowledge acquired from the initial alloy fabrications and take as a starting point the compositionally optimized alloy from the previous section, which has

demonstrated superior compression properties. The idea is to reproduce it with the same composition, employing three different manufacturing methods: sand casting, near solidus forming technology, and directional solidification. Through these manufacturing methods, the aim is to modify the microstructure and observe the effect on both microstructure and mechanical properties.

The optimized  $\text{Al}_{60}\text{Zn}_{27}\text{Mg}_{11}\text{Si}_2 + 0.021\text{SrSb}$  LW-MEA, as discussed in the preceding chapter, was manufactured through the sand-casting process. The resulting sand cast ingots will undergo post-processing using two distinct techniques: Directional Solidification (DS) and Near Solid Forming (NSF). In the case of NSF process, the sand cast ingots will be cut and processed utilizing this technique. Conversely, for the directional solidification process, the sand cast ingots will be remelted and solidified using DS in a controlled manner while maintaining their original composition. Following these procedures, all samples will undergo a heat treatment process. A comparative analysis will be conducted to assess the microstructures and mechanical properties of the specimens under uniaxial compression. Fig. 3-5 provides a schematic diagram illustrating the various processes and heat treatments carried out throughout this study.

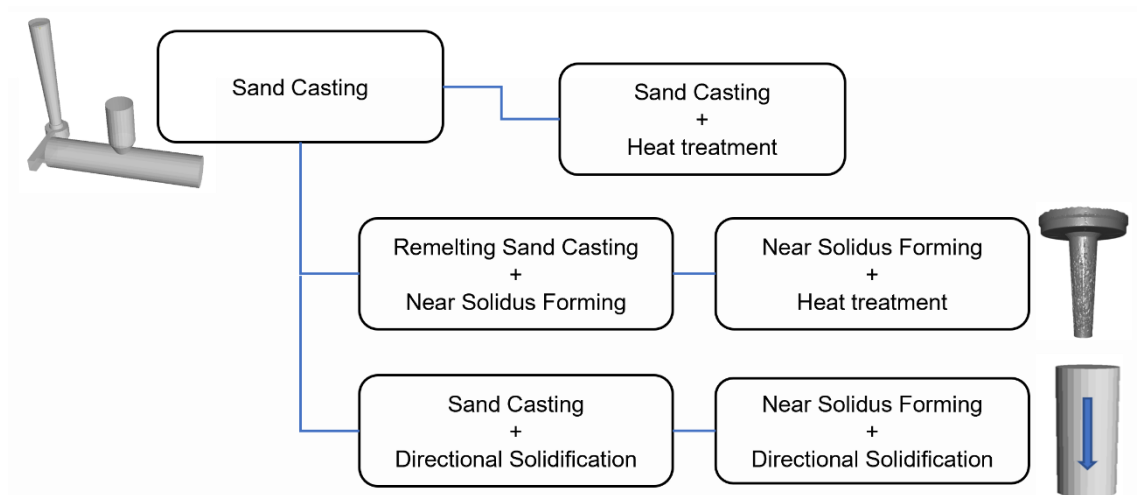


Fig. 3-5 Schematic diagram of the Sand Casting, Near Solidus Forming, Directional Solidification processes, and the associated heat treatments employed in this study.

### 3.3.1. Sand casting process

The optimized alloy  $\text{Al}_{60}\text{Zn}_{27}\text{Mg}_{11}\text{Si}_2 + 0.021\text{SrSb}$  was produced through sand casting. The gating and feeding system design was carried out using FLOW-3D CAST v5.1 software, as shown in Fig. 3-6.

The computational simulation focused on analyzing the filling process to predict the occurrence of premature solidification and solidification defects during the casting process. To obtain accurate computational simulation results, specific material properties were entered into the program. These properties included the liquidus and solidus temperatures, latent heat of solidification, thermal conductivity, and heat transfer coefficient (HTC) between the metal and mold. Differential scanning calorimetry (DSC) and laser flash analysis (LFA) were conducted during the initial sand casting to determine these thermophysical properties. This allowed for the optimization of the gating and feeding system design, resulting in a defect-free part.

However, obtaining the HTC value experimentally can be challenging, and it is commonly measured through numerical simulation. In this study, the HTC values were obtained from the integrated databases within the software. The simulation encompassed the pouring of the metal from the crucible into the mold, with a pouring temperature set at 620 °C.

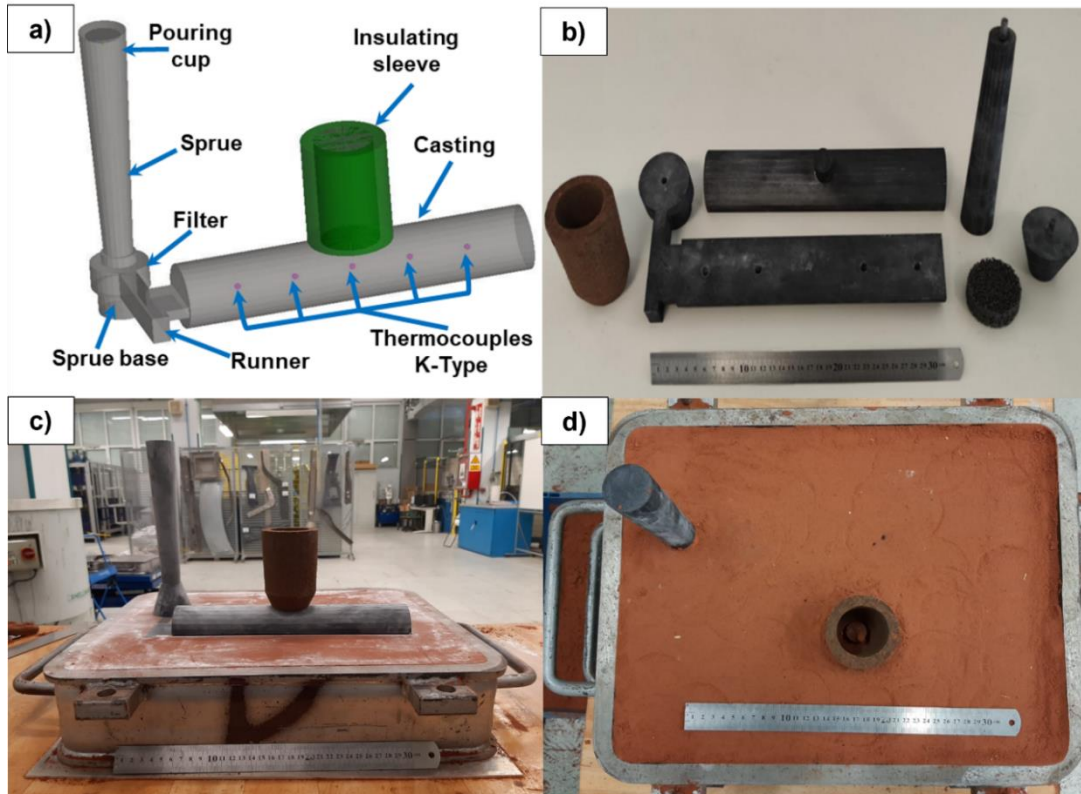


Fig. 3-6 (a) CAD model of the gate and feed system designed using FLOW 3D software; (b) 3D printed mold, filter and insulating sleeve; (c) one half of the mold (cope); (d) the other half the mold(drag).

To carry out the sand-casting process, alloying elements of commercial purity, including Al, Zn, Mg, and Si, were used. Al-10%Sr and Al-10%Sb master alloys were utilized as modifiers. These elements were melted in an alumina crucible inside an induction furnace under an argon atmosphere. This prevented the multicomponent alloy from undergoing oxidation and mold-metal interaction. To minimize the burning loss of Mg, the fusion order of the elements was the same as that used in the section for Alloy casting with optimized composition.

The molten alloy was poured into a mold made of petrobond sand, which included a round sponge filter (SIVEX-FC-20-ppi, FOSECO) and an open insulating sleeve feeder (Kalmin-S, FOSECO) to ensure proper solidification and flow of the alloy. For composition analysis, the same methodology has been used as shown in the previous section. The solidification rate in the cylinder was measured using five K-type thermocouples placed at 50 mm from each other. Temperatures were recorded with a National Instruments NI-cDAQ-9171 chassis and NI-TB-9212 temperature module (Austin, TX, USA) with a data acquisition frequency of 10 Hz.



### 3.3.2. Near Solidus Forming process

To perform the Near Solidus Forming process, a Fagor 400 t AC servomechanical press was utilized in conjunction with NSF tooling developed by Mondragon Unibertsitatea [93]. To design the dies, finite element simulations were conducted using FORGE NxT 3.0 software to determine the entry angle of the conical dies that would ensure uniform deformation in the extruded samples. Three different angles (20°, 45°, and 70°) were evaluated during the simulations, and the 45° angle was selected as it provided the most uniform deformation. The dies used in the NSF tests were fabricated from AISI H13 steel, which underwent a process of quenching, tempering, and nitriding. Fig. 3-7b below shows the 45° die that was specifically manufactured for the NSF tests.

In Fig. 3-7a, the NSF cell and its tooling are depicted. The press used in the cell is a 400-tonne capacity Fagor servo-mechanical press. The deformation stage begins with the punch moving from the top dead center to the bottom. It's important to note that the maximum load is reached only in the final position, where the punch is held for five seconds, compressing the material. To determine the suitable temperature for NSF of the sand-casting cylindrical ingot, we employed a combination of CALPHAD and Differential Scanning Calorimetry. The solidus temperature of the medium entropy alloy was determined to be around 390 °C, so an NSF temperature of approximately 95% of the solidus, which is 380 °C, has been selected for this process.

The operating sequence of the NSF cell comprises several stages. Initially, a billet with a diameter of 60 mm and a length of 42 mm is heated in a muffle furnace (Hobersal 9-CRN5X-18) until it reaches a temperature of 380 °C. During this process, an argon flow of 0.5 L/min is maintained to prevent oxidation. Simultaneously, the dies are heated with oil to a temperature of 270 °C. Additionally, both the dies and the punch are coated with boron nitride to prevent sticking, safeguard against thermal shock, and extend their overall lifespan. Following a 20 min soak at the designated temperature of 380 °C, the billet is manually inserted into the upper part of the tooling. Subsequently, the punch is gradually lowered at an average rate of 200 mm/min where it dwells for 5 s before ramping back to the initial position. At this point, the clamping system is retracted, and the tooling opened to remove the component.

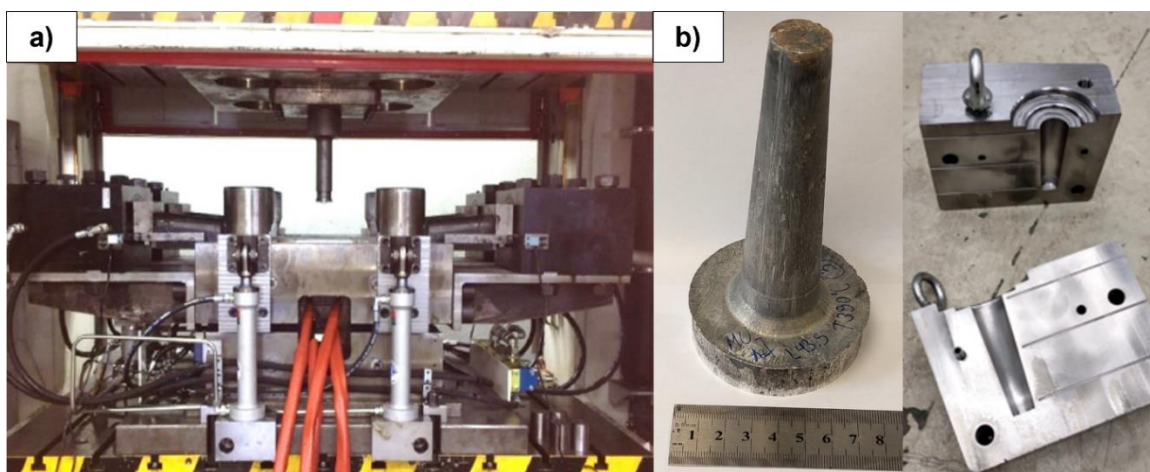


Fig. 3-7 (a) NSF cell (b) The dies used for the NSF process are made of AISI H13 steel, while the forming specimens are fabricated from the LW-MEA.

### 3.3.3. Directional Forming process

The directional solidification mechanism is shown in Fig. 3-8. The equipment consists of a motorized arm for lowering the steel crucible (1), steel crucible coated with boron nitride (2), an induction furnace (3), and a bucket filled with water (4). The directional solidification process is as follows: the sand-casting cylindrical ingot was remelted and solidified by direct-chill casting. The alloy melt was held at a temperature of 720 °C under an argon atmosphere with 3 Vol.% SF<sub>6</sub> added as a protective gas. The melt was stirred for 20 minutes to ensure homogeneity. The melt was then poured into steel molds coated with boron nitride to prevent sticking and thermal shock.

After pouring, the cooling water is controlled to gradually submerge the steel mold. The steel molds are placed on a riser with an induction furnace installed at a temperature of 680°C at the top. Then, the steel mold is slowly immersed in the cooling water at a rate of 62 mm/min. This design is aimed at delaying the cooling of the top of the casting, creating a higher temperature gradient near the solidification interface along the casting height direction. This process ensures rapid solidification, resulting in a refined microstructure and minimal defects. The final cylindrical casting ingots have dimensions of 180 mm in length and 65 mm in diameter.

The solidification rate in the cylinder, during the directional solidification process, was measured using five K-type thermocouples placed at 25 mm from each other. Temperatures were recorded using a National Instruments NI-cDAQ-9171 chassis and NI-TB-9212 temperature module (Austin, TX, USA) with a data acquisition frequency of 10 Hz.

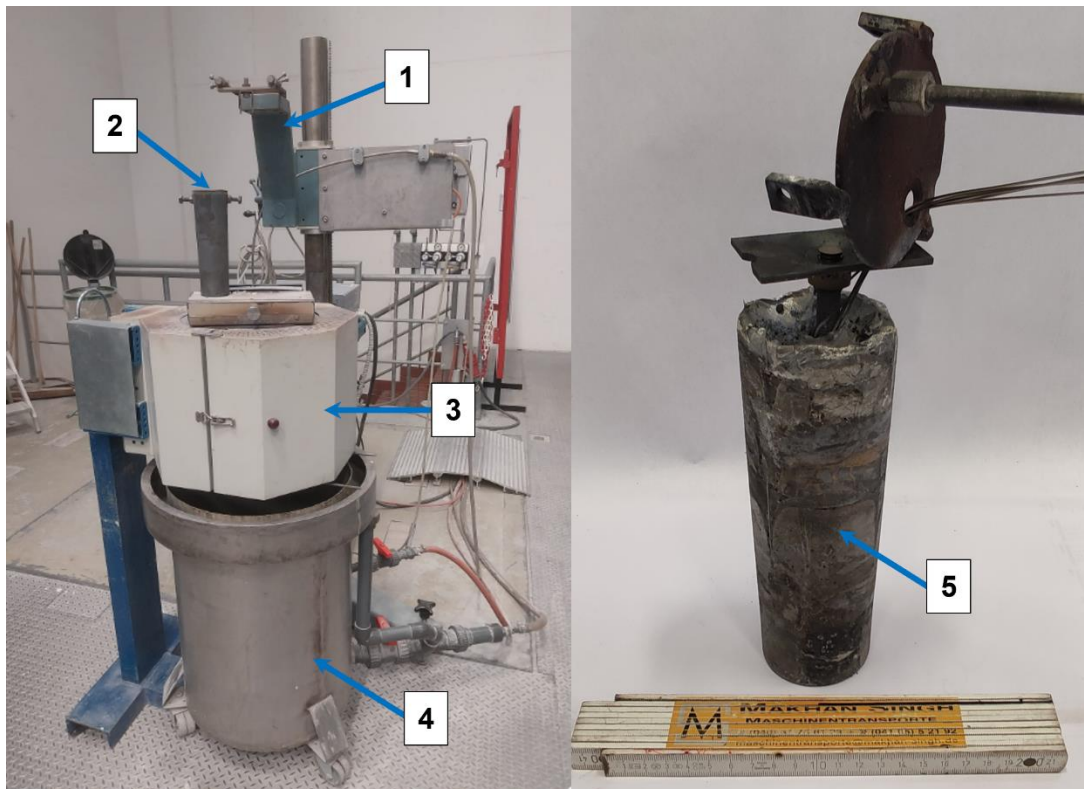


Fig. 3-8 Directional Solidification system. (1) motorized arm; (2) steel crucible coated with boron nitride; (3) induction furnace; (4) bucket filled with water; (5) cylindrical casting ingots.

### 3.4. Design of heat treatments using CALPHAD & DSC

The heat treatment temperatures were selected based on the differential scanning calorimetry (DSC) results and the simulations from the CALPHAD method (Equilibrium Solidification & Scheil solidification). The design of the heat treatments is explained in detail in chapter 4. For heat treatment all the as-cast samples were placed in Nabertherm K4/13 resistance furnace with forced convection in an argon induced atmosphere. After the alloys were heat treated, they were quenched immediately in water.

### 3.5. Material characterization

#### 3.5.1. Preparation for microstructural analysis.

The produced samples underwent preparation for microstructural characterization and testing. Initially, a Buehler Isomet 1000 Precision Saw was used to cut the samples, which were then mounted in a cold mounting resin on a copper base. This method allowed for conductive mounting using Technovit 5000, which was necessary for SEM examinations and to prevent any impact on the samples' heat treatment. Subsequently, the samples were subjected to grinding and polishing using a ATM SAPHIR 550 Grinder-Polisher. The grinding process involved using SiC papers of grade P600 to P1200. Following that, the samples were polished from 6 to 1 $\mu$ m using diamond paste until a flat mirror surface was achieved. A standard guide for preparation of metallographic specimens is described in the ASTM E3-11 standard. This standard was used here for grinding and polishing of samples.

#### 3.5.2. SEM and EDX analysis

The samples were analyzed using an FEI Nova Nano SEM 450 in backscattered electrons (BSEs) and high-contrast mode. This allowed for the examination of the microstructure and determination of the semiquantitative local chemical composition through energy-dispersive X-ray spectroscopy (EDS).



Fig. 3-9 Scanning Electron Microscope model FEI Nova Nano SEM 450.

### 3.5.3. TEM analysis

TEM was used to investigate microstructure details. TEM specimens were mechanically ground to  $\sim 120\mu\text{m}$  thickness, from which 3 mm diameter discs were punched. The discs were electropolished with a two-jet Fischione using an electrolyte mixture of 1/5  $\text{HClO}_4$  and 4/5  $\text{CH}_3\text{OH}$  with  $\text{C}_3\text{H}_8\text{O}_3$ . The liquid was kept at  $-50^\circ\text{C}\pm 5^\circ\text{C}$  with  $\text{CO}_2$ , and the applied voltage and current were 50 V and 100 mA.

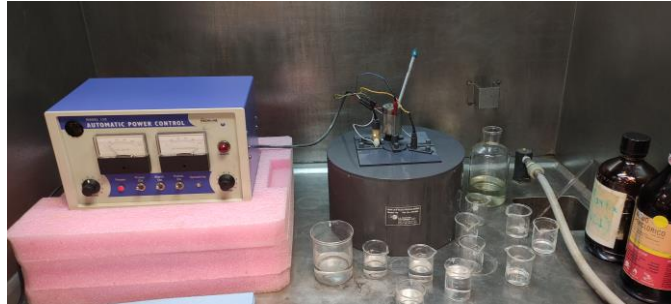


Fig. 3-10 Fischione Model 110 Automatic Twin-Jet Electropolisher.

The TEM observations were carried out in a Jeol 2000 FXII TEM equipped with EDX at 200 kV.



Fig. 3-11 Transmission electron microscope model JEM 2000FXII, JEOL.

### 3.5.4. XRD phase analysis

A BRUKER-binary V3 X-ray diffractometer with  $\text{Cu K}\alpha$  radiation ( $\lambda = 1.5406 \text{ \AA}$ ) radiation operating at 35 kV and 45 mA, with a scanning step of  $4^\circ/\text{min}$  from  $20^\circ$  to  $100^\circ$  ( $2\theta$ ), was used to identify different phases formed in the samples. The X-ray diffraction patterns were indexed using the PDF-4+ 2021 database from the International Center for Diffraction Data (ICDD).





Fig. 3-12 BRUKER-binary V3 X-ray diffractometer.

### 3.5.5. EBSD analysis

Before to perform the EBSD analysis, standard sample preparation methods were employed prior to the final polishing stage, which involved polishing with 0.05  $\mu\text{m}$  colloidal silica for 240 minutes using a BUEHLER VIBROMET 2 vibratory polisher. The EBSD measurements were made on selected metallographic to phase analysis using the FEI Nova Nano SEM 450 operated at 20 kV with the Detector System NordlysMax3 with Nordlys Forescatter with 6 diodes. In addition, the EBSD data were analyzed with the AZtechKL software.



Fig. 3-13 Interface of the AZtechKL acquisition and analysis software; The (SrZn<sub>13</sub>) phase is identified from the candidate list using electron backscatter diffraction pattern (EBSP). This sample corresponds to the Sr and Sb modified alloy detailed in Chapter 6.

### 3.5.6. Compression test

Compression tests at room temperature were conducted on all specimens, both as-cast and thermally treated, following ASTM-E09 standards, using a Zwick 050TM universal testing machine. Cylindrical samples of 13 mm diameter and 38 mm length and a strain rate of 0.01s<sup>-1</sup> were used in

the compression tests and each test was repeated 3 times. The yield strength was calculated as of the intersection of a line constructed parallel to the elastic part of the curve and offset by a strain of 0.2% to the right.



Fig. 3-14 Zwick 050TM universal testing machine (depicting a test specimen during testing).

### 3.5.7. Hardness measurements

Immediately after the heat treatments, microhardness tests were conducted using a Zwick machine with a Vickers indenter, following ASTM E384-22 standard. The test load and the dwell time were 5 kg and 10 s, respectively. These weights were chosen to make sure that the indentation covered several grains and phases, ensuring that the resulting average hardness of the alloy was representative. The spacing between indentations is higher than 2.5 times the diagonal of one indentation, which is the usually recommended separation to avoid interference between results. A minimum of twelve measurements were made for each test to ensure statistical reliability and a standard deviation of less than 5 HV.

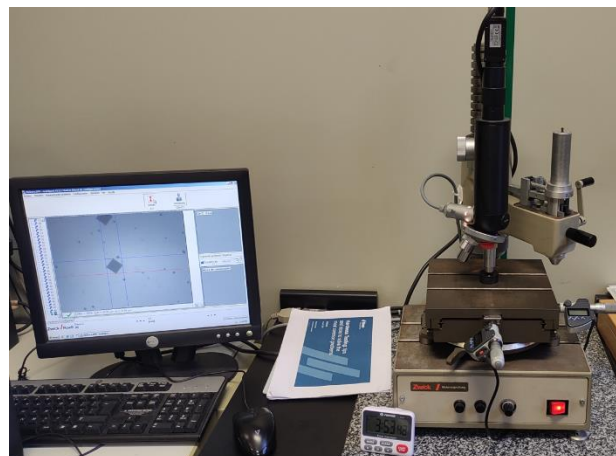


Fig. 3-15 Zwick Micro Vickers hardness tester.

### 3.5.8. DSC

NETZSCH STA 449 F3 Jupiter equipment was used to perform the DSC test. Samples were weighed to an accuracy of  $\pm 0.01$  mg, within the range of 50 to 75 mg. The samples were then ultrasonically cleaned in ethanol and dried before being placed in an Pt crucible with a lid. All tests were conducted at a heating and cooling rate of 10 K/min, and in a temperature range of 25°C to 750°C, thus melting the material “in situ”. The solidus and liquidus temperatures were estimated using the tangent method, based on data obtained from DSC measurements.



Fig. 3-16 DSC equipment model NETZSCH STA 449 F3 Jupiter.

### 3.5.9. Density measurements

The density of the material was obtained using a Precision Balance and the solid body density method. The balance used was a RADWAG model AS 60/220.X2 PLUS.

# Chapter 4

## 4. Alloy design and heat treatments of LW-MEA

*This chapter focuses on alloy design and heat treatment for a specific alloy ( $Al_{58}Zn_{28}Mg_6Si_8$ ). It also provides a detailed analysis of the alloy composition, prediction of solid solution formation and phase evolution. It includes information on empirical parameters, thermodynamic calculations, phase stability simulations, microstructure analysis and hardness measurements. Several phases are identified in the alloy, such as Al,  $MgZn_2$ ,  $Mg_2Si$ , Zn, Si and  $Mg_2Zn_{11}$ . The chapter extensively discusses the phase evolution and precipitation sequence, as well as their stability at different temperatures. In summary, Chapter 4 provides a comprehensive analysis of the  $Al_{58}Zn_{28}Mg_6Si_8$  alloy, emphasizing the intricate relationship between empirical predictions, thermodynamics, phase evolution and heat treatments to understand the microstructure and properties of the alloy.*

### 4.1. Introduction

As mentioned in the literature review, LW-HEAs offer significant opportunities for industries due to their unparalleled properties. However, despite their low density, high hardness, and compression strength, these alloys still exhibit little to no ductility. Additionally, manufacturing these alloys poses a challenge due to the different melting points of the alloying elements.

Motivated by the progress mentioned earlier, this chapter introduces the design of a new medium-entropy alloy, emphasizing its cost-effectiveness and ease of fabrication. The goal is to achieve a majority FCC solid solution phase that provides ductility, reinforced with intermetallics. To accomplish this, approaches like CALPHAD and binary and ternary diagrams were employed to determine the appropriate composition. Experimental results were compared with thermodynamic simulations, providing valuable insights for future designs of lightweight high-entropy alloys. The following Fig. 4-1 provides a simplified schematic illustration of the contents of this chapter.

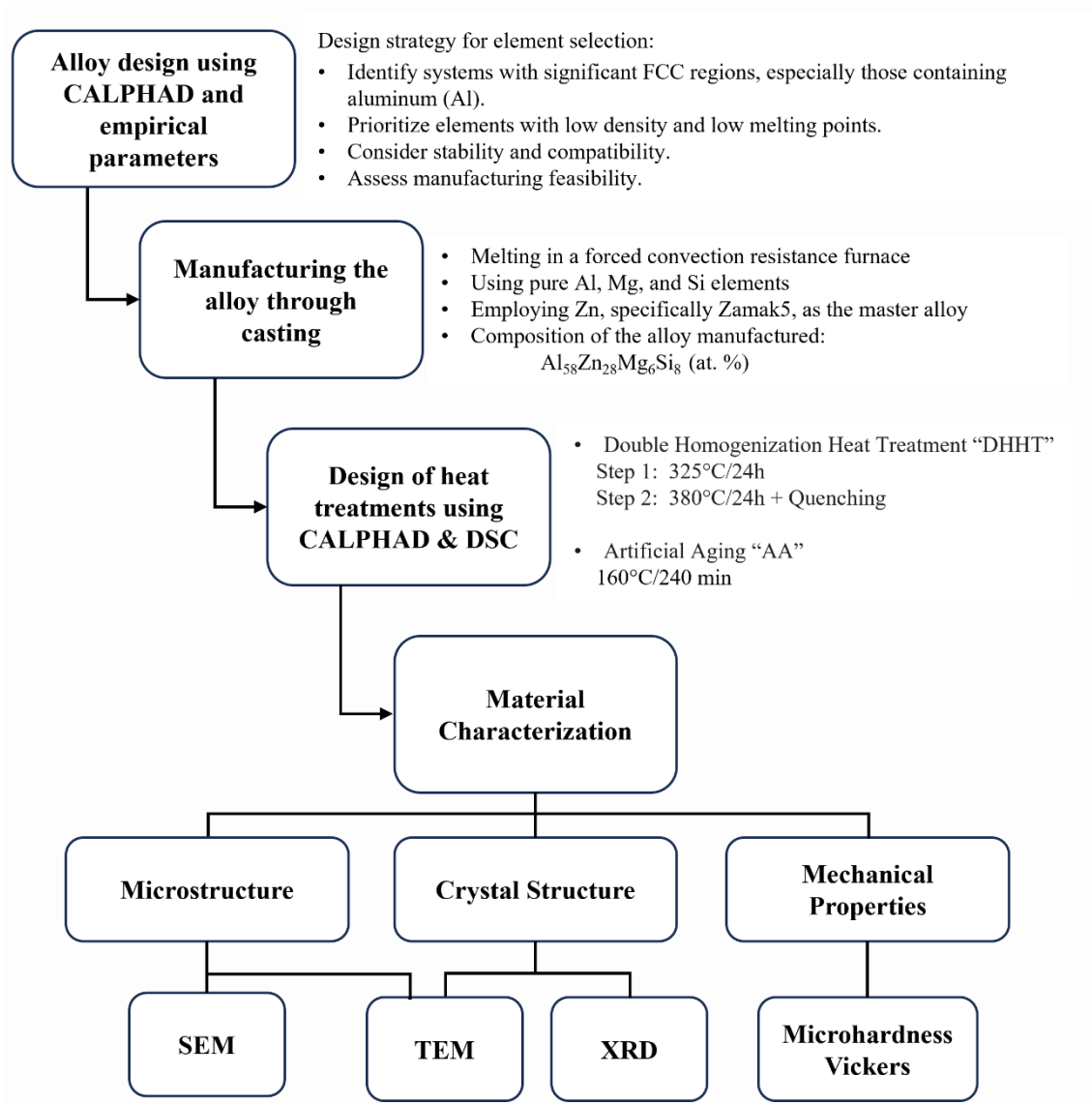


Fig. 4-1 Simplified outline of the contents of Chapter 4: "Alloy design and heat treatments of LW-MEA".

#### 4.1.1. CALPHAD approach to design LW-MEA

While the CALPHAD approach holds great promise for designing HEAs, it is essential to acknowledge certain considerations. One such factor is the potential for large extrapolations from thermodynamic models, which could lead to inaccuracies in evaluating Gibbs energy [20]. Nevertheless, research conducted by Gorsse *et al.* [94] provided insights into these constraints by analyzing CALPHAD databases in relation to multicomponent alloys. Their findings revealed that the thermodynamic properties of quaternary alloys can indeed be accurately predicted through direct extrapolation from fully evaluated binary systems. This underscores the potential and reliability of the CALPHAD approach in HEA design. Therefore, despite the acknowledged limitations of CALPHAD for systems with more than four components, we have chosen it as a tool for designing our alloy.

In this work, the principal elements were selected based on their low density, low melting point, stability, compatibility, and fabrication feasibility via the casting process. Expensive or scarce elements were discarded from the selection. The CALPHAD approach was then applied as a design strategy to determine the concentration of each element, phase stabilities, and heat treatment schedules. The major driver of the alloy design was to reduce the density by increasing the molar % of Al, to obtain an Al-based medium entropy alloy [81].

In line with this design strategy, the target in the simulations was set to identify systems that have relatively large (Al) FCC regions. The main assumption in the calculations was that a higher-order system could have a wide range of FCC only if its sub-systems have relatively large FCC regions [95]. Thus, the initial calculations were performed with binary systems; all possible Al-X binaries from the previously selected alloying elements (X is the alloying element) were examined, and those with the largest FCC solubility range were selected. The same calculation was performed with the ternary and quaternary systems. In accordance with the FCC solubility range, one or more systems were selected from each ternary, quaternary, and quinary system as candidate Al-based lightweight medium entropy alloy. The selected elements that met the previous requirements were Zn, and Mg.

Furthermore, considering the possibility of facing fluidity issues with these alloying elements, the inclusion of silicon in the mix was also contemplated. The aim was to enhance fluidity and reduce contraction during the manufacturing process. The addition of silicon could lead to the formation of intermetallics such as (Si) and (Mg<sub>2</sub>Si). These intermetallics, under certain circumstances, could enhance mechanical properties by impeding the movement of dislocations within the material.

The effects of the elements considered for alloy design are analyzed below.

- Aluminum: This element was selected, as mentioned earlier, due to its low density and a low melting point. Most importantly, the aim is to have an alloy with a higher percentage of the solid solution phase (Al), with a face-centered cubic (FCC) crystal structure. The choice of having an FCC crystal structure is because materials with an FCC crystal structure exhibit greater ductility than those with a body-centered cubic (BCC) or hexagonal close-packed (HCP) crystal structure. This is attributed to the fact that the FCC crystalline structure, besides being closely packed, possesses a higher number of slip systems [96].
- Zinc: This element was chosen for its high solubility in aluminum, despite its elevated density of 7.14 g/cm<sup>3</sup>. The solubility of zinc (Zn) in aluminum (Al) is the highest among all elements, peaking at 67 at.% at 380 °C (see Fig. 4-2a). This substantial solubility is attributed to the weak interaction between Zn and Al atoms, preventing the formation of intermetallic phases. At room temperature (24 °C), the solubility of Zn in Al is 0.85%, while the solubility of Al in Zn is less than 0.5%. The slight difference in atomic radii, with Al at 0.143 nm and Zn at 0.134 nm (approximately 7% difference), significantly influences the microstructure of Al-Zn and Zn-Al alloys [97].
- Magnesium: This element was selected due to being one of the lightest elements with a density of 1.738 g/cm<sup>3</sup>, and it is commonly used for structural applications. Additionally, it is the second element with high solubility in aluminum, reaching approximately 18.9 at. % at 450°C (see Fig. 4-2b). Considering the relative atomic radii of aluminum (Al) and magnesium (Mg), the ratio of the Al radius to the Mg radius is 1.12, suggesting a high level of mutual solid solubility [98].

- Silicon: Although silicon has low solid solubility in the aluminum phase (a maximum of 1.59 atomic % (see Fig. 4-2c)), it is the primary element that imparts high fluidity and low shrinkage to aluminum alloys [99]. As a result, silicon is beneficial for improving castability and weldability. Additionally, being a lightweight element with a density of 2.57 g/cm<sup>3</sup>, it was also selected.

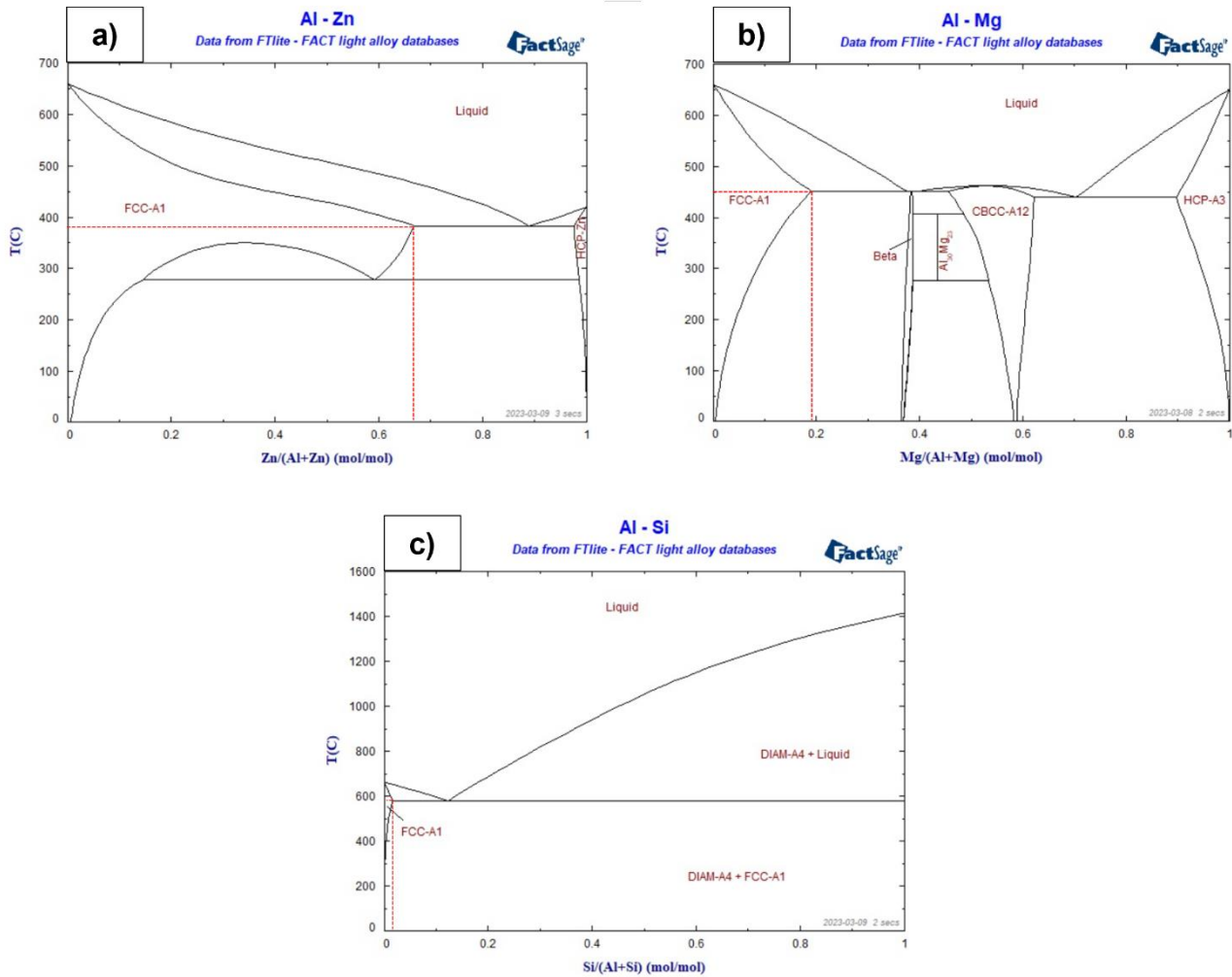


Fig. 4-2 Phase diagrams: a) Al-Zn, b) Al-Mg and c) Al-Si (temperature where maximum FCC solid solution is obtained is shown).

Additionally, Table 4-1 displays certain characteristics and properties of the selected elements.

Table 4-1 Characteristics and properties of the selected elements for the design of the LW-MEA.

<b>Elements</b>	<b>Al</b>	<b>Zn</b>	<b>Mg</b>	<b>Si</b>
<b>Temperature at maximum solid solubility in Al [°C].</b>	-	380	450	577
<b>Maximum solubility in Al, at. %</b>	-	67	18.9	1.59
<b>Fusion enthalpy [kJ/mol]</b>	10.79	7.32	8.48	50.21
<b>Electronegativity</b>	1.61	1.65	1.31	1.90
<b>Atomic radius [nm]</b>	0.143	0.134	0.160	0.111
<b>Melting Point [°C]</b>	661	420	650	1,414
<b>Boiling Point [°C]</b>	2,470	907	1,091	3,265
<b>Density [g/cm<sup>3</sup>]</b>	2.70	7.14	1.74	2.57
<b>Crystal structure</b>	FCC	HCP	HCP	Diamond

Based on the previously selected elements, we decided to focus on the shaded region of the ternary diagrams, as illustrated in Fig. 4-3. Our goal was to find a composition that exhibited a region with a FCC solid solution, adhering to the concept of high entropy and aiming for a central zone in the ternary diagram. As seen in Figures (Fig. 4-3a, Fig. 4-3, and Fig. 4-3c), adding Si to the alloy expands the region with a FCC solid solution. Therefore, we set the composition while maintaining 8% Silicon to keep the region broad.



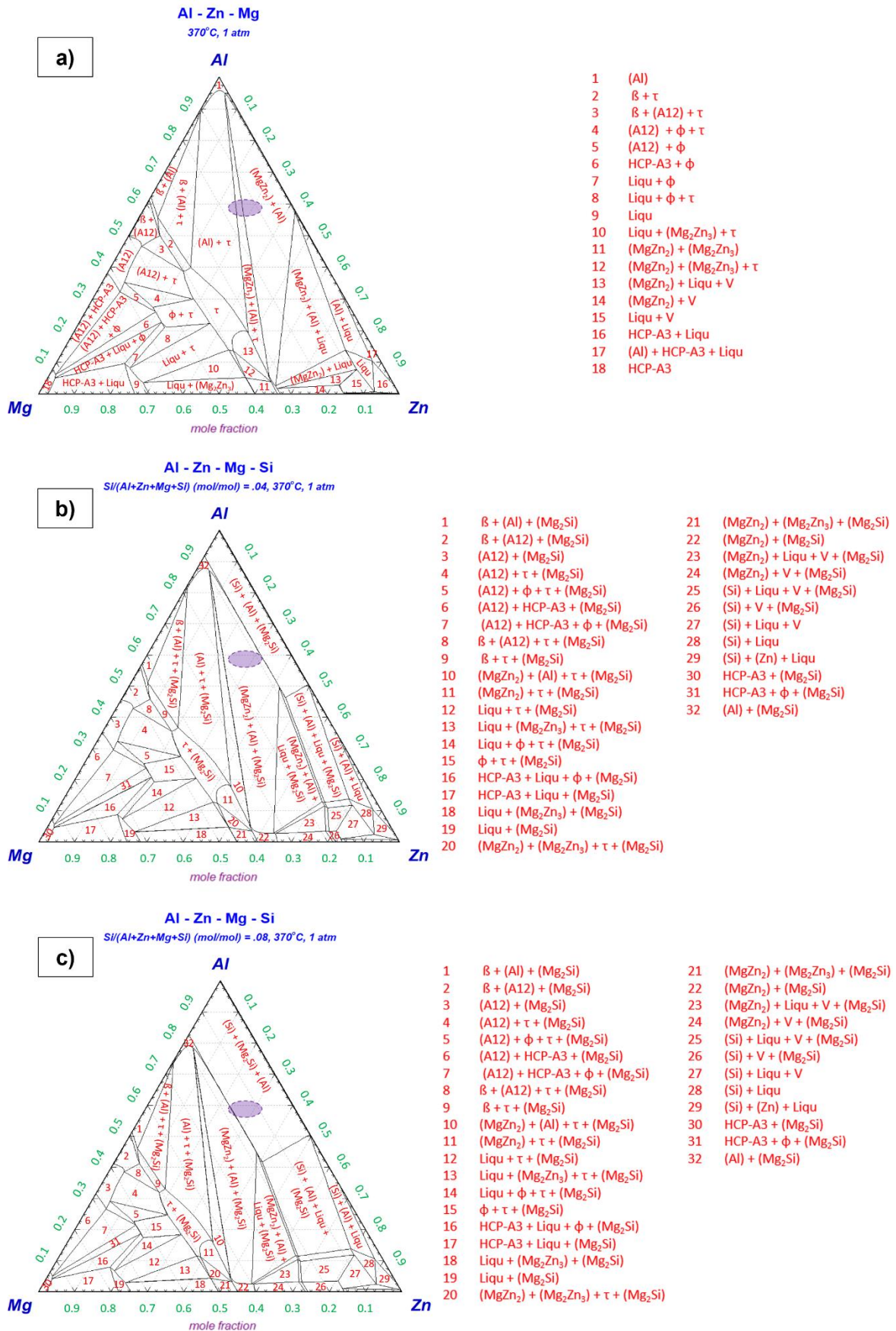


Fig. 4-3 Isothermal sections at 370°C: a) Al-Zn-Mg system, b) Al-Zn-Mg system with 4 at.% Si, and c) Al-Zn-Mg system with 8 at.% Si. (The shaded region corresponds to the studied zone where the target composition is determined).

Through various simulations, we selected the composition  $\text{Al}_{58}\text{Zn}_{28}\text{Mg}_6\text{Si}_8$  (at.%), which showed a high percentage of the solid solution phase (Al) with an FCC crystalline structure, accompanied by a small amount of intermetallics as observed in the following Fig. 4-4.

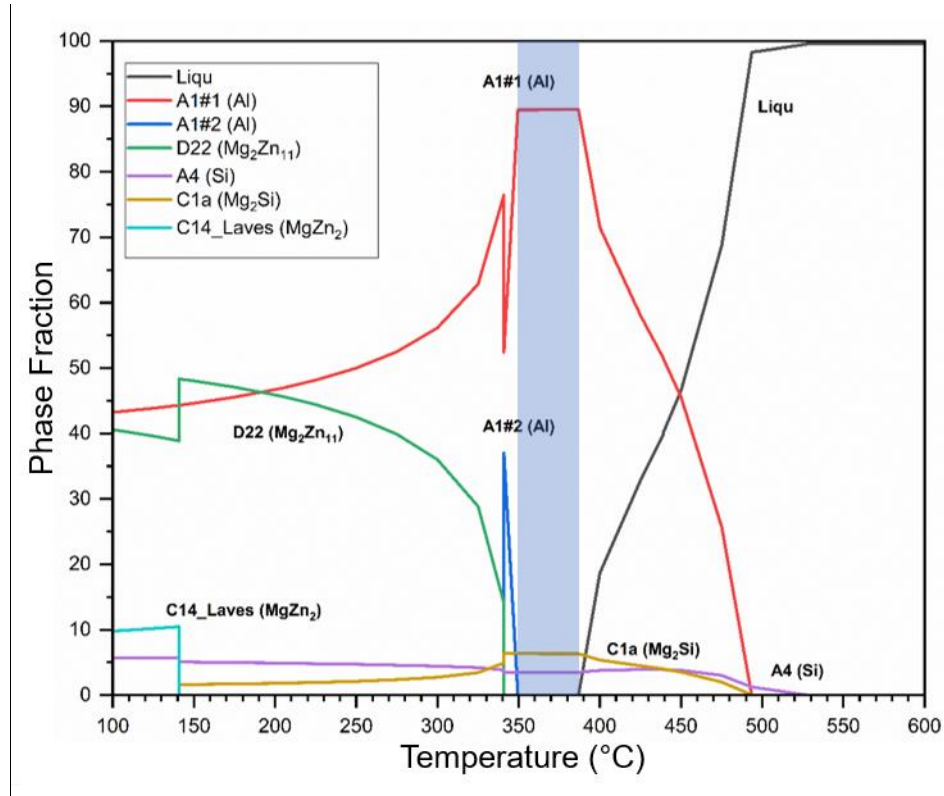


Fig. 4-4 Equilibrium solidification diagram for  $\text{Al}_{58}\text{Zn}_{28}\text{Mg}_6\text{Si}_8$  LW-MEA calculated by FactSage (The shaded region corresponds to the temperature interval where there is a high percentage of solid solution with an FCC crystal structure).

## 4.2. Results

### 4.2.1. Prediction of solid solution formation using empirical parameters

Table 4-2 displays the empirical parameters of the  $\text{Al}_{58}\text{Zn}_{28}\text{Mg}_6\text{Si}_8$  (at. %) alloy that were computed using the equations described in Chapter 2, except for the thermodynamic parameters  $\Delta H_{mix}$  and  $\Delta S_{mix}$ , which were determined using the CALPHAD.

Table 4-2. Thermodynamic, topological, and electronic parameters calculated for the  $\text{Al}_{58}\text{Zn}_{28}\text{Mg}_6\text{Si}_8$  (at. %) alloy to predict the formation of solid solutions and the type of crystalline structure.

Alloy composition	$\Delta H_{mix}$ (kJ/mol)		$\Delta S_{mix}$ (J/K mol)		$\delta$ (%) EQ. 2-7	VEC EQ. 2-15	$\Delta\chi$ EQ. 2-11	$\Omega$ EQ. 2-9
	CALPHAD	CALPHAD	CALPHAD	EQ. 2-5				
$\text{Al}_{58}\text{Zn}_{28}\text{Mg}_6\text{Si}_8$	3.13	8.56	9.12	6.39	2.72	0.123	7.39	

The  $\Delta H_{mix}$  and  $\Delta S_{mix}$  of the LW-MEA in the liquid phase were determined using the CALPHAD method and were found to be 3.13 (kJ/mol) and 8.56 (J/K mol), respectively. Furthermore, the configurational entropy obtained using the CALPHAD approach was compared to the value obtained using equation 2-2 and showed minimal variation in both values.

The smallest atomic size in the  $Al_{58}Zn_{28}Mg_6Si_8$  (at. %) alloy belongs to Si (0.111 nm), followed by Zn (0.134 nm), and then Al (0.143 nm). The largest atomic size belongs to Mg (0.160 nm). According to the Hume-Rothery rules, the atomic size difference between solute and solvent atoms should be less than 15% for binary solid solutions, and less than 8% for complete solubility. Although Si has an atomic size difference greater than 15%, the difference between the elements is only 6.39%, which is less than 8%.

The LW-MEA alloy satisfies the mixing enthalpy and atomic size difference conditions proposed by Zhang *et al.* [52], namely  $-20 \leq \Delta H_{mix} \leq 5$  kJ/mol and  $\delta \leq 6.4\%$ , respectively. However, it fails to meet the mixing entropy criterion of  $12 \leq \Delta S_{mix} \leq 17.5$  J/Kmol.

On the other hand, according to Guo *et al.* [66], the formation of a simple solid solution microstructure should fulfill the following conditions:  $11 \leq \Delta S_{mix} \leq 19.5$  J/Kmol,  $-11.6 \leq \Delta H_{mix} \leq 3.2$  J/Kmol and  $\delta < 5\%$ . In this case, the studied alloy only satisfies the mixing enthalpy criterion, with a value of  $\Delta H_{mix} = 3.13$  KJ/mol.

The LW-MEA has a valence electron concentration of 2.72. This parameter was proposed by Guo *et al.* [68], to predict the type of crystal structure that can be formed in HEAs. According to Guo's criteria, a  $VEC \leq 6.87$  results in the formation of a body-centered cubic (BCC) crystal structure. Therefore, the  $Al_{58}Zn_{28}Mg_6Si_8$  (at. %) alloy must form a BCC crystal structure.

The constituent elements of the alloy designed have different Pauling electronegativity values, namely Al=1.61, Zn=1.65, Mg=1.31, and Si=1.90, resulting in an electronegativity difference of  $\Delta\chi=0.123$ . The Hume-Rothery electronegativity rule states that the solvent and solute in a binary system should have similar electronegativity for the formation of solid solutions.

The last parameter calculated was Omega, which had a value of  $\Omega = 7.39$  for the designed alloy. This parameter, proposed by Zhang *et al.* [54], is used to predict the formation of solid solutions and is defined as the product of the entropy of mixing and the average melting temperature of the elements divided by the enthalpy of mixing. Zhang identified two important parameters,  $\Omega$  and  $\delta$ , for predicting solid solutions in HEAs. A stabilized solid solution is achieved when these parameters fall within the ranges of  $\Omega \geq 1.1$  and  $\delta \leq 6.6\%$ . Fig. 4-5 displays the relationship between  $\delta$  and  $\Omega$  for the high entropy alloys analyzed by Zhang. The designed  $Al_{58}Zn_{28}Mg_6Si_8$  (at. %) alloy falls within the zone where solid solutions plus intermetallics are formed, labeled as "S+I".

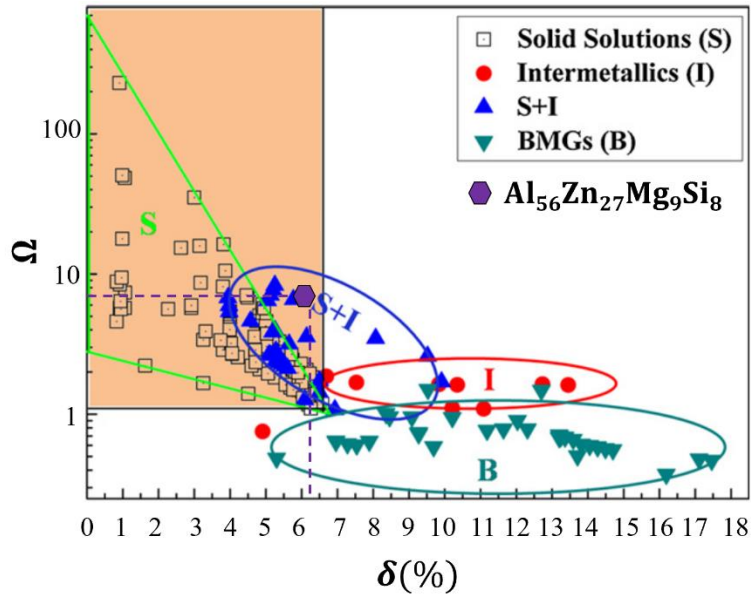


Fig. 4-5 The relationship between the parameters  $\delta$  and  $\Omega$  for multi-component alloys. (“Solid Solutions” indicates the alloy contains only solid solution; “Intermetallics” indicates the alloy mainly contains intermetallic compound and other ordered phases; “S + I” indicates that not only the solid solution could form, but also the ordered compounds could precipitate in multi-component alloys; and “BMGs” indicates the alloy can form amorphous phase) [54].

#### 4.2.2. Phase stability simulations by CALPHAD

Thermodynamic calculations of equilibrium and Scheil solidification of the manufactured alloy were conducted as a function of temperature, and the results are shown in Fig. 4-6. The chemical composition of the alloy was obtained using ICP analysis (see Table 4-3). It is worth noting that the composition obtained by ICP is practically identical to the target composition mentioned in the previous section (4.1.1. CALPHAD approach for LW-MEA design). Consequently, the equilibrium solidification diagram is the same as the one discussed above (see Fig. 4-4). The density of the casting alloy was  $3.46 \text{ g/cm}^3$ .

Table 4-3 Chemical composition of LW-MEA obtained with ICP.

Alloy		Al	Zn	Mg	Si	Cu	Sr
LW-MEA	[wt%]	Balance	48.40	4.11	5.83	0.43	0.03
	[at%]	Balance	27.93	6.38	7.83	0.26	0.01

Fig. 4-6a illustrates the equilibrium solidification sequence of the alloy under consideration. The first phase to precipitate is silicon (Si), at approximately  $530^\circ\text{C}$ , followed by the FCC phase of aluminum (Al) and the intermetallic ( $\text{Mg}_2\text{Si}$ ), both at  $495^\circ\text{C}$ . At  $350^\circ\text{C}$ , a miscibility gap appears with the A1#1 (Al) and A1#2 (Al) phases. Furthermore, the solid solution phase (Al) is present at its maximum percentage in the temperature range of  $350\text{--}380^\circ\text{C}$  during the equilibrium solidification. The precipitation of the ( $\text{Mg}_2\text{Zn}_{11}$ ) phase occurs at a temperature of  $340^\circ\text{C}$ . Lastly, the Laves phase ( $\text{MgZn}_2$ ) is the last phase to form, appearing at a temperature of  $140^\circ\text{C}$ .

On the other hand, in the non-equilibrium Scheil simulation, the first phase to precipitate is silicon (Si) at a temperature of  $530^\circ\text{C}$ , followed by the ( $\text{Mg}_2\text{Si}$ ) and FCC phases of aluminum (Al), which

both appear to precipitate at the same temperature of 493°C. The Laves ( $MgZn_2$ ) phase precipitates at 370°C, followed by the ( $Mg_2Zn_{11}$ ) phase, which appears at 367°C. Finally, at approximately 350°C, the zinc (Zn) phase precipitates last. It is worth noting that CALPHAD predicts an important variation in the precipitation order of the ( $MgZn_2$ ) and ( $Mg_2Zn_{11}$ ) phases. According to Fig. 4-6b, precipitation begins with the ( $Mg_2Zn_{11}$ ) phase at 340°C, and as the temperature decreases towards 140°C, a partial transformation occurs, leading to the appearance of the Laves ( $MgZn_2$ ) phase. Furthermore, the precipitation of the (Zn) phase is only observed in the Scheil curve. The miscibility gap does not occur in the non-equilibrium simulation.

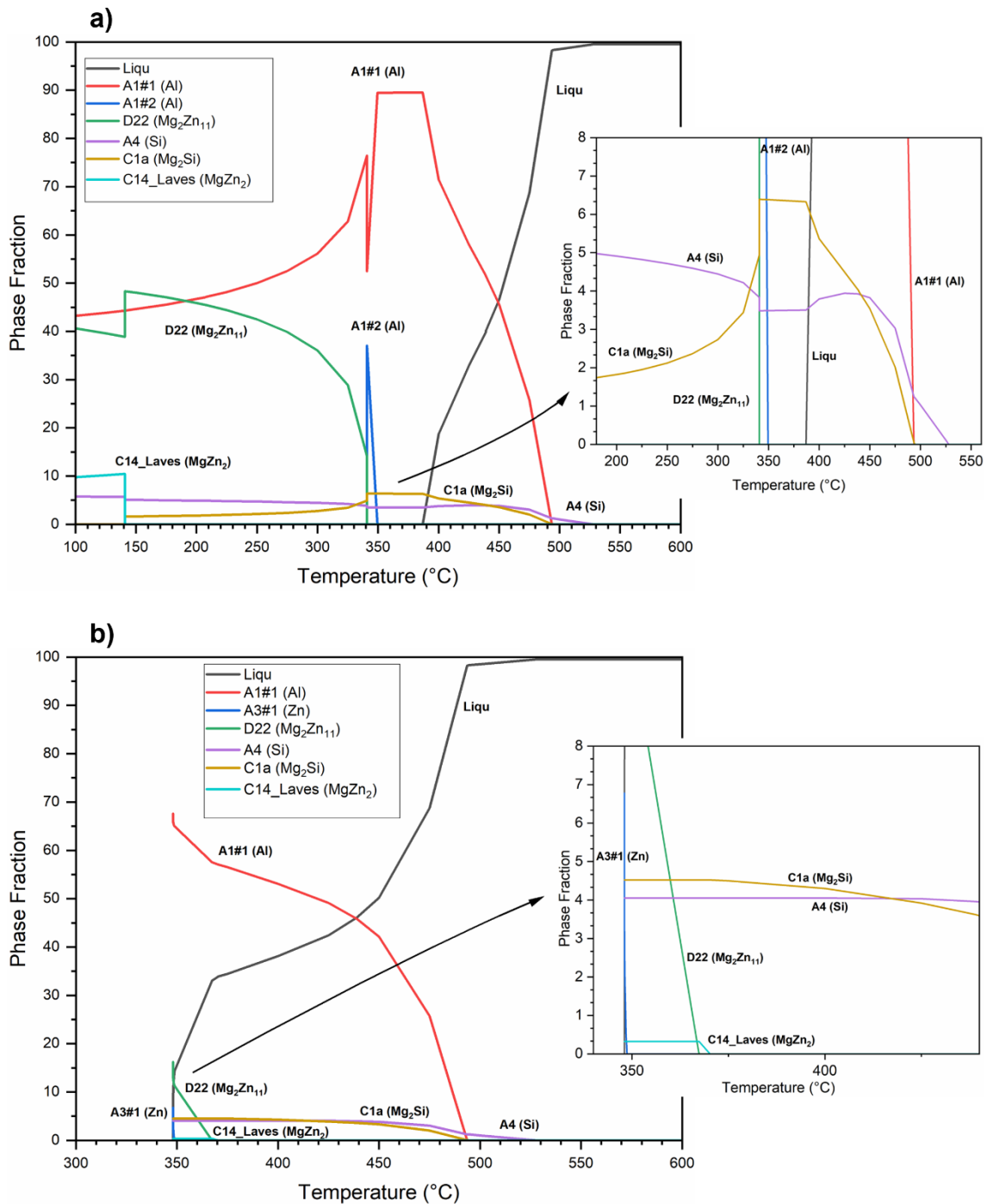


Fig. 4-6 Solidification simulations for  $Al_{58}Zn_{28}Mg_6Si_8$  LW-MEA calculated by FactSage (CALPHAD): a) Equilibrium solidification, and b) non-equilibrium solidification (Gulliver -Scheil).



#### 4.2.3. Analysis of microstructure prior to heat treatments

The as-cast  $\text{Al}_{58}\text{Zn}_{28}\text{Mg}_6\text{Si}_8$  alloy was subjected to an experimental analysis using XRD, DSC, SEM, and EDS techniques. The XRD patterns of the as-cast alloy showed several reflection peaks (Fig. 4-7) that were successfully indexed to the (Al) phase (PDF: 00-004-0787), ( $\text{MgZn}_2$ ) Laves phase (PDF: 04-003-2083), ( $\text{Mg}_2\text{Si}$ ) (PDF: 01-083-5235), (Zn) (PDF: 01-078-9363), (Si) (PDF: 00-027-1402), and ( $\text{Mg}_2\text{Zn}_{11}$ ) (PDF: 04-007-1412). The phases identified by XRD in the as-cast condition are consistent with those predicted by CALPHAD in the Scheil solidification Fig. 4-6b.

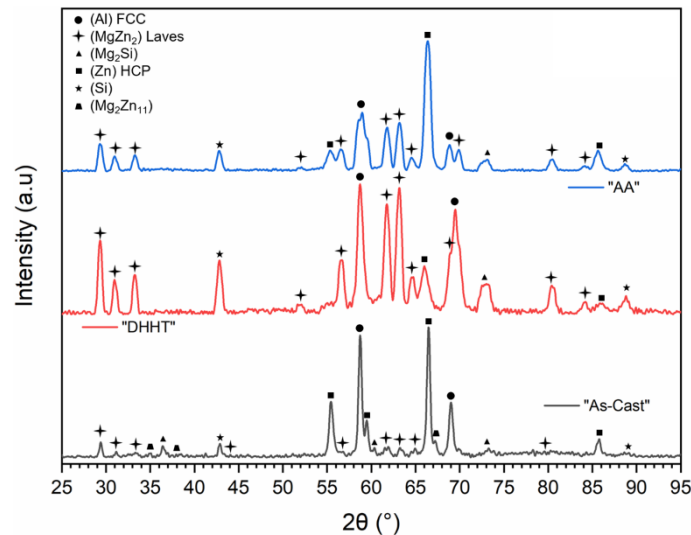


Fig. 4-7 XRD diffraction patterns for the  $\text{Al}_{58}\text{Zn}_{28}\text{Mg}_6\text{Si}_8$  LW-MEA “as-cast”, “DHHT” (Double Homogenization Heat Treatment) and “AA” (Artificial Aging) specimens.

Fig. 4-8a displays a backscattered electron image of the as-cast sample, revealing a complex microstructure consisting of dendritic, eutectic, and interdendritic zones with different contrasts can be observed. The dendritic phase (contour A) corresponds to the FCC phase of aluminum (Al), while the interdendritic zone (contour B) may be some of the phases of the Mg-Zn system, either ( $\text{MgZn}_2$ ) or ( $\text{Mg}_2\text{Zn}_{11}$ ). Contour C corresponds to the eutectic (Al +  $\text{Mg}_2\text{Si}$ ), where the gray zone is associated with the (Al) phase, and the darker zones correspond to the ( $\text{Mg}_2\text{Si}$ ) phase. While the eutectic (contour D) corresponds to the (Al + Si), with the aluminum phase being the gray zone and the (Si) being the dark gray zone. In addition, the Fig. 4-8a reveals bright regions where heavier elements, such as the zinc (Zn) phase, are located.

The EDS composition analysis shown in Fig. 4-8d of the dendritic phase reveals a high concentration of Al (as indicated by points 01), confirming that this phase primarily comprises (Al). The interdendritic zones in the microstructure exhibit variations in their compositions, as indicated by the EDS analysis. For example, point 02 is rich in zinc, followed by magnesium, and based on the atomic composition, corresponds to the laves phase ( $\text{MgZn}_2$ ). The varying shades in the interdendritic zones indicate partitioning and segregation between the solid and liquid phases during solidification. The eutectic phase at point 03 has a higher concentration of Mg and Si, which corresponds to the ( $\text{Mg}_2\text{Si}$ ) phase. The eutectic structure located at point 04 had a high silicon concentration, estimated to be approximately 97 at. % of silicon, followed by aluminum.

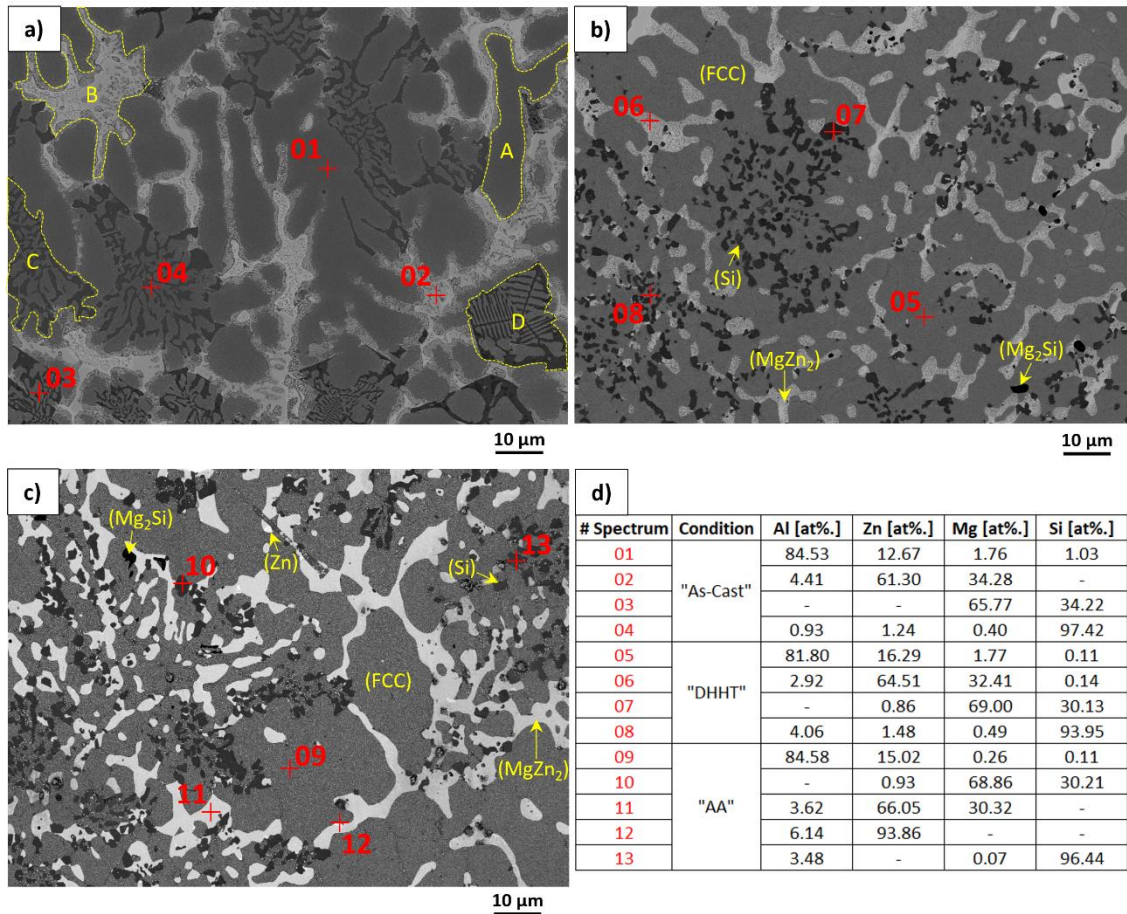


Fig. 4-8 SEM/EDS of the  $\text{Al}_{58}\text{Zn}_{28}\text{Mg}_6\text{Si}_8$  LW-MEA in condition: a) "As-Cast", b) "DHHT" (Double Homogenization Heat Treatment) and c) "AA" (Artificial Aging).

#### 4.2.4. Design of heat treatments

To optimize the material through heat treatments, it is necessary to determine the critical temperatures at which phase changes or melting of the alloy occur. Simulations using CALPHAD calculate a solidus temperature of  $390^\circ\text{C}$  for equilibrium solidification and a liquidus temperature of  $530^\circ\text{C}$ . For non-equilibrium solidification, the solidus temperature is  $350^\circ\text{C}$ , while the liquidus temperature is  $530^\circ\text{C}$ . However, the differential scanning calorimetry analysis (Fig. 4-9) reveals that the curve of the heating cycle for the as-cast sample display a solidus temperature of around  $400^\circ\text{C}$  and a liquidus temperature of approximately  $580^\circ\text{C}$ . Indicating that the selected composition has a relatively low melting point and can be easily melted using a standard laboratory furnace.

The heating cycle (Fig. 4-9) shows the dissolution of seven phases as indicated by the peaks. According to the FactSage results, the highest temperature peak 7 is likely associated with the (Si) phase melting. This is confirmed by the liquid projection of the Al-Si-Zn ternary diagram (

Fig. 4-10), which shows that the phase in question is indeed silicon (Si). In this phase, the solubility of the other alloying elements is close to zero, corresponding to the EDS point 04. The two peaks (peak 6 and peak 5) following silicon (Si) do not appear to be the result of a single-phase transformation, as they show at least two maxima: a peak at about  $502^\circ\text{C}$  (peak 6) and a small peak at about  $480^\circ\text{C}$  (peak 5). Peak 6 is the dendrite (contour A) and peak 5 corresponds to the eutectic

(Al + Mg<sub>2</sub>Si) (contour D). In addition, peaks 4 and 3 may correspond to the dissolution of (MgZn<sub>2</sub>) and (Mg<sub>2</sub>Zn<sub>11</sub>) phases, according to the Scheil solidification results (Fig. 4-6b) and the interdendritic zone (contour B) shown in Fig. 4-8a. Finally, peak 2 could be attributed to the miscibility gap, as indicated by the equilibrium diagram (Fig. 4-6a), while peak 1 can be associated with the dissolution of the (Zn) phase according to the Scheil solidification diagram (Fig. 4-6b).

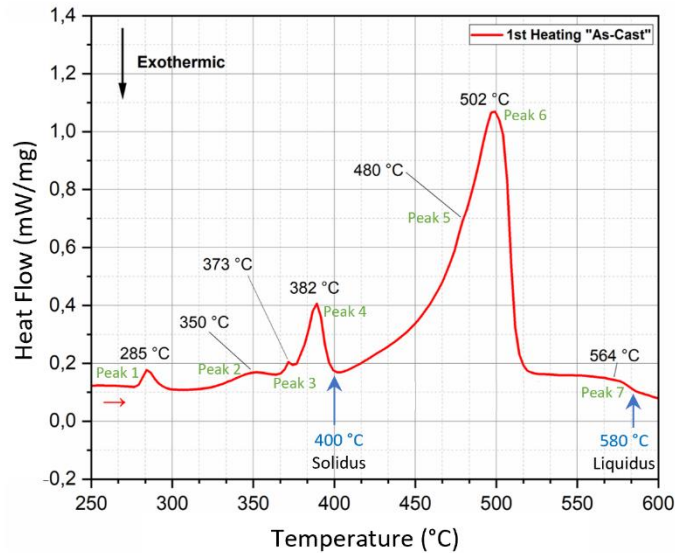


Fig. 4-9 DSC curve of the Al<sub>58</sub>Zn<sub>28</sub>Mg<sub>6</sub>Si<sub>8</sub> LW-MEA heating process.

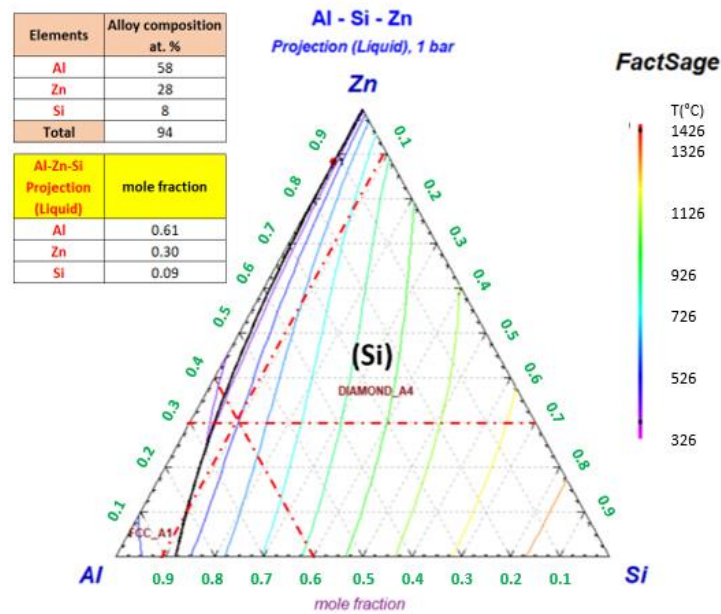


Fig. 4-10 Projection of the liquid on the Al-Si-Zn ternary diagram calculated by FactSage (The intersection of the dotted lines determines the composition of the alloy).



Based on the analysis mentioned earlier, the heat treatments were prescribed as follows: Initially, solution treatments were carried out in the temperature range of 360-380°C, which corresponds to the FCC temperature range of equilibrium solidification (as depicted in Fig. 4-6a), Scheil solidification (Fig. 4-6b), and DSC results (Fig. 4-9).

At the beginning of casting, the solidification kinetics of the samples closely resembled the Scheil simulation due to the rapid cooling rate. This can result in variances in the melting temperatures of the samples, which increases the risk of incipient melting during the solution treatment. To mitigate this risk, a two-step solution treatment process was developed and implemented.

In the first step, the material was heated to 325°C, which is lower than the solidus temperature predicted by FactSage for the Scheil cooling process (Fig. 4-6b). This temperature of 325°C was chosen to homogenize the material and prevent incipient melting as the temperature increases. In the second step, the temperature was raised to 380°C, below the liquidus temperature as indicated by the equilibrium solidification diagram (Fig. 4-6a). This temperature of 380°C was selected to dissolve all the secondary phases in the material, as well as to achieve a high percentage of FCC solid solution. The aim was to reach an equilibrium state at this temperature. The sample was then rapidly cooled in cold water to preserve the structure as much as possible.

Some of the samples were subjected to artificial aging after solution treatment. A temperature of 160°C and 240 minutes were selected for the artificial aging process to observe how the phases evolve. Therefore, the samples analyzed in this study correspond to the heat treatment schedules listed in Table 4-4. The heat treatment labeled DHHT is a double-step solubilization treatment, while the heat treatment marked AA corresponds to artificial aging performed at 160°C for 240 minutes.

Table 4-4 Heat treatment schedules for the  $Al_{58}Zn_{28}Mg_6Si_8$  LW-MEA.

Sample	Solution Treatment		Artificial Aging after Solutionization
	Step 1	Step 2	
Double Homogenization Heat Treatment "DHHT"	325 °C/24 h	380 °C/24 h + Quenching	-
Artificial Aging "AA"	325 °C/24 h	380 °C/24 h + Quenching	160 °C/ 240 min

#### 4.2.5. Effect of the heat treatment on the microstructure

The XRD patterns of the alloy after solubilization treatment show some differences compared to the as-cast alloy, as depicted in Fig. 4-7. In the double homogenization heat treatment, the  $(Mg_2Zn_{11})$  phase disappears, and the amount of the  $(Zn)$  phase is reduced. It is important to note that the sample analysis with the solution treatment was carried out three months after casting. Therefore, it is possible that natural aging occurred, and a small amount of  $(Zn)$  precipitated in the matrix. During the artificial aging, the  $(Mg_2Zn_{11})$  phase completely disappears in the diffraction patterns compared to the as-cast sample. Furthermore, during AA heat treatment, the  $(Zn)$  phase precipitates again, leading to a noticeable increase in the amount of  $(Zn)$  phase compared to the diffraction patterns after the solubilization treatment.

The results of DSC analysis for the heat-treated and non-heat-treated samples are presented in Fig. 4-11. After conducting DSC analysis on the DHHT sample, the phases corresponding to peaks 2 and

3 were completely dissolved in the matrix due to the dissolution treatment. However, a small amount of the phase corresponding to peak 1 was observed to have precipitated. In the artificially aged sample, it was observed that the phases corresponding to peaks 1 and 2 had precipitated again. Additionally, it was found that the phase corresponding to the dissolution temperature of peak 4 was present in all the curves, irrespective of their heat treatment, with a temperature of approximately 390°C.

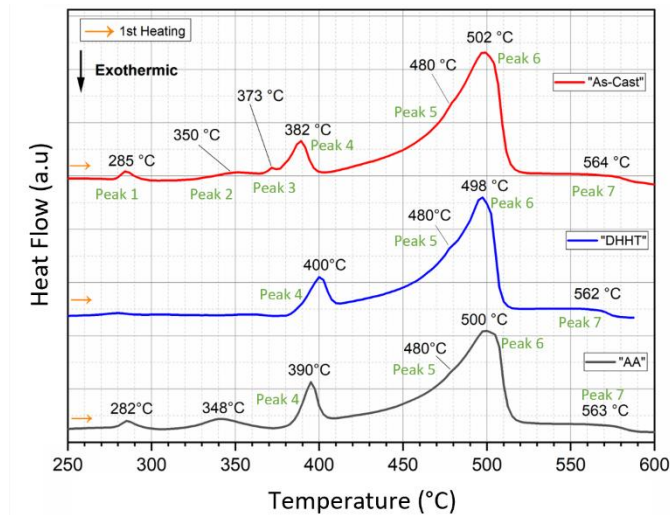


Fig. 4-11 DSC heating curves for the three conditions, “As-Cast”, “DHHT” (Double Homogenization Heat Treatment) and “AA” (Artificial Aging).

Fig. 4-8b illustrates a more homogeneous microstructure of the LW-MEA after solution treatment. A mostly FCC matrix with second phases such as  $(MgZn_2)$ ,  $(Si)$ , and  $(Mg_2Si)$  can be observed. The  $(MgZn_2)$  phase appears the brightest, and the  $(Mg_2Si)$  phase occurs the darkest. These three intermetallics or second phases are clustered and have formed globular shapes. The presence of these phases is confirmed by the compositional analysis results in Fig. 4-8d. Point 05 shows a high Al content of around 82 at.%, corresponding to the  $(Al)$  phase (FCC). Spectrum 06 confirms the stoichiometry of the  $(MgZn_2)$  phase, while spectrum 07 corresponds to the chemical composition of  $(Mg_2Si)$ . Finally, Spectrum 08 indicates a high concentration of silicon, which suggests the presence of the  $(Si)$  phase. The backscattered electron image of the artificially aged sample (Fig. 4-8c) shows a microstructure similar to that in the solubilized condition. However, there are some differences. For example, the matrix in Fig. 4-8c contains precipitates in its interior. Additionally, brighter zones can be observed, which point to the  $(Zn)$  phase, according to the compositional analysis of point 12 (Fig. 4-8d). This  $(Zn)$  phase appears to be located in the interface of the Laves phase  $(MgZn_2)$ , and the matrix  $(Al)$  FCC.

#### 4.2.6. Hardness of samples

The as-cast and heat-treated samples were evaluated for their hardness, and the measured microhardness values are presented in Table 4-5. The as-cast specimen had a hardness value of 184 HV. It can be observed that the solution treatment significantly increases the hardness of the alloy up to a value of 250 HV, while the artificially aged sample shows the lowest microhardness value, with a measurement of 148 HV. This phenomenon may be related to over-aging of the alloy.

Table 4-5 Microhardness of the  $Al_{58}Zn_{28}Mg_6Si_8$  LW-MEA.

<b>Alloy</b>	<b>Condition</b>	<b>Microhardness (HV)</b>
	As-Cast "AC"	184±5
LW-MEA	Double Homogenization Heat Treatment "DHHT"	250±4
	Artificial Aging "AA"	150±2

### 4.3. Discussion

#### 4.3.1. Solid solution prediction by empirical parameters

The use of empirical parameters to predict the formation of solid solutions and the type of crystal structure were used in the  $Al_{58}Zn_{28}Mg_6Si_8$  (at. %) alloy. The results show that the LW-MEA alloy satisfies the mixing enthalpy and atomic size difference conditions proposed by Zhang *et al.* [52], but fails to meet the mixing entropy criterion proposed by Guo *et al.* [54].

The alloy has a valence electron concentration that predicts the formation of a body-centered cubic crystal structure, and its electronegativity difference is within the range suggested by the Hume-Rothery electronegativity rule. However, the experimental results (CALPHAD, XRD, SEM/EDX, and TEM) contradicted this assumption. These results showed that the alloy actually consists of an Al solid solution with a face-centered cubic crystalline structure, along with small amounts of the Zn hexagonal close-packed phase and intermetallics such as  $Mg_2Si$ ,  $MgZn_2$ , and Si.

The designed alloy falls within the zone where more intermetallic solid solutions are formed (Fig. 4-5), based on the ratio between  $\delta$  and  $\Omega$  proposed by Zhang *et al.* [54]. Furthermore, experimental results confirm the presence of solid solution plus intermetallics in the alloy."

#### 4.3.2. Phase evolution analysis

Based on the results obtained from CALPHAD, DSC, XRD, and micrographs of the  $Al_{58}Zn_{28}Mg_6Si_8$  alloy under different conditions, As-Cast, DHHT (Double Homogenization Heat Treatment), and AA (Artificial Aging). The following sequence of phases that appear during cooling has been proposed. The Table 4-6 displays the transformation temperatures identified from the DSC heating curves.

Table 4-6 The proposed invariant points of the system  $\text{Al}_{58}\text{Zn}_{28}\text{Mg}_6\text{Si}_8$  LW-MEA.

Reaction type	Reaction	Temperature (°C)
-	$\text{L} \leftrightarrow (\text{Si})$	565
Eutectic	$\text{L} \leftrightarrow (\text{Al}) + (\text{Si})$	502
Eutectic	$\text{L} \leftrightarrow (\text{Al}) + (\text{Mg}_2\text{Si})$	480
-	$\text{L} \leftrightarrow (\text{MgZn}_2)$	380
Peritectic	$\text{L} + (\text{MgZn}_2) \leftrightarrow \text{Mg}_2\text{Zn}_{11}$	370
Miscibility gap	$(\text{Al})\#1 + (\text{Al})\#2 \leftrightarrow (\text{Al})$	350
Eutectoid	$(\text{Zn}) + (\text{Al})\#1 \leftrightarrow (\text{Al})\#2$	280

The precipitation order during solidification is as follows (Fig. 4-9). Starting with the first phase that forms at high temperature from the liquid, it corresponds to (Si) phase that is supported with the projection of the liquid and the simulation in equilibrium by CALPHAD.

The DSC measurements reveal two additional transition temperatures within the range of 480-500°C. The peak observed at approximately 500°C is attributed to the dissolution of the eutectic phase formed by (Al) and (Si). The second peak at 480°C corresponds to the melting of a eutectic phase formed by (Al) and ( $\text{Mg}_2\text{Si}$ ). These two transformations are supported by the microstructures in Fig. 4-8a, where contour C corresponds to the eutectic formed by (Al) (dark gray) and (Si) (darker zones), and contour D corresponds to the eutectic formed by (Al) (dark gray) and ( $\text{Mg}_2\text{Si}$ ) (black). These two phases were further confirmed by EDS measurements (Fig. 4-8d). Additionally, the precipitation of these two phases agrees with the CALPHAD results.

The fourth phase is associated with the Laves phase ( $\text{MgZn}_2$ ). This phase is observed in all the DSC curves (Fig. 4-9) and all the diffraction patterns (Fig. 4-7), regardless of the heat treatment at 380°C. The microstructural and compositional analysis in Fig. 4-8 validates this intermetallic. It is evident that to dissolve the Laves phase, we must increase the temperature of the solubilization above 400°C, but there is a risk of incipient melting.

The ( $\text{Mg}_2\text{Zn}_{11}$ ) is the fifth phase to precipitate and is the only one that appears in the XRD of the As-Cast alloy, which suggests that it could be associated with the small peak at 370°C that only appears in the DSC curve of the sample in this condition. This phase does not appear in the DHHT and AA samples because the treatment has been above the stability of this phase, at 380°C. This peritectic reaction, according to Fig. 4-12 of the Zn-Mg binary phase diagram, has only formed in the As-Cast state due to the higher presence of liquid, which means that it can form a small amount of primary form (the composition of the liquid runs towards higher Zn contents).

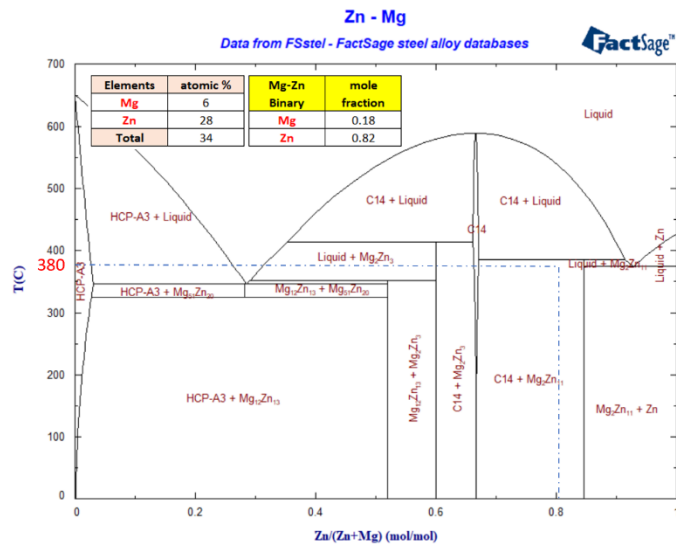


Fig. 4-12 The Zn-Mg binary phase diagram calculated by FactSage.

After equilibrium solidification, a region of immiscibility appears in the (Al) phase, with an (Al)#1 zone containing a low concentration of zinc and an (Al)#2 zone containing a higher amount of Zn, as shown in Fig. 4-13 of the Al-Zn binary phase diagram. Kogo *et al.* [100] conducted a thermodynamic evaluation based on experimental and phase diagram data for the binary Al-Zn system. They found a miscibility gap in the FCC-Al phase below the critical temperature of 350°C. This temperature has been verified to correspond to the second peak of the DSC analysis.

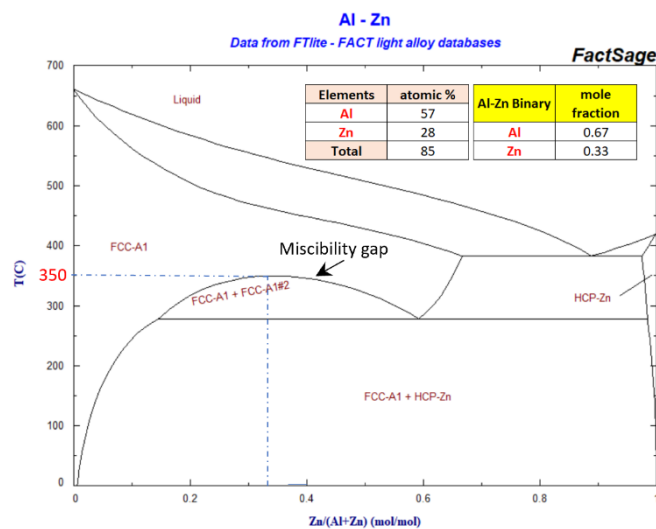


Fig. 4-13 Binary Al-Zn diagram showing the miscibility gap of the (Al) phase calculated by FactSage.

The last phase to precipitate corresponds to (Zn). The XRD results depicted in Fig. 4-7 reveal that the (Zn) phase precipitates after artificial aging, which is further confirmed by the DSC analysis of the AA sample, as illustrated in Fig. 4-11. According to the Al-Zn binary phase diagram (Fig. 4-13), the formation of the (Zn) phase is preferential when (Al)#2 is present in the alloy, and vice versa. The backscattered electron image also confirms this observation, as shown in Fig. 4-8c. The bright regions correspond to the (Zn) phase. This explains the appearance and disappearance of the two lower

temperature peaks in the DSC analysis presented in Fig. 4-11. The first peak is observed during heating at approximately 280°C and corresponds to  $(\text{Zn}) + (\text{Al})\#1 \rightarrow (\text{Al})\#2$ , while the second peak, at around 340°C, corresponds to  $(\text{Al})\#1 + (\text{Al})\#2 \rightarrow (\text{Al})$ .

#### 4.3.3. Miscibility gap validation and HCP evolution

The kinetics of spinodal decomposition in Al-Zn alloys is extremely rapid, even at low aging temperatures. Studies have shown that the Al-50% Zn alloy undergoes rapid spinodal decomposition after solution treatment and cooling [101]. To confirm this phenomenon, transmission electron microscopy was employed to examine the microstructure in the solubilized and quenched samples, with the aim of characterizing the phase separation mechanism. The TEM bright field (BF) image and the corresponding selected area electron diffraction pattern (SADP) for the  $\text{Al}_{58}\text{Zn}_{28}\text{Mg}_6\text{Si}_8$  LW-MEA after double homogenization heat treatment and quenching are shown in Fig. 4-14. These micrographs verify the formation of a supersaturated solid solution in the alloy after quenching. The TEM image in Fig. 4-14b shows a modulated microstructure containing a high-volume fraction of second phase. This type of microstructure is typical in alloys that decompose within low temperature miscibility gaps [102].

The SADP shown in Fig. 4-14c was observed from the zone axis of [013] and indicated a 2.338 Å and 2.024 Å interplanar spacing of the (111) and (200) planes. This is in good agreement with the lattice structure of the (Al) phase FCC with the unit cell parameter of  $a=4.0496$  Å. In addition, the corresponding electron diffraction pattern showed extra spots (satellites) (Fig. 4-14c), which are a product of preferential orientation during the spinodal decomposition. Satellite spots can occur because of the presence of planar defects such as stacking faults, line defects such as dislocations, spinodal decomposition, or regular arrays of crystal defects [103].

Similarly, the SADP in Fig. 4-14d was observed from the zone axis of  $[\bar{1}12]$ , showing interplanar spacings of 3.134 Å, 1.919 Å, and 1.636 Å for the (111), (200), and (311) planes, respectively. These correspond to the diamond cubic crystal structure of the (Si) phase with a unit cell parameter of  $a=5.4282$  Å. The solution treatment has been shown to increase the strength of the alloy because of the solid solution hardening mechanism, which results from the interaction between dissolved alloying elements and dislocations [95]. The microhardness test results support this observation, with the DHHT sample displaying an increase in hardness of 66 HV compared to the as-cast sample, as shown in Table 4-5.



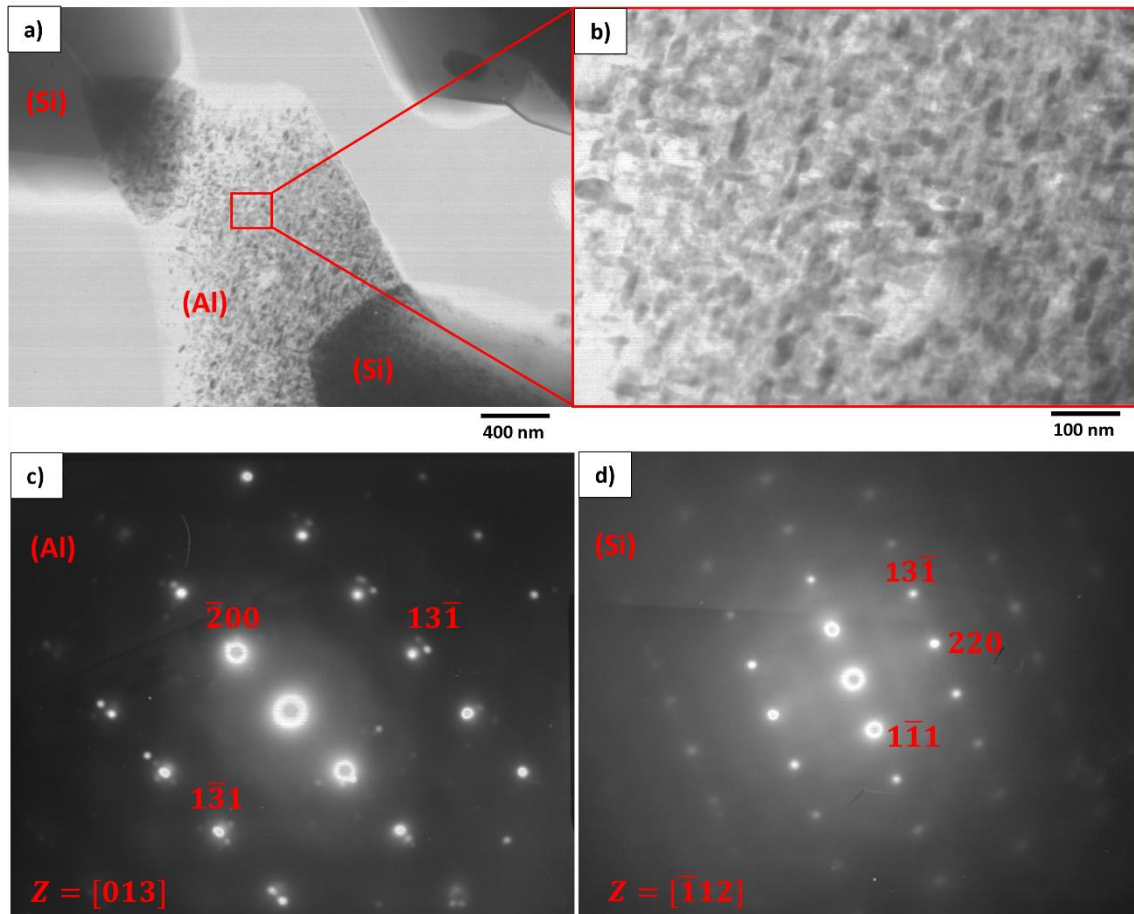


Fig. 4-14 (a-b) Bright-field TEM micrographs and (c-d) selected area electron diffraction patterns (SADP) confirming the phases in the  $\text{Al}_{58}\text{Zn}_{28}\text{Mg}_6\text{Si}_8$  LW-MEA after double homogenization heat treatment and quenching, (c) SADP of the (Al) FCC phase and (d) SADP of the (Si) phase.

In our previous study [104], we investigated the phase evolution of the  $\text{Al}_{58}\text{Zn}_{28}\text{Mg}_6\text{Si}_8$  alloy as a function of temperature using X-ray Thermo-Diffraction. Our analysis revealed the existence of an additional phase with the same space group as aluminum (Fm3m) but a smaller lattice parameter. Based on our observations, we suggested that this phase could be the (Al)#2 phase of the miscibility gap. Due to the smaller atomic size of zinc compared to aluminum, a zinc-rich aluminum phase have a lower lattice parameter than (Al)#1.

According to Popovic *et al.* [105], the sequence of precipitation during aging begins with the formation of (Zn-rich) Guinier-Preston zone (GPZ) spheres, with a size of approximately 1-2 nm, that are completely coherent with the Al-rich (Al) phase matrix. Further aging leads to a change in the morphology of GPZ to an ellipsoidal shape that remains coherent with the (Al) phase matrix, with a size of approximately 10 nm. Subsequent aging causes the formation of the metastable Zn-rich (Al)#2 phase. Finally, prolonged aging of this type of alloy obtains the off-equilibrium hexagonal close-packed (HCP) Zn-rich (Zn) phase, which is incoherent with the matrix, as shown in Fig. 4-15. The XRD and DSC results of the artificially aged alloy, can be attributed to the direct precipitation of (Zn) from the quenched (Al) phase. Upon heating, the second variant of (Al), denoted as (Al)#2, forms at the transformation temperature around 280°C (peak 1), and the end of the miscibility zone is observed with the second peak at 350°C (peak 2) (Fig. 4-11).

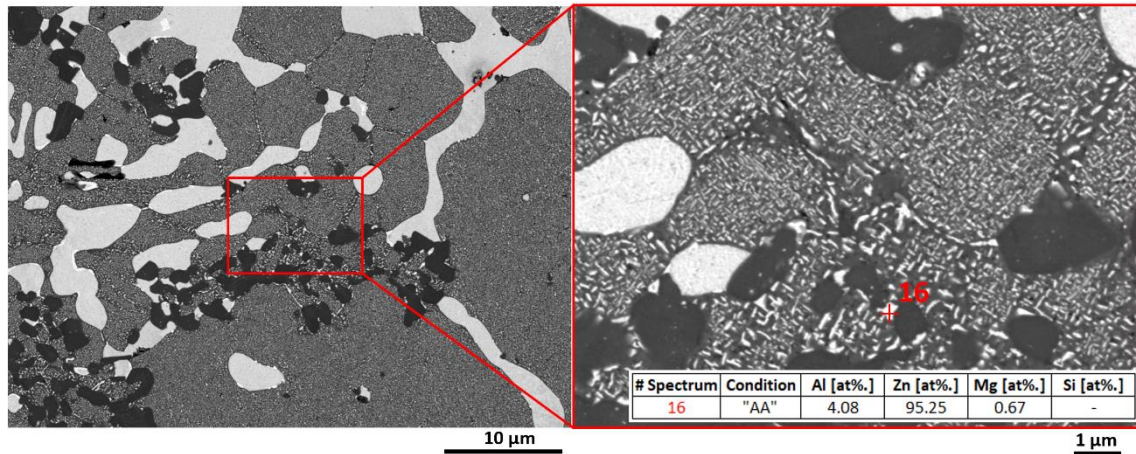


Fig. 4-15 Micrograph of the specimen in the “AA” (Artificial Aging) condition. In detail, aluminum matrix with precipitated zinc phase.

#### 4.4. Conclusions

In this study, the  $\text{Al}_{58}\text{Zn}_{28}\text{Mg}_6\text{Si}_8$  lightweight medium-entropy alloy was designed and the effect of heat treatment on the microstructural phases was studied. Based on the results the following conclusions can be drawn:

- Medium entropy alloys with low density were cast in the Al-Zn-Mg-Si system. The  $\text{Al}_{58}\text{Zn}_{28}\text{Mg}_6\text{Si}_8$  alloy exhibits a density of less than  $3.46 \text{ g/cm}^3$  and a Vickers microhardness value of HV 250 in the solubilized state. Additionally, it shows a liquidus temperature of  $580^\circ\text{C}$  and a solidus temperature of  $400^\circ\text{C}$ .
- Analyses on formation of solid solution in the  $\text{Al}_{58}\text{Zn}_{28}\text{Mg}_6\text{Si}_8$  alloy was performed in this study using both the empirical parameters (including entropy of mixing  $\Delta S_{mix}$ , configurational enthalpy of mixing  $\Delta H_{mix}$ , omega parameter  $\Omega$ , atomic size difference  $\delta$  between the constituent elements, valence electron concentration VEC, and electronegativity difference  $\Delta\chi$ ) and CALPHAD approach. Experimental verification on LW-MEA using XRD, SEM/EDS, and TEM demonstrated the effectiveness of CALPHAD approach over empirical parameters.
- A solidification scheme based on both CALPHAD calculations and experimental results is proposed. Seven phase transformations were determined, which include the (Si) phase, the eutectic phases of (Al)+(Si) and (Al)+(Mg<sub>2</sub>Si), two phases of the Mg-Zn system, (MgZn<sub>2</sub>) and (Mg<sub>2</sub>Zn<sub>11</sub>), a miscibility gap, and the (Zn) phase.
- The combined use of the CALPHAD methodology and experimental techniques has proven to be an effective approach for both predicting and validating the microstructure in medium entropy alloys.



- The TEM results confirm that phase decomposition occurred through the mechanism of spinodal decomposition during the solution treatment.
- The mechanical properties of the designed alloy could only be assessed at a microscopic level using microindentation due to a limited amount of material for macroscopic (uniaxial compression) testing. As a result, the strength and ductility remain undetermined.
- Examining the microstructures reveals the presence of the primary silicon (Si) phase, characterized by a coarse size and irregular shape. This phase likely reduces the mechanical properties of the designed alloy. Thus, refining and modifying the morphology of this phase, or ideally eliminating its precipitation, is considered.

# Chapter 5

## 5. Optimizing and Customizing Chemical Composition of LW-MEA

*This chapter is dedicated to the improvement of the mechanical properties of the  $Al_{58}Zn_{28}Mg_6Si_8$  alloy. This improvement is achieved by adjusting the alloy composition and applying a heat treatment to increase its resistance to compressive forces. The adjusted composition resulted in the alloy  $Al_{60}Zn_{27}Mg_{11}Si_2$ . In addition, the chapter investigates the impact of modifying elements, such as strontium (Sr) and antimony (Sb), on the  $Mg_2Si$  phase, leading to its modification and refinement.*

### 5.1. Introduction

In the previous chapter, the designed medium-entropy alloy ( $Al_{58}Zn_{28}Mg_6Si_8$ ) was examined using empirical parameters and the CALPHAD methodology. Seven phase transformations were identified, ranging from the (Si) phase to the eutectic phases of (Al)+(Si) and (Al)+(Mg<sub>2</sub>Si), as well as two phases from the Mg-Zn system, (MgZn<sub>2</sub>) and (Mg<sub>2</sub>Zn<sub>11</sub>), accompanied by a miscibility gap and the (Zn) phase. These phases were analyzed through various experimental techniques such as SEM/EDS, XRD, DS, and TEM.

From the analysis of the microstructural phases of the LW-MEA, the need arose to eliminate the precipitation of the primary silicon (Si) phase and to modify and refine the intermetallic (Mg<sub>2</sub>Si) to improve mechanical properties. Below is bibliographic information on the (Mg<sub>2</sub>Si) phase and some ways to modify it.

The intermetallic compound Mg<sub>2</sub>Si, it is commonly used to strengthen lightweight alloys. It possesses impressive characteristics, such as a high melting point (1085 °C), low density  $1.99 \times 10^3 \text{ kg} \cdot \text{m}^{-3}$ , high hardness ( $4.5 \times 10^3$  MPa), low coefficient of thermal expansion ( $7.5 \times 10^{-6} \text{ K}^{-1}$ ), and a high elastic modulus (120 GPa). Moreover, Mg<sub>2</sub>Si is non-toxic, exhibits antioxidant properties, resists corrosion, is environmentally friendly, and cost-effective as a semiconductor compound [106].

The stability of the Mg<sub>2</sub>Si phase makes it effective in impeding grain boundary sliding at elevated temperatures. However, when formed at low solidification rates, Mg<sub>2</sub>Si can take on a coarse Chinese script shape, which diminishes the mechanical properties of alloys. The presence of sharp corners in primary Mg<sub>2</sub>Si can create stress concentrations, significantly reducing the strength and ductility of the alloys. Additionally, flake-like eutectic Mg<sub>2</sub>Si may not effectively inhibit crack propagation. Therefore, modifying and refining the Mg<sub>2</sub>Si phase is a crucial approach to enhance the mechanical properties [107,108]. Several studies have been conducted to modify the morphology and refine the size of primary Mg<sub>2</sub>Si or eutectic Mg<sub>2</sub>Si by incorporating modifiers like Sb, Sr, Ca, Gd, Sc, Li, P,

rare-earth Y, and Ba. However, Sr and Sb are the elements that have achieved the best results in the modification of the Mg<sub>2</sub>Si phase [109–119].

The table below summarizes several studies that have examined Sr and Sb as modifiers of the Mg<sub>2</sub>Si intermetallic. It highlights the main effects of these modifiers.

Table 5-1 Impact of the modifying elements Sr and Sb on the modification of the intermetallic Mg<sub>2</sub>Si.

Modifier element	The Effect of Sr on Mg <sub>2</sub> Si Phase Modification	Ref.
Sr	Sr changes the eutectic phases of Mg <sub>2</sub> Si from thick to polygonal shapes in Mg <sub>2</sub> Si-reinforced Mg matrix composites. During solidification, Sr, through Al <sub>4</sub> Sr, reduces the size of Mg <sub>2</sub> Si particles. It is crucial to control the amount of added Sr; an excess of 0.6 wt.% forms a phase called Mg <sub>7</sub> SrSi <sub>2</sub> , potentially causing undesired effects on the material's properties.	[120]
	The addition of 0.01 wt.% Sr improved the structure of the primary Mg <sub>2</sub> Si phase, while higher Sr levels increased the size of this phase in the Al–Mg <sub>2</sub> Si–Cu composites. Surprisingly, the Al–Mg <sub>2</sub> Si eutectic phase remained refined with higher Sr levels. This refinement resulted in improved wear resistance and increased corrosion resistance due to the effective dispersion of Mg <sub>2</sub> Si particles.	[121]
	Sr changed Mg <sub>2</sub> Si to a regular, polygonal shape, and altered eutectic Mg <sub>2</sub> Si to a fibrous structure in the Al–Mg <sub>2</sub> Si composites. Finer Al <sub>4</sub> Sr phases improved Mg <sub>2</sub> Si refinement, aiding spheroid transformation during T6 heat treatment. These changes led to increased tensile strength and elongation in T6-treated alloys.	[107]
	In a study on hypereutectic Mg–4%Si alloy with Sr modification, the addition of Al–10% Sr master alloy reduced the size of primary Mg <sub>2</sub> Si and altered the shape of eutectic Mg <sub>2</sub> Si. The primary Mg <sub>2</sub> Si decreased in size due to Sr-rich particles triggering a nucleation mechanism, while the eutectic Mg <sub>2</sub> Si shape was modified by dissolved Sr affecting its growth pattern. In summary, Sr has a dual effect on Mg <sub>2</sub> Si, reducing its size and altering its shape through nucleation and growth mechanisms.	[122]
	Adding 0.15 wt.% Sr to Al–20Mg <sub>2</sub> Si alloys formed smaller cube-shaped primary Mg <sub>2</sub> Si particles consistently at various cooling rates, ranging from about 50 to 76 C/s and approximately 213 to 230 C/s. This modification process transformed the primary Mg <sub>2</sub> Si phase into smaller cubes.	[123]
Sb	Adding 0.5 wt.% Sb to Mg <sub>2</sub> Si/Mg–9Al composite materials modified Mg <sub>2</sub> Si, creating a refined polygonal structure and reducing the grain size of the Mg matrix. These modifications notably enhanced both tensile properties and damping capacity.	[108]
	The addition of Sb effectively refined the microstructures, transforming the primary Mg <sub>2</sub> Si from coarse dendritic shapes to smaller polyhedral shapes	[116]

	in the Al–20Mg <sub>2</sub> Si–4Cu alloy. Tensile tests showed a substantial 29% increase in ultimate tensile strength.	
	The addition of 2.0 wt.% Sb significantly altered the shape of primary Mg <sub>2</sub> Si to blocky and smaller forms, resulting in a notable 26% reduction in wear loss and superior corrosion resistance. Nano-indentation tests demonstrated enhanced hardness and ductility in the Sb-modified Mg <sub>2</sub> Si/AZ91.	[124]
	The addition of 2.0 wt.% Sb transformed the coarse dendritic shape of Mg <sub>2</sub> Si into blocky polygons, refining the size of primary Mg <sub>2</sub> Si in Mg <sub>2</sub> Si/AZ91 composites. Nanoindentation tests revealed a slight reduction in Young's modulus and a significant improvement in hardness. Additionally, the introduction of Sb led to an increase in ductility in Mg <sub>2</sub> Si.	[125]
	The addition of 2.0 wt.% Sb significantly modified the morphology of primary Mg <sub>2</sub> Si phases, resulting in improved strength and ductility in the AZ91 composites. The formation of Mg <sub>3</sub> Sb <sub>2</sub> during solidification acted as an effective heterogeneous nucleus, further refining the size of primary Mg <sub>2</sub> Si. Moreover, the modification led to increased hardness of Mg <sub>2</sub> Si and a reduction in stress concentration due to the altered morphology and size.	[126]
	The study investigated the refining effect and mechanism of Sb on Mg <sub>2</sub> Si, observing the presence of Mg <sub>3</sub> Sb <sub>2</sub> particles that acted as nucleation sites, promoting the formation of fine polygonal Mg <sub>2</sub> Si. The addition of 0.8% Sb resulted in a 12.2% increase in ultimate tensile strength.	[127]
	A 0.4% Sb content altered the shape of primary Mg <sub>2</sub> Si from dendrites to fine particles, enhancing ultimate tensile strength and elongation in the Mg <sub>2</sub> Si/Al-Si composites. However, excessive Sb has a negative impact on the modification of the composites. When the Sb content exceeds 0.4%, it causes primary Mg <sub>2</sub> Si particles to coarsen. The refinement process is linked to the formation of Mg <sub>3</sub> Sb <sub>2</sub> , which acts as an excellent nucleus for modifying primary Mg <sub>2</sub> Si particles.	[128]
	The addition of 0.2 wt.% Sb to a cast Mg–4Zn alloy transformed the shape of Mg <sub>2</sub> Si particles from a Chinese script to a more rounded edge type, enhancing plasticity during shear deformation. The Sb led to the formation of the stable intermetallic compound Mg <sub>3</sub> Sb <sub>2</sub> .	[129]
	At 0.5 wt.% Sb, different modification mechanisms were observed in Al-20Mg <sub>2</sub> Si alloys at varying cooling rates. At 50 to 76 C/s, Sb introduced Mg <sub>3</sub> Sb <sub>2</sub> particles as nuclei, simultaneously substituting Sb for Si in Mg <sub>2</sub> Si crystals. However, at approximately 213 to 230 C/s, primary Mg <sub>2</sub> Si displayed coarser growth with a dendritic shape due to solute trapping. The modification process was primarily based on substitution, resulting in a distinct morphological outcome compared to lower cooling rates.	[123]

Unfortunately, most of the present results are mainly restricted to single modifying elements. Only very few reports have studied the combined effect (two or more elements) on the modification of the  $Mg_2Si$  phase [130,131].

So far there are two investigations studying the combined effect of Sr and Sb on  $Mg_2Si$  phase modification. Sun *et al.* explored the impact of Sr-Sb on the microstructures and mechanical properties of Al-18 wt.%  $Mg_2Si$ -4.5Cu alloys. Upon adding 0.2 wt.% Sr-Sb, significant changes occurred. The primary  $Mg_2Si$  morphed from equiaxed dendrites to cubes in the as-cast alloys, and the average size reduced from ~50 to ~20  $\mu m$ . Similarly, the shape of eutectic  $Mg_2Si$  transformed from Chinese script to short rods. After extrusion and T6 heat treatment, the modified alloy exhibited improved ultimate tensile strength (UTS) at both room temperature (RT) and 100 °C. Specifically, the UTS increased from 229 to 288 MPa at RT and from 231 to 272 MPa at 100 °C. The elongation-to-failure saw a slight improvement, going from 2.9% to 3.8% at RT and from 3.3% to 3.7% at 100 °C. Additionally, the tensile fracture shifted from brittle to ductile after the modification with 0.2 wt.% Sr-Sb [132].

In another study Wang *et al.* studied the impact of adding Sr and Sb to Mg-x (3.5, 5 wt.%) Si-1Al alloys on the crystalline structure of  $Mg_2Si$ . When Sr and Sb were introduced simultaneously, primary  $Mg_2Si$  crystals in both Mg-3.5Si-1Al and Mg-5Si-1Al alloys transitioned from equiaxed-dendritic shapes to octahedral forms. Similarly, eutectic phases changed from Chinese script shapes to short rods. This transformation resulted from a complex modification process involving the heterogeneous nucleation of primary  $Mg_2Si$  crystals on  $Sr_{11}Sb_{10}$  nuclei. Additionally, the incorporation of Sb into  $Mg_2Si$  crystals caused alterations in their growth patterns. In summary, the combined addition of Sr and Sb significantly influenced both primary and eutectic  $Mg_2Si$  phases in these alloys [133].

In line with the aforementioned, in this study, we propose adjusting the chemical composition of the designed medium-entropy alloy. The goal is to prevent the precipitation of primary silicon and concentrate our efforts on modifying the intermetallic  $Mg_2Si$  to improve the alloy's microstructure and, consequently, its mechanical properties. To achieve this enhancement, we will follow the detailed methodology outlined below.

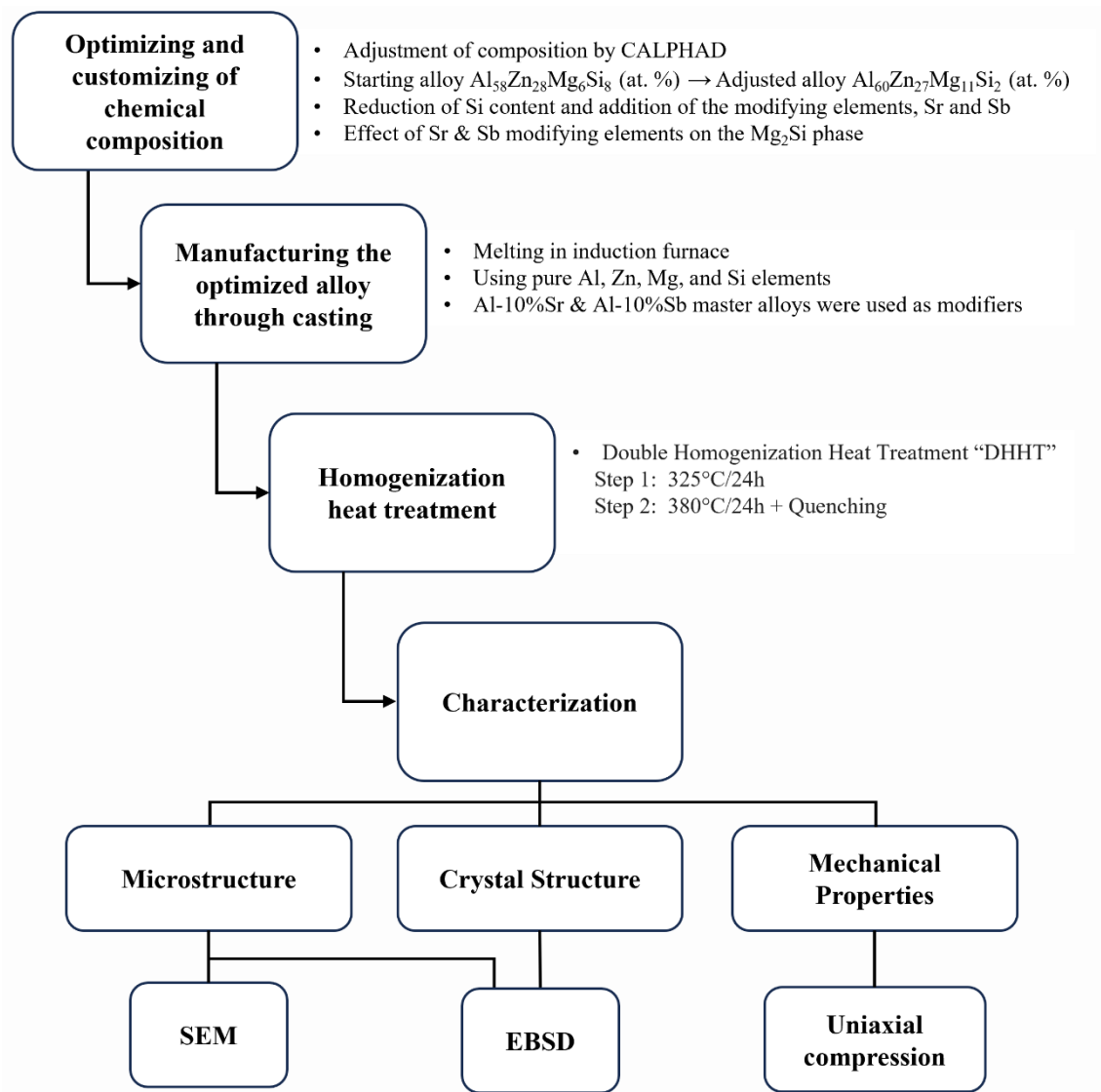


Fig. 5-1 Simplified outline of the contents of Chapter 5: “Optimizing and Customizing the Chemical Composition of LW-MEA”.

## 5.2. Results

### 5.2.1. Composition optimization by CALPHAD

Different CALPHAD simulations revealed that lowering the Si content by 2% effectively removed primary (Si) precipitation while preserving the advantageous attributes conferred by Si addition. These include excellent fluidity, favorable feeding properties, minimal shrinkage, and resistance to hot cracking.

Thermodynamic calculations were conducted using compositions obtained from ICP analysis (refer to Table 5-2) to evaluate solidification under both Scheil and equilibrium conditions for three alloys:  $\text{Al}_{60}\text{Zn}_{27}\text{Mg}_{11}\text{Si}_2$ ,  $\text{Al}_{60}\text{Zn}_{27}\text{Mg}_{11}\text{Si}_2 + \text{Sr}_{0.021}\text{Sb}_{0.001}$ , and  $\text{Al}_{60}\text{Zn}_{27}\text{Mg}_{11}\text{Si}_2 + \text{Sr}_{0.136}\text{Sb}_{0.031}$ .

Table 5-2 Chemical compositions of  $\text{Al}_{60}\text{Zn}_{27}\text{Mg}_{11}\text{Si}_2$  LW-MEA and Sb-Sr modified  $\text{Al}_{60}\text{Zn}_{27}\text{Mg}_{11}\text{Si}_2$  LW-MEA (in atomic percentage at. % and weight percentage wt.%).

Alloy		Zn	Mg	Si	Sr	Sb	Al
Alloy 1	[wt.%]	47.20	7.15	1.23	-	-	Bal.
	[at. %]	26.68	10.87	1.64	-	-	Bal.
Alloy 2	[wt.%]	48.23	7.28	1.27	0.049	0.004	Bal.
	[at. %]	27.49	11.16	1.70	0.021	0.001	Bal.
Alloy 3	[wt.%]	47.70	6.92	1.28	0.320	0.100	Bal.
	[at. %]	27.19	10.62	1.70	0.136	0.031	Bal.

The findings are illustrated in the following figures. Fig. 5-2a displays the equilibrium solidification sequence of the  $\text{Al}_{60}\text{Zn}_{27}\text{Mg}_{11}\text{Si}_2$  alloy, also referred to as Alloy 1. The first two phases to form are the intermetallic phase ( $\text{Mg}_2\text{Si}$ ) and the aluminum FCC phase (Al), which precipitate around 520°C. The aluminum phase has the highest phase fraction. The solid solution phase (Al) is most prominent in the temperature range of 310-410°C during equilibrium solidification. The precipitation of the ( $\text{MgZn}_2$ ) phase occurs at a temperature of 460°C. Lastly, the phase ( $\text{Mg}_2\text{Zn}_{11}$ ) is the last phase to form, appearing at a temperature of 300°C.

In the non-equilibrium Scheil simulation depicted in Fig. 5-2b, the order and temperature of phase precipitation are the same for the (Al) FCC, ( $\text{Mg}_2\text{Si}$ ), and Laves ( $\text{MgZn}_2$ ) phases and intermetallics. However, the ( $\text{Mg}_2\text{Zn}_{11}$ ) phase forms at 365°C, and an additional phase emerges at around 350°C, corresponding to the HCP (Zn) phase.

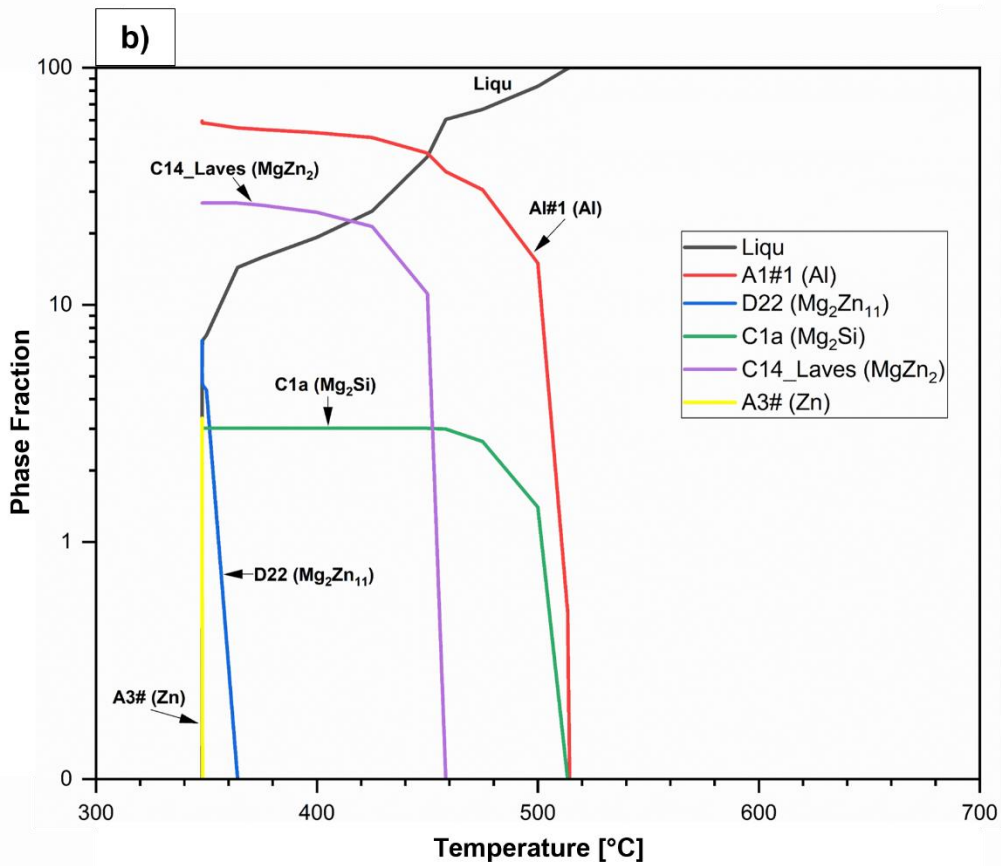
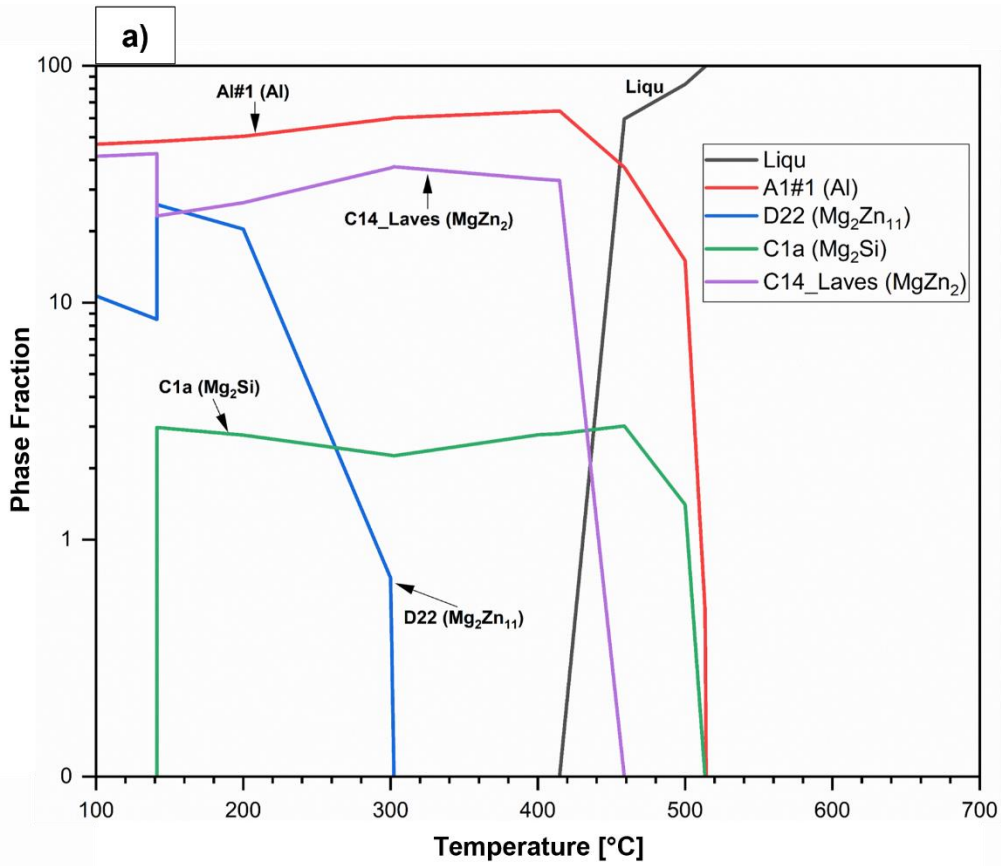


Fig. 5-2 Solidification simulations for the optimized  $Al_{60}Zn_{27}Mg_{11}Si_2$  (Alloy 1), lightweight multicomponent alloy calculated by FactSage (CALPHAD): a) Equilibrium solidification, and b) non-equilibrium solidification (Gulliver - Scheil).



Fig. 5-3a illustrates the equilibrium solidification sequence of the  $\text{Al}_{60}\text{Zn}_{27}\text{Mg}_{11}\text{Si}_2 + \text{Sr}_{0.021}\text{Sb}_{0.001}$  alloy, also denoted to as Alloy 2. The initial phase to form is the high-temperature compound ( $\text{Mg}_3\text{Sb}_2$ ), which precipitates at around  $540^\circ\text{C}$ , followed by the intermetallic ( $\text{Mg}_2\text{Si}$ ) forming at approximately  $520^\circ\text{C}$ . Subsequently, the solid solution phase (Al) with a face-centered cubic (FCC) crystal structure appears at  $510^\circ\text{C}$ . Notably, the aluminum (Al) phase exhibits a significant phase percentage in the temperature range from  $310^\circ\text{C}$  to  $420^\circ\text{C}$ .

At about  $460^\circ\text{C}$ , the intermetallic ( $\text{SrZn}_{13}$ ) precipitates with a relatively low phase fraction. Immediately after the precipitation of this intermetallic ( $\text{SrZn}_{13}$ ), the formation of the Laves phase ( $\text{MgZn}_2$ ) occurs, representing the second phase with a substantial phase fraction. Finally, at  $300^\circ\text{C}$ , the last phase to form is the ( $\text{Mg}_2\text{Zn}_{11}$ ) phase. In the non-equilibrium Scheil-type cooling curves (see

Fig. 5-3b), the order of precipitation for most phases is the same as in the equilibrium solidification curves. However, the ( $\text{Mg}_2\text{Zn}_{11}$ ) phase exhibits differences in its precipitation temperature, which is approximately  $360^\circ\text{C}$ . Additionally, an additional phase emerges around  $350^\circ\text{C}$ , corresponding to the HCP (Zn) phase.

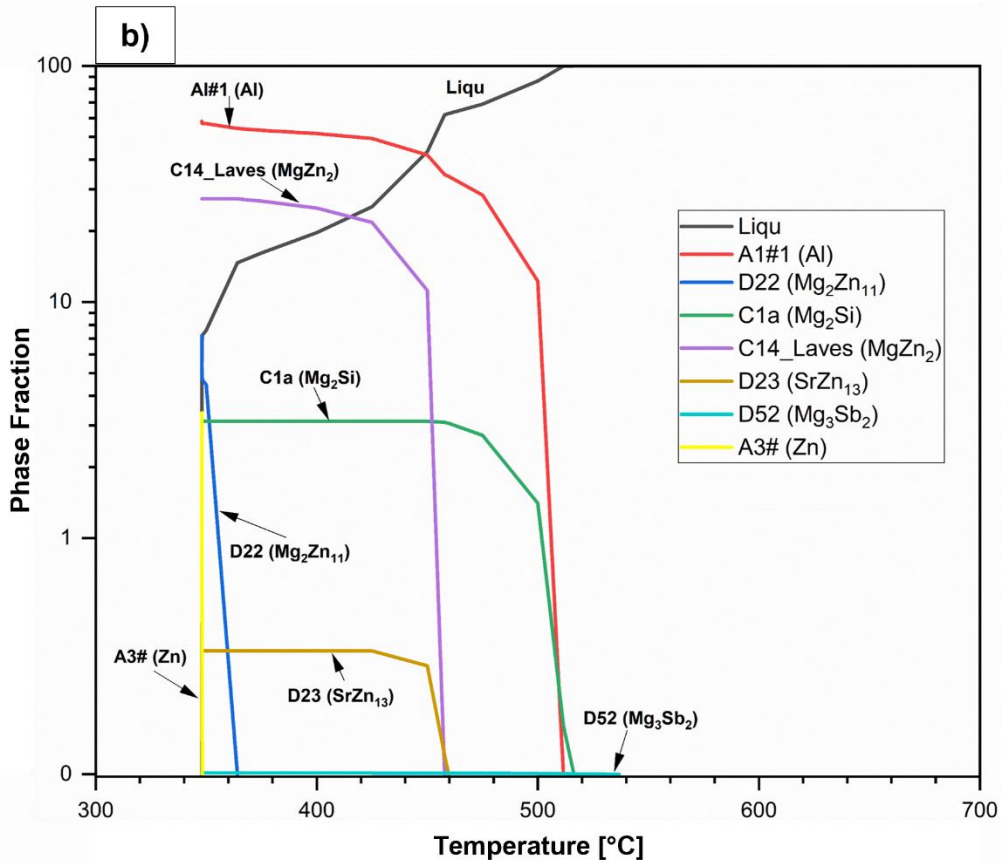
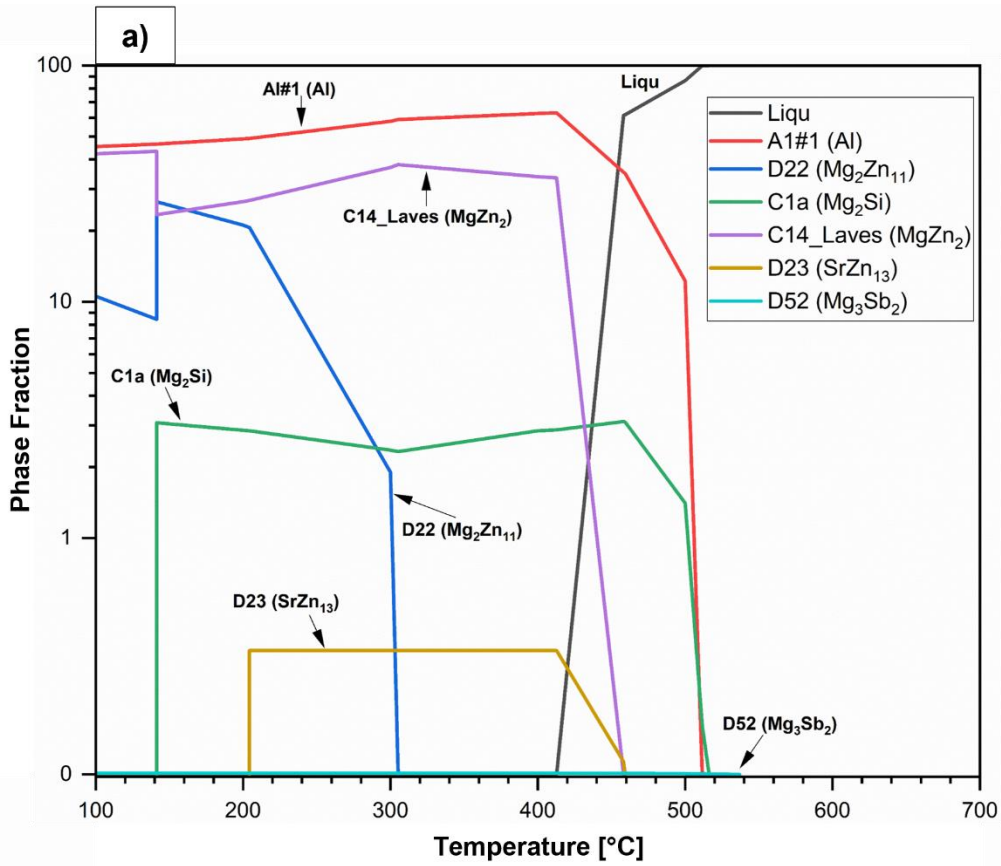


Fig. 5-3 Solidification simulations for the optimized  $\text{Al}_{60}\text{Zn}_{27}\text{Mg}_{11}\text{Si}_2 + \text{Sr}_{0.021}\text{Sb}_{0.001}$  (Alloy 2), lightweight multicomponent alloy calculated by FactSage (CALPHAD): a) Equilibrium solidification, and b) non-equilibrium solidification (Gulliver -Scheil).

In Fig. 5-4a, the phases formed during the equilibrium solidification of the  $\text{Al}_{60}\text{Zn}_{27}\text{Mg}_{11}\text{Si}_2 + \text{Sr}_{0.136}\text{Sb}_{0.031}$  alloy, also denoted as Alloy 3, are depicted. Initially, the high-temperature intermetallic compound ( $\text{Mg}_3\text{Sb}_2$ ) is the first to precipitate at a temperature of  $680^\circ\text{C}$ , followed by the intermetallic phase ( $\text{SrSi}_2\text{Al}_2$ ), which precipitates at  $560^\circ\text{C}$ .

The solid solution phase (Al) makes its appearance at about  $515^\circ\text{C}$ . It is important to note that the aluminum (Al) phase remains prominent in the temperature range of  $290 - 420^\circ\text{C}$ . At  $510^\circ\text{C}$ , the intermetallic phase ( $\text{Mg}_2\text{Si}$ ) begins to form, albeit in smaller quantities. Subsequently, at  $460^\circ\text{C}$ , both the intermetallic phase ( $\text{SrZn}_{13}$ ) and the Laves phase ( $\text{MgZn}_2$ ) precipitate. The ( $\text{MgZn}_2$ ) phase represents the second phase with a substantial phase fraction.

It is worth highlighting that within the temperature range of  $200-460^\circ\text{C}$ , the intermetallic phases ( $\text{Mg}_2\text{Si}$ ) and ( $\text{SrZn}_{13}$ ) display comparable phase fractions. To conclude, the ( $\text{Mg}_2\text{Zn}_{11}$ ) phase is the final one to develop at  $300^\circ\text{C}$ .

As for the Scheil-type non-equilibrium cooling curves (see Fig. 5-4b), the sequence of phase precipitation aligns with the equilibrium solidification curve for most phases, except for the ( $\text{Mg}_2\text{Zn}_{11}$ ) phase, which appears at a slightly higher temperature than  $360^\circ\text{C}$ . Additionally, a new phase precipitates at a temperature of  $345^\circ\text{C}$ , and it corresponds to the HCP (Zn) phase.

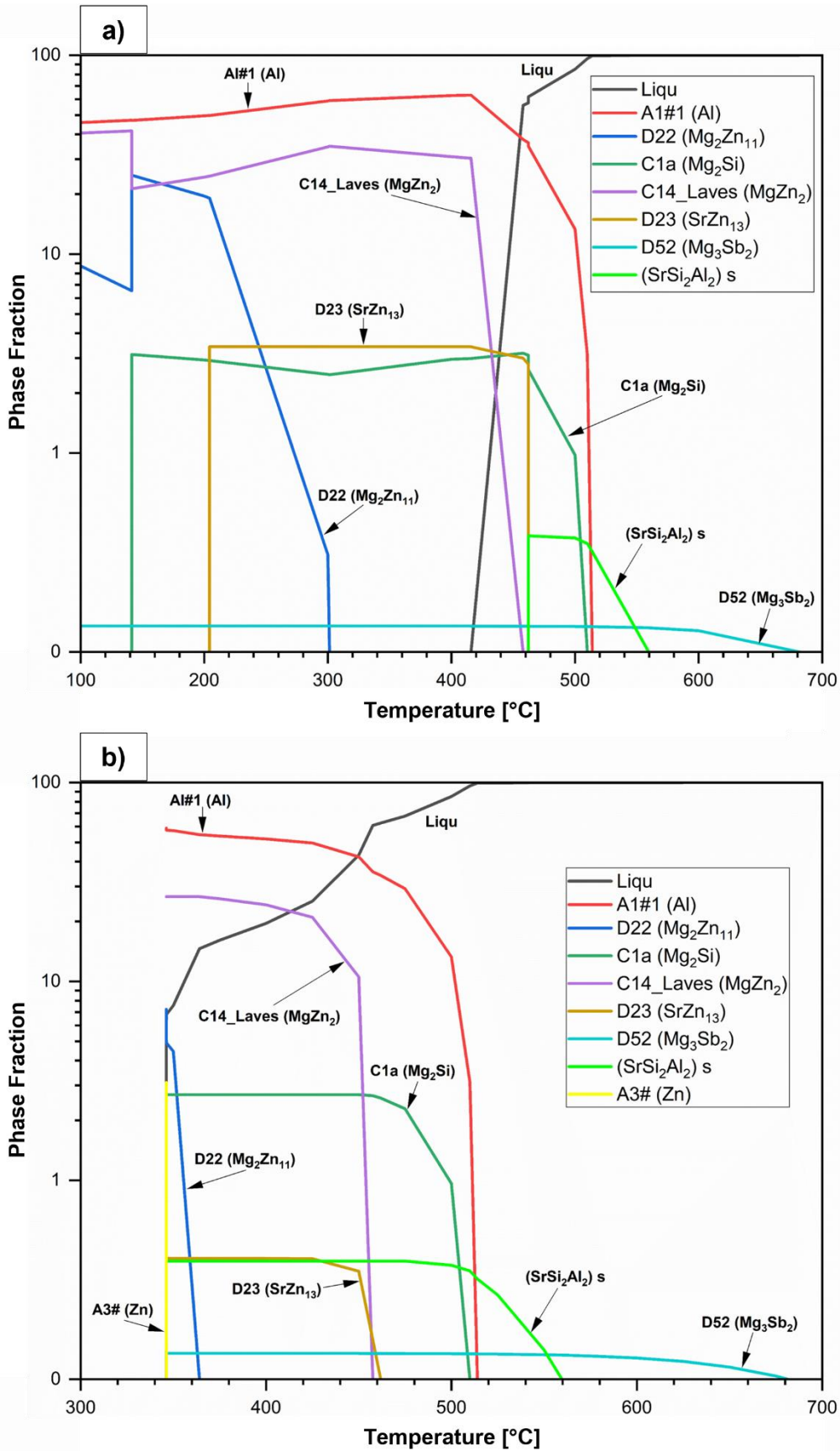


Fig. 5-4 Solidification simulations for the optimized  $\text{Al}_{60}\text{Zn}_{27}\text{Mg}_{11}\text{Si}_2 + \text{Sr}_{0.136}\text{Sb}_{0.031}$  (Alloy 3), lightweight multicomponent alloy calculated by FactSage (CALPHAD): a) Equilibrium solidification, and b) non-equilibrium solidification (Gulliver-Scheil).

### 5.2.2. Microstructural analysis of the alloy and Mg<sub>2</sub>Si phase modification

The following figures show the low and high magnification backscatter SEM images of the as-cast alloys and the distributed mappings of the alloys.

Fig. 5-5 displays the Alloy 1 in its as-cast state. Furthermore, the illustration incorporates an EDS-derived elemental composition distribution map, featured in Fig. 5-5b. Additionally, a magnified view of this microstructure is presented in Fig. 5-5c.

The micrograph illustrates a gray dendritic microstructure with a high concentration of Al, indicating the presence of the solid solution phase (Al) FCC. Additionally, there is an interdendritic region with elevated concentrations of Zn and Mg, as revealed by the composition maps. This suggests the existence of the laves phase (MgZn<sub>2</sub>). Particularly within the interdendritic region, there are bright zones with a high Zn concentration, implying the presence of the (Zn) phase with an HCP crystal structure (see Fig. 5-5c).

Moreover, the microstructure features scattered black intermetallics with a high concentration of Mg, followed by Si, as indicated by the composition maps. These intermetallics exhibit two distinct morphologies, as seen in the enlargement of Fig. 5-5c. One morphology takes the form of a block surrounded by the FCC (Al) matrix, corresponding to the primary intermetallic (Mg<sub>2</sub>Si). The second morphology corresponds to the eutectic (Mg<sub>2</sub>Si) with the (Al) phase, and the structure of this eutectic resembles a fishbone structure.

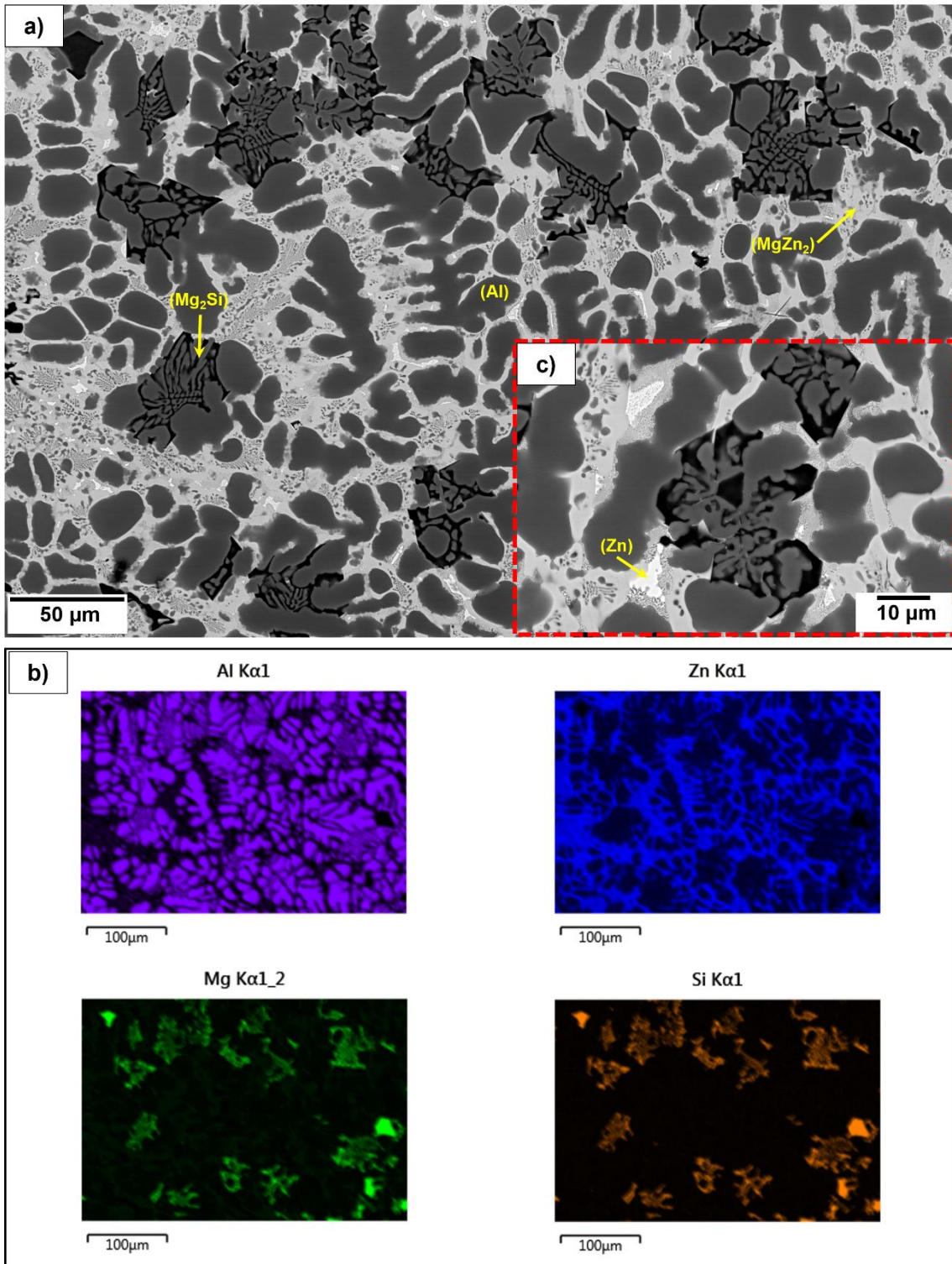


Fig. 5-5 a) SEM-BSE of cast  $Al_{60}Zn_{27}Mg_{11}Si_2$  (Alloy 1); b) EDS elemental mapping of the cast  $Al_{60}Zn_{27}Mg_{11}Si_2$  (Alloy 1) and, c) high magnification of the  $Mg_2Si$  phase.

The microstructure presented in Fig. 5-6a corresponds to the Alloy 2 in the as-cast state, which has been modified with Sr and Sb. Additionally, an elemental composition distribution map obtained through EDS is included in the illustration (see Fig. 5-6b), along with an enlarged area of this microstructure shown in Fig. 5-6c.

This microstructure reveals a dendritic configuration primarily composed of Al, as indicated by the composition maps, suggesting the presence of the solid solution phase (Al) with an FCC crystalline structure. On the other hand, the interdendritic region exhibits elevated concentrations of Zn, followed by magnesium, indicating the potential presence of the laves phase ( $\text{MgZn}_2$ ). It is noteworthy that within this laves phase ( $\text{MgZn}_2$ ), small bright zones are observed (see Fig. 5-6c), which, according to the composition maps, represent the (Zn) phase. Additionally, it is noteworthy that the Sb element has migrated to the areas where this laves phase ( $\text{MgZn}_2$ ) is located.

The microstructure also displays a black eutectic phase in the form of square plates, some with internal formations resembling fishbones. According to the composition maps, this phase contains a higher amount of Mg followed by Si and is surrounded by a matrix rich in (Al), which could correspond to the ( $\text{Mg}_2\text{Si}$ ) phase. It is also essential to note that the element Sr is dissolved in this intermetallic phase. In Fig. 5-6c, small bright zones are observed inside ( $\text{Mg}_2\text{Si}$ ) of this eutectic phase, which could be related to the ( $\text{SrZn}_{13}$ ) phase, according to composition maps and CALPHAD simulation.



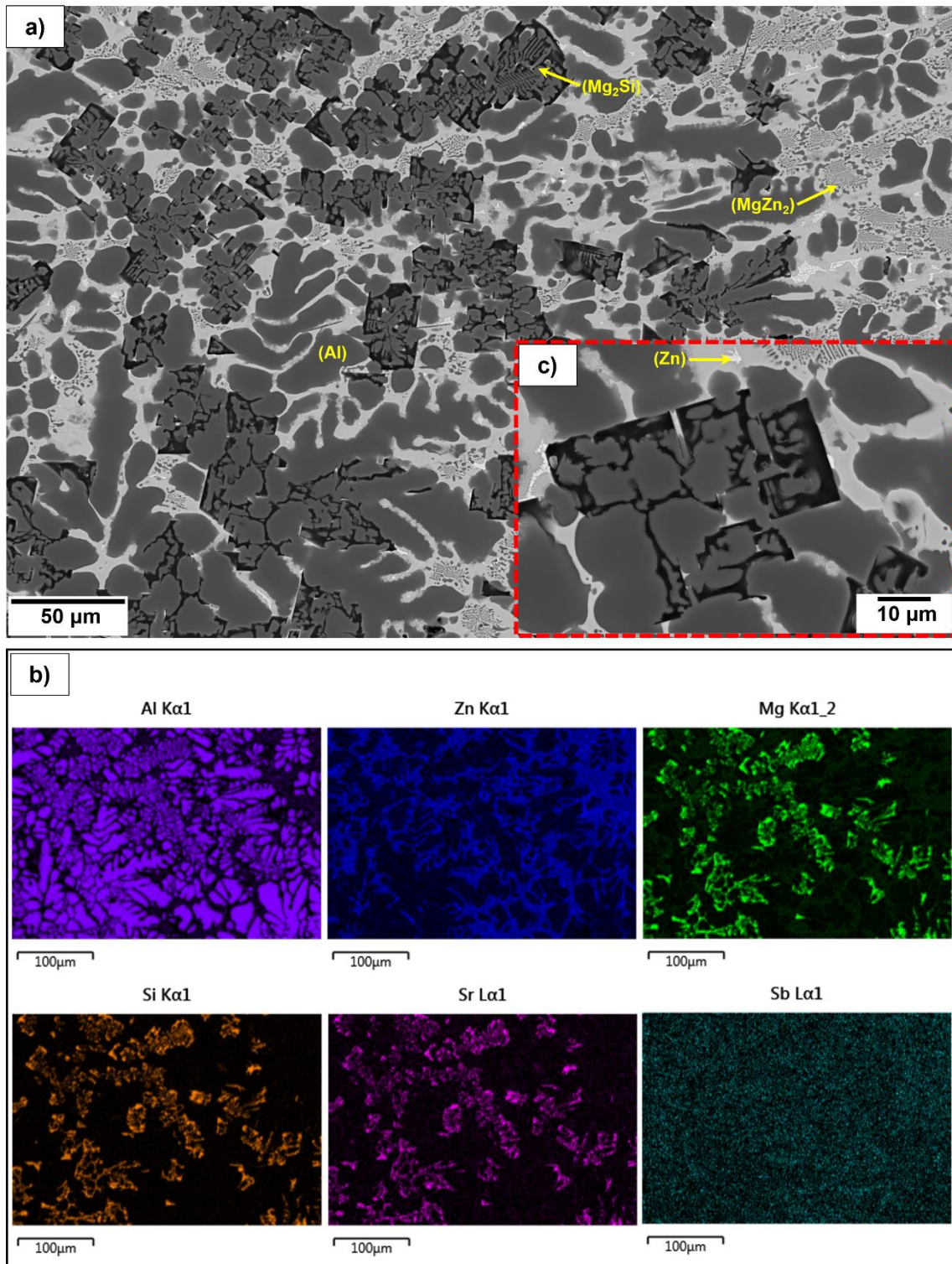


Fig. 5-6 a) SEM-BSE of cast  $Al_{60}Zn_{27}Mg_{11}Si_2 + Sr_{0.021}Sb_{0.001}$  (Alloy 2); b) EDS elemental mapping of the cast  $Al_{60}Zn_{27}Mg_{11}Si_2 + Sr_{0.021}Sb_{0.001}$  (Alloy 2) and, c) high magnification of the  $Mg_2Si$  phase.



The microstructure depicted in Fig. 5-7a represents the as-cast state of the Alloy 3, which has been modified by incorporating higher amounts of Sr and Sb. Additionally, the illustration includes a map displaying the distribution of elemental composition obtained through EDS (see Fig. 5-7b). Furthermore, an enlarged section of this microstructure is featured in Fig. 5-7c.

As can be observed, the structure displays a dendritic configuration with isolated areas that exhibit high concentrations of aluminum. These regions correspond to the solid solution phase (Al) with an FCC crystal structure. In addition, interdendritic regions can be identified, which, according to the composition maps (refer to Fig. 5-7b), show a zinc-rich composition followed by magnesium, indicating the presence of the laves phase ( $\text{MgZn}_2$ ). Furthermore, antimony is observed to be in a solid solution phase, as indicated by these composition maps.

We also notice a eutectic phase in black, surrounded by the aluminum matrix. This eutectic phase manifests two distinct morphologies: one in the form of square blocks and the other resembling a fishbone-like structure. According to the composition maps in Fig. 5-7b, this phase exhibits high concentrations of magnesium, followed by silicon. Additionally, it can be observed that strontium is dissolved within this phase.

An important aspect to highlight is the presence of feather-like lamellae within this phase, which could correspond to the intermetallic ( $\text{SrZn}_{13}$ ). These lamellae possess a high zinc concentration in accordance with the composition data and CALPHAD information.

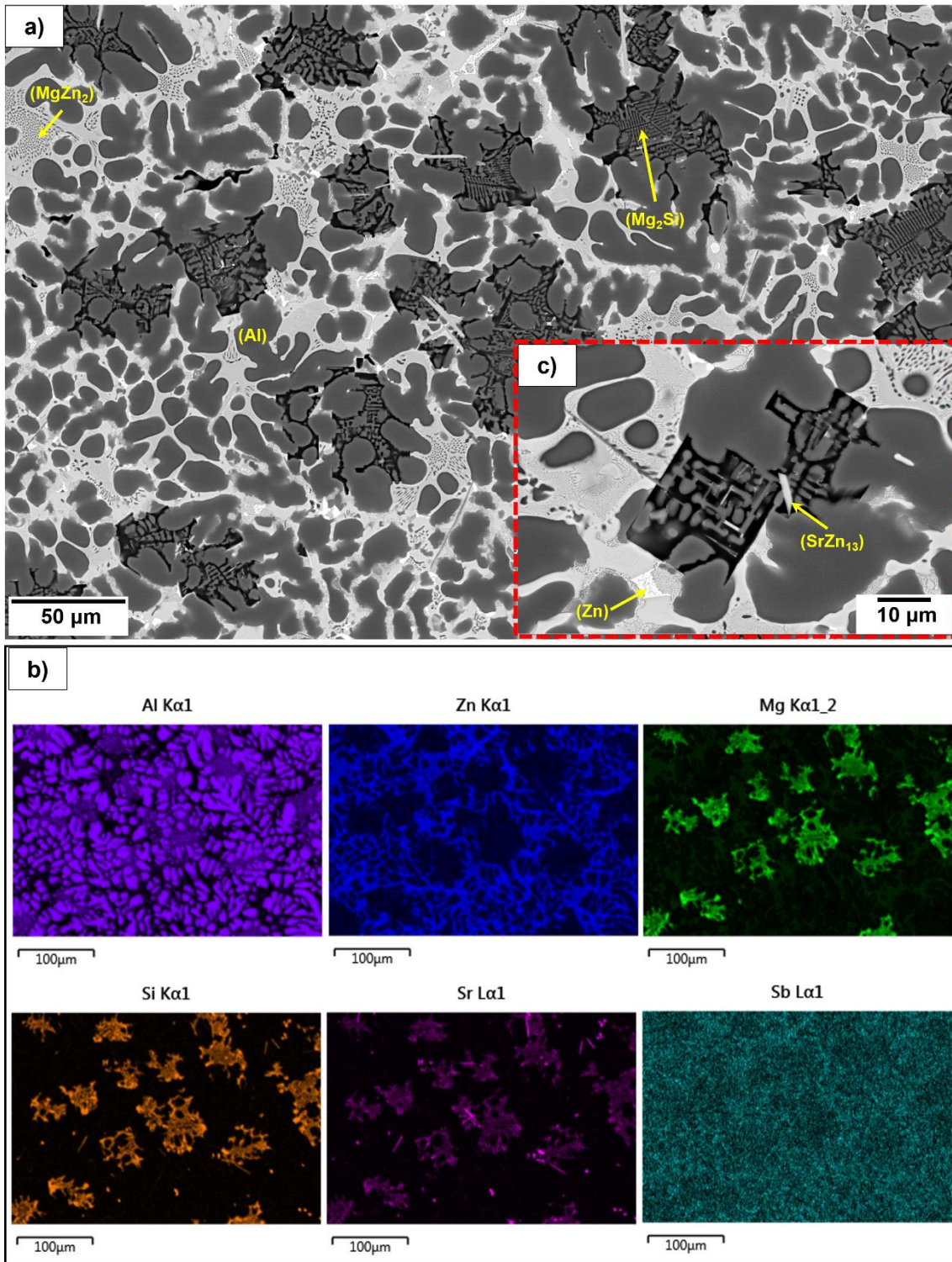


Fig. 5-7 a) SEM-BSE of cast  $Al_{60}Zn_{27}Mg_{11}Si_2 + Sr_{0.136}Sb_{0.031}$  (Alloy 3); b) EDS elemental mapping of the cast  $Al_{60}Zn_{27}Mg_{11}Si_2 + Sr_{0.136}Sb_{0.031}$  (Alloy 3) and, c) high magnification of the  $Mg_2Si$  phase.

### 5.2.3. Impact of heat treatment on microstructure and Mg<sub>2</sub>Si phase modification

Samples of an Al<sub>60</sub>Zn<sub>27</sub>Mg<sub>11</sub>Si<sub>2</sub> alloy, with and without Sr-Sb modification, underwent a double homogenization heat treatment (DHHT) in argon atmosphere and quenched in water as specified in Table 5-3. The heat treatment temperatures were selected based on the results of a prior study.

Table 5-3 Heat treatment for the Al<sub>60</sub>Zn<sub>27</sub>Mg<sub>11</sub>Si<sub>2</sub> lightweight multicomponent alloy.

Sample	Solution Treatment	
	Step 1	Step 2
Double Homogenization Heat Treatment "DHHT"	325 °C/24 h	380 °C/24 h + Quenching

The subsequent images illustrate backscattered SEM visuals of the heat-treated alloys, captured at both low and high magnifications. Additionally, these images are accompanied by elemental distribution maps.

Fig. 5-8a shows to the Alloy 1 after undergoing a heat treatment process (homogenization at 380°C followed by quenching). As observed, it exhibits a dendritic microstructure with high concentrations of aluminum, as indicated by the compositional map in Fig. 5-8b. This points to the presence of the (Al) phase with a face-centered cubic (FCC) crystal structure.

Furthermore, there's an interdendritic region of a lighter color, showing high concentrations of zinc, followed by magnesium. This suggests that it represents the laves phase (MgZn<sub>2</sub>). Additionally, there is a black-colored phase surrounded by the aluminum matrix. This intermetallic phase exhibits various morphologies, with one resembling a block and the other taking the form of a plate, Chinese characters, and a fishbone-like structure (see Fig. 5-8c). The composition of this phase is rich in magnesium, followed by silicon, indicating that it is the (Mg<sub>2</sub>Si) phase.



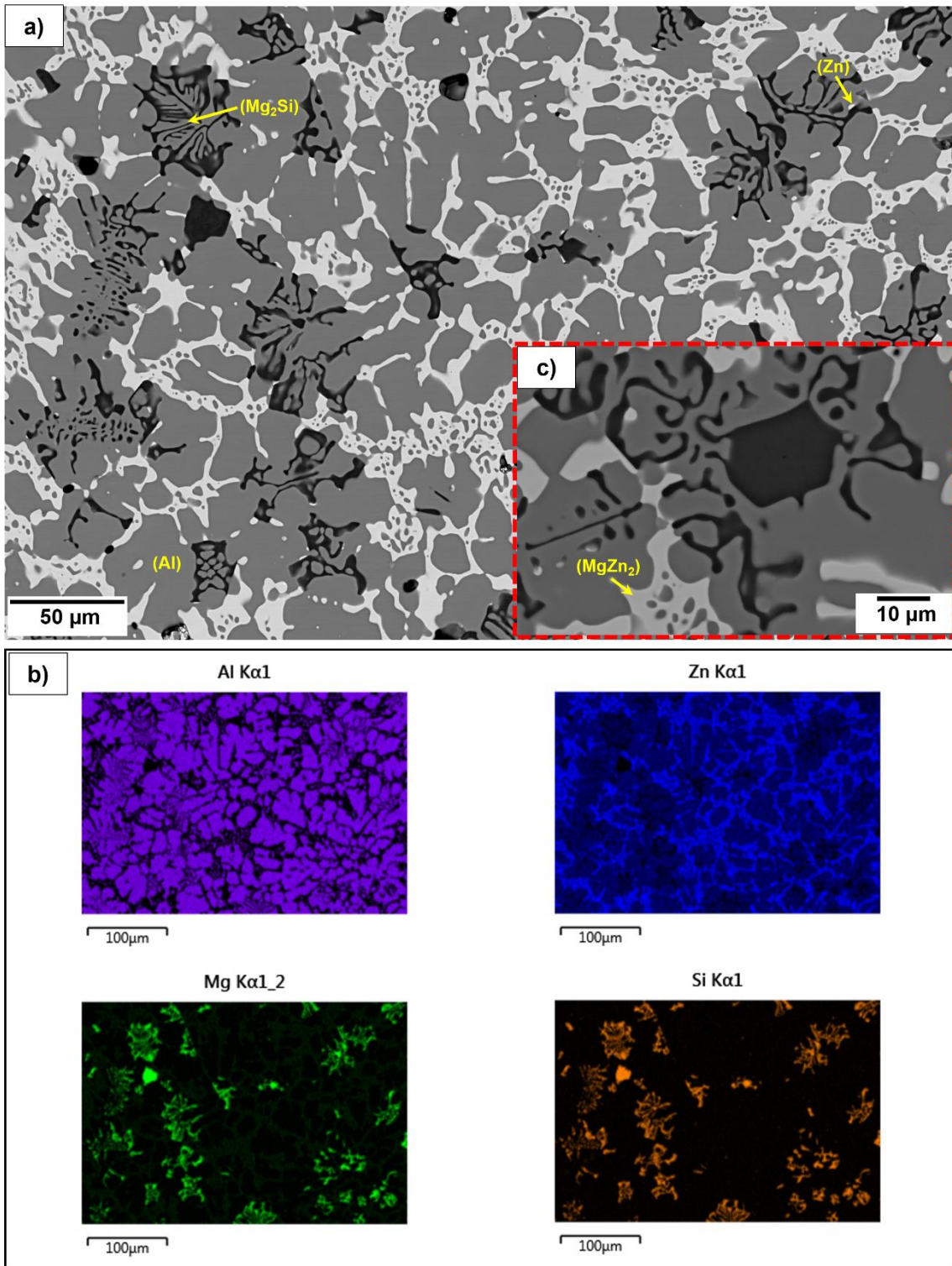


Fig. 5-8 a) SEM-BSE of the heat-treated  $Al_{60}Zn_{27}Mg_{11}Si_2$  (Alloy 1); b) EDS elemental mapping of the heat-treated  $Al_{60}Zn_{27}Mg_{11}Si_2$  (Alloy 1) and, c) high magnification of the  $Mg_2Si$  phase.

Fig. 5-9a corresponds to the Alloy 2, which has been modified with strontium (Sr) and antimony (Sb) and subjected to a heat treatment (homogenization at 380°C followed by quenching). As observed, it exhibits a dendritic microstructure with a high content of aluminum, as indicated by the compositional map in Fig. 5-9b. This suggests the presence of the solid solution phase (Al).

Additionally, there is an interdendritic structure of bright color with high concentrations of zinc, followed by magnesium, which points to it being the laves phase ( $MgZn_{12}$ ). Furthermore, it can be observed that the element antimony, added as a modifier in this alloy, is dissolved within this phase.

Lastly, there is a black-colored phase surrounded by the aluminum (Al) matrix with an FCC crystal structure. This intermetallic phase exhibits plate-like morphologies with fishbone-like structures inside, and some of them have rounded edges (see Fig. 5-9c). According to the compositional maps, this phase has a high concentration of magnesium, followed by silicon, which aligns with the identification of the intermetallic ( $Mg_2Si$ ). It's worth noting that within this intermetallic ( $Mg_2Si$ ), the modifier element strontium is dissolved, as observed in Fig. 5-9b.

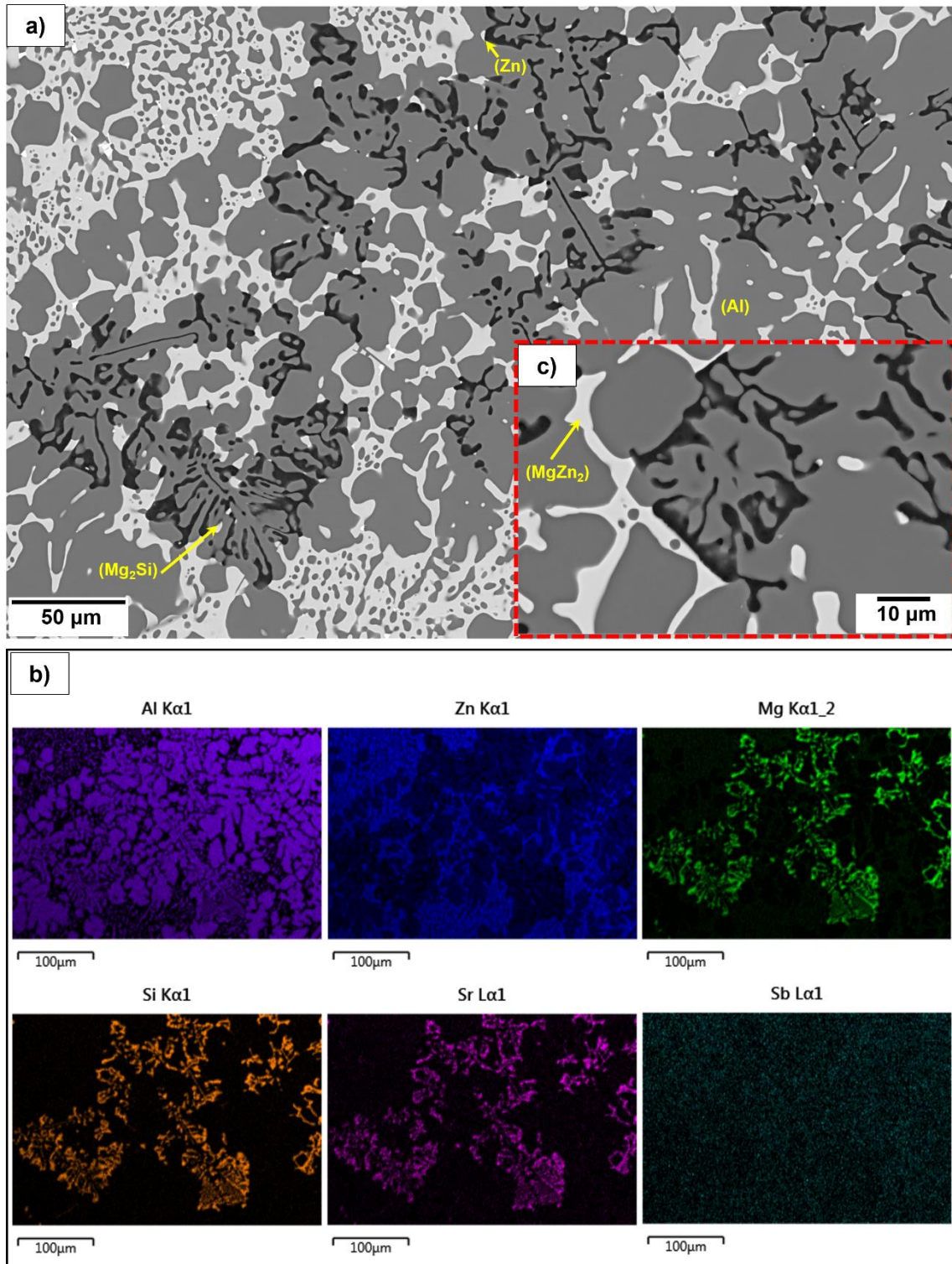


Fig. 5-9 a) SEM-BSE of the heat-treated  $\text{Al}_{60}\text{Zn}_{27}\text{Mg}_{11}\text{Si}_2 + \text{Sr}_{0.021}\text{Sb}_{0.001}$  (Alloy 2); b) EDS elemental mapping of the heat-treated  $\text{Al}_{60}\text{Zn}_{27}\text{Mg}_{11}\text{Si}_2 + \text{Sr}_{0.021}\text{Sb}_{0.001}$  (Alloy 2) and, c) high magnification of the  $\text{Mg}_2\text{Si}$  phase.

In Fig. 5-10a, we can observe the microstructure of the Alloy 3, which has undergone significant modifications with increased levels of strontium (Sr) and antimony (Sb). This alloy was also subjected to a heat treatment process involving homogenization at 380°C followed by quenching. The microstructure reveals a dendritic pattern that is notably rich in aluminum. This aluminum-rich area, as clearly shown in the compositional maps in Figure 6b, suggests the presence of the solid solution phase (Al). It's interesting to note the presence of bright white particles within these dendrites.

Furthermore, there is an interdendritic structure characterized by elevated concentrations of zinc and magnesium, as indicated by the compositional maps, which strongly implies the presence of the laves phase ( $MgZn_2$ ). Notably, antimony is found to be dissolved within this laves phase.

Additionally, there are distinct intermetallic phases, represented in black, mostly enclosed by the aluminum (Al) solid solution matrix with an FCC crystal structure. These intermetallic phases exhibit at least two distinct morphologies, one in block-like formations and the other resembling fishbone structures. These black intermetallics are also distinguished by their high magnesium and silicon content, indicating the formation of the ( $Mg_2Si$ ) phase. Furthermore, the compositional maps in Fig. 5-10b reveal that the modifier element, strontium, is incorporated within this phase. Of significance, within or in the proximity of these intermetallic phases, a bright phase with feather-like morphology is present (see Fig. 5-10c). This phase exhibits high concentrations of zinc and strontium, which suggests a potential correspondence to the intermetallic ( $SrZn_{13}$ ), according to findings from CALPHAD analysis.



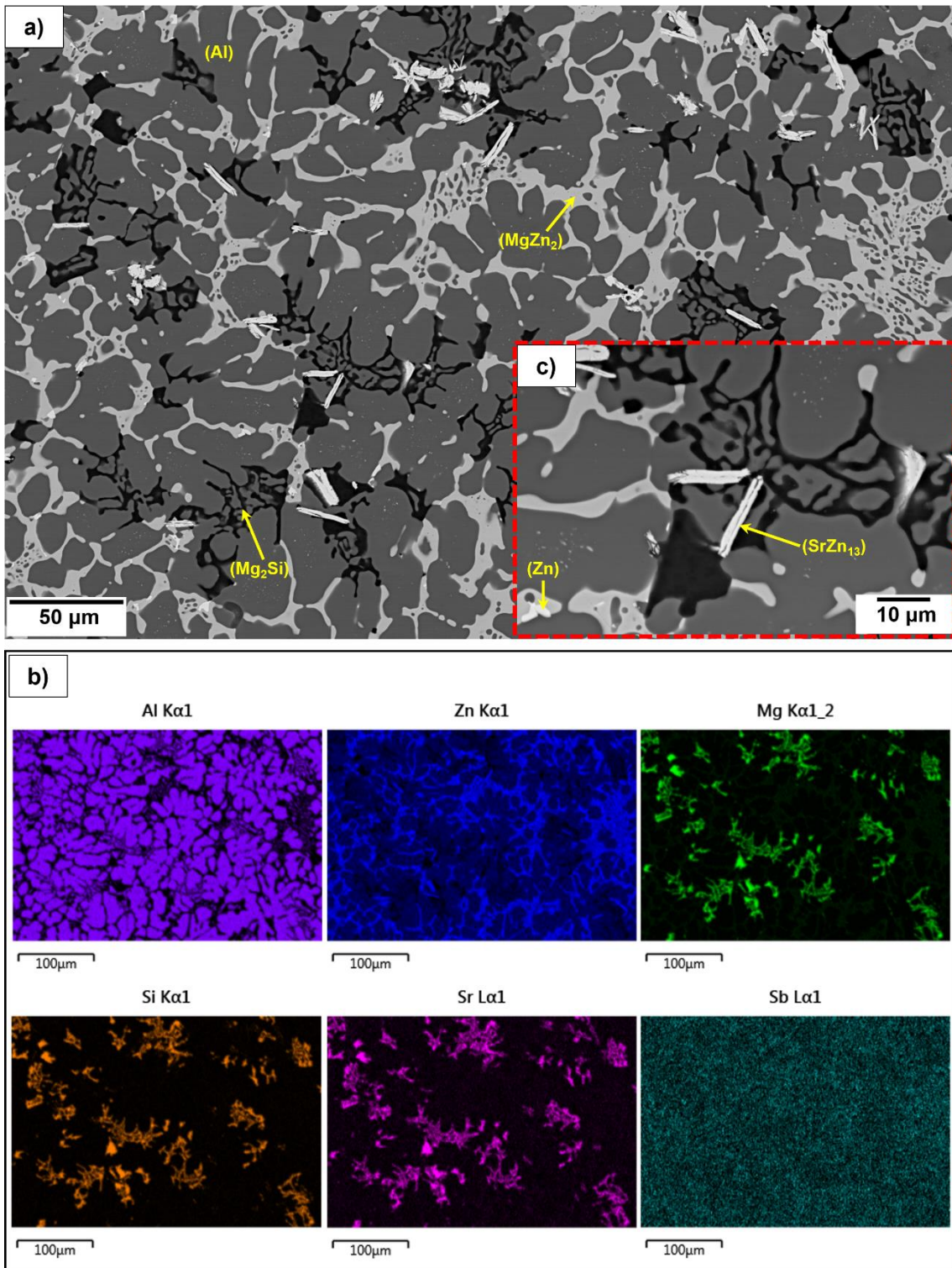


Fig. 5-10 a) SEM-BSE of the heat-treated  $\text{Al}_{60}\text{Zn}_{27}\text{Mg}_{11}\text{Si}_2 + \text{Sr}_{0.136}\text{Sb}_{0.031}$  (Alloy 3); b) EDS elemental mapping of the heat-treated  $\text{Al}_{60}\text{Zn}_{27}\text{Mg}_{11}\text{Si}_2 + \text{Sr}_{0.136}\text{Sb}_{0.031}$  (Alloy 3) and, c) high magnification of the Mg<sub>2</sub>Si phase.

#### 5.2.4. Mechanical properties in compression of optimized alloys.

In Fig. 5-11, uniaxial compression curves are displayed for the Alloy 1, and the alloys modified with strontium and antimony, Alloy 2 and Alloy 3. Fig. 5-11a represents the alloys in their as-cast state, while Fig. 5-11b corresponds to the alloys after undergoing heat treatment (homogenization followed by quenching). The mechanical properties, including yield strength (YS) and ultimate strength (UTS), for all the curves have been recorded and are presented in Table 5-4.

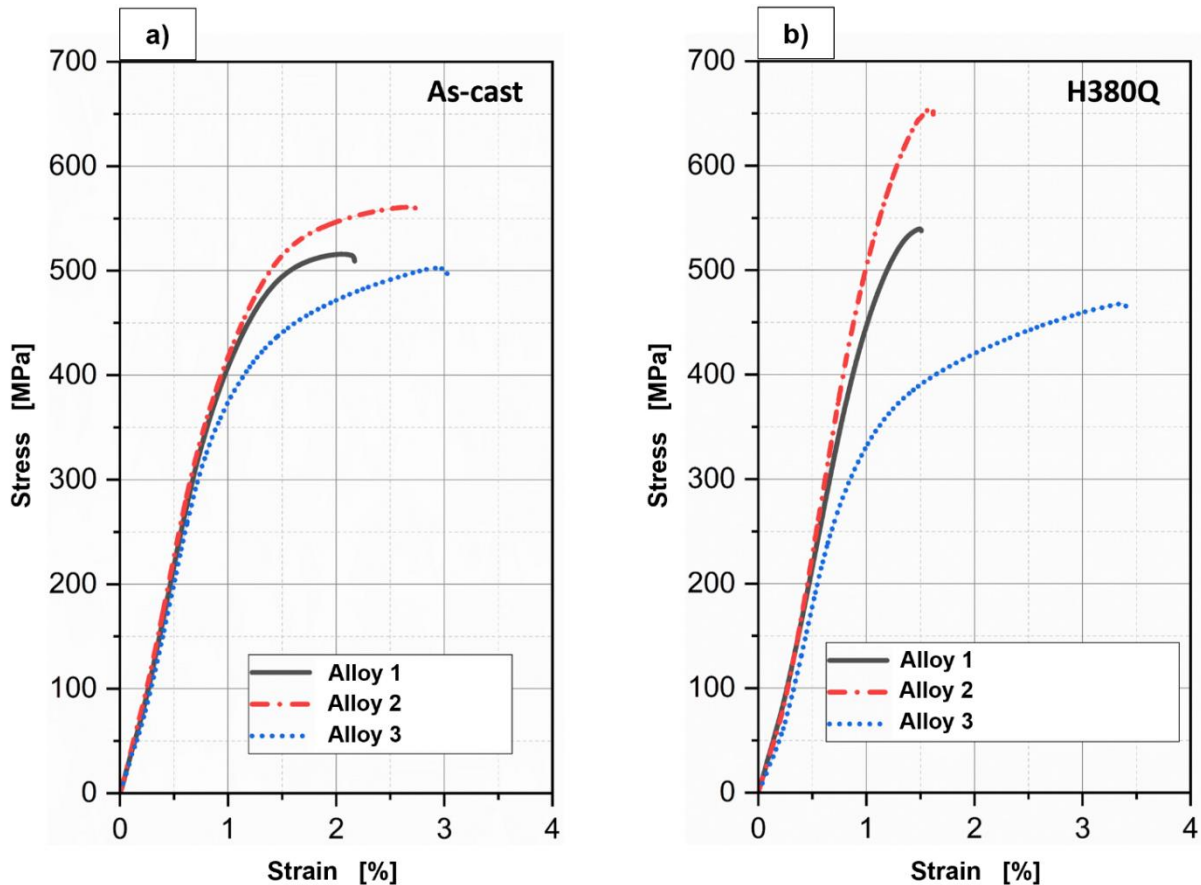


Fig. 5-11 Compressive curves of Sr-Sb modified and unmodified  $Al_{60}Zn_{27}Mg_{11}Si_2$  alloy at room temperature.

As observed in Fig. 5-11a, the alloy exhibiting the highest UTS (Ultimate Tensile Strength) of 560 MPa and YS (Yield Strength) of 448 MPa corresponds to the Alloy 2. Following that, the unmodified Alloy 1 shows YS values of 405 MPa and UTS values of 516 MPa. In contrast, the alloy with the lowest YS of 345 MPa and UTS of 502 MPa is the Alloy 3, which contains higher levels of Sr and Sb as modifying elements.

Similarly, in Fig. 5-11b, the uniaxial compression curve with the highest YS (560 MPa) and UTS (654 MPa) corresponds to the Alloy 2, which has been modified with Sr and Sb. The Alloy 1 follows with YS values of 502 MPa and UTS values of 539 MPa. Finally, the alloy with the lowest YS of 323 MPa and UTS of 467 MPa remains the Alloy 3, which, as previously mentioned, contains a higher concentration of modifying elements, Sr and Sb.

Table 5-4 Compressive mechanical properties of Sr-Sb modified and unmodified Al<sub>60</sub>Zn<sub>27</sub>Mg<sub>11</sub>Si<sub>2</sub> alloy at room temperature.

Condition	Alloy	Yield strength (MPa)	Ultimate strength (MPa)
As-cast	Alloy 1	405±5	516±4
	Alloy 2	448±2	560±2
	Alloy 3	345±7	502±11
H380Q	Alloy 1	502±3	539±2
	Alloy 2	560±2	654±2
	Alloy 3	323±15	467±18

### 5.3. Discussion

#### 5.3.1. Composition optimization analysis

Primary silicon in light alloys reduces mechanical properties due to its thickness and near-zero elongation, making it prone to crack formation and serving as a preferred pathway for crack propagation. Even with relatively small primary silicon particles, the presence of a significant amount of flaky eutectic silicon acts as a channel for crack propagation between primary silicon particles, thereby limiting ductility enhancement [134–136]. Consequently, researchers have endeavored to refine primary silicon to improve ductility, leading to the development of new technologies such as modification treatments aimed at refining primary silicon [134,137,138].

Based on the CALPHAD results (see Fig. 5-2), when the Si percentage is reduced in the Al<sub>58</sub>Zn<sub>28</sub>Mg<sub>6</sub>Si<sub>8</sub> alloy while maintaining a balanced composition to retain a high solid solution, the precipitation of the primary Si phase is eliminated. The optimized composition is adjusted to Al<sub>60</sub>Zn<sub>27</sub>Mg<sub>11</sub>Si<sub>2</sub>. This result is validated through SEM micrographs (Fig. 5-5), which confirm the precipitation of four phases: (1) aluminum (Al) in the face-centered cubic (FCC) structure, (2) Laves\_C14 phase (MgZn<sub>2</sub>), (3) (Mg<sub>2</sub>Si), and (4) the hexagonal close-packed (HCP) phase (Zn). However, the predicted (Mg<sub>2</sub>Zn<sub>11</sub>) phase, as per CALPHAD, was not detected even by SEM.

It is well known that the larger the electronegativity difference between elements, the more is their tendency to form stable compounds [139]. Table 5-5 provides the electronegativity values for Al, Zn, Mg, Si, Sr, and Sb. From these values, it can be deduced that there is a significant tendency for the elements Sr and Sb to combine and create a stable compound, as indicated by their electronegativity difference of 1.1, resulting in the compound (Sr<sub>11</sub>Sb<sub>10</sub>). Similarly, the elements Sb and Mg, with an electronegativity difference of 0.74, tend to form the compound (Mg<sub>3</sub>Sb<sub>2</sub>). Finally, the elements Sr and Zn, with an electronegativity difference of 0.66, exhibit a propensity to generate the compound (SrZn<sub>13</sub>).

Among these potential phases, only the intermetallic compounds (Mg<sub>3</sub>Sb<sub>2</sub>) and (SrZn<sub>13</sub>) coincide with the phases calculated by FactSage for the two studied alloys containing Sr and Sb.

Table 5-5 Electronegativity of Al, Zn, Mg, Si, Sr and Sb elements.

Element	Al	Zn	Mg	Si	Sb	Sr
Electronegativity	1.61	1.65	1.31	1.80	2.05	0.95

### 5.3.2. Modification of Mg<sub>2</sub>Si phase

The addition of strontium Sr and antimony Sb to the alloys has a substantial influence on the structure of the (Mg<sub>2</sub>Si) phase, effectively preventing the formation of primary (Mg<sub>2</sub>Si) blocks as seen in the micrograph of the Al<sub>60</sub>Zn<sub>27</sub>Mg<sub>11</sub>Si<sub>2</sub> alloy. Instead, this modification leads to the exclusive presence of the eutectic (Mg<sub>2</sub>Si) phase. With an increase in the strontium and antimony content in both Alloy 1 and Alloy 2, the structure of the eutectic (Mg<sub>2</sub>Si) phase undergoes a transformation, taking on a more square and compact appearance. This newly formed structure exhibits an internal pattern reminiscent of fishbone structure.

### 5.3.3. Mechanisms for modification and refinement of Mg<sub>2</sub>Si phase

According to the research by Chen *et al.* [114], two key mechanisms have been identified for modifying and refining (Mg<sub>2</sub>Si) grains in alloys. The first focuses on improving nucleation, involving the creation of numerous nucleation sites in the molten mass, which in turn reduces the size of (Mg<sub>2</sub>Si) grains. The second mechanism involves restricting grain growth by manipulating solidification conditions. This approach interferes with grain growth rather than promoting nucleation.

In the nucleation process, the critical factor is the energy at the interface between a foreign nucleus and the crystallization phase, which depends on the crystal face structures that come into contact. An important criterion for heterogeneous nucleation is that there must be minimal mismatch (misfit) of less than 6% between the planes of the foreign nucleus and the host material [109].

Following this research, Yang *et al.* [140], separately explored the impact of elements Sb and Sr on the modification of the intermetallic phase (Mg<sub>2</sub>Si) in an AZ61-0.7Si magnesium alloy. The results revealed that adding 0.4% by weight of Sb to the AZ61-0.7Si alloy refined the (Mg<sub>2</sub>Si) phase without altering its morphology. In contrast, adding 0.12% by weight of Sr to the AZ61-0.7Si magnesium alloy changed the morphology of the (Mg<sub>2</sub>Si) intermetallic from an initial coarse structure to one of fine and/or irregular grains. This change was due to the mismatch between the planes of the foreign nucleus and the host material, being 1.72% for (0001)Mg<sub>3</sub>Sb<sub>2</sub>//(111)Mg<sub>2</sub>Si and 0.69% for (100)Al<sub>4</sub>Sr//(100)Mg<sub>2</sub>Si. This mismatch of less than 6% led to the conclusion that these compounds act as heterogeneous nuclei for (Mg<sub>2</sub>Si) particles. From this study, it can be inferred that the intermetallic compound (Mg<sub>3</sub>Sb<sub>2</sub>) can act as a nucleation agent for (Mg<sub>2</sub>Si) phase in alloys 2 and 3 modified with Sr and Sb. This is supported by the isopleth for Al<sub>60</sub>Zn<sub>27</sub>Mg<sub>11</sub>Si<sub>2</sub>Sb<sub>0.13</sub>Sr<sub>x</sub> shown in Fig. 5-12, where it is evident that the compound (Mg<sub>3</sub>Sb<sub>2</sub>) remains stable and is the initial precipitate. However, it is worth noting that upon introducing the strontium (Sr) element to the alloy, CALPHAD predicts the formation of only two intermetallics, (SrSi<sub>2</sub>Al<sub>2</sub>) and (SrZn<sub>13</sub>), in accordance with the phase diagram.



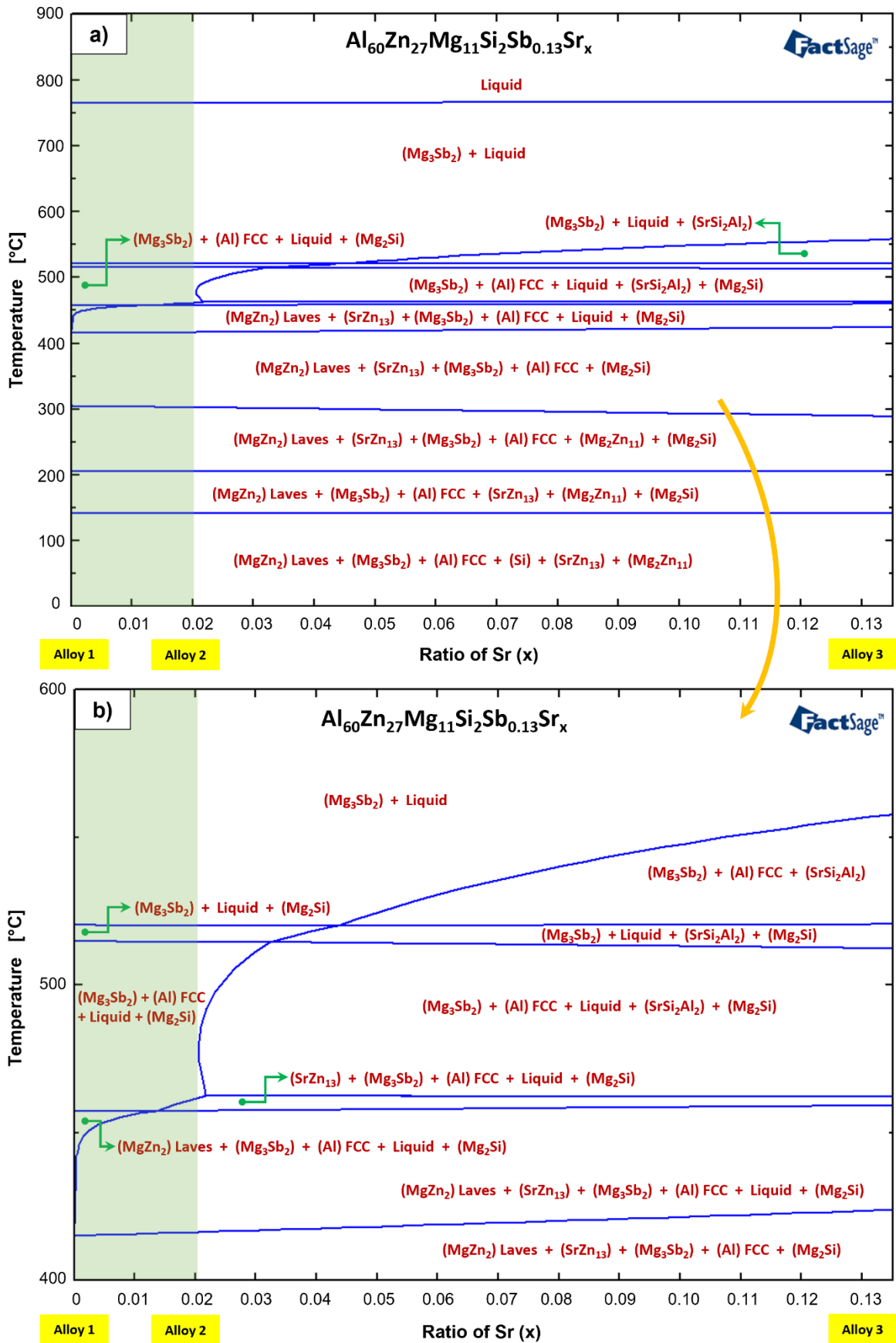


Fig. 5-12 Phase diagram prediction. a) Isoleth of  $\text{Al}_{60}\text{Zn}_{27}\text{Mg}_{11}\text{Si}_2\text{Sb}_{0.13}\text{Sr}_x$  highlighting the composition ranges for each alloy, from the unmodified alloy (Alloy 1) to those modified with Sr and Sb (Alloy 2 and Alloy 3) b) Zoom of isopleth diagram.

The intermetallic ( $\text{SrSi}_2\text{Al}_2$ ) only forms in the Alloy 3, which contains a higher amount of Sr and Sb. It is important to note that this intermetallic ( $\text{SrSi}_2\text{Al}_2$ ) is stable over a temperature range of 460-560°C. Additionally, in the composition maps of alloys 2 and 3, it is observed that the ( $\text{Mg}_2\text{Si}$ ) intermetallic contains a significant amount of dissolved Sr, suggesting that Sr could replace Si and dissolve in ( $\text{Mg}_2\text{Si}$ ).

Dong *et al.* [141] investigated the impact of Sr on modifying the eutectic  $\text{Mg}_2\text{Si}$  phase in an AZ61 alloy. Their findings revealed a shift in the morphology of  $\text{Mg}_2\text{Si}$  from a Chinese script-like shape to a polygonal form with the addition of Sr. Moreover, they detected some dissolved Sr atoms within the  $\text{Mg}_2\text{Si}$  lattice, leading to alterations in the growth mode and an enhancement in its morphology. Additionally, the  $\text{Al}_4\text{Sr}$  compound formed during solidification acted as a heterogeneous nucleation core for  $\text{Mg}_2\text{Si}$ , refining its size. Considering this prior study and observing the changes in the eutectic structure of the LW-MEA, it could be inferred that this intermetallic might have formed as a secondary nucleation and phase modification agent for the ( $\text{Mg}_2\text{Si}$ ) phase in alloys 2 and 3.

Regarding the ( $\text{SrZn}_{13}$ ) compound, its formation has been observed in alloys 2 and 3, as predicted by the isopleth diagram in Fig. 5-12.

Strontium has attracted interest for its promising influence on Zn-Al alloys [142]. Adding 0.1% of Sr to Zn alloys has significantly improved strength and elongation due to the formation of the ( $\text{SrZn}_{13}$ ) intermetallic, which acts as nucleation sites [143]. However, it is important to note that an increase in Sr content up to 0.8% leads to a decrease in strength due to an increase in the size of ( $\text{SrZn}_{13}$ ) particles.

The existence of the D23 phase ( $\text{SrZn}_{13}$ ), as predicted by FactSage, has been confirmed through EBSD analysis in alloy 3, as shown in Fig. 5-13. This phase has a feather-like morphology and is surrounded by the ( $\text{Mg}_2\text{Si}$ ) intermetallic. These findings are consistent with the research by Bilbao *et al.* [104], who studied phase evolution in the  $\text{Al}_{58}\text{Zn}_{28}\text{Mg}_6\text{Si}_8$  alloy as the temperature varies using X-ray Thermo-Diffraction. They identified the ( $\text{SrZn}_{13}$ ) intermetallic compound when the alloy was heated between 30°C and 280°C. Additionally, they observed that strontium, added as a modifier, interacted with zinc to form ( $\text{SrZn}_{13}$ ).

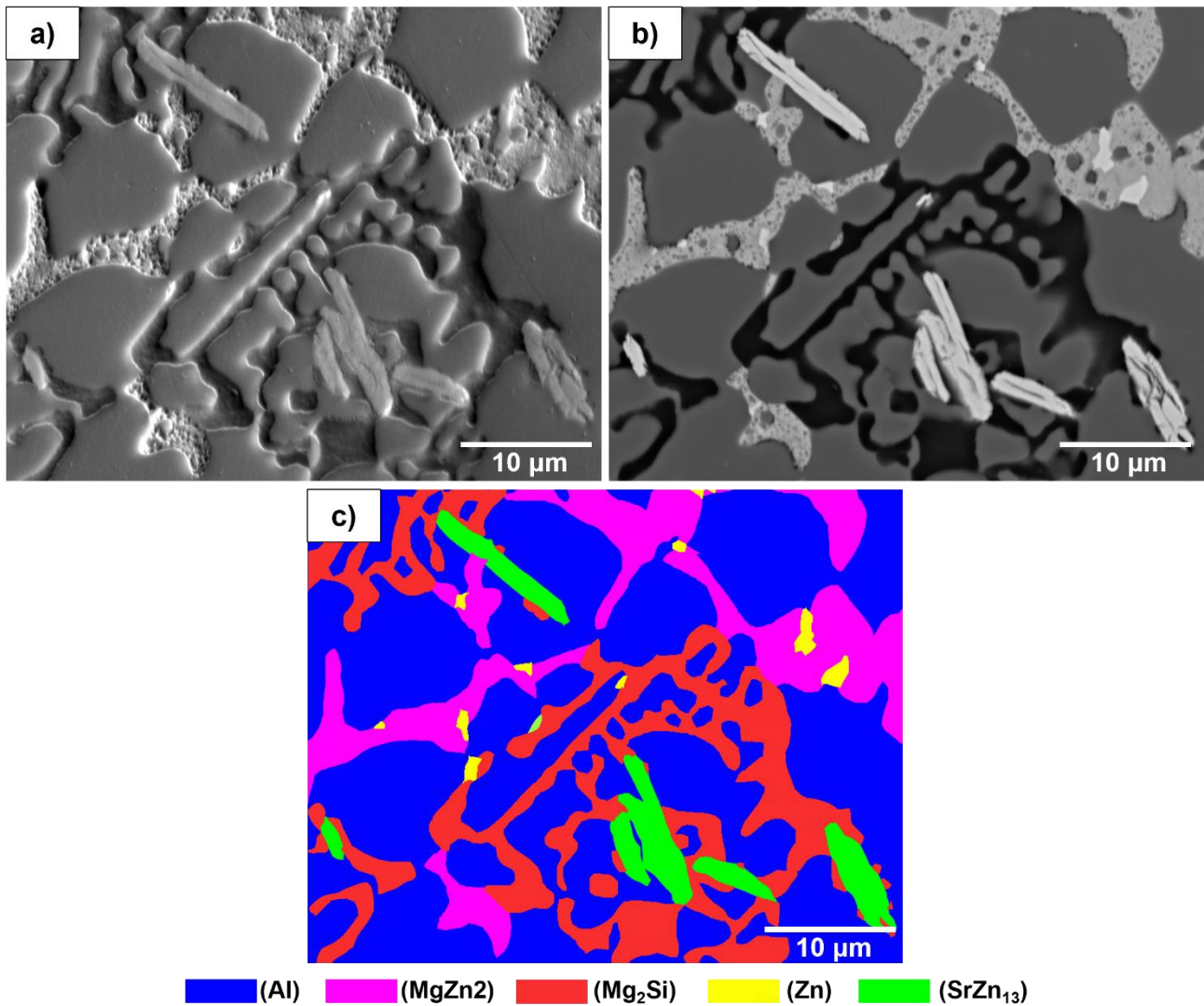


Fig. 5-13 Phase mapping of the  $\text{Al}_{60}\text{Zn}_{27}\text{Mg}_{11}\text{Si}_2 + \text{Sr}_{0.136}\text{Sb}_{0.031}$  (Alloy 3): a) SEM Secondary electron (SE) image, b) Backscattered electron (BSE) image, and c) Hough transform EBSD map with user-selected libraries for (Al), (MgZn<sub>2</sub>), (Mg<sub>2</sub>Si), (Zn) and (SrZn<sub>13</sub>).

It is important to note that in Alloy 3, which contains a higher amount of Sr and Sb, the presence of the (SrZn<sub>13</sub>) intermetallic with larger particles significantly affects the tensile mechanical properties, resulting in a marked decrease in strength.

#### 5.3.4. Compression behaviours of modified alloys

In general, there is a consistent improvement in compression strength properties with the controlled addition of Sr-Sb, with Alloy 2 emerging as the most robust variant in both conditions (As-cast and H380Q). In contrast, Alloy 3, with the highest concentration of Sr and Sb, experiences a decrease in strength due to precipitation and an increase in particle size (SrZn<sub>13</sub>), as mentioned earlier. These results suggest the existence of an optimal point in modifying the composition to achieve superior mechanical properties.



## 5.4. Conclusions

In this study, the chemical composition of the medium-entropy light alloy  $\text{Al}_{58}\text{Zn}_{28}\text{Mg}_6\text{Si}_8$  was systematically optimized. Additionally, the influence of modifying elements, specifically strontium (Sr) and antimony (Sb), on the  $\text{Mg}_2\text{Si}$  phase was investigated. As a result of the optimization process, the alloy composition was fixed at  $\text{Al}_{60}\text{Zn}_{27}\text{Mg}_{11}\text{Si}_2$ . The main conclusions drawn from the results obtained are as follows:

- The CALPHAD results and SEM micrographs suggest that reducing the silicon (Si) percentage in the  $\text{Al}_{58}\text{Zn}_{28}\text{Mg}_6\text{Si}_8$  alloy eliminates the precipitation of primary silicon while maintaining a high percentage of aluminum solid solution (FCC). The optimized composition is identified as  $\text{Al}_{60}\text{Zn}_{27}\text{Mg}_{11}\text{Si}_2$ .
- The incorporation of strontium (Sr) and antimony (Sb) into the alloys has a notable impact on the structure of the  $(\text{Mg}_2\text{Si})$  phase. This influence prevents the formation of primary blocks and leads to the exclusive presence of the eutectic  $(\text{Mg}_2\text{Si})$ . As the content of Sr and Sb increases, the phase undergoes a transformation, adopting a more square and compact appearance. This newly formed structure displays an internal pattern reminiscent of a fishbone structure.
- The addition of Sb and Sr introduces intermetallic compounds  $(\text{Mg}_3\text{Sb}_2)$  and  $(\text{Al}_4\text{Sr})$  which act as nucleation agents for the  $(\text{Mg}_2\text{Si})$  particles.
- The addition of antimony (Sb) and strontium (Sr) is thought to result in the formation of intermetallic compounds, namely  $(\text{Mg}_3\text{Sb}_2)$  and  $(\text{Al}_4\text{Sr})$ , which function as nucleation agents for the  $(\text{Mg}_2\text{Si})$  particles.
- Controlled addition of Sr and Sb improves compression strength properties, with Alloy 2 emerging as the most robust variant. However, Alloy 3, with the highest concentration of Sr and Sb, experiences a decrease in strength due to the presence of  $(\text{SrZn}_{13})$  intermetallic with larger particles.
- Despite adjusting the chemical composition and modifying the  $(\text{Mg}_2\text{Si})$  intermetallic with Sr and Sb, there has been no improvement in ductility. This alloy remains extremely hard with high strength, but ductility is virtually absent. Exploring alternative manufacturing methods to address this lack of ductility in these alloys would be interesting.

# Chapter 6

## 6. Enhancing Microstructure via Manufacturing Methods of LW-MEA

*This chapter focuses on enhancing a previously optimized alloy  $Al_{60}Zn_{27}Mg_{11}Si_2$  using a variety of processing techniques. The process begins with conventional sand casting, followed by deformation using Near Solidus Forming (NSF) technology and directional solidification (DS). These processes aim to increase the material's density, eliminate porosities and defects, and improve its internal structure. Subsequently, a heat treatment is applied to the samples. A detailed comparison of the microstructures and mechanical properties of the samples subjected to uniaxial compression tests is conducted. The main goal is to assess how each method affects the mechanical performance of the alloy and determine which technique is more effective in improving its properties.*

### 6.1. Introduction

In the previous chapter, we adjusted the chemical composition to prevent the precipitation of primary silicon. Additionally, we used the modifying elements Sr and Sb to alter the  $Mg_2Si$  intermetallic, aiming to enhance the mechanical properties of the medium-entropy alloy. The optimized alloy resulted in  $Al_{60}Zn_{27}Mg_{11}Si_2 + Sr_{0.021}Sb_{0.001}$ . Despite notable improvements in microstructural modification and increased compressive strength, these optimized alloys have exhibited virtually no ductility. Therefore, we have decided to continue studying this alloy and evaluate a manufacturing method that can modify the microstructure to potentially achieve ductility.

Various process technologies, including casting, forging, rolling, and extrusion, are associated with lightweight materials. Advanced casting techniques, such as high-pressure die casting, gravity casting, and squeeze casting, have addressed the limitations of traditional casting processes [144–148]. These techniques result in improved mechanical strength, refined microstructure, enhanced dimensional accuracy, and increased productivity. They help overcome inconsistencies and defects, such as gas or shrinkage porosity, commonly found in cast parts [145]. However, these processes require adjustments based on different casting parameters. To date, there is no cost-effective and simple processing method for manufacturing LW-MEAs.

Semi-Solid Metal (SSM) processing has been confirmed to produce multicomponent alloys with superior mechanical properties. SSM improves the plasticity of performance alloys by maintaining them at a temperature between the solidus and liquidus points [149]. Under the umbrella of SSM, a new technology called Near Solidus Forming (NSF) has emerged, offering as-forged properties (tensile and fatigue) while reducing energy and raw material consumption. NSF operates just below the solidus temperature, where the material has limited ductility, providing the benefits of both conventional forging (better material properties due to grain refinement) and semi-solid processing

(lower pressing loads). NSF allows for the creation of complex geometries with a single deformation step, saving time and resources compared to multiple strikes and reheats in conventional forging [150,151].

Directional Solidification (DS) technology is a process in which a strong cooling source is applied to the bottom of a casting, creating a significant temperature gradient in a specific direction between the solidified metal and the molten metal [152–155]. This temperature gradient allows the molten metal to solidify in the direction opposite to the heat flow [156,157]. The controlled cooling rate during DS facilitates the formation of fine and uniform microstructures with improved mechanical properties of both strength and ductility [154,158,159].

According to the information provided above, in this chapter, our goal is to explore, through manufacturing methods, the possibility of achieving ductility by modifying the microstructure of the chemically optimized alloy from the previous chapter, LW- MEA  $\text{Al}_{60}\text{Zn}_{27}\text{Mg}_{11}\text{Si}_2 + \text{Sr}_{0.021}\text{Sb}_{0.001}$ , using various processing techniques. We begin with conventional solidification in a sand mold, followed by deformation using NSF technology. This method focuses on enhancing density by eliminating any porosities and defects that could occur during sand casting. Additionally, it aims to improve the microstructure of the alloy by disrupting the phases and dispersing them evenly within the matrix.

As an alternative method, we employ directional solidification to refine alloys previously sand-cast. The purpose of this technique is to obtain a dense material that, like NSF, effectively eliminates pores and defects. Additionally, due to the high solidification speed, directional solidification facilitates the development of a finer microstructure. Our goal is to evaluate the mechanical properties based on these three processing techniques. Through this evaluation, we seek to understand the impact of each method on the alloy's mechanical performance and determine the most effective approach to optimizing its properties, aiming for high strength and ductility in the alloys.

The following Fig. 6-1 provides a simplified schematic illustration of the contents of this chapter.

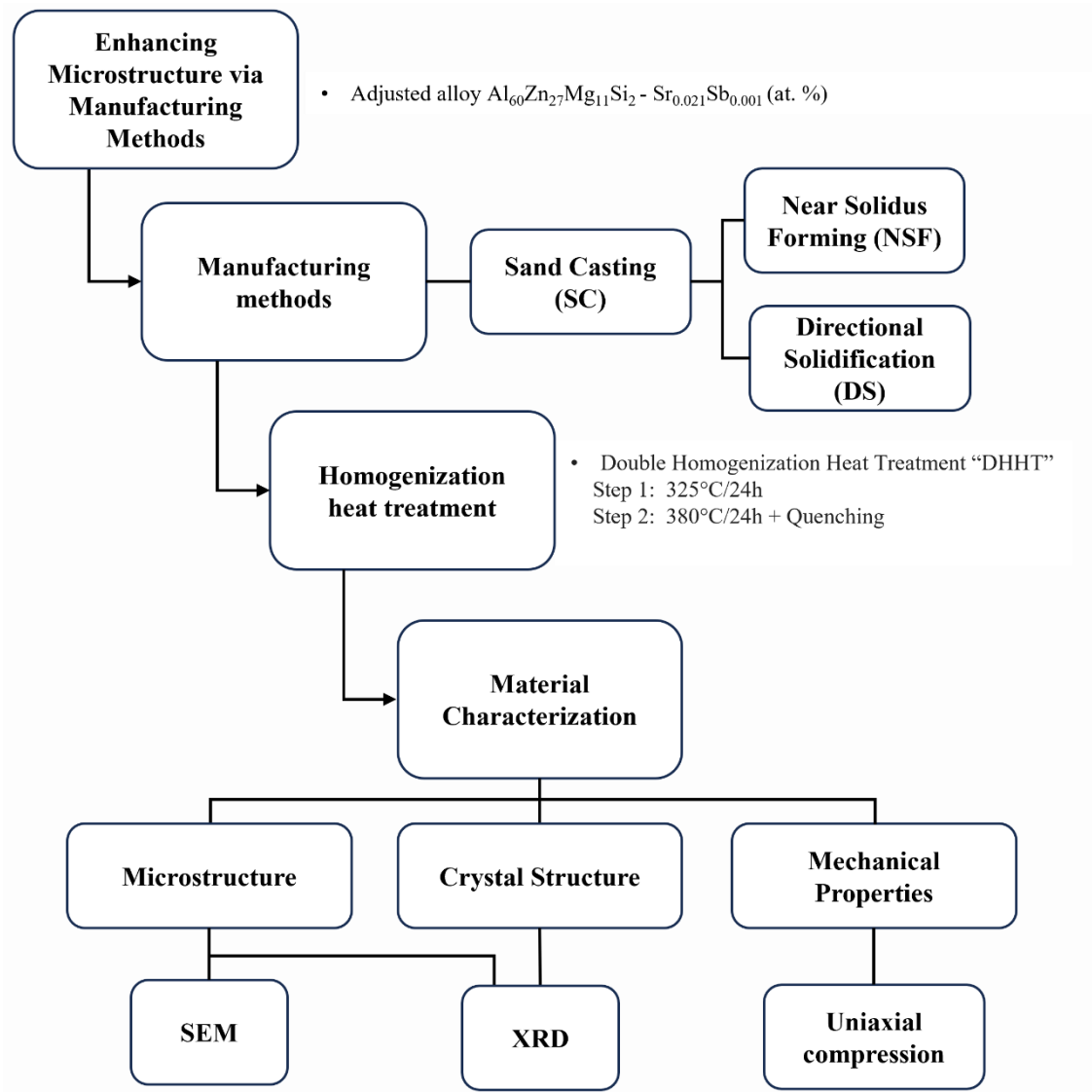


Fig. 6-1 Simplified outline of the contents of Chapter 6: “Microstructure improvement by LW-MEA fabrication methods”.

## 6.2. Results

### 6.2.1. Solidification rate in sand casting

As mentioned in Chapter 3, the filling and feeding system for the sand casting manufacturing method was designed using FLOW-3D CAST v5.1 software. Fig. 6-2 presents the thermophysical properties determined in situ for the optimized LW-MEA, which were then used as inputs for the computational simulation. The liquidus and solidus temperatures, latent heat of solidification, and specific heat were obtained through DSC analysis. The liquidus temperature was found to be 600°C, while the solidus temperature was estimated at 390°C using the tangent method based on data derived from DSC measurements. Additionally, the latent heat of solidification was determined to be 195.50 J/g. The

results of the sand-casting simulation indicated that the ingot cylinder was successfully filled without any defects.

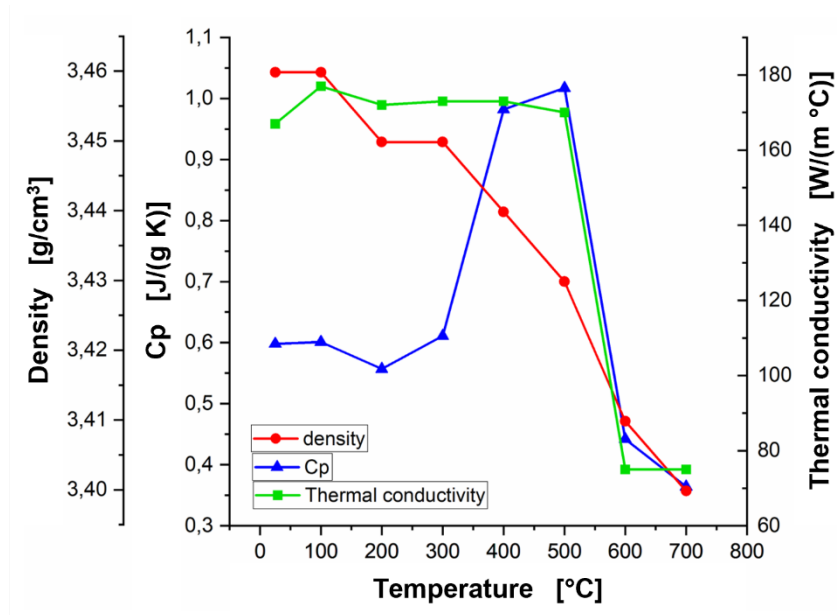


Fig. 6-2 Thermophysical properties of the optimized LW-MEA alloy.

The solidification rate was determined from the initial crystal formation to complete crystallization in the sand-casting method to serve as a reference point and to understand the microstructure and phases in an initial state. The cooling curves recorded by the thermocouples in different sections of the cylinder are illustrated in Fig. 6-3. To calculate the cooling rate (CR), the slope of the curves within the temperature range of 460 to 580°C was measured. The cooling rates for different zones are detailed in Table 6-1.

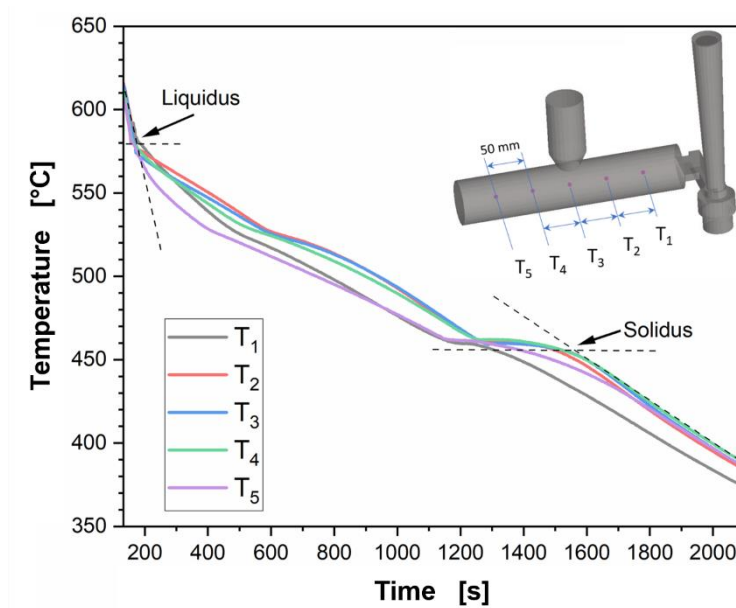


Fig. 6-3 Cooling curves obtained during the sand-casting process.

The cooling rate for thermocouples T<sub>2</sub>, T<sub>3</sub>, and T<sub>4</sub> was calculated at 0.09 °C/s, while the thermocouples located at the ends of the ingot cylinder exhibited a value of 0.11 °C/s. The overall average cooling rate is 0.10 °C/s, indicating a constant solidification rate along the entire cylinder. This value will be used as a reference point compared to the directional solidification process, where a significant increase in the cooling rate is expected, and thus, an effect on the microstructure.

Table 6-1 Average cooling rate during solidification

# Thermocouple	Cooling Rate (CR) °C/s
T <sub>1</sub>	0.11
T <sub>2</sub>	0.09
T <sub>3</sub>	0.09
T <sub>4</sub>	0.09
T <sub>5</sub>	0.11
T <sub>average</sub>	0.10

### 6.2.2. Component manufacturing by NSF

As mentioned in Chapter 3, FORGE NxT 3.0 was used to design dies that would provide uniform deformation across their entire section to break intermetallic phases and distribute them evenly throughout the samples, aiming to achieve ductility in the alloy. Four alloys were selected for finite element simulation due to the lack of available parameters to model the flow behavior of the designed lightweight medium entropy alloy. The chosen alloys were AlZn7, AlZn7.7Mg2.4Cu1.6, Al6061, and CuZn40Al2. It is important to emphasize that the objective of this section is to analyze the parameters that can qualitatively influence the NSF process, rather than obtaining quantitative results.

Additionally, this study aims to determine the angle that produces the most homogeneous deformation. To achieve this objective, 8 sensors were strategically placed along the specimen to record the average effective strain during the finite element simulation. These sensors were positioned in the central part of the cone-shaped specimen with a separation of 10 mm between them. The simulation results clearly indicate that the geometry of the extruded material has a more significant impact on the equivalent mean deformation along the specimens compared to the specific material used.

This observation is supported by the data presented in Table 6-2, which demonstrates minimal variation in the average effective equivalent deformation among the four different materials. As observed, deformations are higher in the specimen with a 45° entry angle, with an equivalent strain of 2.67. This is followed by the 20° angle, where the value is 2.34. Conversely, the 70° angle exhibits the lowest average equivalent strain, with a value of 2.18.

Table 6-2 The average equivalent strain of the NSF (Non-Steady State Flow) process for four different materials extruded in dies with different entry angles (20°/45°/70°).

Alloys	Average Equivalent Strain		
	20°	45°	70°
AlZn7	2.34	2.62	2.26
AlZn7.7Mg2.4Cu1.6	2.33	2.72	2.13
Al6061	2.43	2.68	2.18
CuZn40Al2	2.27	2.69	2.15
Average	2.34±0.06	2.67±0.04	2.18±0.05

In addition, the dies with a 45° angle generate the most uniform equivalent strain along the specimen, as illustrated in Fig. 6-4. Consequently, the die with this angle was selected for NSF testing.

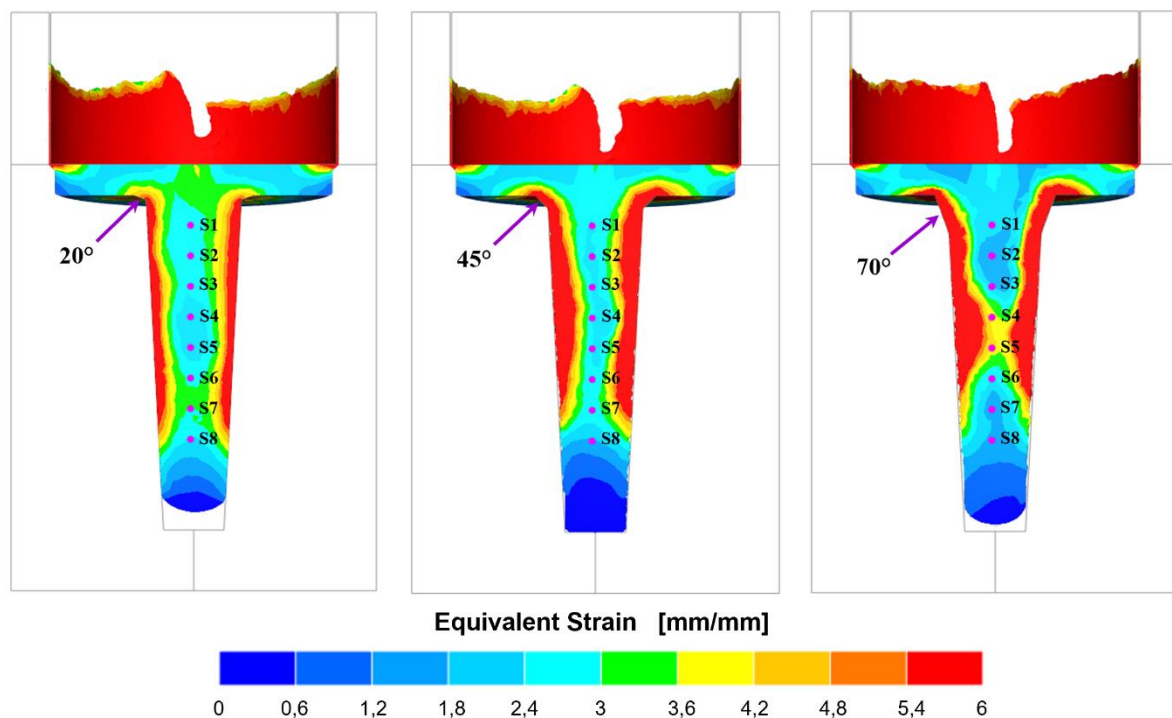


Fig. 6-4 Equivalent strain distribution along the specimens with different angles 20°/45°/70°.

Fig. 6-5 illustrates the distribution of equivalent strain along the cone specimen with an entry angle of 45° during the NSF test at various time points. During the NSF stage II, it is noticeable that the equivalent strain is concentrated at the 45° entry angle. As the punch continues its descent, the equivalent strain gradually increases at the edges of the dies, eventually reaching a maximum value of 6 mm/mm. It should be noted that the high equivalent strain is limited to the location of the S7



sensor. However, it is evident that the central part of the specimen exhibits a nearly uniform equivalent deformation, as observed in the final stage of filling VIII.

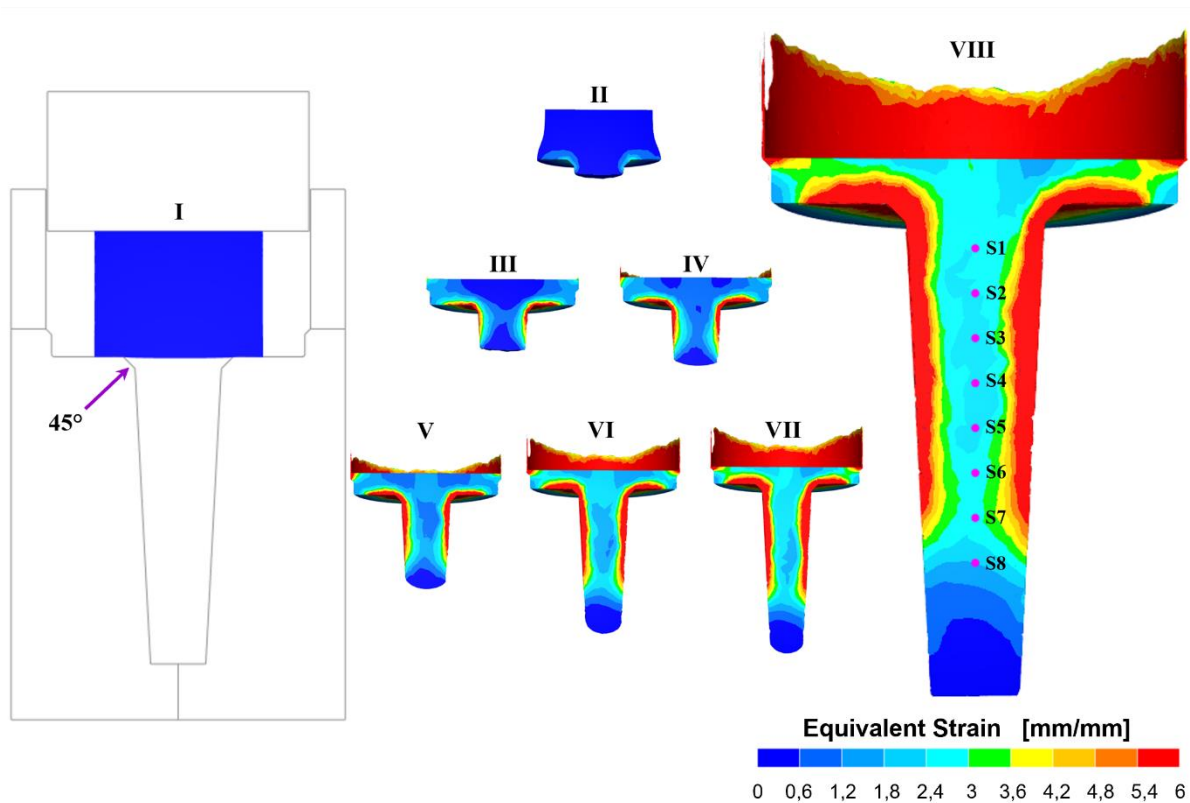


Fig. 6-5 The equivalent strain distribution along the specimen with a 45° angle during the NSF process at different times.

### 6.2.3. Solidification rate in directional solidification process

Finalmente el ultimo metodo de procesamiento es la solidificacion direccional, el cual fue propuesto con el objetivo de obtener una pieza densa, sin defectos y sobre todo y mas importante tener una modificacion en las fases presents es decir reducir el tamaño de las fases intermetalicas y distribuirlas por la matrix con el objetivo de no solo incrementar la Resistencia de la aleacion sino gana run poco de ductilidad, para ello se determino el cooling rate para ver el efecto que tiene en la microestructura.

The cooling curves recorded by the thermocouples in different sections of the cylinder are illustrated in Fig. 6-6. To calculate the cooling rate (CR), the slope of the curves within the temperature range of 510-590 °C was measured. The cooling rates for different zones are listed in Table 6-3.

Depending on the placement of the thermocouple, different cooling rates are achieved due to the thermal gradient created by the directional solidification equipment. This variability in the cooling rates allows for the obtaining of different microstructures. The highest cooling rate was observed for thermocouple T<sub>1</sub>, with a value of 8.26 °C/s. Thermocouple T<sub>2</sub> followed with a CR of 2.33 °C/s, representing a 3.5-fold reduction compared to thermocouple T<sub>1</sub>. As the steel crucible remained immersed in the bucket of water, the CR decreased for the following thermocouples. The last

thermocouple, T<sub>5</sub>, recorded a CR value of 0.71 °C/s, which is an 11.60-fold reduction compared to T<sub>1</sub>.

For this study, the microstructure of the zone between thermocouples T<sub>2</sub> and T<sub>3</sub>, which has a solidification range of (2.33 - 1.51 °C/s), was analysed. This zone was chosen because of its higher cooling rate and minimal variation within this range.

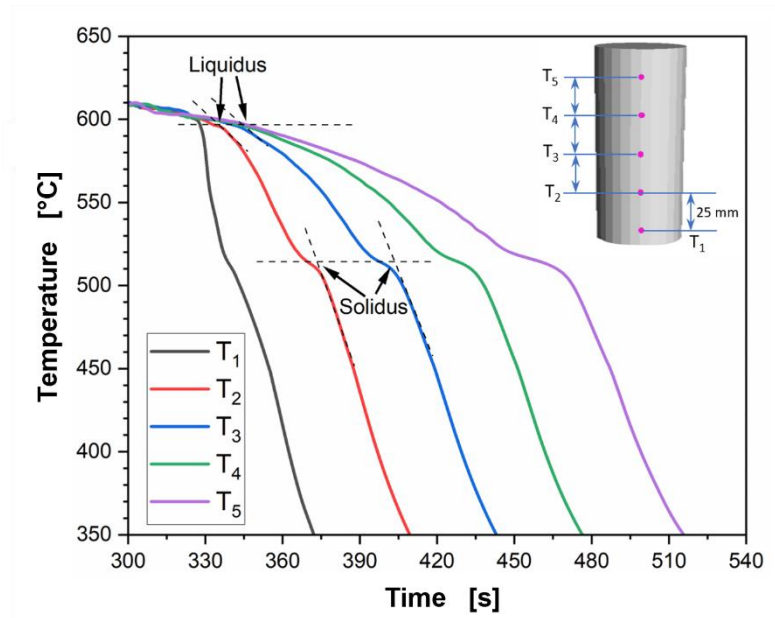


Fig. 6-6 Cooling curves obtained during the directional solidification process.

Table 6-3 Average cooling rate during the directional solidification.

# Thermocouple	Cooling Rate (CR)
	°C/s
T1	8.26
T2	2.33
T3	1.51
T4	0.98
T5	0.71

Finally, the last processing method is directional solidification, proposed with the aim of achieving a dense and defect-free piece. However, the most important aspect is the modification of existing

phases. This involves reducing the size of intermetallic phases and dispersing them within the matrix. The objective is not only to improve the strength of the alloy but also to seek ductility. To better understand this process, the cooling rate was determined, allowing us to observe its impact on the microstructure.

The cooling curves recorded by the thermocouples in different sections of the cylinder are illustrated in Fig. 6-7. To calculate the cooling rate (CR), the slope of the curves within the temperature range of 510-590 °C was measured. The cooling rates for different zones are listed in Table 6-4.

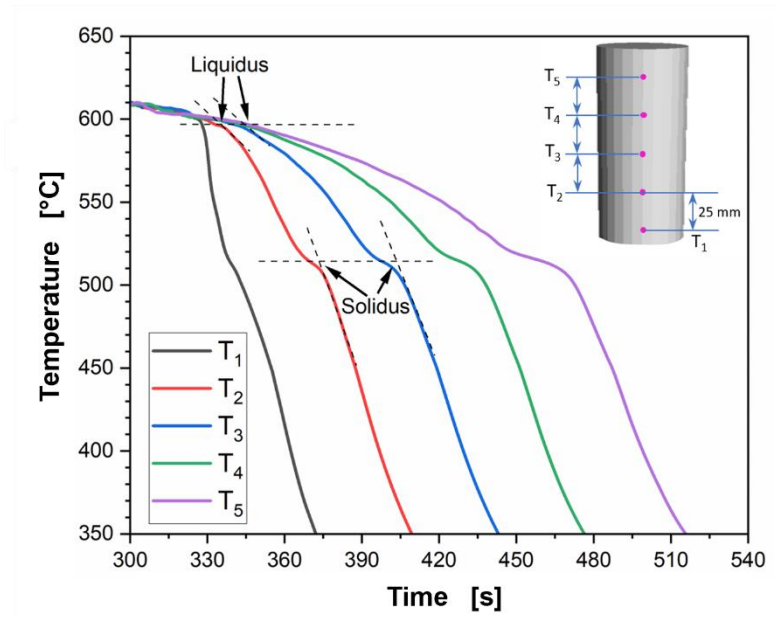


Fig. 6-7 Cooling curves obtained during the directional solidification process.

Depending on the placement of the thermocouple, different cooling rates are achieved due to the thermal gradient created by the directional solidification equipment. This variability in the cooling rates allows for the obtaining of different microstructures. The highest cooling rate was observed for thermocouple  $T_1$ , with a value of 8.26 °C/s. Thermocouple  $T_2$  followed with a CR of 2.33 °C/s, representing a 3.5-fold reduction compared to thermocouple  $T_1$ . As the steel crucible remained immersed in the bucket of water, the CR decreased for the following thermocouples. The last thermocouple,  $T_5$ , recorded a CR value of 0.71 °C/s, which is an 11.60-fold reduction compared to  $T_1$ .

For this study, the microstructure of the zone between thermocouples  $T_2$  and  $T_3$ , which has a solidification range of (2.33 - 1.51 °C/s), was analysed. This zone was chosen because of its higher cooling rate and minimal variation within this range.

Table 6-4 Average cooling rate during the directional solidification.

# Thermocouple	Cooling Rate (CR)
	°C/s
T1	8.26
T2	2.33
T3	1.51
T4	0.98
T5	0.71

#### 6.2.4. Microstructural examination

The microstructures of the optimized  $\text{Al}_{60}\text{Zn}_{27}\text{Mg}_{11}\text{Si}_2 + \text{Sr}_{0.021}\text{Sb}_{0.001}$  alloy, obtained through different fabrication processes, are depicted in Fig. 6-8. The figures show both the as-cast state and the microstructures after heat treatment. The heat treatment consisted of a double homogenization (DHHT) in an argon atmosphere followed by quenching in water, as specified in Table 5-3 of Chapter 5.

Fig. 6-8a presents a backscattered electron image of the sand-cast sample in its as-cast condition. It reveals a complex microstructure consisting of dendritic, eutectic, and interdendritic zones with varying contrasts. The dendritic phase corresponds to the face-centered cubic (FCC) phase of aluminum (Al), while the interdendritic zone corresponds to the phase ( $\text{MgZn}_2$ ). The eutectic phase ( $\text{Al} + \text{Mg}_2\text{Si}$ ) appears as a black region, where the gray zone represents the (Al) phase, and darker zones correspond to the ( $\text{Mg}_2\text{Si}$ ) phase. Additionally, brighter regions indicate the presence of heavier elements, such as the zinc (Zn) phase.

In Fig. 6-8b, the microstructure of the alloy after being heat treated in a sand mold is shown. The FCC matrix appears cleaner with fewer precipitates compared to Fig. 6-8a. The Laves ( $\text{MgZn}_2$ ) phase is more grouped and exhibits a more rounded morphology, similar to the ( $\text{Mg}_2\text{Si}$ ) phase. While the observed phases remain consistent in other microstructures, their morphology and size vary depending on the specific manufacturing process employed.

Fig. 6-8c and Fig. 6-8d depict micrographs of samples remelted and solidified through the directional solidification process. Fig. 6-8c displays a fine and homogeneous microstructure with well-distributed phases, although some segregation can be observed. However, after undergoing solution treatment, the segregation is eliminated, resulting in a cleaner microstructure, as shown in Fig. 6-8d.

Micrographs Fig. 6-8e and Fig. 6-8f correspond to specimens formed through the Near Solidus Forming process. Fig. 6-8e displays a deformed microstructure, indicating that the NSF process has caused the breaking of the ( $\text{MgZn}_2$ ) and ( $\text{Mg}_2\text{Si}$ ) phases, dispersing them throughout the matrix. Moreover, the microstructure appears torn in the direction of the applied load. After heat treatment

of the deformed NSF specimens, Fig. 6-8f demonstrates that the Laves ( $MgZn_2$ ) phases and the ( $Mg_2Si$ ) phase have become more rounded, and traces of plastic deformation have been eliminated. In addition, good surface quality was found in the NSF samples.

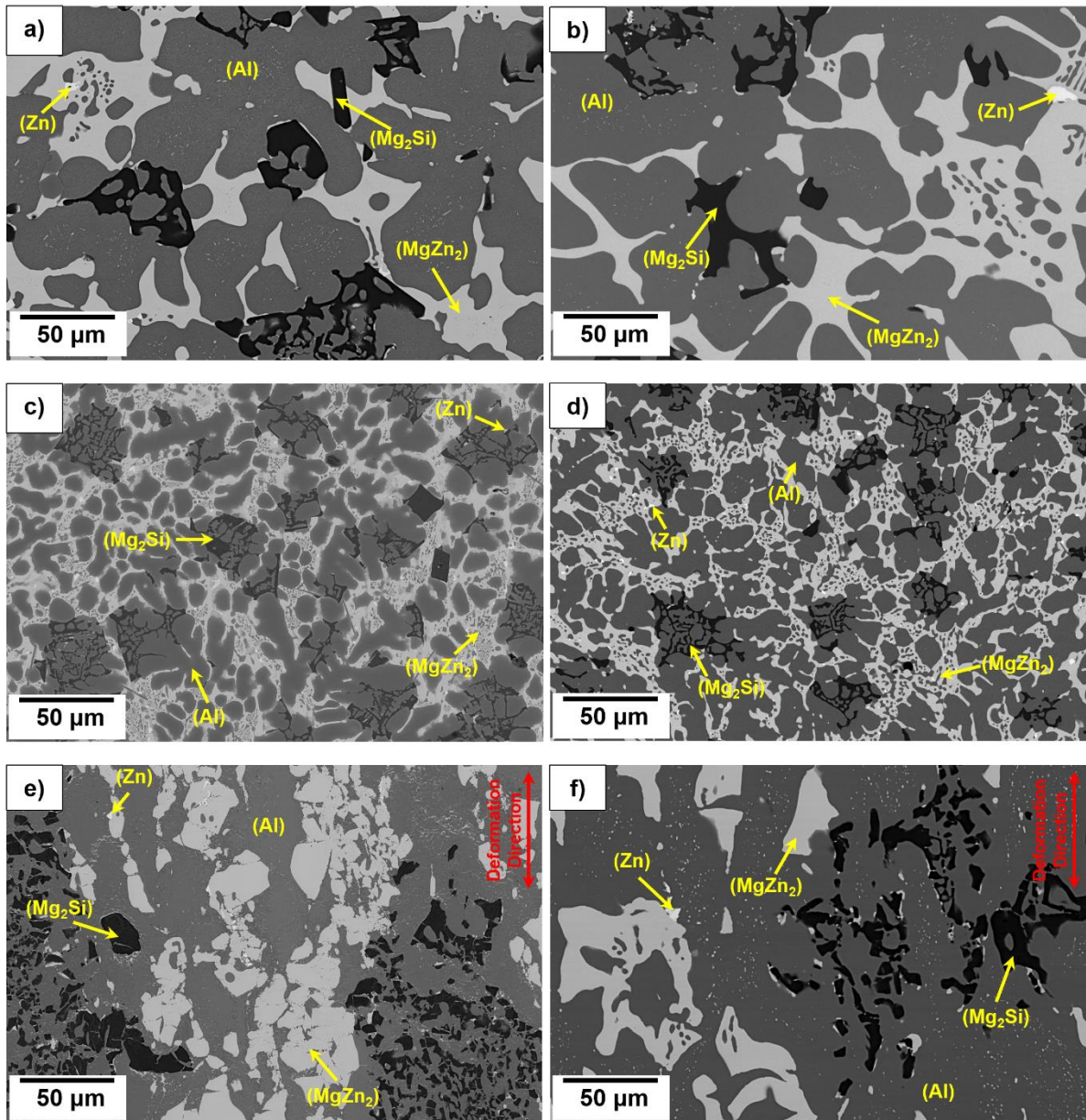


Fig. 6-8 SEM of the  $Al_{60}Zn_{27}Mg_{11}Si_2 + Sr_{0.021}Sb_{0.001}$  LW-MEA in condition: a) "Sand Casting As-Cast", b) "Sand Casting DHHT", c) "Directional Solidification As-Cast", d) "Directional Solidification DHHT", e) "Near Solidus Forming As-Cast", f) "Near Solidus Forming DHHT".

### 6.2.5. XRD analysis of the optimized LW-MEA

To confirm the CALPHAD predicted phases of the optimized  $Al_{60}Zn_{27}Mg_{11}Si_2 + Sr_{0.021}Sb_{0.001}$  alloy from the previous chapter. XRD analysis was performed. It should be noted that the chemical composition is consistent across all Sand-Casting, NSF, and DS samples.



For instance, the XRD results for the DS samples in both its as-cast and heat-treated states are displayed in Fig. 6-9. In the XRD patterns of the fused DS alloy, numerous reflection peaks were successfully matched to the following phases: (Al) (PDF: 00-004-0787), (MgZn<sub>2</sub>) Laves (PDF: 04-003-2083), (Mg<sub>2</sub>Si) (PDF: 01-083-5235), and (Zn) (PDF: 01-078-9363). The phases identified by XRD in the as-cast state align with those predicted by CALPHAD during Scheil solidification, as depicted in Chapter 5, Fig. 5-3b.

In the heat-treated sample, the diffraction patterns no longer detect the presence of the (Zn) phase. This hexagonal close-packed phase (HCP) dissolves into the aluminum matrix (FCC) following the dissolution treatment.

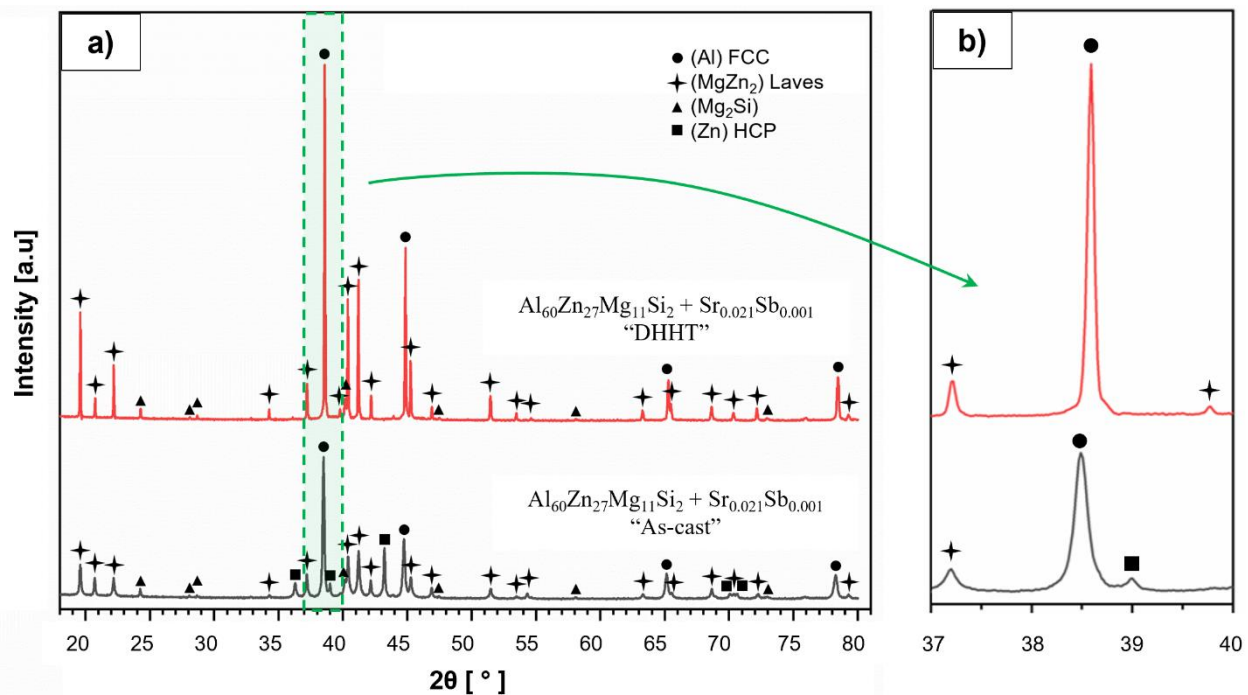


Fig. 6-9 XRD diffraction patterns for the  $\text{Al}_{60}\text{Zn}_{27}\text{Mg}_{11}\text{Si}_2 + \text{Sr}_{0.021}\text{Sb}_{0.001}$  LW-MEA: a) before and after heat treatment “as-cast” and “DHHT” (Double Homogenization Heat Treatment); comparison of the FCC peak of as-cast and solutionized sample.

#### 6.2.6. Compression properties

The true stress versus true strain curves obtained from compression tests are presented in Fig. 6-10. The compression mechanical properties of the alloys are compared in Table 6-5.

Fig. 6-10a displays the curves of the optimized multicomponent alloy after undergoing various manufacturing processes: Sand Casting, Near Solidus Forming, and Directional Solidification. It is evident that the DS process demonstrates the highest compressive strength, measuring 658 MPa. The NSF-processed alloy follows with a compressive strength of 552 MPa, while the alloy manufactured by sand casting exhibits a strength of 471 MPa.

Fig. 6-10b illustrates the heat-treated alloys. The directionally solidified alloy, when subjected to the solubilizing treatment, shows an increase in compressive strength with a value of 769 MPa. Following closely is the alloy formed through the NSF process, combined with the solubilizing treatment, showing a compressive strength value of 679 MPa. Lastly, the alloy produced via the sand-casting process, accompanied by the solubilizing treatment, demonstrates a strength value of 647 MPa.

Significant improvements in strength are observed after the heat treatment of the alloys. The sand-cast alloys experience an approximate 38% increase in strength following the heat treatment. In the case of NSF-processed alloys, there is a 23% increase in strength after the solubilizing treatment. On the other hand, the directionally solidified alloys exhibit the smallest increase in strength after heat treatment, with a value of 17%.

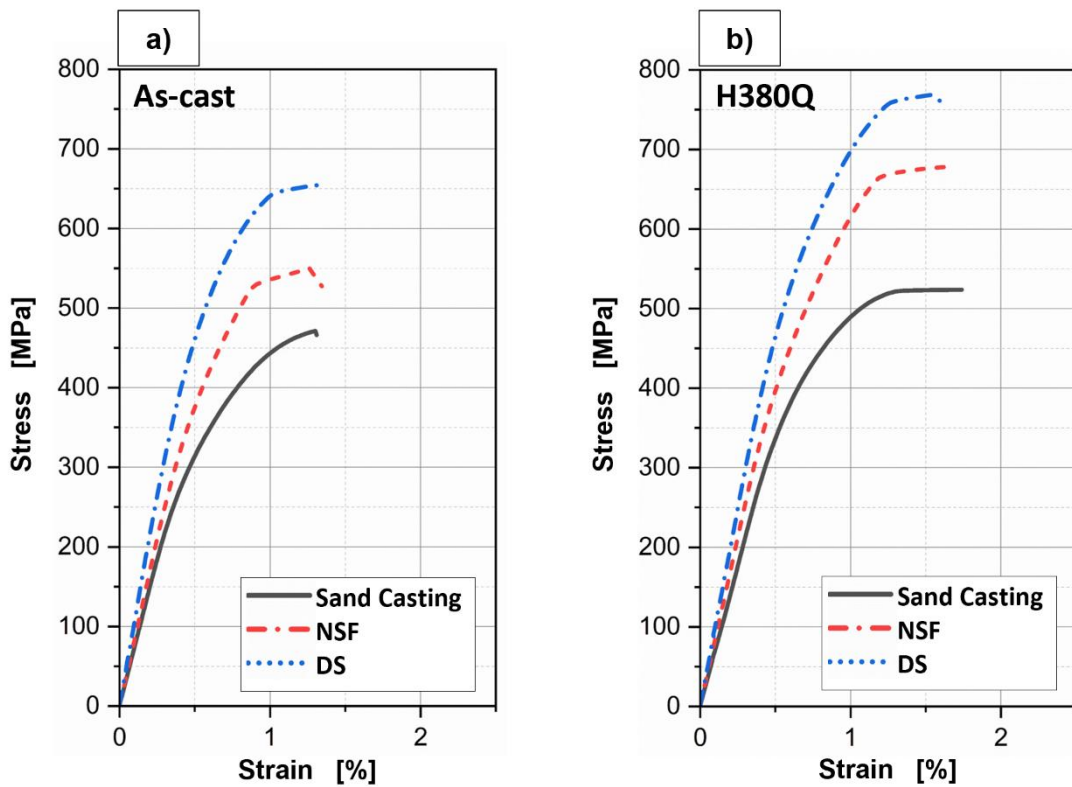


Fig. 6-10 Stress-strain curves in uniaxial compression: a) Non-heat treated alloys processed by Sand Casting, Directional Solidification, and Near Solidus Forming; b) Heat treated alloys processed by Sand Casting, Directional Solidification, and Near Solidus Forming.



Table 6-5 Compression mechanical properties of the  $\text{Al}_{60}\text{Zn}_{27}\text{Mg}_{11}\text{Si}_2 + \text{Sr}_{0.021}\text{Sb}_{0.001}$  LW-MEA at ambient temperature.

State	Alloy	Yield strength (MPa)	Ultimate strength (MPa)
As-cast	Sand Casting	306±5	471±10
	NSF	366±3	552±9
	Directional Solidification	497±5	658±6
H380Q	Sand Casting	402±7	523±8
	NSF	426±2	679±5
	Directional Solidification	548±3	769±5

### 6.2.7. Fractographic observations

Figures (Fig. 6-11, Fig. 6-12, and Fig. 6-13) illustrate the compression fracture surfaces of the optimized  $\text{Al}_{60}\text{Zn}_{27}\text{Mg}_{11}\text{Si}_2 + \text{Sr}_{0.021}\text{Sb}_{0.001}$  LW-MEA, which underwent processing through sand casting, NSF, and DS, with and without heat treatment. In all three figures, a consistent fracture pattern emerges, regardless of the processing methods applied.

This pattern involves crack initiation and propagation predominantly within the interdendritic space, primarily attributed to the Laves ( $\text{MgZn}_2$ ) phase. In certain micrographs, these cracks extend to connect with the ( $\text{Mg}_2\text{Si}$ ) phase. However, there is no discernible evidence of plastic deformation or any connection between the crack and the (Al) FCC phase. The (Al) FCC matrix remains intact in these cases, effectively arresting the progression of the cracks.

Fractography analysis reveals a brittle cleavage fracture. For example, the micrograph in the Fig. 6-11b displays a fracture surface characterized by a complex arrangement of bright and reflective cleavage facets. Upon examination, the fracture surface shows no indications of plastic deformation, mechanical damage, or contamination. The hexagonal C14 structure of the Laves phase  $\text{MgZn}_2$  plays a crucial role in strengthening Mg-Zn alloys. However, its application is limited due to the challenges posed by low ductility and brittle fracture at room temperature. These characteristics arise from the complex atomic configuration, interplanar locking, and the absence of active slip systems at ambient temperatures [160–162].

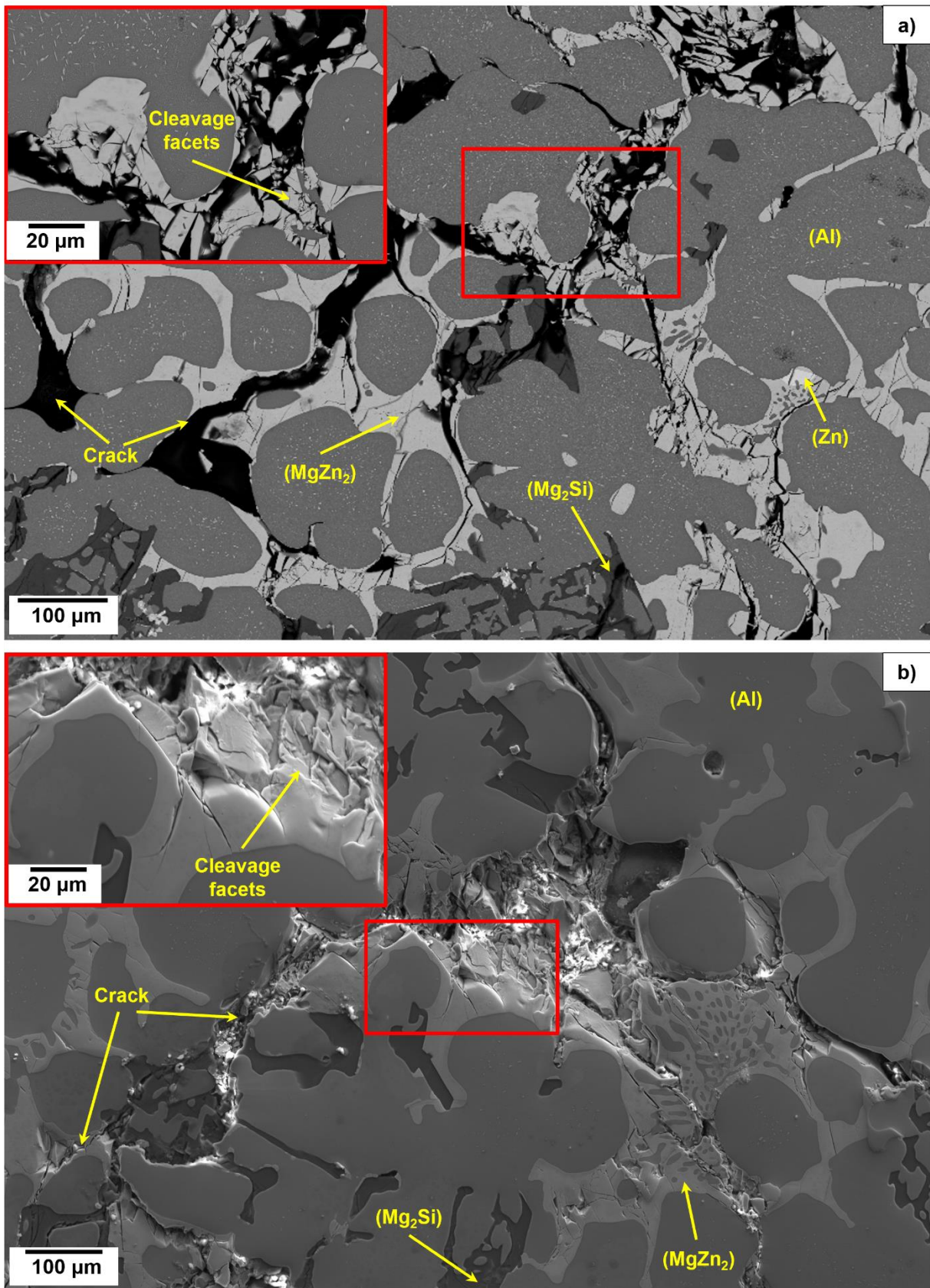


Fig. 6-11 Fracture surfaces of the  $\text{Al}_{60}\text{Zn}_{27}\text{Mg}_{11}\text{Si}_2 + \text{Sr}_{0.021}\text{Sb}_{0.001}$  LW-MEA under the following conditions: a) Sand casting “As-cast”, and b) Sand casting “Heat-treated” (Cleavage crack initiated in Laves phase  $\text{MgZn}_2$ ).



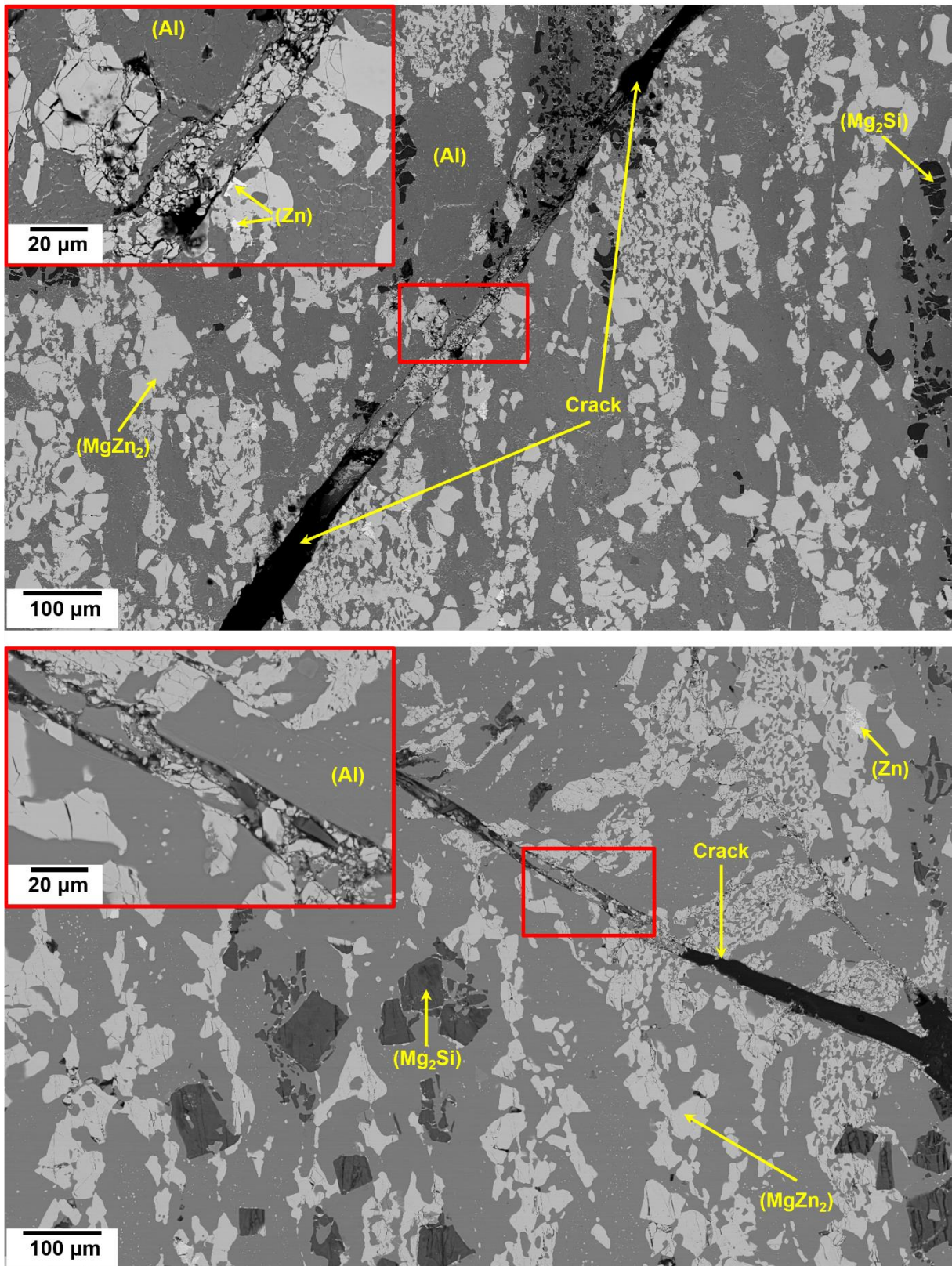


Fig. 6-12 Fracture surfaces of the  $\text{Al}_{60}\text{Zn}_{27}\text{Mg}_{11}\text{Si}_2 + \text{Sr}_{0.021}\text{Sb}_{0.001}$  LW-MEA under the following conditions: a) NSF “As-cast”, and b) NSF “Heat-treated”.



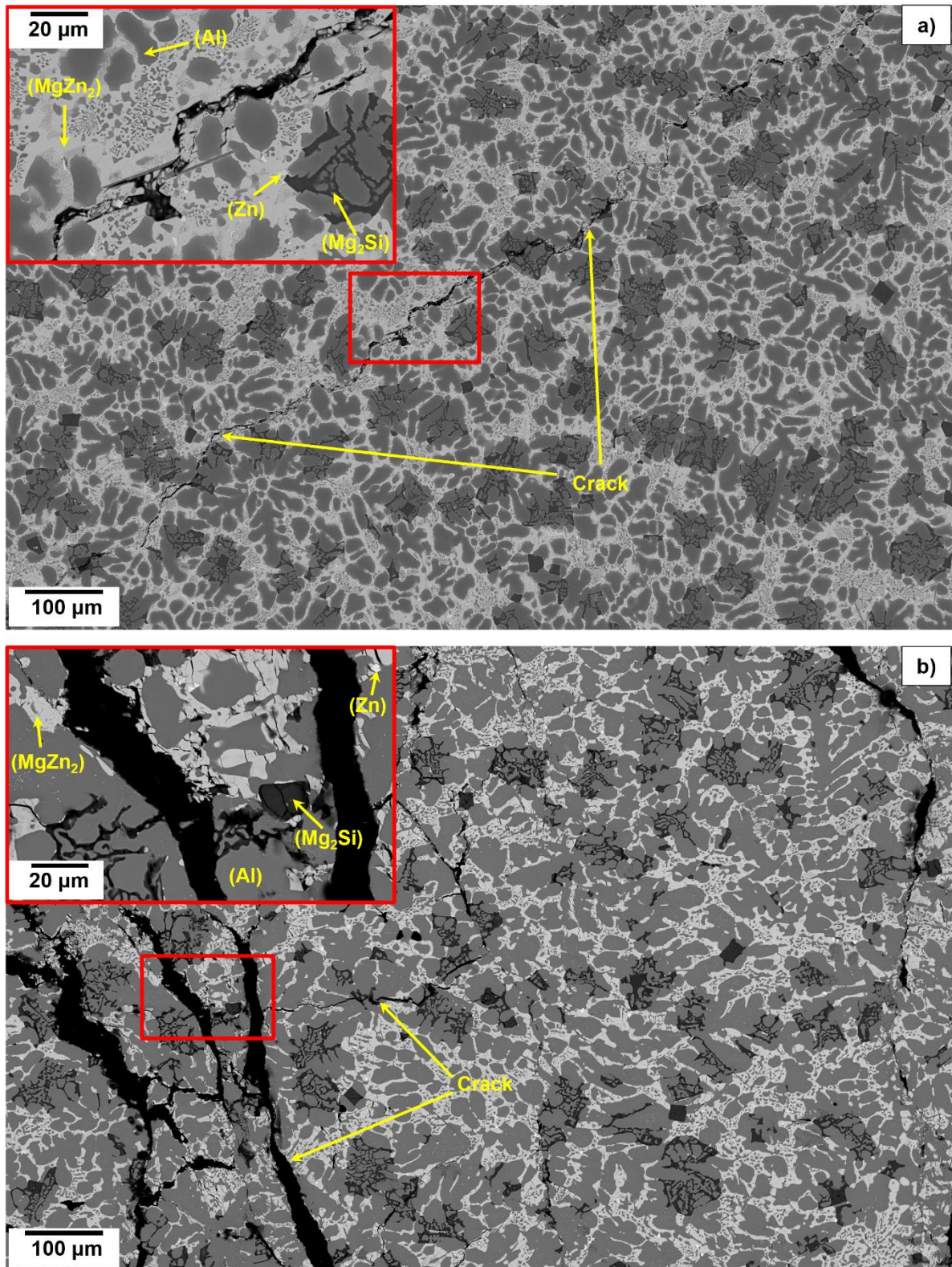


Fig. 6-13 Fracture surfaces of the  $\text{Al}_{60}\text{Zn}_{27}\text{Mg}_{11}\text{Si}_2 + \text{Sr}_{0.021}\text{Sb}_{0.001}$  LW-MEA under the following conditions: a) DS "As-cast", and b) DS "Heat-treated".

## 6.3. Discussion

### 6.3.1. Effect of different manufacturing processes on LW-MEA.

The effect of different manufacturing processes on the microstructure and mechanical compression properties of the  $\text{Al}_{60}\text{Zn}_{27}\text{Mg}_{11}\text{Si}_2 + \text{Sr}_{0.021}\text{Sb}_{0.001}$  LW-MEA has been investigated. The manufacturing processes of sand casting, directional solidification and Near Solidus formation were studied.

Different manufacturing processes lead to variations in phase size, phase distribution, and alloy morphology, as observed through microstructure analysis. The directional solidification process, for instance, produces a fine microstructure with a homogeneous distribution of phases. The higher cooling rate during solidification results in the formation of a finer lamellar-dendritic structure. The lamellar interface is considered an effective barrier to the motion of dislocations, leading to the accumulation of dislocations on slip planes at the lamellar interface [163,164]. Due to the reduced mean free path of dislocations in the material, the directional solidification  $\text{Al}_{60}\text{Zn}_{27}\text{Mg}_{11}\text{Si}_2$  alloy with a refined lamellar structure exhibits the highest yield strength of 650 MPa.

In the NSF process, the microstructure of the samples is finer compared to sand casting, resulting in a unique structure Fig. 6-8. This is achieved through specific process conditions, such as high shear during alloy flow, rapid cooling, pressure applied during solidification, and the consequent formation of a strong non-equilibrium state of the material [150,151,165]. The careful selection of parameters ensures that the NSF mold is defect-free, with complete filling of the metal in the mold cavity and absence of microporosity. The observed increase in yield strength of 540 MPa in the alloys processed by near solidus forming, compared to sand-cast alloys with a yield strength of 450 MPa, can be attributed to the fracture and dispersion of  $(\text{Mg}_2\text{Si})$  phases, particularly the Laves phase  $(\text{MgZn}_2)$ , during the NSF process. By disrupting the continuity of the Laves phase, crack propagation is hindered, and it gets arrested within the FCC aluminum matrix or the  $(\text{Mg}_2\text{Si})$  intermetallic phase until it encounters a critical resolved shear stress (CRSS) value. These findings highlight the importance of process selection in achieving the desired material characteristics for specific applications.

### 6.3.2. Effect of the heat treatment on LW-MEA.

Fig. 6-8 illustrates the microstructure of the  $\text{Al}_{60}\text{Zn}_{27}\text{Mg}_{11}\text{Si}_2 + \text{Sr}_{0.021}\text{Sb}_{0.001}$  LW-MEA processed using three different methods: sand mold, directional solidification, and near solidus forming. The microstructures are shown both before and after undergoing solution treatment. It is evident that segregation has been eliminated in all the microstructures, and the intermetallic phases  $(\text{Mg}_2\text{Si})$  and  $(\text{MgZn}_2)$  have become rounded, regardless of the processing method, following solubilization treatment.

The XRD patterns in Fig. 6-9a reveal that the  $(\text{Zn})$  phase, which was detected as a precipitate in the as-cast sample, was completely dissolved into the FCC matrix after solution treatment. Consequently, the FCC lattice size increased due to the dissolution of Mg, Si, and Zn into the matrix. Additionally, the coherence between the sizes of adjacent FCC lattices improved throughout the structure. This conclusion was inferred from the XRD results shown in Fig. 6-9b, where the two FCC peaks merged into a broadened peak after solution treatment, indicating an increase in FCC lattice size coherency.

This increase in FCC lattice size coherency, or coherency strain, is believed to minimize lattice misfit and enhance mechanical properties [166,167].

After undergoing heat treatment, the sand-casting alloy exhibited a significant increase in compressive strength, reaching 647 MPa, while the directional solidification alloy displayed an increase to 769 MPa. Similarly, the near solidus forming alloy achieved a compressive strength of 679 MPa. This remarkable enhancement in strength was accomplished through the process of solution treatment, involving the dissolution and dispersion of an alloying element into the (Al) FCC matrix. This resulted in the generation of a solid solution-strengthening mechanism [145,166,168].

#### 6.4. Conclusions

In this study, the optimized  $\text{Al}_{60}\text{Zn}_{27}\text{Mg}_{11}\text{Si}_2 + \text{Sr}_{0.021}\text{Sb}_{0.001}$  LW-MEA was produced using three different processes: sand casting, directional solidification, and near solidus forming. The effects of these processing methods on the microstructure and mechanical properties of the alloy were evaluated under uniaxial compression, both before and after heat treatment. Based on the obtained results, the following conclusions can be drawn.

- The increased cooling rate during directional solidification leads to the formation of a finer lamellar dendritic structure. This manufacturing process results in the alloy exhibiting the highest yield strength among the three processes studied, with a value of 658 MPa before heat treatment and 769 MPa after solution treatment.
- The near solidus forming process enables the improvement of mechanical properties by inducing effective deformation throughout the specimen, resulting in the breaking and distribution of phases throughout the entire matrix. An approximate 17% increase in compressive strength is achieved compared to sand-casting alloys without heat treatment, and a 5% increase in compressive strength is observed with solution treatment. However, ductility remains at zero.
- The heat treatment induces significant changes in the structure and mechanical properties of the alloy. By eliminating segregation, rounding off intermetallic phases, and dissolving (Zn) into the matrix, it leads to an increase in compression strength due to solid solution strengthening.
- The Laves ( $\text{MgZn}_2$ ) phase is responsible for crack nucleation and growth in the optimized multicomponent lightweight alloy. It is necessary to either eliminate the precipitation of this phase or modify its morphology to enhance the mechanical properties of the alloy.



# Chapter 7

## 7. Conclusions and Future Work

*In this concluding chapter, we thoroughly examine the key findings derived from the current research project, aligning them with the goals established in Chapter 1. Building on these conclusions, we propose potential paths for advancing the work presented in this study.*

### 7.1. General Conclusions

The main objective of this doctoral thesis was to design a lightweight alloy by applying the concept of high-entropy alloys for its development and to explore in depth the nature of this alloy, with a central focus on achieving ductility. The research focused on three main lines.

-Firstly, designs were conducted by selecting elements compatible with each other with the primary goal of maximizing the percentage of solid solution (FCC) and minimizing the presence of intermetallic phases that could increase the strength of the alloy. The resulting alloy from this methodology was  $\text{Al}_{58}\text{Zn}_{28}\text{Mg}_6\text{Si}_8$ , designed using empirical parameters and the CALPHAD tool to anticipate solid solution formation and predict phases that would precipitate during solidification. CALPHAD played a predominant role in this process. A comprehensive study of the first alloy was carried out to understand its nature, limiting the characterization to microstructural aspects due to laboratory-scale manufacturing constraints that prevented exhaustive mechanical tests, such as compression tests. However, a microindentation analysis was performed. The results of experimental tests and the use of CALPHAD enabled the establishment of a solidification scheme, identification of seven phase transformations, and design of heat treatments, providing a comprehensive view of the microstructural phases. The collaboration between CALPHAD methodology and experimental techniques proved successful in predicting and validating microstructures in medium-entropy alloys, as well as in designing an effective heat treatment that increased compression strength through solid solution strengthening.

-The second line of research originated from the designed medium-entropy alloy. Understanding its phase transformations led to addressing two crucial aspects: eliminating the precipitation of the (Si) phase, known for its negative impact on mechanical properties, and modifying the morphology of the intermetallic ( $\text{Mg}_2\text{Si}$ ) in the alloy by adding Sr and Sb, along with heat treatments. These changes were made with the aim of eliminating the hard and brittle phases observed in the microstructures, which could negatively affect mechanical properties, especially ductility.

We decided to continue exploring this alloy system, conserving the previously selected alloy elements, and focusing on optimizing the alloy. This approach involved reducing the amount of Si in the alloy and balancing its composition to preserve the high percentage of solid solution. To carry out this stage, we used CALPHAD to optimize the alloy composition. Larger quantities of the alloy were manufactured to produce uniaxial compression specimens and evaluate their mechanical properties.



The results of this systematic optimization led to the refined composition  $\text{Al}_{60}\text{Zn}_{27}\text{Mg}_{11}\text{Si}_2$ , eliminating the precipitation of primary silicon and maintaining a solid solution with a high aluminum content. The addition of Sr and Sb transformed the structure of the eutectic phase ( $\text{Mg}_2\text{Si}$ ), adopting a distinctive fishbone and compact morphology. Controlled additions of Sr and Sb were observed to improve compression strength, demonstrating an increase in toughness. However, with higher Sr and Sb content, a decrease in strength was experienced due to the presence of large particles of the intermetallic ( $\text{SrZn}_{13}$ ) with a feather-like morphology. Despite these efforts, the alloys designed at this stage exhibited no ductility.

-Finally, the last line of development in this research aimed to maintain the system  $\text{Al}_{60}\text{Zn}_{27}\text{Mg}_{11}\text{Si}_2+\text{Sr}_{0.021}\text{Sb}_{0.001}$ , using the compositionally optimized alloy studied in the previous line as a base. Two different manufacturing methods were chosen to modify the microstructural phases of these alloys and evaluate their behavior with the aim of achieving ductility through these means. Among the selected methods, near-solidus forming technology and directional solidification were opted for.

The results of this task revealed that the increase in cooling rate during directional solidification led to the formation of a finer lamellar dendritic structure. This manufacturing process resulted in the alloy exhibiting the highest tensile strength among the three studied processes, with a value of 658 MPa before heat treatment and 769 MPa after solution treatment. Meanwhile, near-solidus forming technology improved mechanical properties by inducing effective deformation throughout the sample, resulting in fracture and phase distribution throughout the matrix.

An approximate 17% increase in compression strength was achieved compared to sand-cast alloys without heat treatment, and a 5% increase in compression strength was observed with solution treatment. However, once again, while tensile mechanical properties were improved through these two manufacturing methods, the manufactured alloys showed no ductility. Additionally, a fractographic analysis of alloys manufactured by different methods was performed, revealing that the Laves phase ( $\text{MgZn}_2$ ) was responsible for nucleating and growing cracks in the optimized LW-MEA. Therefore, it is necessary to eliminate the precipitation of this phase or modify its morphology to improve the mechanical properties of the alloy (ductility). In other words, although this alloy does not exhibit ductility, its exceptional strength suggests potential applications in wear resistance or other properties that should be further explored.

In the following Fig. 7-1, the designed and optimized alloy has been graphically represented based on its density and compressive strength. The other alloys presented correspond to those detailed in the Table 2-5 from the Literature Review chapter, where only alloys evaluated through uniaxial compression were included.

When examining the figure, it is noteworthy that the designed alloy occupies the region where alloys developed using the concept of lightweight high entropy alloy are located. It is evident that this alloy shares this space with other alloys based on magnesium or aluminum. It is worth mentioning that, within the density range of 4.5 to 5.5, indicated on the x-axis, no alloy following the high-entropy concept has been identified so far. Therefore, it would be interesting to investigate and explore this zone in future studies.

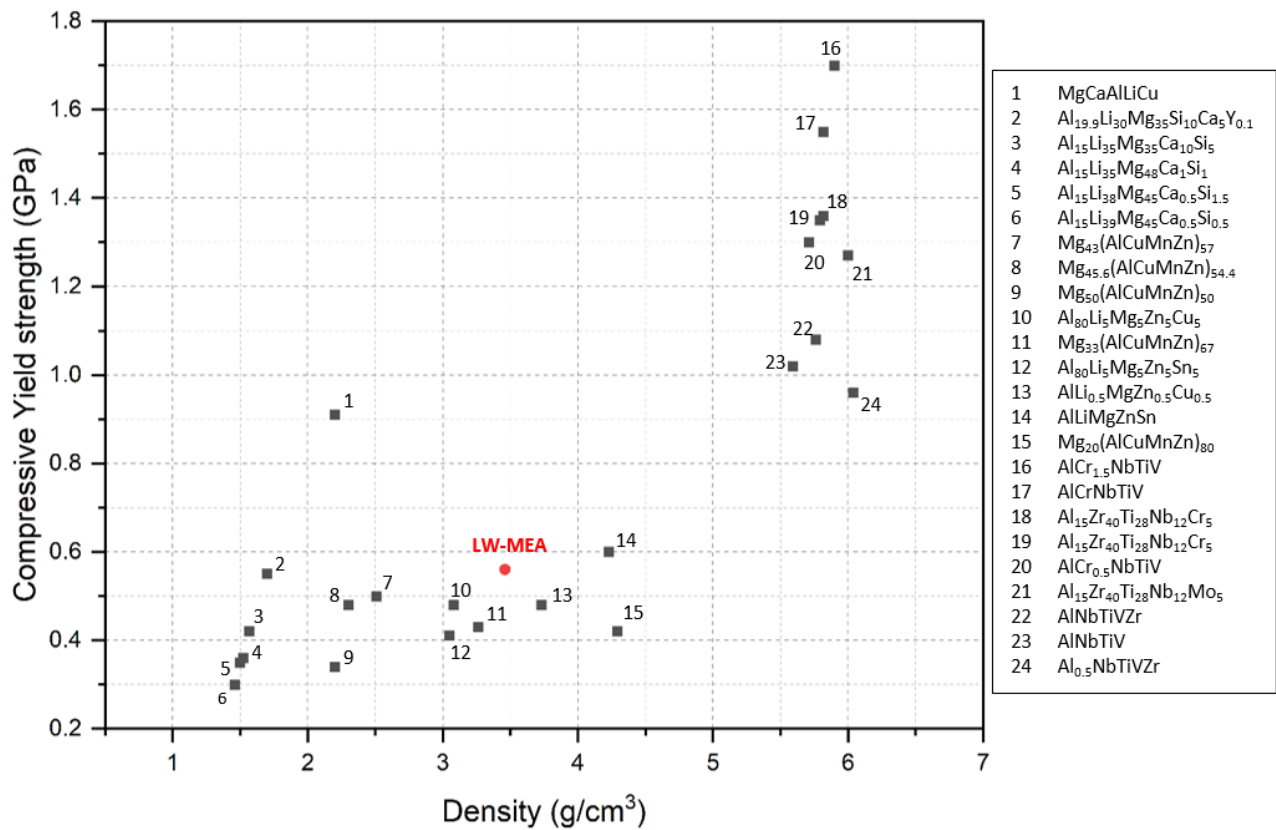


Fig. 7-1 Compressive yield strength vs Density of light alloys designed using the high entropy concept.

## 7.2. Future work

This research has provided a comprehensive and detailed understanding of the nature of the developed medium-entropy alloy. It is important to note that, while the developed alloy exhibits high compressive strength, it lacks ductility. Therefore, its suitability for applications in other fields should be explored. However, further research is recommended to address the raised issues comprehensively, with the aim of advancing the design of new alloys based on the high-entropy concept. This can be accomplished by utilizing empirical parameters and numerical methodologies like CALPHAD. The primary focus of this scientific advancement is to develop alloys with significant industrial applications.

Expanding on the previously mentioned points, proposals for exploring applications for the developed LW-MEA have been put forward, including:

- **Wear-Resistant Coatings:** LW-HEAs, with their combination of low density and high hardness, could be applied as protective coatings on components experiencing wear, such as industrial tools, bearings, and machinery parts.
- **Cutting and Drilling Tools:** Application in cutting tools, drills, and other drilling tools where wear resistance and durability are essential to maintain efficient performance over time.

- Components for Abrasive Environments: Use in components operating in abrasive environments, such as parts of mining equipment, mills, and crushers, to withstand wear caused by hard particles.
- Oil and Gas Industry: Utilization in coatings and components for drilling equipment and tools used in challenging and corrosive drilling conditions.

Furthermore, it is proposed to continue the study of this alloy, as it would be interesting to explore ways to modify the Laves phase ( $MgZn_2$ ) due to its brittle nature and investigate if this modification can lead to ductility in the alloy.

Also, it has been suggested to assess the combined impact of directional solidification and the near solidus forming process. In other words, investigate the effects of the directional solidification process, followed by post-processing using near solidus forming technology, on the microstructure and mechanical performance of the designed alloys.

These future research directions aim to broaden the scope of practical applications for the developed alloy and address potential limitations identified during the current research.

### 7.3. Publications and conferences

Trujillo-Tadeo JJ, Arruebarrena G, Dorantes-Rosales HJ, Bilbao Y, Vicario I, Guraya T, Hurtado I. Design and characterization of a novel lightweight multicomponent alloy  $Al_{58}Zn_{28}Mg_6Si_8$ . *Journal of Materials Research and Technology* 2023. <https://doi.org/10.1016/j.jmrt.2023.10.102>

Bilbao Y, Trujillo JJ, Vicario I, Arruebarrena G, Hurtado I, Guraya T. X-ray Thermo-Diffraction Study of the Aluminum-Based Multicomponent Alloy  $Al_{58}Zn_{28}Mg_6Si_8$ . *Materials* 2022;15:5056. <https://doi.org/10.3390/ma15145056>

Trujillo-Tadeo JJ, Hurtado I, Arruebarrena, Guraya T, Bilbao Y, Vicario I, Burgos. “Diseño y fabricación de la aleación multicomponente compleja  $Al_{58}Zn_{28}Mg_6Si_8$ ”, *Proceedings of the XV Congreso Nacional de Materiales CNMAT 2020, Ciudad Real (Spain), June 28th to July 1st. (Oral Presentation)*

## Bibliographic References

- [1] Wang X, Guo W, Fu Y. High-entropy alloys: Emerging materials for advanced functional applications. *J Mater Chem A Mater* 2021;9:663–701. <https://doi.org/10.1039/d0ta09601f>.
- [2] Murty BS, Yeh JW, Ranganathan S. *High-Entropy Alloys*. Second Edition. Elsevier; 2019. <https://doi.org/10.1016/B978-0-12-816067-1.09987-2>.
- [3] Gao MC, Yeh J-W, Liaw PK, Zhang Y. *High-Entropy Alloys*. Cham: Springer International Publishing; 2016. <https://doi.org/10.1007/978-3-319-27013-5>.
- [4] Yeh JW, Chen SK, Lin SJ, Gan JY, Chin TS, Shun TT, et al. Nanostructured high-entropy alloys with multiple principal elements: Novel alloy design concepts and outcomes. *Adv Eng Mater* 2004;6:299–303. <https://doi.org/10.1002/adem.200300567>.
- [5] Cantor B, Chang ITH, Knight P, Vincent AJB. Microstructural development in equiatomic multicomponent alloys. *Materials Science and Engineering A* 2004;375–377:213–8. <https://doi.org/10.1016/j.msea.2003.10.257>.
- [6] Tsai MH. Physical properties of high entropy alloys. *Entropy* 2013;15:5338–45. <https://doi.org/10.3390/e15125338>.
- [7] Yin X, Xu S. Properties and Preparation of High Entropy Alloys. *MATEC Web of Conferences* 2018;142:03003. <https://doi.org/10.1051/mateconf/201814203003>.
- [8] Li Z, Zhao S, Ritchie RO, Meyers MA. Mechanical properties of high-entropy alloys with emphasis on face-centered cubic alloys. *Prog Mater Sci* 2019;102:296–345. <https://doi.org/10.1016/j.pmatsci.2018.12.003>.
- [9] Jiang W, Zhu Y, Zhao Y. Mechanical Properties and Deformation Mechanisms of Heterostructured High-Entropy and Medium-Entropy Alloys: A Review. *Front Mater* 2022;8. <https://doi.org/10.3389/fmats.2021.792359>.
- [10] Miracle DB, Senkov ON. A critical review of high entropy alloys and related concepts. *Acta Mater* 2017;122:448–511. <https://doi.org/10.1016/j.actamat.2016.08.081>.
- [11] Luan H, Huang L, Kang J, Luo B, Yang X, Li J, et al. Spinodal decomposition and the pseudo-binary decomposition in high-entropy alloys. *Acta Mater* 2023;248. <https://doi.org/10.1016/j.actamat.2023.118775>.
- [12] Lu W, Guo W, Wang Z, Li J, An F, Dehm G, et al. Advancing strength and counteracting embrittlement by displacive transformation in heterogeneous high-entropy alloys containing sigma phase. *Acta Mater* 2023;246:118717. <https://doi.org/10.1016/j.actamat.2023.118717>.
- [13] Ashby MF. *Materials Selection in Mechanical Design*. Fourth Edition. Elsevier; 2011.

- [14] Jahangiri H, Mohagheghi S, Asghari Alamdari A, Yilmaz R, Gürcan Bayrak K, Yu F, et al. Microstructure development and mechanical performance of Al<sub>2</sub>CrFeMnTi light-weight high entropy alloy. *Intermetallics (Barking)* 2021;139:107376. <https://doi.org/10.1016/j.intermet.2021.107376>.
- [15] Heydari H, Tajally M, Habibolahzadeh A. Calculations to introduce some light high entropy alloys based on phase formation rules. *J Alloys Compd* 2022;912:165222. <https://doi.org/10.1016/j.jallcom.2022.165222>.
- [16] Guo Q, Xu X, Pei X, Duan Z, Liaw PK, Hou H, et al. Predict the phase formation of high-entropy alloys by compositions. *Journal of Materials Research and Technology* 2023;22:3331–9. <https://doi.org/10.1016/j.jmrt.2022.12.143>.
- [17] Wu H, Xie J, Yang H, Shu D, Hou G, Li J, et al. A cost-effective eutectic high entropy alloy with an excellent strength-ductility combination designed by VEC criterion. *Journal of Materials Research and Technology* 2022;19:1759–65. <https://doi.org/10.1016/j.jmrt.2022.05.165>.
- [18] Yin KX, Dong GY, Zhang GJ, Tian QW, Wang YN, Huang JC. Prediction of phase structures of solid solutions for high entropy alloys. *Journal of Materials Research and Technology* 2023;24:7654–65. <https://doi.org/10.1016/j.jmrt.2023.04.191>.
- [19] Zhu W, Huo W, Wang S, Wang X, Ren K, Tan S, et al. Phase formation prediction of high-entropy alloys: a deep learning study. *Journal of Materials Research and Technology* 2022;18:800–9. <https://doi.org/10.1016/j.jmrt.2022.01.172>.
- [20] Gao MC, Yeh J-W, Liaw PK, Zhang Y. *High-Entropy Alloys*. Cham: Springer International Publishing; 2016. <https://doi.org/10.1007/978-3-319-27013-5>.
- [21] Feng R, Gao MC, Zhang C, Guo W, Poplawsky JD, Zhang F, et al. Phase stability and transformation in a light-weight high-entropy alloy. *Acta Mater* 2018;146:280–93. <https://doi.org/10.1016/j.actamat.2017.12.061>.
- [22] Miracle DB, Senkov ON. A critical review of high entropy alloys and related concepts. *Acta Mater* 2017;122:448–511. <https://doi.org/10.1016/j.actamat.2016.08.081>.
- [23] Zhang W, Liaw PK, Zhang Y. Science and technology in high-entropy alloys. *Sci China Mater* 2018;61:2–22. <https://doi.org/10.1007/s40843-017-9195-8>.
- [24] Miracle DB. High-Entropy Alloys: A Current Evaluation of Founding Ideas and Core Effects and Exploring “Nonlinear Alloys.” *JOM* 2017;69:2130–6. <https://doi.org/10.1007/s11837-017-2527-z>.
- [25] Zhang Y, Zuo TT, Tang Z, Gao MC, Dahmen KA, Liaw PK, et al. Microstructures and properties of high-entropy alloys. *Prog Mater Sci* 2014;61:1–93. <https://doi.org/10.1016/j.pmatsci.2013.10.001>.

- [26] Senkov ON, Miller JD, Miracle DB, Woodward C. Accelerated exploration of multi-principal element alloys with solid solution phases. *Nat Commun* 2015;6. <https://doi.org/10.1038/ncomms7529>.
- [27] Senkov ON, Miller JD, Miracle DB, Woodward C. Accelerated exploration of multi-principal element alloys for structural applications. *CALPHAD* 2015;50:32–48. <https://doi.org/10.1016/j.calphad.2015.04.009>.
- [28] Lee K, Ayyasamy M V., Delsa P, Hartnett TQ, Balachandran P V. Phase classification of multi-principal element alloys via interpretable machine learning. *NPJ Comput Mater* 2022;8. <https://doi.org/10.1038/s41524-022-00704-y>.
- [29] Jensen JK, Welk BA, Williams REA, Sosa JM, Huber DE, Senkov ON, et al. Characterization of the microstructure of the compositionally complex alloy Al1Mo0.5Nb1Ta0.5Ti1Zr1. *Scr Mater* 2016;121:1–4. <https://doi.org/10.1016/j.scriptamat.2016.04.017>.
- [30] Gorsse S, Miracle DB, Senkov ON. Mapping the world of complex concentrated alloys. *Acta Mater* 2017;135:177–87. <https://doi.org/10.1016/j.actamat.2017.06.027>.
- [31] Klenam DEP, Egowan G, Bodunrin MO, van der Merwe JW, Rahbar N, Soboyejo W. Complex Concentrated Alloys: A Cornucopia of Possible Structural and Functional Applications. Reference Module in Materials Science and Materials Engineering, Elsevier; 2022. <https://doi.org/10.1016/b978-0-12-822944-6.00056-6>.
- [32] Klenam D, Rahbar N, Soboyejo W. Critical Review of Factors Hindering Scalability of Complex Concentrated Alloys. Reference Module in Materials Science and Materials Engineering, Elsevier; 2022. <https://doi.org/10.1016/b978-0-12-822944-6.00051-7>.
- [33] Zhang W, Liaw PK, Zhang Y. Science and technology in high-entropy alloys. *Sci China Mater* 2018;61:2–22. <https://doi.org/10.1007/s40843-017-9195-8>.
- [34] Porter DA, Easterling KE, Sherif MY. Phase Transformations in Metals and Alloys. Taylor & Francis. Broken Sound Parkway NW : CRC Press; 2009.
- [35] Machlin ES. An Introduction to Aspects of Thermodynamics and Kinetics Relevant to Materials Science. vol. Third edition. 2007.
- [36] Fultz B. Vibrational thermodynamics of materials. *Prog Mater Sci* 2010;55:247–352. <https://doi.org/10.1016/j.pmatsci.2009.05.002>.
- [37] Yeh JW. Recent progress in high-entropy alloys. *Annales de Chimie: Science Des Materiaux* 2006;31:633–48. <https://doi.org/10.3166/acsm.31.633-648>.
- [38] Tian F, Varga LK, Chen N, Shen J, Vitos L. Empirical design of single phase high-entropy alloys with high hardness. *Intermetallics (Barking)* 2015;58:1–6. <https://doi.org/10.1016/j.intermet.2014.10.010>.
- [39] Tsai MH, Yeh JW. High-entropy alloys: A critical review. *Mater Res Lett* 2014;2:107–23. <https://doi.org/10.1080/21663831.2014.912690>.



- [40] Cantor B. Multicomponent and high entropy alloys. *Entropy* 2014;16:4749–68. <https://doi.org/10.3390/e16094749>.
- [41] Gao MC, Yeh J-W, Liaw PK, Zhang Y. *High-entropy alloys: fundamentals and applications*. Springer; 2015.
- [42] Murty BS, Yeh JW, Ranganathan S. *High-entropy alloys*. Elsevier; 2014.
- [43] Miracle DB, Senkov ON. A critical review of high entropy alloys and related concepts. *Acta Mater* 2017;122:448–511. <https://doi.org/10.1016/j.actamat.2016.08.081>.
- [44] Gorsse S, Couzinié JP, Miracle DB. From high-entropy alloys to complex concentrated alloys. *C R Phys* 2018;19:721–36. <https://doi.org/10.1016/j.crhy.2018.09.004>.
- [45] Tsai KY, Tsai MH, Yeh JW. Sluggish diffusion in Co-Cr-Fe-Mn-Ni high-entropy alloys. *Acta Mater* 2013;61:4887–97. <https://doi.org/10.1016/j.actamat.2013.04.058>.
- [46] Murty EBS, Yeh JW, Ranganathan S, Bhattacharjee PP. *High-Entropy Alloys*. vol. Second Edition. Second Edition. ELSEVIER; 2019.
- [47] Yeh JW, Chang SY, Hong Y der, Chen SK, Lin SJ. Anomalous decrease in X-ray diffraction intensities of Cu-Ni-Al-Co-Cr-Fe-Si alloy systems with multi-principal elements. *Mater Chem Phys* 2007;103:41–6. <https://doi.org/10.1016/j.matchemphys.2007.01.003>.
- [48] Ranganathan S. *Alloyed pleasures: Multimetallic cocktails*. vol. 85. 2003.
- [49] Cai Z, Guo Y, Liu J, Liu J, Guo J, Du X, et al. *Progress in Light-weight High Entropy Alloys*. *Journal Wuhan University of Technology, Materials Science Edition* 2021;36:737–53. <https://doi.org/10.1007/s11595-021-2467-x>.
- [50] Kumar A, Gupta M. An Insight into Evolution of Light Weight High Entropy Alloys: A Review. *Metals (Basel)* 2016;6:199. <https://doi.org/10.3390/met6090199>.
- [51] Feng R, Gao MC, Lee C, Mathes M, Zuo T, Chen S, et al. Design of light-weight high-entropy alloys. *Entropy* 2016;18. <https://doi.org/10.3390/e18090333>.
- [52] Zhang Y, Zhou YJ, Lin JP, Chen GL, Liaw PK. Solid-solution phase formation rules for multi-component alloys. *Adv Eng Mater* 2008;10:534–8. <https://doi.org/10.1002/adem.200700240>.
- [53] Zhang Y, Yang X, Liaw PK. Alloy design and properties optimization of high-entropy alloys. *JOM* 2012;64:830–8. <https://doi.org/10.1007/s11837-012-0366-5>.
- [54] Yang X, Zhang Y. Prediction of high-entropy stabilized solid-solution in multi-component alloys. *Mater Chem Phys* 2012;132:233–8. <https://doi.org/10.1016/j.matchemphys.2011.11.021>.
- [55] Nong ZS, Zhu JC, Cao Y, Yang XW, Lai ZH, Liu Y. Stability and structure prediction of cubic phase in as cast high entropy alloys. *Materials Science and Technology (United Kingdom)* 2014;30:363–9. <https://doi.org/10.1179/1743284713Y.0000000368>.

- [56] Dong Y, Lu Y, Jiang L, Wang T, Li T. Effects of electro-negativity on the stability of topologically close-packed phase in high entropy alloys. *Intermetallics (Barking)* 2014;52:105–9. <https://doi.org/10.1016/j.intermet.2014.04.001>.
- [57] Takeuchi A, Amiya K, Wada T, Yubuta K, Zhang W, Makino A. Entropies in alloy design for high-entropy and bulk glassy alloys. *Entropy* 2013;15:3810–21. <https://doi.org/10.3390/e15093810>.
- [58] Wang Z, Huang Y, Yang Y, Wang J, Liu CT. Atomic-size effect and solid solubility of multicomponent alloys. *Scr Mater* 2015;94:28–31. <https://doi.org/10.1016/j.scriptamat.2014.09.010>.
- [59] Poletti MG, Battezzati L. Electronic and thermodynamic criteria for the occurrence of high entropy alloys in metallic systems. *Acta Mater* 2014;75:297–306. <https://doi.org/10.1016/j.actamat.2014.04.033>.
- [60] King DJM, Middleburgh SC, McGregor AG, Cortie MB. Predicting the formation and stability of single phase high-entropy alloys. *Acta Mater* 2016;104:172–9. <https://doi.org/10.1016/j.actamat.2015.11.040>.
- [61] Senkov ON, Miracle DB. A new thermodynamic parameter to predict formation of solid solution or intermetallic phases in high entropy alloys. *J Alloys Compd* 2016;658:603–7. <https://doi.org/10.1016/j.jallcom.2015.10.279>.
- [62] Senkov ON, Miracle DB. A new thermodynamic parameter to predict formation of solid solution or intermetallic phases in high entropy alloys. *J Alloys Compd* 2016;658:603–7. <https://doi.org/10.1016/j.jallcom.2015.10.279>.
- [63] Toda-Caraballo I, Rivera-Díaz-Del-Castillo PEJ. A criterion for the formation of high entropy alloys based on lattice distortion. *Intermetallics (Barking)* 2016;71:76–87. <https://doi.org/10.1016/j.intermet.2015.12.011>.
- [64] Hayun S, Lilova K, Salhov S, Navrotsky A. Enthalpies of formation of high entropy and multicomponent alloys using oxide melt solution calorimetry. *Intermetallics (Barking)* 2020;125. <https://doi.org/10.1016/j.intermet.2020.106897>.
- [65] Zhang RF, Zhang SH, He ZJ, Jing J, Sheng SH. Miedema Calculator: A thermodynamic platform for predicting formation enthalpies of alloys within framework of Miedema's Theory. *Comput Phys Commun* 2016;209:58–69. <https://doi.org/10.1016/j.cpc.2016.08.013>.
- [66] Guo S, Hu Q, Ng C, Liu CT. More than entropy in high-entropy alloys: Forming solid solutions or amorphous phase. *Intermetallics (Barking)* 2013;41:96–103. <https://doi.org/10.1016/j.intermet.2013.05.002>.
- [67] Asensio Dominguez L. Combinatorial high throughput synthesis of high entropy alloys. University Sheffield, 2016.
- [68] Guo S, Ng C, Lu J, Liu CT. Effect of valence electron concentration on stability of fcc or bcc phase in high entropy alloys. *J Appl Phys*, vol. 109, 2011. <https://doi.org/10.1063/1.3587228>.

- [69] Zhang C, Zhang F, Chen S, Cao W. Computational thermodynamics aided high-entropy alloy design. *JOM* 2012;64:839–45. <https://doi.org/10.1007/s11837-012-0365-6>.
- [70] Zhang C, Zhang F, Diao H, Gao MC, Tang Z, Poplawsky JD, et al. Understanding Phase Stability of Al-Co-Cr-Fe-Ni High Entropy Alloys. n.d.
- [71] Raghavan R, Hari Kumar KC, Murty BS. Analysis of phase formation in multi-component alloys. *J Alloys Compd* 2012;544:152–8. <https://doi.org/10.1016/j.jallcom.2012.07.105>.
- [72] Maulik O, Kumar D, Kumar S, Dewangan SK, Kumar V. Structure and properties of lightweight high entropy alloys: A brief review. *Mater Res Express* 2018;5. <https://doi.org/10.1088/2053-1591/aabbca>.
- [73] Xiong W, Cheng L, Zhan S, Guo AXY, Liaw PK, Cao SC. Recent Advances on Lightweight High-Entropy Alloys: Process, Design, and Applications. *High Entropy Alloys & Materials* 2023;1:175–94. <https://doi.org/10.1007/s44210-023-00014-y>.
- [74] Garcia-Michelena P, Chamorro X, Herrero-Dorca N, Bernal D, Hurtado I, Ruiz-Reina E, et al. Effect of the crucible composition on the Inconel 718 vacuum induction melting process efficiency. *Journal of Materials Research and Technology* 2023;23:3351–61. <https://doi.org/10.1016/j.jmrt.2023.01.213>.
- [75] Jang BY, Soo Kim J, Soo Ahn Y. Induction melting process using segmented graphite crucible for silicon melting. *Solar Energy Materials and Solar Cells*, vol. 95, 2011, p. 101–6. <https://doi.org/10.1016/j.solmat.2010.04.062>.
- [76] Li R, Gao J, Fa K. Study to microstructure and mechanical properties of Mg containing high entropy alloys. *Materials Science Forum*, vol. 650, Trans Tech Publications Ltd; 2010, p. 265–71. <https://doi.org/10.4028/www.scientific.net/MSF.650.265>.
- [77] Stepanov ND, Yurchenko NY, Skibin D V., Tikhonovsky MA, Salishchev GA. Structure and mechanical properties of the AlCr<sub>x</sub>NbTiV (x = 0, 0.5, 1, 1.5) high entropy alloys. *J Alloys Compd* 2015;652:266–80. <https://doi.org/10.1016/j.jallcom.2015.08.224>.
- [78] Stepanov ND, Yu Yurchenko N, Shaysultanov DG, Salishchev GA, Tikhonovsky MA. Effect of Al on structure and mechanical properties of Al<sub>x</sub>NbTiVZr (x = 0, 0.5, 1, 1.5) high entropy alloys. *Materials Science and Technology (United Kingdom)* 2015;31:1184–93. <https://doi.org/10.1179/1743284715Y.0000000032>.
- [79] Tseng KK, Yang YC, Juan CC, Chin TS, Tsai CW, Yeh JW. A light-weight high-entropy alloy Al<sub>20</sub>Be<sub>20</sub>Fe<sub>10</sub>Si<sub>15</sub>Ti<sub>35</sub>. *Sci China Technol Sci* 2018;61:184–8. <https://doi.org/10.1007/s11431-017-9073-0>.
- [80] Jia Y, Jia Y, Wu S, Ma X, Wang G. Novel ultralight-weight complex concentrated alloys with high strength. *Materials* 2019;12. <https://doi.org/10.3390/ma12071136>.
- [81] Sanchez JM, Vicario I, Albizuri J, Guraya T, Garcia JC. Phase prediction, microstructure and high hardness of novel light-weight high entropy alloys. *Journal of Materials Research and Technology* 2019;8:795–803. <https://doi.org/10.1016/j.jmrt.2018.06.010>.

- [82] Stepanov ND, Yu Yurchenko N, Shaysultanov DG, Salishchev GA, Tikhonovsky MA. Effect of Al on structure and mechanical properties of  $\text{Al}_x\text{NbTiVZr}$  ( $x = 0, 0.5, 1, 1.5$ ) high entropy alloys. *Materials Science and Technology (United Kingdom)* 2015;31:1184–93. <https://doi.org/10.1179/1743284715Y.0000000032>.
- [83] Li Y, Liaw PK, Zhang Y. Microstructures and Properties of the Low-Density  $\text{Al}_{15}\text{Zr}_{40}\text{Ti}_{28}\text{Nb}_{12}\text{M}(\text{Cr}, \text{Mo}, \text{Si})_5$  High-Entropy Alloys. *Metals (Basel)* 2022;12. <https://doi.org/10.3390/met12030496>.
- [84] Stepanov ND, Shaysultanov DG, Salishchev GA, Tikhonovsky MA. Structure and mechanical properties of a light-weight  $\text{AlNbTiV}$  high entropy alloy. *Mater Lett* 2015;142:153–5. <https://doi.org/10.1016/j.matlet.2014.11.162>.
- [85] Maulik O, Kumar D, Kumar S, Fabijanic DM, Kumar V. Structural evolution of spark plasma sintered  $\text{AlFeCuCrMg}_x$  ( $x = 0, 0.5, 1, 1.7$ ) high entropy alloys. *Intermetallics (Barking)* 2016;77:46–56. <https://doi.org/10.1016/j.intermet.2016.07.001>.
- [86] Hammond VH, Atwater MA, Darling KA, Nguyen HQ, Kecskes LJ. Equal-Channel Angular Extrusion of a Low-Density High-Entropy Alloy Produced by High-Energy Cryogenic Mechanical Alloying. *JOM* 2014;66:2021–9. <https://doi.org/10.1007/s11837-014-1113-x>.
- [87] Yang X, Chen SY, Cotton JD, Zhang Y. Phase Stability of Low-Density, Multiprincipal Component Alloys Containing Aluminum, Magnesium, and Lithium. *JOM* 2014;66:2009–20. <https://doi.org/10.1007/s11837-014-1059-z>.
- [88] Chauhan P, Yebaji S, Nadakuduru VN, Shanmugasundaram T. Development of a novel light weight  $\text{Al}_{35}\text{Cr}_{14}\text{Mg}_6\text{Ti}_{35}\text{V}_{10}$  high entropy alloy using mechanical alloying and spark plasma sintering. *J Alloys Compd* 2020;820:153367. <https://doi.org/10.1016/j.jallcom.2019.153367>.
- [89] Youssef KM, Zaddach AJ, Niu C, Irving DL, Koch CC. A novel low-density, high-hardness, high-entropy alloy with close-packed single-phase nanocrystalline structures. *Mater Res Lett* 2014;3:95–9. <https://doi.org/10.1080/21663831.2014.985855>.
- [90] Du XH, Wang R, Chen C, Wu BL, Huang JC. Preparation of a light-weight  $\text{MgCaAlLiCu}$  high-entropy alloy. *Key Eng Mater*, vol. 727, Trans Tech Publications Ltd; 2017, p. 132–5. <https://doi.org/10.4028/www.scientific.net/KEM.727.132>.
- [91] Bale CW, Bélisle E, Chartrand P, Decterov SA, Eriksson G, Gheribi AE, et al. FactSage thermochemical software and databases, 2010–2016. *CALPHAD* 2016;54:35–53. <https://doi.org/10.1016/j.calphad.2016.05.002>.
- [92] Trujillo-Tadeo JJ, Arruebarrena G, Dorantes-Rosales HJ, Bilbao Y, Vicario I, Guraya T, et al. Design and characterization of a novel lightweight multicomponent alloy  $\text{Al}_{58}\text{Zn}_{28}\text{Mg}_6\text{Si}_8$ . *Journal of Materials Research and Technology* 2023. <https://doi.org/10.1016/j.jmrt.2023.10.102>.
- [93] Lozares J, Plata G, Hurtado I, Sánchez A, Loizaga I. Near solidus forming (NSF): Semi-solid steel forming at high solid content to obtain as-forged properties. *Metals (Basel)* 2020;10. <https://doi.org/10.3390/met10020198>.

- [94] Gorsse S, Senkov ON. About the reliability of CALPHAD predictions in multicomponent systems. *Entropy* 2018;20. <https://doi.org/10.3390/e20120899>.
- [95] Asadikiya M, Zhang Y, Wang L, Apelian D, Zhong Y. Design of ternary high-entropy aluminum alloys (HEAs). *J Alloys Compd* 2022;891:161836. <https://doi.org/10.1016/j.jallcom.2021.161836>.
- [96] Lim SJ, Huh H. Ductile fracture behavior of BCC and FCC metals at a wide range of strain rates. *Int J Impact Eng* 2022;159. <https://doi.org/10.1016/j.ijimpeng.2021.104050>.
- [97] Skoko Ž, Popović S, Štefanić G. Microstructure of Al-Zn and Zn-Al Alloys\*. *CROATICA CHEMICA ACTA* 2009;82:405–20.
- [98] Mezbahul-Islam M, Mostafa AO, Medraj M. Essential Magnesium Alloys Binary Phase Diagrams and Their Thermochemical Data. *J Mater* 2014;2014:1–33. <https://doi.org/10.1155/2014/704283>.
- [99] Haga T, Imamura S, Fuse H. Fluidity Investigation of Pure Al and Al-Si Alloys. *Materials* 2021;14:5372. <https://doi.org/10.3390/ma14185372>.
- [100] Kogo S, Hirosawa S. Thermodynamic Assessment and Determination of Spinodal Lines for Al-Zn Binary System. *Materials Science Forum* 2014;794–796:634–9.
- [101] Lopez-Hirata VM, Avila-Davila EO, Saucedo-Muñoz M-L, Villegas-Cardenas JD, Soriano-Vargas O. Analysis of Spinodal Decomposition in Al-Zn and Al-Zn-Cu Alloys Using the Nonlinear Cahn-Hilliard Equation. *Materials Research* 2017;20:639–45. <https://doi.org/10.1590/1980-5373-mr-2015-0373>.
- [102] Miller MK, Burke MG, Brenner SS. Morphological interpretation of modulated microstructures. *Le Journal de Physique Colloques* 1984;45:C9-239-C9-244. <https://doi.org/10.1051/jphyscol:1984940>.
- [103] Edington JW. *The Operation and Calibration of the Electron Microscope*. London: Macmillan Education UK; 1974. <https://doi.org/10.1007/978-1-349-02574-9>.
- [104] Bilbao Y, Trujillo JJ, Vicario I, Arruebarrena G, Hurtado I, Guraya T. X-ray Thermo-Diffraction Study of the Aluminum-Based Multicomponent Alloy Al<sub>58</sub>Zn<sub>28</sub>Si<sub>8</sub>Mg<sub>6</sub>. *Materials* 2022;15:5056. <https://doi.org/10.3390/ma15145056>.
- [105] Popovic S, Grèta B. Precipitation and Dissolution Phenomena in Al-Zn Alloys\*. *CROATICA CHEMICA ACTA* 1999;72:621–43.
- [106] Biswas P, Paliwal M, Mondal MK. Thermochemical behaviour, solidification, thermal stability and oxidation of Al-Mg<sub>2</sub>Si composites: An experimental and thermodynamic study. *Mater Today Commun* 2023;35. <https://doi.org/10.1016/j.mtcomm.2023.105913>.
- [107] Jiang W, Xu X, Zhao Y, Wang Z, Wu C, Pan D, et al. Effect of the addition of Sr modifier in different conditions on microstructure and mechanical properties of T6 treated Al-Mg<sub>2</sub>Si in-

situ composite. *Materials Science and Engineering: A* 2018;721:263–73. <https://doi.org/10.1016/j.msea.2018.02.100>.

- [108] Liao L, Zhang X, Wang H, Li X, Ma N. Influence of Sb on damping capacity and mechanical properties of Mg<sub>2</sub>Si/Mg-9Al composite materials. *J Alloys Compd* 2007;430:292–6. <https://doi.org/10.1016/j.jallcom.2006.05.006>.
- [109] Yuan GY, Liu ZL, Wang QD, Ding WJ. Microstructure refinement of Mg-Al-Zn-Si alloys. *Mater Lett* 2002;56:53–8.
- [110] Nam KY, Song DH, Lee CW, Lee SW, Park YH, Cho KM, et al. Modification of Mg<sub>2</sub>Si Morphology in As-Cast Mg-Al-Si Alloys with Strontium and Antimony. *Materials Science Forum* 2006;510–511:238–41. <https://doi.org/10.4028/www.scientific.net/msf.510-511.238>.
- [111] Wang KY, Zhao R da, Wu FF, Wu XF, Chen MH, Xiang J, et al. Improving microstructure and mechanical properties of hypoeutectic Al-Mg<sub>2</sub>Si alloy by Gd addition. *J Alloys Compd* 2020;813. <https://doi.org/10.1016/j.jallcom.2019.152178>.
- [112] Wu XF, Wang KY, Wu FF, Zhao R da, Chen MH, Xiang J, et al. Simultaneous grain refinement and eutectic Mg<sub>2</sub>Si modification in hypoeutectic Al-11Mg<sub>2</sub>Si alloys by Sc addition. *J Alloys Compd* 2019;791:402–10. <https://doi.org/10.1016/j.jallcom.2019.03.326>.
- [113] Moussa ME, Waly MA, El-Sheikh AM. Combined effect of high-intensity ultrasonic treatment and Ca addition on modification of primary Mg<sub>2</sub>Si and wear resistance in hypereutectic Mg-Si alloys. *J Alloys Compd* 2014;615:576–81. <https://doi.org/10.1016/j.jallcom.2014.06.154>.
- [114] Chen K, Li ZQ, Liu JS, Yang JN, Sun YD, Bian SG. The effect of Ba addition on microstructure of in situ synthesized Mg<sub>2</sub>Si/Mg-Zn-Si composites. *J Alloys Compd* 2009;487:293–7. <https://doi.org/10.1016/j.jallcom.2009.07.111>.
- [115] Qin QD, Zhao YG, Zhou W, Cong PJ. Effect of phosphorus on microstructure and growth manner of primary Mg<sub>2</sub>Si crystal in Mg<sub>2</sub>Si/Al composite. *Materials Science and Engineering: A* 2007;447:186–91. <https://doi.org/10.1016/j.msea.2006.10.076>.
- [116] Wang HY, Liu F, Chen L, Zha M, Liu GJ, Jiang QC. The effect of Sb addition on microstructures and tensile properties of extruded Al-20 Mg<sub>2</sub>Si-4Cu alloy. *Materials Science and Engineering: A* 2016;657:331–8. <https://doi.org/10.1016/j.msea.2016.01.063>.
- [117] Prach O, Hornik J, Mykhalekov K. Effect of the addition of Li on the structure and mechanical properties of hypoeutectic Al-Mg<sub>2</sub>Si alloys. *Acta Polytechnica* 2015;55:253–9. <https://doi.org/10.14311/AP.2015.55.0253>.
- [118] Jafari Nodooshan HR, Liu W, Wu G, Bahrami A, Pech-Canul MI, Emamy M. Mechanical and tribological characterization of Al-Mg<sub>2</sub>Si composites after yttrium addition and heat treatment. *J Mater Eng Perform* 2014;23:1146–56. <https://doi.org/10.1007/s11665-014-0900-4>.
- [119] Li C, Wang C, Ju H, Xue XN, Zha M, Wang HY. Prediction of modified morphology for primary Mg<sub>2</sub>Si induced by trace-element adsorption: A first-principles study. *Materialia (Oxf)* 2020;14. <https://doi.org/10.1016/j.mtla.2020.100875>.



- [120] Dong Y, Xiao P, Gao Y, Zhao Q, Yang H. Microstructure refinement and mechanical properties of eutectic Mg<sub>2</sub>Si reinforced Mg matrix composites containing Sr element. *Journal of Materials Research and Technology* 2022;17:2614–23. <https://doi.org/10.1016/j.jmrt.2022.02.035>.
- [121] Farahany S, Ghandvar H, Bozorg M, Nordin A, Ourdjini A, Hamzah E. Role of Sr on microstructure, mechanical properties, wear and corrosion behaviour of an Al–Mg<sub>2</sub>Si–Cu in-situ composite. *Mater Chem Phys* 2020;239. <https://doi.org/10.1016/j.matchemphys.2019.121954>.
- [122] Tang SQ, Zhou JX, Tian CW, Yang YS. Morphology modification of Mg<sub>2</sub>Si by Sr addition in Mg–4Si alloy. *Transactions of Nonferrous Metals Society of China (English Edition)* 2011;21:1932–6. [https://doi.org/10.1016/S1003-6326\(11\)60952-7](https://doi.org/10.1016/S1003-6326(11)60952-7).
- [123] Li C, Zhao MC, Jia HL, Wang C, Ma PK, Zha M, et al. Varied Modification Mechanisms of Sr and Sb Under Diverse Cooling Rates on Primary Mg<sub>2</sub>Si in an Al-20Mg<sub>2</sub>Si Alloy. *Metallurgical and Materials Transactions B: Process Metallurgy and Materials Processing Science* 2022;53:2066–76. <https://doi.org/10.1007/s11663-022-02506-5>.
- [124] Xiao P, Gao Y, Sheng Y, Yang C, Liu Z, Yi Y, et al. Improving wear and corrosion resistances of Mg<sub>2</sub>Si/AZ91 composites via tailoring microstructure and intrinsic properties of Mg<sub>2</sub>Si induced by Sb modification. *Journal of Magnesium and Alloys* 2023. <https://doi.org/10.1016/j.jma.2023.07.021>.
- [125] Xiao P, Gao Y, Yang C, Dong Y, Huang X, Wang Y, et al. Effect of Sb doping on microstructure, mechanical and electronic properties of Mg<sub>2</sub>Si in Mg<sub>2</sub>Si/AZ91 composites by experimental investigation and first-principles calculation. *J Alloys Compd* 2022;902. <https://doi.org/10.1016/j.jallcom.2022.163859>.
- [126] Xiao P, Gao Y, Mao P, Yang C, Tun KS, Yang S, et al. Revealing modification mechanism of Mg<sub>2</sub>Si in Sb modified Mg<sub>2</sub>Si/ AZ91 composites and its effect on mechanical properties. *J Alloys Compd* 2021;850. <https://doi.org/10.1016/j.jallcom.2020.156877>.
- [127] Yan H, Hu Y, Wu XQ. Influence of Sb modification on microstructures and mechanical properties of Mg<sub>2</sub>Si/AM60 composites. *Transactions of Nonferrous Metals Society of China (English Edition)* 2010;20. [https://doi.org/10.1016/S1003-6326\(10\)60508-0](https://doi.org/10.1016/S1003-6326(10)60508-0).
- [128] Ren B, Liu ZX, Zhao RF, Zhang TQ, Liu ZY, Wang MX, et al. Effect of Sb on microstructure and mechanical properties of Mg<sub>2</sub>Si/Al-Si composites. *Transactions of Nonferrous Metals Society of China (English Edition)* 2010;20:1367–73. [https://doi.org/10.1016/S1003-6326\(09\)60306-X](https://doi.org/10.1016/S1003-6326(09)60306-X).
- [129] Alizadeh R, Mahmudi R. Effects of Sb addition on the modification of Mg<sub>2</sub>Si particles and high-temperature mechanical properties of cast Mg–4Zn–2Si alloy. *J Alloys Compd* 2011;509:9195–9. <https://doi.org/10.1016/j.jallcom.2011.06.109>.
- [130] Chen K, Li Z. Effect of co-modification by Ba and Sb on the microstructure of Mg<sub>2</sub>Si/Mg–Zn–Si composite and mechanism. *J Alloys Compd* 2014;592:196–201. <https://doi.org/10.1016/j.jallcom.2013.12.041>.

- [131] Li C, Fan Z, Jia HL, Wang C, Ma PK, Ren MW, et al. Synergetic modification effects on primary Mg<sub>2</sub>Si in Al-20Mg<sub>2</sub>Si alloy induced by the co-addition of beryllium and antimony. *J Alloys Compd* 2021;888. <https://doi.org/10.1016/j.jallcom.2021.161477>.
- [132] Sun Y, Ma S, Wang H, Chen L, Gao K, Ma Y, et al. Effects of complex modification by Sr-Sb on the microstructures and mechanical properties of Al-18 wt % Mg<sub>2</sub>Si-4.5Cu alloys. *Materials* 2016;9. <https://doi.org/10.3390/ma9030157>.
- [133] Wang HY, Chen L, Liu B, Li XR, Wang JG, Jiang QC. Heterogeneous nucleation of Mg<sub>2</sub>Si on Sr 11Sb 10 nucleus in Mg-x(3.5, 5 wt.%)Si-1Al alloys. *Mater Chem Phys* 2012;135:358–64. <https://doi.org/10.1016/j.matchemphys.2012.04.058>.
- [134] Zhang L, Chen S, Li Q, Chang G. Formation mechanism and conditions of fine primary silicon being uniformly distributed on single  $\alpha$ Al matrix in Al-Si alloys. *Mater Des* 2020;193. <https://doi.org/10.1016/j.matdes.2020.108853>.
- [135] Chandra K, Kain V. Brittle Failure of Hypereutectic Al-Si Alloy Component. *Journal of Failure Analysis and Prevention* 2015;15:679–85. <https://doi.org/10.1007/s11668-015-9996-6>.
- [136] Joseph S, Tewari A, Kumar S. The fracture characteristics of a near eutectic Al-Si based alloy under compression. *Metall Mater Trans A Phys Metall Mater Sci*, vol. 44, 2013, p. 2358–68. <https://doi.org/10.1007/s11661-012-1580-z>.
- [137] Xu CL, Jiang QC. Morphologies of primary silicon in hypereutectic Al-Si alloys with melt overheating temperature and cooling rate. *Materials Science and Engineering A* 2006;437:451–5. <https://doi.org/10.1016/j.msea.2006.07.088>.
- [138] Xu CL, Jiang QC, Yang YF, Wang HY, Wang JG. Effect of Nd on primary silicon and eutectic silicon in hypereutectic Al-Si alloy. *J Alloys Compd* 2006;422. <https://doi.org/10.1016/j.jallcom.2005.03.128>.
- [139] Alizadeh R, Mahmudi R. Effects of Sb addition on the modification of Mg<sub>2</sub>Si particles and high-temperature mechanical properties of cast Mg-4Zn-2Si alloy. *J Alloys Compd* 2011;509:9195–9. <https://doi.org/10.1016/j.jallcom.2011.06.109>.
- [140] YANG M bo, PAN F sheng, SHEN J, BAI L. Comparison of Sb and Sr on modification and refinement of Mg<sub>2</sub>Si phase in AZ61-0.7Si magnesium alloy. *Transactions of Nonferrous Metals Society of China (English Edition)* 2009;19:287–92. [https://doi.org/10.1016/S1003-6326\(08\)60266-6](https://doi.org/10.1016/S1003-6326(08)60266-6).
- [141] Dong Y, Xiao P, Gao Y, Zhao Q, Yang H. Microstructure refinement and mechanical properties of eutectic Mg<sub>2</sub>Si reinforced Mg matrix composites containing Sr element. *Journal of Materials Research and Technology* 2022;17:2614–23. <https://doi.org/10.1016/j.jmrt.2022.02.035>.
- [142] Gutiérrez-Menchaca J, Torres-Torres D, Garay-Tapia AM. Microstructural, mechanical and thermodynamic study of the as-cast Zn-Al-Sr alloys at high Sr content. *J Alloys Compd* 2020;829. <https://doi.org/10.1016/j.jallcom.2020.154511>.

- [143] KE G zhou, YUE R, HUANG H, KANG B, ZENG H, YUAN G yin. Effects of Sr addition on microstructure, mechanical properties and in vitro degradation behavior of as-extruded Zn–Sr binary alloys. *Transactions of Nonferrous Metals Society of China* 2020;30:1873–83. [https://doi.org/10.1016/S1003-6326\(20\)65346-8](https://doi.org/10.1016/S1003-6326(20)65346-8).
- [144] Kapranos P, Carney C, Pola A, Jolly M. *Advanced Casting Methodologies: Investment Casting, Centrifugal Casting, Squeeze Casting, Metal Spinning, and Batch Casting*. *Comprehensive Materials Processing*, vol. 5, Elsevier Ltd; 2014, p. 39–67. <https://doi.org/10.1016/B978-0-08-096532-1.00539-2>.
- [145] Samat S, Omar MZ, Baghdadi AH, Mohamed IF, Aziz AM. Mechanical properties and microstructures of a modified Al-Si-Cu alloy prepared by thixoforming process for automotive connecting rods. *Journal of Materials Research and Technology* 2021;10:1086–102. <https://doi.org/10.1016/j.jmrt.2020.12.085>.
- [146] Li R, Liu L, Zhang L, Sun J, Shi Y, Yu B. Effect of Squeeze Casting on Microstructure and Mechanical Properties of Hypereutectic Al-xSi Alloys. *J Mater Sci Technol* 2017;33:404–10. <https://doi.org/10.1016/j.jmst.2017.02.004>.
- [147] Ma Z, Zhang H, Song W, Wu X, Jia L, Zhang H. Pressure-driven mold filling model of aluminum alloy melt/semi-solid slurry based on rheological behavior. *J Mater Sci Technol* 2020;39:14–21. <https://doi.org/10.1016/j.jmst.2019.07.048>.
- [148] Qi M, Li J, Kang Y. Correlation between segregation behavior and wall thickness in a rheological high pressure die-casting AC46000 aluminum alloy. *Journal of Materials Research and Technology* 2019;8:3565–79. <https://doi.org/10.1016/j.jmrt.2019.03.016>.
- [149] Rogal. On the microstructure and mechanical properties of the AlCoCrCuNi high entropy alloy processed in the semi-solid state. *Materials Science and Engineering A* 2018;709:139–51. <https://doi.org/10.1016/j.msea.2017.10.012>.
- [150] Slater C, Plata G, Sánchez A, Lozares J, Hurtado I. A novel forming technique to coforge bimetal components into complex geometries. *Manuf Lett* 2020;26:21–4. <https://doi.org/10.1016/j.mfglet.2020.09.006>.
- [151] Plata G, Lozares J, Sánchez A, Hurtado I, Slater C. Preliminary study on the capability of the novel near solidus forming (NSF) technology to manufacture complex steel components. *Materials* 2020;13:1–14. <https://doi.org/10.3390/ma13204682>.
- [152] Wang Y, Liu X, Zhu D, Ding H, Chen R, Guo J, et al. Temperature-dependent Mechanical Properties and Fracture Behavior of Directionally Solidified Ti47Al2Cr2Nb Alloy. *Journal of Materials Research and Technology* 2023. <https://doi.org/10.1016/j.jmrt.2023.05.182>.
- [153] Zhang Y, Zhou J, Yin Y, Ji X, Shen X, Guo Z. Study on the solutal convection during dendrite growth of superalloy under directional solidification condition. *Journal of Materials Research and Technology* 2023;23:3916–27. <https://doi.org/10.1016/j.jmrt.2023.02.042>.

- [154] Zhang S, Xu Z, Wang Z. Numerical modeling and simulation of water cooling-controlled solidification for aluminum alloy investment casting. *International Journal of Advanced Manufacturing Technology* 2017;91:763–70. <https://doi.org/10.1007/s00170-016-9808-5>.
- [155] Xu J, Kang J, Zheng L, Mao W, Wang J. Numerical simulation of the directional solidification process with multi-shell mold being gradually immersed in water. *Journal of Materials Research and Technology* 2022;19:2705–16. <https://doi.org/10.1016/j.jmrt.2022.06.037>.
- [156] Ye C, Jia L, Jin Z, Wang Y, Zhang H. Directional solidification of hypereutectic Nb-Si-Ti alloy: Influence of drawing velocity change on microstructures. *J Alloys Compd* 2020;844. <https://doi.org/10.1016/j.jallcom.2020.156123>.
- [157] Peng P, Lu L, Zheng W, Wang J, Zhou S. Thermosolutal convection-induced freckle formation in steady and unsteady directional solidification: Analysis in Sn-Ni peritectic alloy. *J Alloys Compd* 2021;872. <https://doi.org/10.1016/j.jallcom.2021.159558>.
- [158] Xu X, Hao Y, Wu Q, Dong R, Zhao Y, Hou H. Microstructure refinement mechanisms in undercooled solidification of binary and ternary nickel based alloys. *Journal of Materials Research and Technology* 2023. <https://doi.org/10.1016/j.jmrt.2023.03.004>.
- [159] Wang H, Long H, Sun M, Yang G, Wei H, Mao S, et al. Effect of directional solidification methods on solid solution window in Ni-based single-crystal superalloy. *Journal of Materials Research and Technology* 2023;24:8307–19. <https://doi.org/10.1016/j.jmrt.2023.05.089>.
- [160] Wang S, Zhao Y, Hou H, Wen Z, Zhang P, Liang J. Effect of anti-site point defects on the mechanical and thermodynamic properties of MgZn<sub>2</sub>, MgCu<sub>2</sub> Laves phases: A first-principle study. *J Solid State Chem* 2018;263:18–23. <https://doi.org/10.1016/j.jssc.2018.04.001>.
- [161] Liu CT, Zhu JH, Brady MP, Mckamey CG, Pike LM. *Physical metallurgy and mechanical properties of transition-metal Laves phase alloys*. 2000.
- [162] Scudino S, Donnadiou P, Surreddi KB, Nikolowski K, Stoica M, Eckert J. Microstructure and mechanical properties of Laves phase-reinforced Fe-Zr-Cr alloys. *Intermetallics (Barking)* 2009;17:532–9. <https://doi.org/10.1016/j.intermet.2009.01.007>.
- [163] Liu G, Liu L, Liu X, Wang Z, Han Z, Zhang G, et al. Microstructure and mechanical properties of Al<sub>0.7</sub>CoCrFeNi high-entropy-alloy prepared by directional solidification. *Intermetallics (Barking)* 2018;93:93–100. <https://doi.org/10.1016/j.intermet.2017.11.019>.
- [164] Zheng H, Chen R, Qin G, Li X, Su Y, Ding H, et al. Microstructure evolution, Cu segregation and tensile properties of CoCrFeNiCu high entropy alloy during directional solidification. *J Mater Sci Technol* 2020;38:19–27. <https://doi.org/10.1016/j.jmst.2019.08.019>.
- [165] Rogal L, Kania A, Berent K, Janus K, Lityńska-Dobrzyńska L. Microstructure and mechanical properties of Mg-Zn-RE-Zr alloy after thixoforming. *Journal of Materials Research and Technology* 2019;8:1121–31. <https://doi.org/10.1016/j.jmrt.2018.09.002>.

- [166] Asadikiya M, Zhang Y, Wang L, Apelian D, Zhong Y. Design of ternary high-entropy aluminum alloys (HEAs). *J Alloys Compd* 2022;891. <https://doi.org/10.1016/j.jallcom.2021.161836>.
- [167] Zenk CH, Neumeier S, Stone HJ, Göken M. Mechanical properties and lattice misfit of  $\gamma/\gamma'$  strengthened Co-base superalloys in the Co-W-Al-Ti quaternary system. *Intermetallics (Barking)* 2014;55:28–39. <https://doi.org/10.1016/j.intermet.2014.07.006>.
- [168] Souza FA, Costa MO, Magno IA, Nascimento JM, Silva AP, Costa TS, et al. Investigation on microstructural and microhardness evolution in as-cast and T6/heat-treated samples of a horizontally solidified AlSiCu alloy. *Journal of Materials Research and Technology* 2019;8:5046–52. <https://doi.org/10.1016/j.jmrt.2019.06.054>.